Cycles biogéochimiques océaniques : apports des traceurs élémentaires et isotopiques, l'aluminium et le fer couplés à une approche hydrodynamique

Lise Artigue

THÈSE

En vue de l'obtention du

DOCTORAT DE L'UNIVERSITÉ DE TOULOUSE

Délivré par : *l'Université Toulouse 3 Paul Sabatier (UT3 Paul Sabatier)*

Présentée et soutenue le *03/06/2020* **par :**

LISE ARTIGUE

Cycles biogéochimiques océaniques : apports des traceurs élémentaires et isotopiques, l'aluminium et le fer couplés à une approche hydrodynamique

---

JURY

MATTHIEU ROY-BARMAN	LSCE, Versailles	Rapporteur
CÉCILE GUIEU	LOV, Villefranche-sur-mer	Rapportrice
GÉRALDINE SARTHOU	LEMAR, Brest	Examinatrice
CATHERINE JEANDEL	LEGOS, Toulouse	Examinatrice
VALÉRIE CHAVAGNAC	GET, Toulouse	Invitée
FRANÇOIS LACAN	LEGOS, Toulouse	Directeur de thèse

École doctorale et spécialité :
SDU2E : Océan, Atmosphère et Surfaces Continentales
Unité de Recherche :
LEGOS - Laboratoire d'Études en Géophysique et Océanographie Spatiales
Directeur de Thèse :
François LACAN
Rapporteurs :
Matthieu ROY-BARMAN et *Cécile GUIEU*

Résumé

L'objectif global de cette thèse est de progresser sur la compréhension des cycles biogéochimiques océaniques (sources, cycles internes, puits) à l'aide de traceurs présents dans l'eau de mer (la concentration d'aluminium dissous et la composition isotopique du fer dissous) combinés à des outils hydrodynamiques. L'aluminium est utilisé comme traceur des sources lithogéniques à l'océan alors que les isotopes du fer nous renseignent sur le cycle du fer dans l'océan. Cette thèse se concentre en premier lieu sur l'analyse de masses d'eau d'une section longitudinale à 22ºN dans l'Atlantique Nord réalisée dans le cadre de la campagne GEOTRACES GApr08. Cette étude combine pour la première fois une analyse multiparamétrique optimale des masses d'eau (extended optimum multiparameter analysis eOMPA) à une estimation de leurs trajectoires Lagrangiennes issues d'un modèle hydrodynamique. Par ailleurs, les mesures d'aluminium dissous (dAl) effectuées ont permis de produire une première section de dAl à 22ºN et ces mêmes outils, une analyse poussée. En effet, l'utilisation conjointe du modèle 1D d'advection-dépôt de poussière en surface et des résultats de l'eOMPA a mis en valeur les processus prédominants associés aux concentrations de dAl mesurées. (i) En surface, l'advection et le dépôt de poussière atmosphérique sont tous deux essentiels pour expliquer les concentrations de dAl observées bien que dans l'ouest, une source externe supplémentaire est nécessaire. Cette source pourrait provenir soit du fleuve Amazone, soit de l'érosion des petites Antilles. (ii) Entre 200 et 800m, alors qu'on se situe dans une zone de fort dépôt atmosphérique (sous le panache saharien), les fortes concentrations de dAl résultent du transport océanique. Le bilan net des interactions dissous-particules est pourtant une soustraction de dAl, probablement par adsorption sur les particules. (iii) En dessous de 800 m, l'effet des interactions dissous-particules s'inverse et le scavenging réversible est une source nette de dAl. (iv) En dessous de 3340 m, la source hydrothermale Snakepit s'avère être une source locale importante de dAl.

Contrairement à l'aluminium, le fer (Fe) est un micronutriment essentiel à la production primaire. Ce micronutriment limite la production primaire dans 30 à 40 % de l'océan. Dans le cadre des campagnes GEOTRACES KEOPS 1 et 2, nos mesures d'isotopes de Fe présentées dans cette thèse permettent l'étude des sources de micronutriments dans une zone naturellement fertilisée de l'océan Austral, les îles Kerguelen. Nos mesures d'isotopes de Fe révèlent plusieurs éléments sur son cycle. (i) En l'absence d'apport externe, les signatures isotopiques de Fe des masses d'eau sont conservées sur plus de 4500 kilomètres, ce qui permet d'utiliser ce traceur pour suivre l'origine du Fe dans l'océan. (ii) Une source sédimentaire réductrice de Fe dissous provenant de la marge des îles Kerguelen alimente la production primaire en aval. (iii) Une source sédimentaire locale non réductrice de Fe dissous impacte les eaux de fond des stations situées au niveau du plateau des Kerguelen, mais ne semble pas contribuer significativement aux eaux moins profondes. Ce résultat est identifié pour la première fois directement dans une région HNLC.

L'ensemble de ces travaux souligne le caractère essentiel 1) de la prise en compte des transports horizontaux, si possible de manière quantitative, dans l'interprétation des distributions d'éléments traces et d'isotopes, 2) des interactions dissous particules, notamment le processus dit de scavenging réversible (adsorption-désorption), sur les cycles des éléments traces et isotopes.

Mots clés : Aluminium dissous, Isotopes de fer, eOMPA, Expériences Lagrangiennes, Océan Austral, Océan Atlantic Nord Subtropical, GEOTRACES, KEOPS, GApr08.

Abstract

The overall objective of this thesis is to further our understanding of ocean biogeochemical cycles (sources, internal cycles, sinks) using tracers present in seawater (the concentration of dissolved aluminium and the isotopic composition of dissolved iron) combined with hydrodynamic tools. Aluminum is used as a tracer from lithogenic sources to the ocean, while iron isotopes tell us about the iron cycle in the ocean. This thesis focuses first on the analysis of water masses of the 22ºN longitudinal section in the North Atlantic carried out in the framework of the GEOTRACES GApr08 campaign. This study combines for the first time an extended optimum multiparameter analysis (eOMPA) of water masses with an estimation of their Lagrangian trajectories from a hydrodynamic model. In addition, the dissolved aluminium (dAl) measurements carried out have made it possible to produce a first section of dAl at 22ºN and these same tools have enabled an advanced analysis. The joint use of the 1D model of surface dust advection-deposition and the eOMPA results highlighted the predominant processes associated with the measured dAl concentrations. (i) At the surface, both advection and deposition of atmospheric dust are essential to explain the observed dAl concentrations, although in the west, an additional external source is required. This source could come either from the Amazon River or from erosion in the Petites Antilles. (ii) Between 200 and 800m, in an area of strong atmospheric deposition (below the Saharan plume), high dAl concentrations result from oceanic transport. The net balance of dissolved-particle interactions, however, is a subtraction of dAl, probably by adsorption onto particles. (iii) Below 800 m, the effect of dissolved-particle interactions is reversed and reversible scavenging results in a net source of dAl. (iv) Below 3340 m, the Snakepit hydrothermal source is found to be a significant local source of dAl.
Unlike aluminium, iron (Fe) is an essential micronutrient for primary production. This micronutrient limits the primary production in 30-40% of the ocean. In the framework of the GEOTRACES KEOPS 1 and 2 campaigns, the Fe isotope measurements presented in this thesis allow the study of micronutrient sources in a naturally fertilized area of the Southern Ocean, the Kerguelen Islands. Our Fe isotope measurements reveal several elements on its cycle. (i) In the absence of external input, the Fe isotope signatures of water masses are preserved over 4500 kilometers, which allows us to use this tracer to follow the origin of Fe in the ocean. (ii) A reducing sedimentary source of dissolved Fe from the Kerguelen Island margin feeds primary production downstream. (iii) A local non-reducing sedimentary source of dissolved Fe impacts the bottom waters of the Kerguelen Plateau stations, but does not appear to contribute significantly to the shallower waters. This result is identified for the first time directly in an HNLC region.
This PhD work highlights the key importance of 1) taking into account horizontal transport, if possible quantitatively, in the interpretation of trace element and isotope distributions, and 2) the interactions of dissolved particles, in particular the so-called reversible scavenging process (adsorption-desorption), on the cycles of trace elements and isotopes.

Key words: Dissolved aluminum, Iron isotopes, eOMPA, Lagrangian experiment, Austral ocean, Subtropical North Atlantic, GEOTRACES, KEOPS, GApr08.

Remerciements

Ça y est… 3 ans 5 mois et 3 jours plus tard, la grande et très belle aventure qu'a été cette thèse se termine. Et quelle aventure ! J'ai passé 3 ans dans une équipe formidable, à étudier un sujet qui me passionne, à partir en mission en mer, en conférence, en école d'été et dans un laboratoire à l'étranger. J'ai aussi dû faire face à un peu, beaucoup, de challenges (pour ne pas dire de difficultés) mais toujours en étant accompagnée de personnes formidables. Il est grand temps de les remercier comme il se doit, avec à mon habitude « un peu » de contexte.

Cette belle aventure a débuté alors que je participais à la mission Green Edge 2016 à Qikiqtarjuaq, petit village dans la région du Nunavut, au-delà du cercle polaire Arctique. Pour obtenir la bourse ministérielle qui a permis de financer cette thèse, j'ai dû passer à 4h du matin mon oral en visio, depuis l'école de Qikiqtarjuaq, seul endroit du village possédant le wifi. Je remercie François, mon futur directeur de thèse, qui m'avait déjà montré son soutien dans la préparation de cet oral à distance et tous les scientifiques et non scientifiques qui faisaient partie de cette mission et ceux qui m'ont fait répéter mon oral. Surtout merci d'avoir célébré avec moi l'obtention de cette bourse de thèse en trinquant … à la camomille (seule boisson différente de l'eau que nous avions). Particulièrement merci à Audrey ma super coloc de chambre, Patrick, Bernard, Justine, Camille… Je remercie profondément Jean-François Rontani mon encadrant de stage de fin d'étude pour sa gentillesse infinie et pour m'avoir donné la chance incroyable de participer à ce fameux camp de glace. Rémi je te remercie de m'avoir transmis tes connaissances sur ton sujet et de m'avoir laissé te suivre à la trace au MIO. Marie-Aimée je te remercie de m'avoir montré à quel point la science c'était méga fun.

En octobre 2016, j'ai donc commencé ma thèse au LEGOS au sein de la formidable et très soudée équipe TIM. Tout d'abord merci à François, mon super directeur de thèse. Merci pour ton soutien constant au cours de ces années, pour ta disponibilité illimitée dès qu'il y en avait besoin. Véritable mentor, tu m'as presque tout appris sur le domaine de la géochimie marine mais aussi sur ce que c'est vraiment d'être un chercheur (notamment toujours garder un esprit critique). Je te remercie d'avoir encadré cette thèse avec humour, compétence et exigence mais aussi de m'avoir permis de dévier (légèrement…) du sujet initial (quel casse-tête de trouver un titre à cette thèse in fine). Merci à tous les autres membres de l'équipe TIM. Catherine, je t'avais rencontrée il y a quelques années au cours d'un ciné/débat sur le film « La Glace et le Ciel ». J'étais loin de m'imaginer que je serais un jour dans la même équipe que toi et que tu me ferais l'honneur d'être la présidente de mon jury de thèse. Kathy, merci de m'avoir appris à maniper en salle blanche, mais surtout merci de ta bienveillance et de ton soutien constant. Tu es une super ingénieure ! Pieter, Marc, merci à tous les deux pour votre bonne humeur quotidienne et pour m'avoir fait rire à chaque pause-café. Jessy, merci d'avoir partagé ton expérience sur les isotopes du fer avec moi et d'avoir été ma co-paillasse de salle blanche et ma super co-bureau. Merci pour la petite sculpture de Ganesh. Mélanie, Joe, Viet, merci pour nos agréables discussions au détour d'un couloir ou d'un café. Elena, merci pour

ta gentillesse et merci d'avoir répondu à toutes mes questions sur le programme GEOTRACES. Moustafa, merci pour ta gentillesse infinie. Un grand merci à la paire Simon et Émilie, respectivement mon grand frère et ma grande sœur de thèse. Merci d'avoir mis une ambiance de folie dans cette équipe, de m'avoir intégrée dès mon arrivée, d'avoir partagé de nombreux pots de départ et d'arrivée ainsi que de nombreux fous rires. Restez comme vous êtes ! Marion, ma petite sœur de thèse, un grand merci à toi d'avoir été là pendant la dernière année de cette thèse littéralement au jour le jour en tant que co-bureau, collègue et surtout amie. Merci pour ton soutien dans tous les domaines, et merci de m'avoir nourrie de pain et de dattes. Dans peu de temps ce sera à ton tour de soutenir ta thèse et tu le feras avec brio ! Maintenant tu as toi aussi une petite sœur de thèse, Morgane que je remercie pour sa présence à la toute fin de ma thèse, et à qui je lègue (bon ce n'est pas comme si j'avais eu le choix) mon bureau.

Je remercie grandement tous les co-bureau que j'ai eu au cours de ces années, avec qui on s'est serré les coudes et qui sont devenus de vrais amis. Pour celles et ceux que je n'ai pas encore cité, merci à Charlotte tu es un véritable modèle à suivre pour une fin de thèse équilibrée, Fifi pour tes phrases philosophiques et ta bonne humeur constante. Merci à Cori, la psychologue attitrée du LEGOS, un grand merci à toi pour ton soutien en fin de thèse, merci d'avoir été une oreille attentive et bienveillante, une super coach toujours un chronomètre à la main. Merci à Benjamin qui est arrivé la toute dernière semaine avant mon rendu, j'espère ne pas t'avoir fait trop peur…

Je remercie également la belle bande des doctorants/CDD du LEGOS avec qui j'ai partagé de nombreux déjeunés. Merci aux deux Marine, à Vanessa, Florence, Kévin, Boucle d'or/Hakim le forgeron, Michel (même si tu m'as piqué quelques gâteaux...), Aude merci pour ta sagesse (je sais que tu vas adorer cette phrase). Merci aux thésardes de mon année, Alice, Violaine et Inès, trois acolytes géniales. Merci à notre artiste en chef Manon Q. Merci à Simon B. pour tes soirées cinémas et la fête de mes 25 ans. Merci à Manon G. pour ton aide avec Matlab, les soirées jeux de société, et pour m'avoir laissé dormir chez vous quelque fois. Merci à Audrey D. (ta soutenance va être superbe), à Romain pour ces supers week-end à Billière, à Pierre pour ta bonne humeur à toute épreuve, à Adélaïde merci pour nos longues discussions, et à Lisa merci d'être devenue ma super coloc. Merci aussi à Nolwenn, Marco, Gabriela et celles et ceux que j'ai probablement oublié.

Je remercie également les doctorants étrangers qui ne sont passés que quelques mois au LEGOS mais avec qui j'ai lié de belles amitiés. Un grand merci à Susanna pour ton rire et ces dimanches scones/The crown. J'espère te revoir vite à Seattle ou ailleurs. Muchas gracias a mi amiga Carmen (o Ana), gracias por todas esas risas, sigue siendo como eres, una mujer llena de vida, humor y corazón en la mano. Espero verte pronto. Et … on n'oublie pas les postdocs ! Merci Audrey H. d'avoir été là en fin de thèse, toujours pleine d'énergie, et d'humour. Et merci d'avoir relu mon abstract !

Que serait le LEGOS sans les fées du Gessec … Un grand merci à Martine, Nadine, Agathe et Brigitte pour m'avoir guidée dans les méandres de l'administration. Merci pour votre gentillesse, bienveillance, et votre humour quotidien. Et un merci spécial à Nadine ! On se connait depuis toujours et je suis absolument ravie d'avoir passé 3 ans à deux pas de ta porte.

From December 20th, 2017 to February 1st, 2018, I had the chance to participate to the Fridge GA13 cruise. I would like to thanks all the member of the Fridge cruise, the scientist and the

staff, which who I lived an incredible adventure crossing the Atlantic, celebrating Christmas, and New Year onboard. Many thanks to Maeve Lohan, Alessandro Tagliabue, and all the members of the trace metal team Dakota, Arthur, Wenhao, and Travis. Many thanks to Amber my roommate on the cruise, Allison, Azy, Carl, Dave and David, Haley, Joe, Kate, Malcolm, Noah, Pascal, Rachel, Sarah, Sean, Shaun, and Valérie. Thanks to Dave, I can't hear the song, Africa, without thinking about all of you.
In April 2018, I had the chance to spend one month and a half at the NOC, Southampton. Many thanks to Maeve Lohan for giving me this opportunity, Neil for learning me the FIA system, Koko you integrated me so well in the lab, many thanks for that! I had a lot of fun with your amazing PhD group (the two Alex, Sarah, Africa, and the others).
Je remercie mon comité de thèse qui lors de nos réunions annuelles m'a toujours guidé avec bienveillance, Damien Cardinal et Jeroen Sonke.
Je remercie Simon van Gennip, pour notre collaboration fructueuse. Merci pour ta gentillesse, ta disponibilité et ton professionnalisme.
Je remercie le directeur du LEGOS pendant mes années de doctorat, Alexandre Ganachaud. Merci d'avoir toujours été à l'écoute et de m'avoir permis d'être financée quelque mois de plus alors que je ne pouvais pas soutenir à cause du confinement.
Je remercie l'école doctorale SDU2E, Geneviève Soucail, Marie-Claude Cathala et Tanya Robinson pour leur gentillesse et leur accompagnement, particulièrement lors du confinement où nous étions dans l'incertitude totale sur la date et les conditions dans lesquelles je pourrais soutenir.
Un grand merci aux membres de mon jury de thèse, Cécile Guieu, Matthieu Roy-Barman, Géraldine Sarthou, Catherine Jeandel, et Valérie Chavagnac. J'étais honorée que vous ayez évalué mon travail de thèse, merci pour cette soutenance et les discussions qui en ont découlées. Valérie, merci de me permettre de continuer l'aventure de la géochimie marine avec toi en postdoc, sur les sources hydrothermales.
Je remercie les deux personnes qui ont relue cette thèse pour vérifier l'orthographe, Kathy Pradoux et Hugues Martin.
Merci à tous mes amis d'enfance, de lycée (notamment Camille et Laure), de CPE Lyon (Poupou, Sylvain, J-B, Marion, Elé, Laura, aux filles du groupe Italia/Scotland), de l'Insa Toulouse (merci à tous les membres de la super coloc du 28 rue des Marchands) pour m'avoir écouté quand je vous parlais sans relâche de ma passion pour l'océanographie et de mon rêve d'en faire mon métier. Et merci à toi Roxane, pour tes messages vocaux quotidiens qui m'ont soutenue pendant cette dernière année de thèse. Tu es une amie incroyable et bientôt future docteure également.

Enfin, je tiens à remercier ceux qui sont là depuis le tout début. Merci à ma famille de m'avoir toujours soutenue. Merci à mes parents de m'avoir ouvert à de nombreux domaines, de m'avoir permis de développer ma passion pour l'océanographie notamment en retapissant ma chambre de dauphins et en me payant mes premières plongées en Corse. Merci de m'avoir soutenue tout au long de ces longues études en particulier pendant la période difficile de la prépa. Il est difficile de trouver les mots pour vous exprimer ma reconnaissance et mon amour. Merci à mon petit frère Clément, tu es absolument génial. Merci à mes oncles et tantes, mes cousins/cousine et à mes grands-parents.

A ma grand-mère, Marie Artigue, ta force, ta sagesse, et ton intelligence me guideront toujours.

Liste des figures

Liste des tableaux

Sommaire

1 Introduction

1.1 Le réservoir océan

Pour comprendre le fonctionnement de la planète, il est nécessaire d'étudier la distribution des éléments chimiques au sein des différents réservoirs (atmosphère, océan etc.), de quantifier les flux de matières entre et au sein de ces différents réservoirs et de comprendre les processus sous-jacents.
La chimie de l'océan a des impacts sur (i) la composition chimique de l'atmosphère et donc le climat, (ii) la production biologique primaire marine, et ainsi le réseau trophique aquatique et les ressources halieutiques, et (iii) la qualité de l'eau et la pollution du littoral.
Indirectement, l'étude du cycle des éléments chimiques marins nous renseigne également sur les processus auxquels ces éléments prennent part, ces éléments sont alors utilisés comme traceurs. Ils permettent ainsi par exemple de quantifier la circulation océanique et donc les flux de chaleur qui, via l'interface air-mer, ont un impact sur le climat.
Cette thèse s'intéresse à la biogéochimie marine qui consiste en l'étude du cycle des éléments chimiques dans l'océan (distribution, quantification des flux, processus) et de leurs propriétés de traceur pour étudier le fonctionnement physique, chimique et biologique de l'océan (Roy-Barman & Jeandel, 2016).

1.2 Les métaux traces

À partir des années 1970, l'évolution de la chimie analytique, de l'instrumentation et des techniques de prélèvement et de mesures dites « ultra-propres » (exemples en annexe 7.1) a permis de fortement progresser dans nos connaissances sur la biogéochimie des éléments à des concentrations inférieures à ~10 µmol/kg (1ppm) dans l'océan, appelés éléments traces ou métaux traces (Bruland & Lohan, 2006). Depuis, nos connaissances de ces derniers n'ont cessé de se développer notamment grâce à leurs mesures au sein de programmes mondiaux d'études tel que Geochemical Ocean Section Study (GEOSECS, 1972-1978), Transient Tracers in the Ocean (TTO, 1981-1983), World Ocean Circulation Experiment (WOCE, 1990-1997) et GEOTRACES (lancé en 2010). Les métaux à l'état de traces dans l'eau de mer peuvent exister sous diverses formes physiques (particulaires ou dissoutes) et chimiques, avoir un rôle direct dans la production primaire ou encore être des traceurs des processus océaniques actuels et passés.

1.2.1 Les nutriments

Parmi les éléments nutritifs, on distingue les macronutriments des micronutriments (Moore et al., 2013). Les macronutriments, tels que le carbone (C), l'azote (N), et le phosphore (P) sont assimilés par le phytoplancton sous différentes formes au cours de la photosynthèse et sont donc essentiels à la production de matière vivante dans l'océan. D'autres

macronutriments tels que le calcium (Ca) et le silicium (Si) sont essentiels à la formation des tests de certains organismes phytoplanctoniques comme les coccolithophoridés et les diatomées. Les micronutriments sont des métaux traces eux aussi nécessaires aux fonctions métaboliques essentielles des organismes marins (transporteurs d'électrons dans les processus de respiration et de photosynthèse, et cofacteurs d'enzymes). La Figure 1 illustre l'implication des micronutriments fer (Fe), molybdène (Mo), nickel (Ni), zinc (Zn), cadmium (Cd) et cobalt (Co) dans l'acquisition et l'assimilation des nutriments N, C, et P par le phytoplancton marin. On y voit que le Fe et le Mo sont des cofacteurs des nitrates et nitrites réductases (réduction du nitrate NO_3^- et nitrite NO_2^-) et de la nitrogénase (fixation du nitrogène N_2), que le Ni est un cofacteur de l'urease (hydrolyse de l'urée $CO(NH_2)_2$), que le Zn est un cofacteur de la phosphatase alcaline (hydrolyse des esters de phosphate), et que le Zn, Cd et Co sont des cofacteurs de l'anhydrase carbonique (hydratation et déshydratation du CO_2).

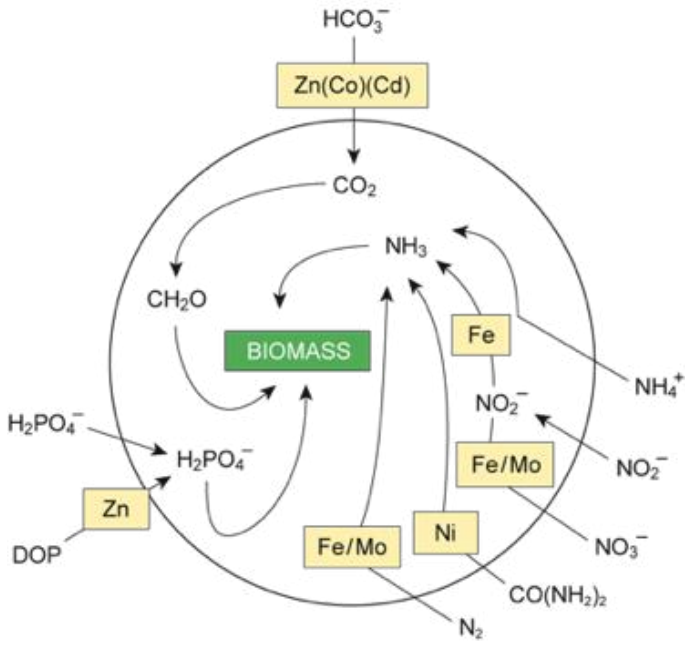

Figure 1: Besoins en métaux primaires pour l'acquisition et l'assimilation du carbone, de l'azote et du phosphore par le phytoplancton marin (Morel & Price, 2003).

Du fait de cette forte implication dans les fonctions métaboliques des organismes marins et de leurs faibles concentrations dans certaines régions, certains micronutriments limitent la production primaire. La Figure 2 présente les trois grandes régions océaniques (l'océan Austral, le Pacifique équatorial Est, et le Pacifique Nord) où la production primaire n'a pas consommé l'intégralité du macronutriment nitrate disponible. Ces régions sont appelées high-nutrient low chlorophyll (HNLC). C'est à la fin des années 1980 que Martin et al (1988a; 1988b) suggèrent que si la production primaire n'a pas consommé l'intégralité des macronutriments c'est parce qu'elle y est carencée en Fe. Depuis, de nombreuses expériences de fertilisation artificielles et naturelles (indiquées sur la Figure 2) ont permis de confirmer l'importance des micronutriments, et en particulier du Fe, sur la dynamique de la production primaire (Boyd et al., 2007 et références incluses).

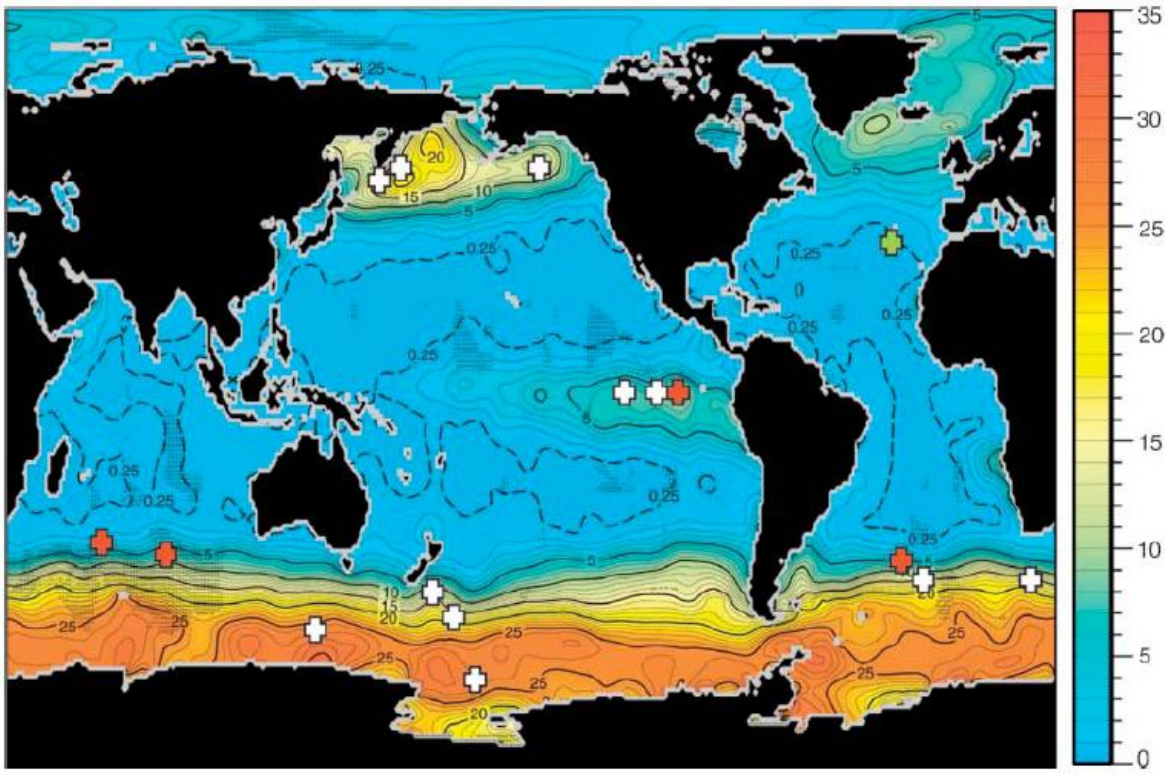

Figure 2 : Concentration de nitrates (µmol/L) dans la couche mélangée de surface, en moyenne annuelle, mettant en évidence les régions HNLC. Sont indiquées les positions des sites d'expériences de fertilisation en fer, artificielles (croix blanches) et naturelles (croix rouges), ainsi que de fertilisation en Fe et P (croix vertes, Boyd et al., 2007).

Ainsi depuis une vingtaine d'années, le Fe est inclus dans les modèles biogéochimiques qui suggèrent que la production primaire est limitée dans 30 à 50 % de l'océan mondial (Moore & Braucher, 2008 et références incluses). La Figure 3 propose une estimation des facteurs limitant les taux de croissance de différentes espèces phytoplanctoniques dont les macronutriments N, P et Si et le micronutriment Fe (Moore et al., 2004). Dans certaines régions océaniques, la production primaire est limitée par l'association de deux ou plusieurs micronutriments et/ou macronutriments, c'est la co-limitation (ex. co-limitation azote-fer, Browning et al., 2017; Moore et al., 2013).

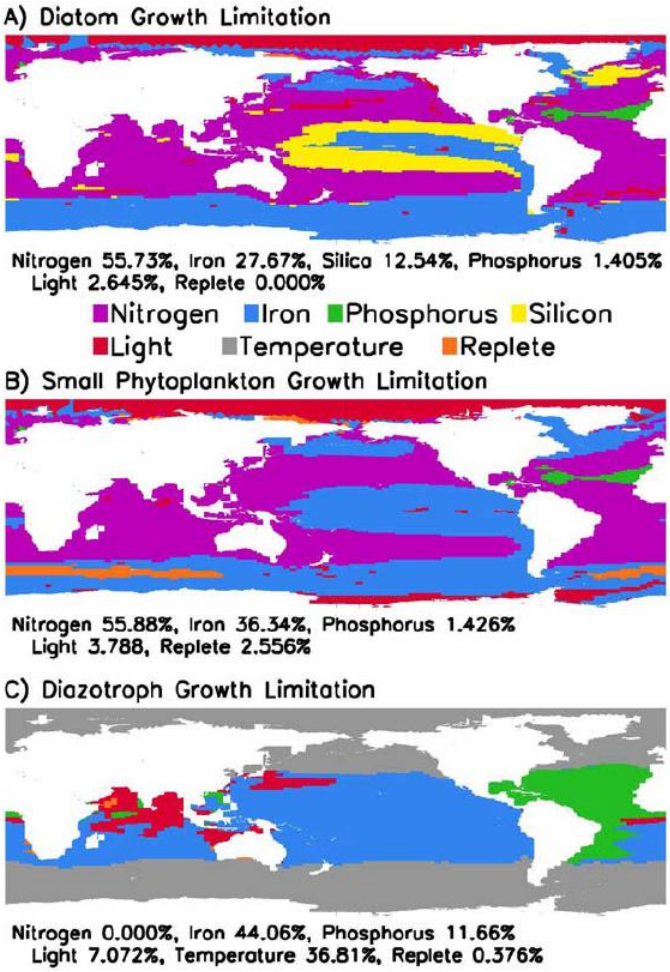

Figure 3: Facteurs limitant les taux de croissance pour chaque groupe de phytoplancton pour les mois d'été de chaque hémisphère (Moore et al., 2004).

Le type et la quantité de métaux traces nécessaires à la croissance des différentes espèces phytoplanctoniques dépend de l'évolution de ces espèces au cours du temps et de leur stratégie d'adaptation face à la disponibilité de ces métaux traces (Cullen et al., 1999; Peers & Price, 2006; Strzepek & Harrison, 2004). Par exemple, les diatomées et certains autres groupes d'algues situées dans l'océan ouvert sont moins sensibles à la limitation en Fe que les espèces côtières (Peers et al., 2005; Ryther & Kramer, 1961; Sunda & Huntsman, 1995).

Ainsi en contrôlant l'amplitude de la production primaire mais aussi les variations adaptatives des propriétés structurales des espèces phytoplanctoniques, les micronutriments contrôlent des facteurs clés de la régulation du cycle du carbone océanique. L'étude des cycles biogéochimiques des métaux traces (distribution, sources externes, cycles internes, flux et processus sous-jacents) est donc essentielle dans le contexte du changement climatique.

1.2.2 Les traceurs

Les traceurs sont des éléments chimiques qui permettent de suivre (tracer) un processus dans l'océan (Roy-Barman & Jeandel, 2016). On distingue les traceurs « actifs » qui impactent directement les processus auxquels on s'intéresse (comme la température et la salinité qui sont des traceurs actifs de la circulation océanique) des traceurs « passifs » qui n'influencent pas directement ces processus.
Parmi les traceurs passifs on peut citer le tritium, produit par des essais nucléaires, qui est un traceur de l'écoulement des fluides dans l'océan. La pénétration de ce traceur dans l'Atlantique Nord, indique le point d'entrée de l'eau nouvellement ventilée dans la circulation thermohaline globale. Ainsi les distributions de tritium permettent de visualiser les voies de ventilation et les échelles de temps de la circulation océanique (Jenkins, 2003). Les isotopes du néodyme permettent quant à eux d'identifier l'origine des masses d'eau et de tracer les interactions marge continentale/océan (Jeandel, 1993; Lacan & Jeandel, 2005). Les terres rares permettent de distinguer les différents types d'apports lithogéniques (Zhang et al., 2008). Les isotopes radioactifs (naturels et anthropogéniques) sont également largement utilisés comme « chronomètres » des processus marins ou pour étudier la dynamique des masses d'eau, des particules et les interactions dissous/particules. Le radium 224, par exemple, élément soluble avec sa courte demi-vie de quatre jours, est utilisé comme traceur des mélanges horizontaux à petite échelle (Jenkins, 2003), alors que le thorium 234 élément insoluble, avec une demi-vie de 24 jours est utilisé comme traceur de flux de particules dans les eaux de surface (Buesseler et al., 1998).

1.2.3 L'aluminium et le fer

Dans cette thèse nous nous intéresserons à deux métaux traces en particulier, tous les deux très abondant dans la croûte terrestre. On dit que ce sont des éléments d'origine lithogénique (originaire de la lithosphère).
L'un d'eux, l'aluminium (Al), est considéré comme un traceur de sources lithogéniques et l'autre, le fer (Fe), est un micronutriment essentiel à la production primaire. Ces deux traceurs, leurs sources externes et cycles internes seront présentés plus en détail dans les chapitres 3 et 4.

1.3 Sources externes et cycles internes des éléments dans l'océan

Les cycles biogéochimiques peuvent être décomposés en trois parties:

1- Les sources externes : ces sources sont les voies d'entrée des différents éléments au différentes interfaces de l'océan (atmosphère/océan, marges/océan etc.). Sur la Figure 4 les sources externes principales d'éléments à l'océan sont représentées (flèches rouges) i.e. les poussières atmosphériques, les rivières, les sédiments et l'hydrothermalisme.

2- Les cycles internes : une fois introduit dans l'océan, les éléments, présents dans différentes phases physico-chimiques, sont impactés par des processus biologiques, chimiques, et physiques (cf. Figure 4, flèches vertes, violettes et noires). Ces processus conduisent à des flux entre les différentes phases physico-chimiques. L'étude des cycles internes s'intéresse ces différents réservoirs, flux et processus.

3- Les puits : les éléments sont éliminés plus ou moins rapidement de la colonne d'eau via des puits d'éléments (cf. Figure 4, flèches grises).

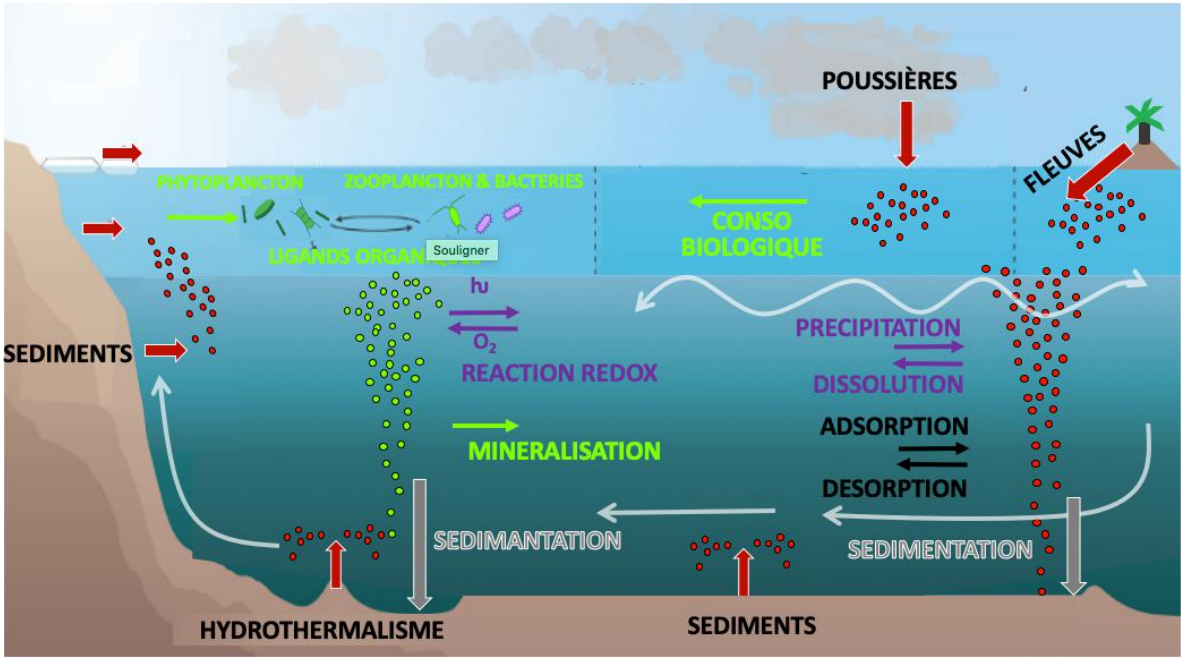

Figure 4 : Les cycles biogéochimiques océaniques. Les sources externes (flèches rouges), les cycles internes comprenant, processus biologiques (flèches vertes), chimiques (flèches violettes) et physiques (flèches noires), et les puits (flèches grises) sont indiqués (adaptée de Tagliabue et al., 2017).

Les sections suivantes présentent, de manière non-exhaustive, l'état actuel des connaissances sur les cycles biogéochimiques, dans un premier temps les sources externes et dans un deuxième temps les cycles internes et les puits (regroupés dans une même partie) pour une dizaine d'éléments traces.

1.3.1 Les sources externes

Element	Flux fluvial brut total (particulaire + dissous)	Flux atmosphérique total (particulaire +soluble)	Flux fluvial net dissous	Flux hydrothermal dissous	Flux atmosphérique soluble	Flux fluvial brut particulaire	Flux fluvial net particulaire	Flux atmosphérique particulaire
Al	5,4E+13	2,5E+11	3,5-6,0*E+10	1,2-6,0E+8	1,2E+10	5,4E+13	5,4E+12	2,4E+11
Fe	1,3E+13	6,5E+10	0,5-2,3*E+10	2,3-19E+10	4,9E+09	1,3E+13	1,3E+12	6,0E+10
Mn	3,0E+11	1,4E+11	5,0E+09	1,1-3,4E+10	5,0E+08	2,9E+11	2,9E+10	1,0E+09
Ni	2,4E+10	<0,1E+10	5,0E+08	-	<5E+8	2,0E+10	2,3E+09	<7,5E+8
Co	5,6E+09	4,0E+07	1,0E+08	6,6-68E+5	1E+07	5,2E+09	5,0E+08	3,0E+07
Cr	3,1E+10	<0,1E+10	3,6E+08	-	<1E+8	3E+10	3E+09	<9E+8
V	5,2E+10	<0,1E+10	7,0E+08	-	<2E+8	5E+10	5E+09	<5E+8
Cu	2,5E+10	6,0E+08	0,1-0,5E+10	3-13E+8	2E+08	2,4E+10	2,4E+09	4,0E+08
Pb	7,5E+09	1,3E+09	0,2-1,5E+8	2,7-110E+5	4E+08	7,5E+09	7,5E+08	9,0E+08
Zn	6,0E+10	3,1E+09	0,04-1,4E+10	0,1-0,3E+10	1,0E+09	6E+10	6E+09	1,7E+09
Cd	1,5E+09	<0,3E+8	3E+07	-	<2E+7	1,4E+08	1,4E+07	<7E+8

Tableau 1: Flux d'éléments provenant de sources majeures apportés à l'océan mondial, à l'exclusion des apports anthropiques modernes (d'après Libes, 2009).

1.3.1.1 Sources atmosphériques

Les apports atmosphériques délivrent des éléments à l'océan sous forme particulaire et dissoute. La plupart des particules éoliennes qui pénètrent dans l'océan ont une taille inférieure à 10 µm et sont appelées aérosols (Libes, 2009).

Duce et al (1991) ont été les premiers à fournir une indication à l'échelle régionale de la distribution et des flux mondiaux de métaux traces à l'océan, des espèces azotées et de composés organiques synthétiques à partir de mesures sur le terrain des aérosols atmosphériques. Dès lors, de nombreuses études sur l'importance des apports atmosphériques comme source d'éléments à l'océan ont été réalisées. La dissolution des aérosols atmosphériques est aujourd'hui considérée comme la principale source d'aluminium dissous dans l'océan ouvert (Jickells et al., 1994; Maring & Duce, 1987; Tria et al., 2007) et comme la principale source d'apport de fer à l'océan dans certaines régions océaniques (Tagliabue et al., 2017). Deux types d'estimation des flux de dépôts de poussières à l'océan (dépôt sec et humide) sont aujourd'hui utilisés. Premièrement, les estimations par modèles, basées sur les données de distribution mondiale des aérosols atmosphériques fournis par les satellites (Figure 5). Deuxièmement, les estimations par mesures directes (i) des aérosols, (ii) des métaux traces dissous dans l'eau de mer, (iii) des matières particulaires filtrées de la colonne d'eau, (iv) des particules collectées dans les pièges à sédiments et des sédiments (Anderson et al., 2016). Parmi les estimations par mesures directes des métaux traces dissous, celle de l'aluminium dissous est largement utilisée. En effet, l'aluminium dissous étant un composant majeur de la croûte continentale, pas ou peu impliqué dans les processus biologiques dans la majorité des régions océaniques et avec un temps de résidence court dans les eaux de surface (3 à 5 ans, Orians & Bruland, 1986b), il est utilisé comme traceur des apports atmosphériques à l'océan (Bruland & Lohan, 2006). Le modèle « MADCOW » est un des exemples les plus connus de l'utilisation de l'aluminium dissous pour reconstruire les

flux de dépôts atmosphériques à l'océan (Measures et al., 2005; Measures & Brown, 1996; Vink & Measures, 2001).

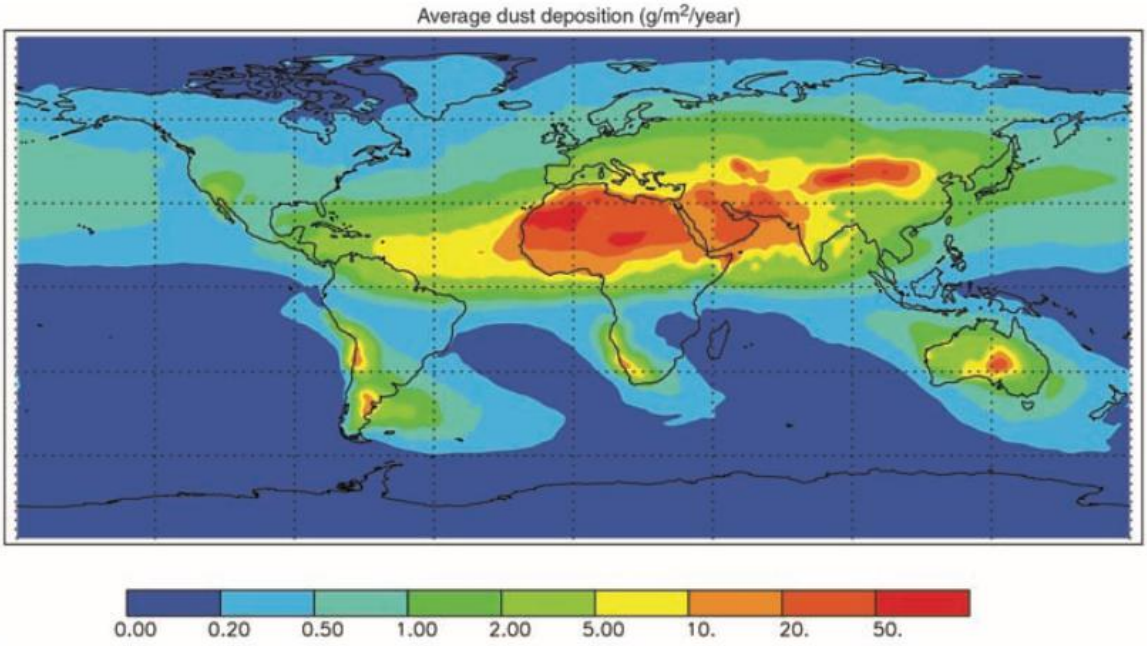

Figure 5: Flux de poussières vers les océans du monde basés sur un composite de trois études de modélisation. Total des apports de poussières atmosphériques dans les océans = 450 Tg an-1. Les pourcentages d'apports dans les bassins océaniques basés sur ce chiffre sont les suivants : Atlantique Nord, 43% ; Atlantique Sud, 4% ; Pacifique Nord, 15% ; Pacifique Sud, 6% ; Indien, 25% ; et océan Austral, 6% (Jickells et al., 2005).

Suivant les méthodes utilisées, les estimations de flux de poussière à l'océan présentent de larges gammes de variations. Du fait de nombreuses incertitudes, la quantification des dépôts de poussières et d'éléments à l'océan reste incertaine (Anderson et al., 2016). Parmi ces incertitudes, on peut notamment citer celles concernant les pourcentages de solubilité des métaux traces. Dans l'Atlantique par exemple leurs valeurs peuvent varier d'un facteur 100 : entre 0.1%-98% pour le fer (Sholkovitz et al., 2012), 0.2%-87% pour l'aluminium et 4.5%-96% pour le manganèse (Baker et al., 2013). Cette large gamme de solubilité s'explique par les nombreux paramètres pouvant l'influencer comme la source d'aérosol (ex saharienne, anthropique, Bonnet & Guieu, 2004), la taille des particules (Baker & Jickells, 2006), la minéralogie des poussières (Journet et al., 2008), les processus atmosphériques impactant la spéciation des éléments (photoréduction, complexation organique..), la durée de vie des poussières ou encore les techniques de mesure de solubilité utilisées (Mahowald et al., 2005). Une autre incertitude concerne la variabilité temporelle des apports atmosphériques dont le flux peut varier significativement suivant les saisons. Enfin les flux de métaux traces provenant d'aérosols anthropiques sont mal contraints et suivant des études récentes très probablement sous-estimés (Conway et al., 2019; Ito et al., 2019).

1.3.1.2 Sources fluviales

Les apports fluviaux sont généralement considérés comme étant la source principale d'ions majeurs apportés à l'océan (Bruland & Lohan, 2006). L'importance des apports fluviaux de métaux traces à l'océan est cependant plus difficile à établir du fait de nombreux facteurs :

1- Peu de données historiques sont valables car échantillonnées avant le développement de techniques propres de prélèvement des métaux traces (Bruland & Lohan, 2006).

2- Bien que les flux bruts de métaux traces dissous et particulaires apportés par les rivières à l'océan soient très importants (Tableau 1), il est nécessaire de comprendre les processus (interactions dissous-particule, biologie) ayant lieu à l'interface rivière-océan – dans les estuaires – pour réellement en estimer l'impact sur l'océan.
   Concernant les apports de métaux traces dissous, il a par exemple été montré que de très grandes proportions de fer dissous étaient éliminées dans les estuaires par des mécanismes de floculation et de sédimentation (90%, Boyle et al., 1977). Ce mécanisme de floculation est d'autant plus important dans les estuaires de rivières riches en matières organiques où les métaux traces dissous tel que le fer, le cuivre, le nickel et le zinc peuvent s'associer aux acides humiques et ainsi précipiter dans de larges proportions (Sholkovitz & Copland, 1981). D'autres métaux tels que l'aluminium dissous peuvent s'adsorber sur des particules puis sédimenter (scavenging) dans les estuaires. Ainsi, bien que les rivières étaient initialement considérées comme la source principale d'aluminium dissous à l'océan, elles sont aujourd'hui perçues comme une source négligeable (Hydes, 1979; Orians & Bruland, 1986b; Stoffyn & Mackenzie, 1982).
   Concernant les apports de particules fluviales, plusieurs études ont montré que pour de nombreux éléments, le flux de particules fluviales était bien supérieur au flux dissous correspondant (jusqu'à 1000 fois supérieur pour l'Al, Gaillardet et al., 1999, 2003; Oelkers et al., 2011; Viers et al., 2009). La Figure 6 synthétise les résultats de ces études et présente le ratio entre le flux global de particules fluviales et le flux dissous de nombreux éléments, dont plusieurs métaux traces. On y observe que pour tous les éléments présentés excepté le sodium (Na), le flux particulaire est supérieur au dissous. Une grande partie de ces particules fluviales se dépose sur les marges continentales et peut par la suite être remobilisée pour être transmise, sous forme dissoute ou particulaire, vers la colonne d'eau. Pour plusieurs éléments, il a été montré au cours des vingt dernières années qu'une fraction faible mais non nulle de ces particules terrigènes remobilisées dans la colonne d'eau se dissout et peut ensuite être transportée sur de longues distances, par exemple 3 à 5 % pour le néodyme (Arsouze et al., 2009; Jeandel et al., 2011; Lacan & Jeandel, 2005). La dissolution de particules terrigènes déchargées par les rivières à l'océan est donc aujourd'hui considérée comme ayant un impact important sur le cycle global de certains éléments tel que les terres rares, le néodyme, le silicium, ou le fer (Jeandel & Oelkers, 2015; Radic et al., 2011a). La section suivante traite plus en détail des processus de sources sédimentaires de métaux traces.

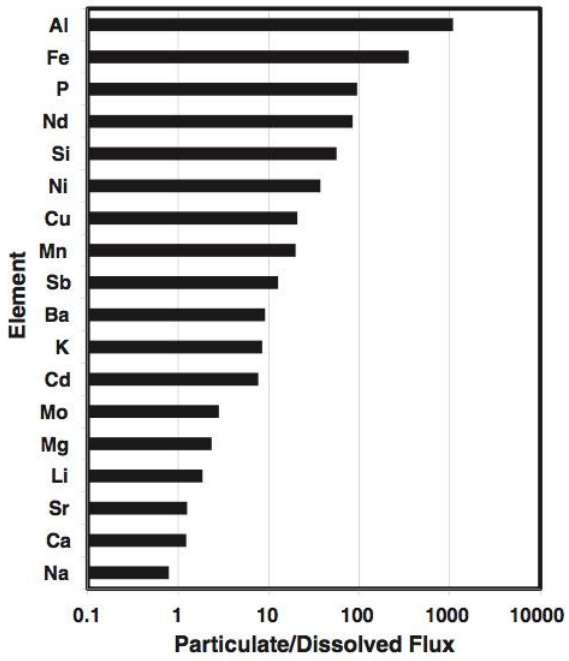

Figure 6 : Rapport entre le flux global de particules fluviales et le flux dissous correspondant pour plusieurs éléments (Jeandel & Oelkers, 2015 et références incluses).

3- Les décharges d'eau souterraines en mer (« SGD, Submarine Groundwater Discharge ») constituent des flux d'eau et d'éléments chimiques qui ont été moins étudiés que les apports de surface. Les flux d'eau souterraine d'origine continentale représentent de l'ordre de 6 % des apports par les fleuves (Moore, 1996).

En conclusion, l'importance des apports fluviaux de métaux traces à l'océan soulève encore beaucoup de questions et dépend principalement des processus en jeu dans les estuaires et à l'interface sédiments/eau de mer.

1.3.1.3 Sources sédimentaires

Comme expliqué précédemment, lorsqu'ils se déposent dans les sédiments de surface, les métaux traces peuvent être recyclés dans la phase dissoute et servir de sources pour l'océan (Bruland & Lohan, 2006). Ainsi des augmentations de concentration de nombreux métaux dissous à l'interface eau-sédiment ont été mesurées notamment pour le fer (ex Klar et al., 2017a, 2018; Planquette et al., 2007) et l'aluminium (Middag et al., 2009; Moran & Moore, 1991). Les apports de fer benthique à l'eau de mer sont maintenant inclus dans de nombreux modèles biogéochimiques (Aumont et al., 2003; Moore et al., 2004) et peuvent être tracés grâce notamment aux isotopes du radium (van Beek et al., 2008), à l'actinium 227 (Geibert et al., 2002), aux terres rares (Zhang et al., 2008), ou encore grâce aux isotopes du fer (Klar et al., 2018; Radic et al., 2011a). Cependant, de nombreuses questions restent en suspens concernant les flux de métaux traces à l'interface sédiment/eau de mer et les processus sous-jacents. Parmi les processus de remobilisation sédimentaire identifiés, on peut citer la réduction dissimilatoire du fer (DIR, Canfield et al., 1993) qui fait intervenir des processus redox et la dissolution non réductrice (NRD, Radic et al., 2011a) qui, contrairement à la DIR,

est indépendante des conditions redox et pourrait impacter de nombreux métaux traces. Ces processus seront expliqués plus en détail dans le chapitre 4.

1.3.1.4 Sources hydrothermales

Les émissions hydrothermales sont généralement considérées comme des puits océaniques pour les ions majeurs tels que le magnésium et le sulfate, des sources importantes de métaux traces telles que le fer, le manganèse et le zinc et des sources moins importantes pour l'aluminium, le cuivre, le cobalt et le plomb (Bruland & Lohan, 2006; Libes, 2009). Le transport des éléments à la sortie de ces sources hydrothermales est dépendant des processus physico-chimiques et de l'activité microbienne qui les impactent. Par exemple, bien que la concentration de fer et de manganèse puisse être un million de fois plus élevée dans les sources hydrothermales que dans l'eau de mer, une grande partie du fer hydrothermal est rapidement oxydé puis précipité et déposé sous forme de sédiments sur les dorsales médio-océaniques (Bruland & Lohan, 2006). En revanche, le manganèse dissous étant oxydé plus lentement que le fer dissous dans l'eau de mer, il est généralement considéré comme pouvant être transporté plus loin (> 2000 km) que le fer avant son oxydation et sa précipitation (Bruland & Lohan, 2006).

Il a donc été longtemps considéré que les émissions hydrothermales des fonds marins ne constituaient pas une source majeure de fer ou d'aluminium dissous dans l'océan, contrairement au manganèse. Cependant des études plus récentes montrent le contraire. La présence d'aluminium dissous d'origine hydrothermale a déjà été identifiée au-dessus de la ride Médio-Atlantique (source hydrothermale TAG, Lunel et al., 1990; Measures et al., 2015). Sur la dorsale est-Pacifique, l'hydrothermalisme pourrait être à l'origine de panaches de fer et d'aluminium dissous s'étendant sur plusieurs milliers de kilomètres (4000 km et 3000 km respectivement, Figure 7, Resing et al., 2015). Dans la région de l'arc de Tonga, une source hydrothermale peu profonde pourrait être à l'origine de la fertilisation en fer dissous des eaux photiques du Pacifique sud-ouest (Guieu et al., 2018).

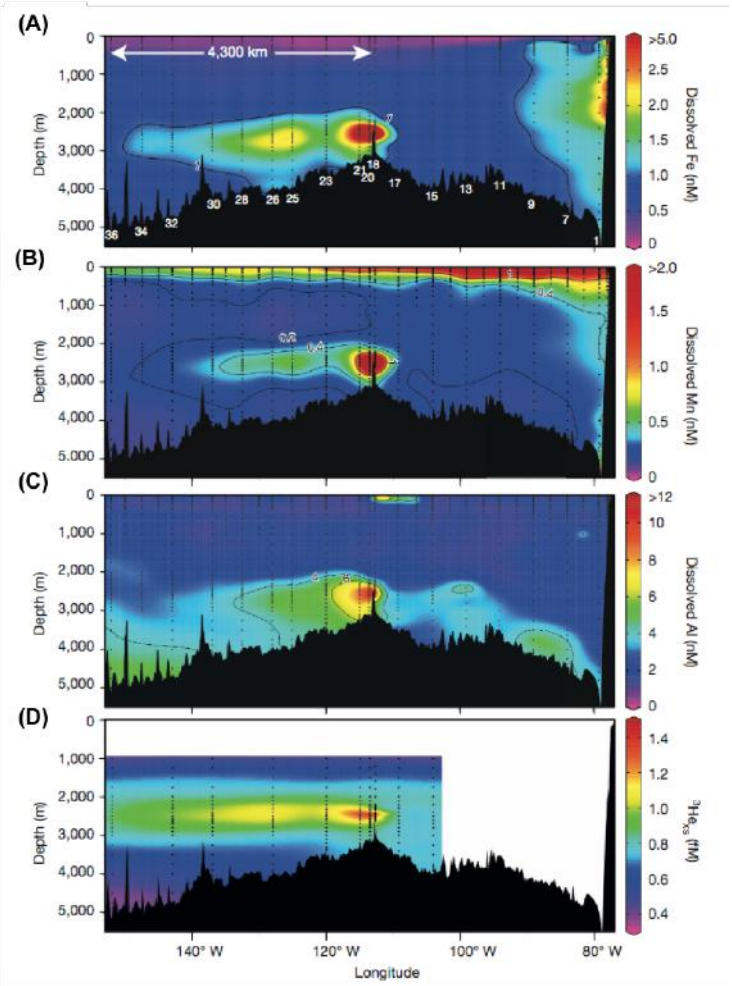

Figure 7: Concentration zonale interpolée pour le Transect Zonal du Pacifique Est US GEOTRACES pour (A) le fer dissous, (B) le manganèse dissous, (C) l'aluminium dissous et (D) l'excès d'hélium-3 (Resing et al., 2015).

L'estimation des apports des métaux traces provenant des sources hydrothermales à l'océan reste incertaine et surtout dépendante de la source hydrothermale, de la région océanique étudiée et des processus physico-chimiques intervenant à l'interface.

1.3.1.5 Autres sources

Les sources d'éléments évoquées dans les paragraphes précédents sont les sources majeures d'éléments à l'océan global. A l'échelle locale, d'autres sources, telles que par exemple la fonte des glaces de mer, des glaciers et des icebergs, contribuent significativement aux apports d'éléments à l'océan (Raiswell et al., 2008).

1.3.2 Cycles internes des éléments traces

Nous avons vu les sources externes d'apport de métaux traces à l'océan qui se jouent aux différentes interfaces (atmosphère/océan, marge/océan, sédiment profond/océan, source hydrothermale/océan). Nous allons maintenant nous intéresser à leurs cycles internes. L'étude du cycle interne des métaux repose sur l'étude des différents réservoirs - ou phases

- de métaux traces (dissous vs particulaire, organique vs inorganique), des flux entre ces réservoirs, et des divers processus responsables de ces flux. Ces processus peuvent être biologiques (consommation biologique/reminéralisation, complexation organique), chimiques (précipitation/dissolution, réactions d'oxydoréduction), ou physiques (adsorption/désorption, scavenging). La frontière est parfois difficile à définir entre ce qui relève des processus biologiques, chimiques et physiques (ex. la complexation organique est à la fois un processus qui relève de la biologie et de la chimie). La section suivante présente une description des processus majeurs contrôlant les cycles internes des éléments.

1.3.2.1 Le transport des masses d'eau

Tout d'abord, quelle que soit la phase des éléments chimiques (dissoute, particulaire, complexée etc.), leur distribution dans l'océan est contrôlée par le transport physique et le mélange des masses d'eau. Ces processus physiques doivent être pris en considération pour extraire des informations sur les processus biogéochimiques sous-jacents qui sont décrits ci-dessous. Cependant, encore aujourd'hui, de nombreuses études sur le cycle des éléments dans l'océan ne prennent pas en compte l'impact de ces processus physiques (par ex. Conway & John, 2014; Measures et al., 2005; Menzel Barraqueta et al., 2018).

1.3.2.2 Les processus biologiques

La Figure 8 présente la pompe biologique de carbone et met en évidence la dynamique des particules (Lam & Marchal, 2015). On y voit, les processus d'agrégation biotique et abiotique de particules, la chute des particules dans la colonne d'eau, la désagrégation des particules et la dégradation de la matière organique ou reminéralisation.

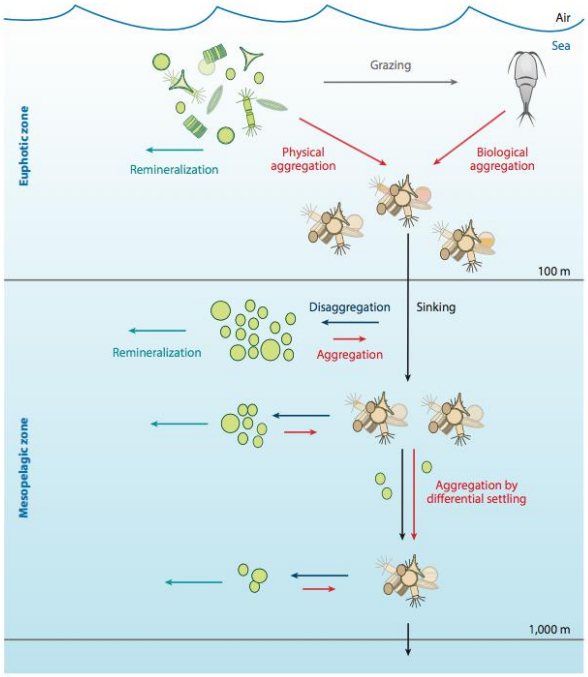

Figure 8 : Représentation schématique de la pompe biologique de carbone mettant en évidence la dynamique des particules (Lam & Marchal, 2015). Sont représentés, les processus d'agrégation biotique et abiotique de particules (flèches rouges), la chute des particules dans la colonne d'eau (flèches noires), la désagrégation des particules (flèches bleu foncé) et la dégradation de la matière organique ou reminéralisation (flèches bleu clair).

A la vision simplifiée ci-dessus, s'ajoutent en réalité d'autres processus. On peut distinguer la pompe biologique gravitationnelle (BGP), présentée précédemment, des pompes à injection de particules (PIPs) au sein desquelles d'autres mécanismes biologiques (ex. large migrateurs mésopélagiques) et physiques (ex. subduction) injectent des particules en suspension ou qui chutent en profondeur (Boyd, 2019). Cette vision de la pompe biologique présentée en Figure 9, permet de clore le budget carbone.

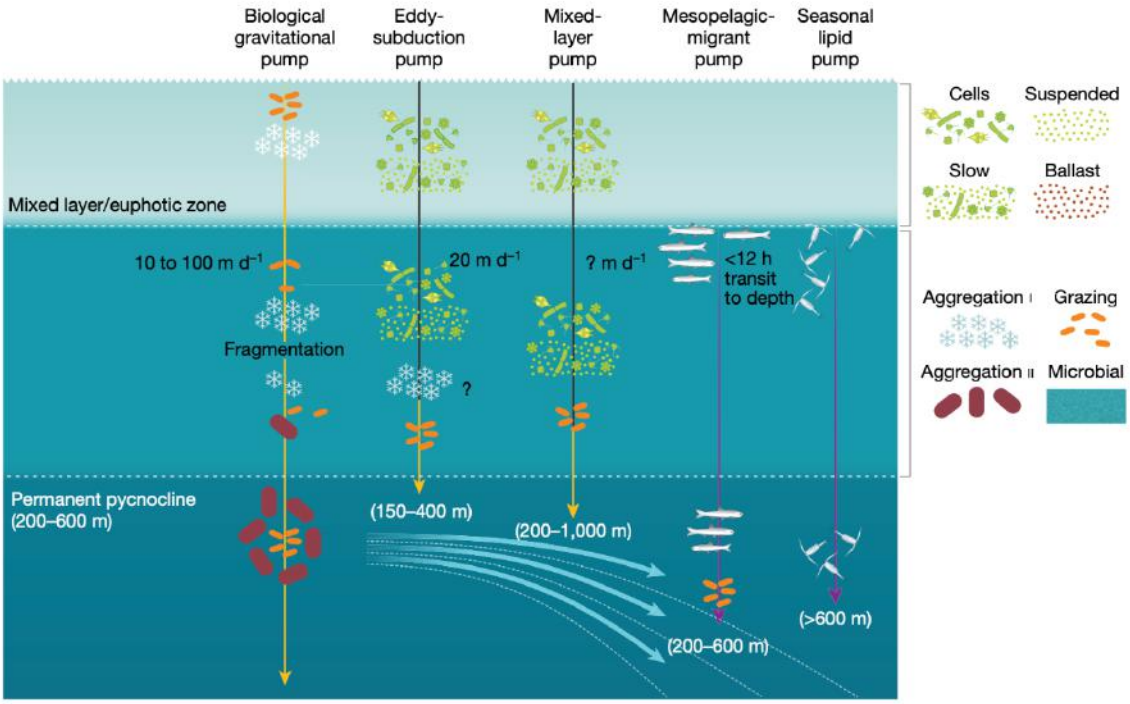

Figure 9 : Interactions entre les particules, le mode d'exportation (BGP ou PIP), la profondeur et la circulation océanique à grande échelle pour une série de pompes. La flèche verticale jaune indique la BGP, les lignes noires les PIPs induites par des mécanismes physiques et les lignes violettes les PIPs induites par des mécanismes biologiques (Boyd, 2019).

De nombreux éléments nutritifs (macronutriments et micronutriments) sont impliqués de façon active dans la production primaire. Ainsi, ces éléments vont être directement impactés par les processus décrits sur les Figure 8 & 9 et connaître de multiples cycles d'assimilation dans les particules biogènes dans les eaux de surface et de libération ou de reminéralisation en profondeur. Ils pourront donc être recyclés de nombreuses fois dans l'océan avant d'être finalement enfouis dans les sédiments (Bruland & Lohan, 2006). La distribution de ces nutriments (macronutriment et micronutriment) est alors caractérisée par des profils de type « nutritif » reflétant le cycle de la matière biogénique (Figure 8&9). Leurs concentrations sont plus faibles en surface, où les nutriments sont assimilés par le phytoplancton et/ou adsorbés par les particules biogènes, et augmentent en profondeur du fait de la dégradation des particules organiques qui sédimentent. Le temps de résidence des métaux traces de type nutritif est estimé entre ~10^2 et 10^5 années.

L'impact de la biologie sur les cycles internes d'éléments non-nutritifs a également été observé de façon « indirecte ». C'est le cas de l'aluminium, qui peut être incorporé dans les parois siliceuses des diatomées conduisant à des profils d'aluminium dissous de type nutritif dans certaines régions de l'océan et non de type « scavenged » comme normalement observé pour cet élément (Hydes et al., 1988; Middag et al., 2009; van Hulten et al., 2013). C'est aussi le cas de nombreux éléments réactifs tels que le thorium, le protactinium ou encore certaines terres rares qui peuvent s'adsorber à la surface des particules biogènes.

La complexation organique joue un rôle majeur sur la distribution de plusieurs éléments dans l'océan. Le phytoplancton produit des ligands organiques qui lui permettent de complexer et

donc d'acquérir des métaux parfois présents à de très faibles concentrations. Ainsi, il est considéré que les fractions dissoutes de Fe, Cu, Zn, Cd et Co dans l'eau de mer sont majoritairement sous forme de complexes organiques (Morel & Price, 2003). Certains de ces complexes sont formés avec des ligands de faible masse moléculaire produits spécifiquement pour le transport, la séquestration ou la détoxification des métaux. D'autres complexes possèdent des masses moléculaires élevées qui permettent d'échanger des métaux (plus ou moins facilement) et peuvent être séparés sous forme de matières colloïdales (Morel & Price, 2003). Malgré le fait que la complexation organique semble jouer un rôle majeur sur la distribution de plusieurs éléments dans l'océan, la nature, l'origine et les propriétés chimiques et biologiques des ligands organiques restent encore peu connues (Bruland & Lohan, 2006; Hassler et al., 2017).
Les cycles biologiques sont donc un élément fondamental des cycles biogéochimiques océaniques, pour les éléments bioactifs, mais aussi pour de nombreux autres éléments réactifs vis-à-vis des particules.

1.3.2.3 Les processus chimiques

Parmi les processus chimiques, on peut citer les mécanismes de précipitation/dissolution qui peuvent impacter les cycles internes de certains éléments. C'est le cas par exemple du baryum qui précipite dans des micro-environnements spécifiques résultant de la dégradation de la matière organique. Il s'agit ici d'un impact indirect du cycle de la matière organique.
On peut également citer les réactions d'oxydoréduction, qui vont impacter les éléments possédant plus d'un état d'oxydation dans l'eau de mer (ex Fe, Mn, Cu, and Co). La Figure 10 présente les cycles redox du fer et du manganèse et les processus photochimiques et biogéochimiques impliqués dans ces cycles (Morel & Price, 2003). On y voit que la photochimie (hv) réduit les complexes et oxydes de Fe(III) en Fe(II) et les oxydes de Mn(IV) en Mn(II). On y voit également que les diatomées (en vert) réduisent extracellulairement les complexes de ligands du Fe(III) pendant l'absorption du Fe (Berman-Frank et al., 2001) et que les bactéries marines hétérotrophes (en bleu) oxydent le Mn(II), formant une enveloppe de MnO_2 autour de la cellule (Lane & Morel, 2000; Tortell et al., 2000).

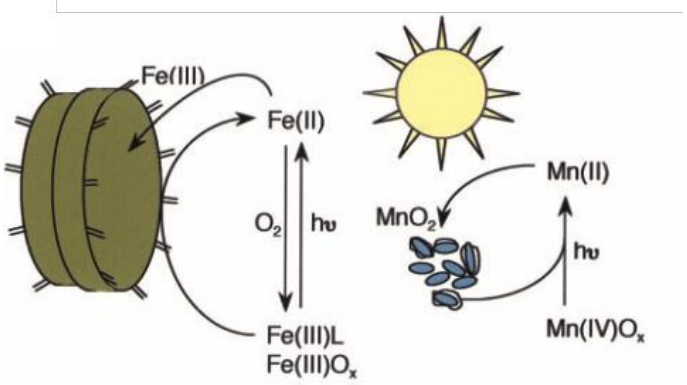

Figure 10 : Cycle redox du fer (Fe) et du manganèse (Mn) par des processus photochimiques et biochimiques. Les diatomées sont représentés en vert, et les bactéries marines hétérotrophes en bleu. (Morel & Price, 2003)

1.3.2.4 Les processus physiques

Le "scavenging" est le processus combiné d'adsorption d'un élément dissous à la surface des particules, suivi de la sédimentation des particules (Goldberg, 1954; Turekian, 1977). Le scavenging et l'enfouissement dans les sédiments marins sont les principaux puits d'éléments dans l'océan. Le taux et le degré auxquels un métal dissous est « scavengé » dans l'océan dépend (i) de la nature de l'élément, (ii) de l'abondance et la nature de la matière particulaire, (iii) des concentrations d'autres solutés possiblement en compétition sur les sites d'adsorption, (iv) de la profondeur de la colonne d'eau (Libes, 2009). Parmi les éléments impactés par les processus de scavenging, nous pouvons citer les métaux traces tels que le plomb, l'aluminium, le fer, le gallium, les isotopes du thorium, ou encore les terres rares. Pour établir les taux et comprendre les processus du scavenging, les isotopes du thorium (quatre isotopes avec des demi-vies différentes) ont été utilisés comme traceur du scavenging (Bacon & Anderson, 1982; Hayes et al., 2013; Nozaki et al., 1981; Roy-Barman et al., 1996). Les isotopes de thorium ont notamment permis de comprendre que le processus de scavenging pouvait être « réversible » pour certains métaux. En effet, plusieurs études ont montré que les profils d'isotopes du thorium ne pouvaient s'expliquer que s'il on considère que le thorium est soumis simultanément à des processus d'adsorption et de désorption accompagnant la chute des particules (Bacon & Anderson, 1982; Nozaki et al., 1981; Roy-Barman et al., 1996). Cette dynamique de scavenging réversible a par la suite été proposée comme un processus significatif, notamment en profondeur, dans les cycles internes des terres rares (Nozaki & Alibo, 2003), du cuivre (Little et al., 2013), du fer (Abadie et al., 2017), du zinc (Tagliabue et al., 2018) et de l'aluminium (van Hulten et al., 2013).

1.4 Objectifs et plan de thèse

Comme nous l'avons vu, l'étude des cycles biogéochimiques des métaux traces est essentielle pour étudier le fonctionnement physique, chimique et biologique de l'océan. La section précédente a permis de faire l'état actuel de nos connaissances sur les cycles biogéochimiques mais aussi de mettre en lumière de nombreux points qui restent en suspens. Certaines de ces points sont listées ci-dessous.

- **Au niveau des sources externes**

  - **Sources atmosphériques** : les flux de poussières atmosphériques peuvent être estimés via des modèles ou des mesures in situ (Jickells et al., 2005, 2016; Measures et al., 2005). Mais du fait de nombreuses incertitudes (ex. la solubilité des éléments), cette quantification reste incertaine (Anderson et al., 2016).

  - **Sources fluviales** : il reste de grosses incertitudes concernant les processus estuariens.

  - **Sources sédimentaires** : on ne connait pas bien les mécanismes en jeu à l'interface sédiment/océan ni le flux d'éléments à cette interface (Radic et al., 2011a).

  - **Sources hydrothermales** : elles ont pendant longtemps été négligées comme source de nombreux éléments dans divers travaux or des travaux récents montrent au contraire que ces sources peuvent être importantes dans le cycle des éléments (Guieu et al., 2018; Measures et al., 2015; Resing et al., 2015). De nombreuses questions demeurent concernant les processus et les flux à cette interface.

- **Au niveau des cycles internes**

  - **Interactions dissous-particules** : les cycles internes dépendent hautement des éléments considérés et des différentes phases en présence. Or pour de nombreux éléments la phase dissoute a longtemps été la seule phase considérée. Il y a donc de nombreuses incertitudes qui demeurent concernant les interactions entre les différentes phases d'éléments.

  - **Transport de masses d'eau** : il n'est pas toujours pris en compte dans l'étude de la distribution des éléments.

L'ensemble de ces points sur les sources, les cycles internes et l'importance de la prise en compte de l'hydrodynamique sur les cycles biogéochimiques sera étudié, dans cette thèse, au travers des traceurs aluminium et isotopes du fer.
L'objectif général de cette thèse est donc de **progresser sur la compréhension des cycles biogéochimiques en général (sources, cycles internes, puits) à l'aide des traceurs aluminium et fer isotopique combinés à des outils hydrodynamiques.**

Cet objectif général se décompose en plusieurs objectifs qui sont de :

- Fournir les outils permettant de prendre en compte les processus hydrodynamiques (transports par les courants) dans l'interprétation des données biogéochimiques – **Chapitre 2.**
- Apporter une meilleure compréhension des processus impactant les cycles biogéochimiques dans l'Atlantique Nord subtropical, en couplant ces outils hydrodynamiques avec des mesures de concentration d'aluminium utilisées comme traceurs de sources lithogéniques – **Chapitre 3**.
- Apporter une meilleure compréhension des cycles biogéochimiques dans une zone naturellement fertilisée de l'océan Austral en utilisant les isotopes du fer – **Chapitre 4**.

Ces travaux se basent sur les campagnes en mer GApr08 (pour l'analyse des masses d'eau et l'aluminium) dans l'Atlantique Nord subtropical et KEOPS 1&2 (pour le fer) dans l'océan Austral. Les campagnes GApr08 et KEOPS2 font parties du programme international GEOTRACES (**Erreur ! Source du renvoi introuvable.**). Plus de 30 pays sont impliqués d ans ce programme autour d'une mission commune qui est « d'identifier les processus et de quantifier les flux qui contrôlent la distribution des principaux éléments traces et de leurs isotopes dans l'océan et d'établir la sensibilité de ces distributions à l'évolution des conditions environnementales » (https://www.geotraces.org/mission/). Les objectifs de cette thèse s'inscrivent donc pleinement dans ceux de ce programme.

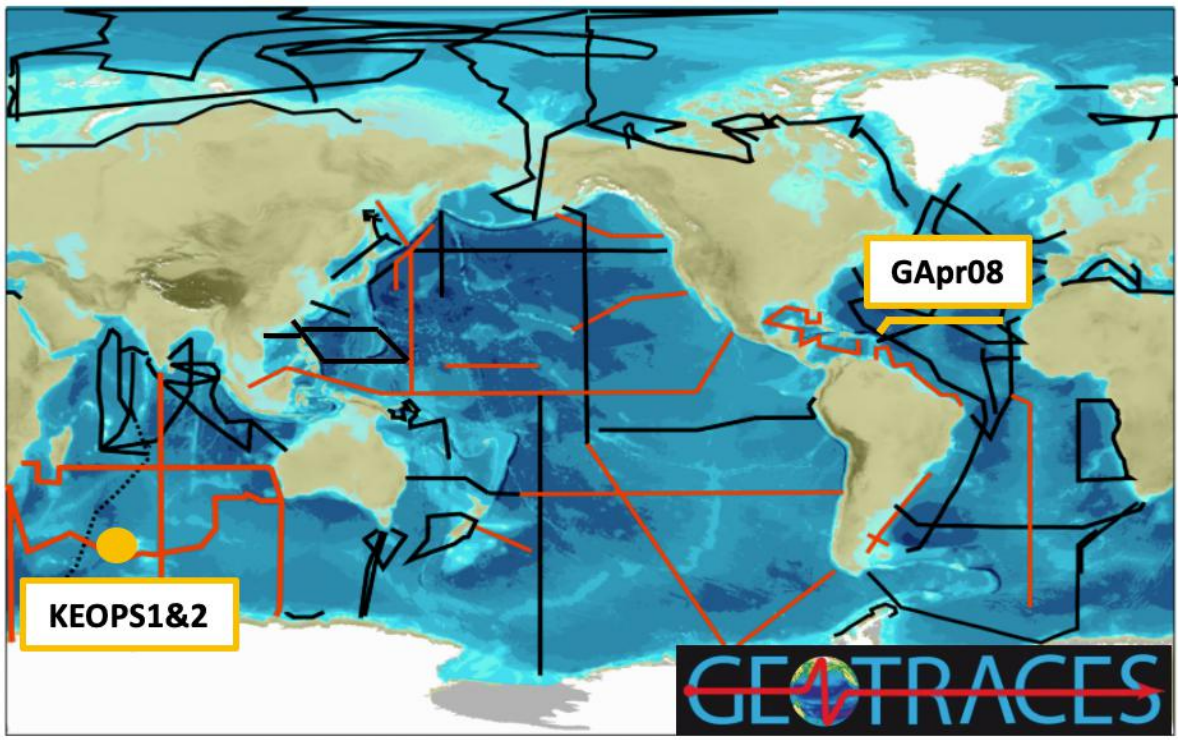

Figure 11 : Section GEOTRACES. Les sections planifiées et réalisées sont représentées en rouge et noir respectivement. En jaune : sections étudiées dans cette thèse (adaptée de www.geotraces.org/cruise-overview/, consulté le 01/02/2021).

2 Analyse des masses d'eau dans l'Atlantique Nord subtropical

Les distributions des éléments chimiques dans l'océan résultent de processus biogéochimiques et de transport par les courants. Afin d'exploiter ces distributions pour l'étude des cycles biogéochimiques, il est nécessaire de s'affranchir de l'impact des courants. Cela peut être fait par la mise en place d'un modèle couplant hydrodynamique et cycles biogéochimiques. Cela requiert cependant des moyens lourds et une expertise importante. Il est aujourd'hui difficile d'envisager la mise en place systématique de tels modèles pour chaque étude de la distribution d'un élément et pour chaque campagne en mer. Alternativement, la technique dite Optimum Multiparameter Analysis (OMPA) est une solution beaucoup plus légère à mettre en place (bien que restant non triviale, et représentant un travail à part entière). Une OMPA donne la contribution (en pourcentage) des différentes masses d'eau à une section ce qui permet de les prendre en compte lors de l'étude de la distribution des éléments. Ce genre de technique a été utilisé sur les campagnes récentes du programme GEOTRACES, notamment les campagnes US-GEOTRACES (Jenkins et al., 2015; Peters et al., 2018) et GEOVIDE (García-Ibáñez et al., 2015, 2018). Une autre technique, pour la prise en compte de l'hydrodynamique, est l'estimation des trajectoires des masses d'eau grâce à l'outil lagrangien. Cet outil utilise une sortie de modèle hydrodynamique qui est exploitée pour calculer des trajectoires lagrangiennes à rebours dans le temps (rétro-trajectoires) et ainsi estimer l'origine des masses d'eau. Ces types d'études (OMPA et lagrangienne), non seulement permettent d'exploiter les distributions d'éléments chimiques pour étudier les cycles biogéochimiques en prenant en compte les transports hydrodynamiques, mais elles permettent aussi de progresser sur nos connaissances de l'hydrodynamique elle-même (masses d'eau, courants). Ce chapitre présente une analyse des masses d'eau dans l'Atlantique Nord subtropical qui combine pour la première fois à notre connaissance ces deux techniques.

2.1 Introduction : les masses d'eau dans l'océan

2.1.1 Le cycle de vie des masses d'eau

On définit une masse d'eau comme un corps d'eau ayant une histoire de formation commune et son origine dans une région particulière de l'océan (Tomczak, 1999). Tout comme les masses d'air dans l'atmosphère, les masses d'eau sont des entités physiques (Tomczak, 1999). Une masse d'eau est caractérisée par sa température et sa salinité qu'elle acquiert généralement en surface par échange direct avec l'atmosphère. On peut considérer que les masses d'eau suivent un « cycle de vie » au sein de l'océan. Elles se sont formées dans une région particulière de l'océan, évoluent dans l'océan intérieur, puis se dégradent (voir Tableau 2, Tomczak, 1999).

A l'échelle de l'océan mondial, trois processus physiques sont à l'origine de la formation des masses d'eau : la convection, la subduction et le mélange sous la surface.

La convection est un processus de formation de masse d'eau qui a lieu lorsque la densité de l'eau à la surface augmente par refroidissement ou par évaporation ce qui conduit à la plongée de cette eau plus dense jusqu'à la profondeur où elle se stabilise (à quelques centaines de mètres de profondeur généralement) puis se répand dans l'océan intérieur (Tomczak, 1999). On peut par exemple citer l'exemple de la *Labrador Sea Water* qui est formée dans la mer du Labrador par convection hivernale (Lazier et al., 2002).

La subduction correspond à l'enfoncement de masses d'eau le long des isopycnes sous les eaux de surface plus légères (Roy-Barman & Jeandel, 2016). Ce processus amorce le plongeon des eaux modales qui par la suite se répandent dans l'océan intérieur. Parmi les eaux modales, on peut par exemple citer la *18° water* formée dans la mer des Sargasses (Talley et al., 2011).

La convection et la subduction sont les deux processus les plus courants de formation de masse d'eau.

Le mélange sous la surface est « le seul processus de formation qui ne repose pas sur l'échange de propriétés à l'interface océan/atmosphère » (Tomczak, 1999). Ce processus se produit lorsque plusieurs fractions de masses d'eau se mélangent entre elles de manière très approfondie produisant une nouvelle masse d'eau occupant une large gamme de profondeur dans sa région de formation et possédant des propriétés clairement distinctes de celles des masses d'eau qui l'ont formée (Tomczak, 1999). On peut par exemple citer l'*Upper Circumpolar Deep Water* ou la *Lower Circumpolar Deep Water*, deux masses d'eau formées dans l'océan Austral, en profondeur, par ce processus de "mélange sous la surface" (Broecker et al., 1985).

Une fois la masse d'eau formée et ses propriétés acquises, elle quitte sa région de formation et se répand dans l'océan intérieur où elle va rentrer dans une phase d'évolution. Durant cette phase, plusieurs processus peuvent se produire : La consolidation, le vieillissement ou modification et le mélange (Tableau 2).

La consolidation se produit lorsqu'une masse d'eau précédemment formée (ex. lors d'un hiver) va se mélanger avec cette même masse d'eau nouvellement formée (ex. lors de l'hiver

suivant). Cela conduit à une homogénéisation encore plus poussée des propriétés de cette masse d'eau par mélange en son sein (Tomczak, 1999).
Le vieillissement ou modification, correspond à la modification des propriétés uniquement non conservatives d'une masse d'eau (nutriments, oxygène…Tomczak, 1999).
Le mélange entre les masses d'eau est un processus fréquent. L'eau résultante de ce mélange a de nouvelles propriétés qui reflètent la fraction des différentes masses d'eau qui se sont mélangées (Tomczak, 1999).
Finalement, chaque masse d'eau finit par disparaître soit en se transformant en une nouvelle masse d'eau soit en étant absorbée par une autre masse d'eau (Tomczak, 1999).

Formation	Convection
	Subduction
	Mélange sous la surface
Evolution	Consolidation
	Viellissement/Modification
	Mélange
Dégradation	Absorption
	Transformation

Tableau 2: Le « cycle de vie » des masses d'eau (adapté de Tomczak, 1999).

2.1.2 Évolution des méthodes d'analyse des masses d'eau

L'analyse des masses d'eau, qui consiste à étudier leur cycle de vie est essentielle pour comprendre le fonctionnement de l'océan. Les méthodes utilisées pour l'analyse des masses d'eau ont largement évolué au cours des dernières décennies.
Helland-Hensen (1916) a été le premier à rassembler la température et la salinité, les deux propriétés conservatives caractéristiques des masses d'eau, dans des diagrammes T-S (ou préférentiellement θ-S, Figure 12). Cette technique est largement utilisée encore de nos jours comme base de toute étude de mélange des masses d'eau. Cependant, les diagrammes θ-S ne peuvent être utilisés que pour quantifier les proportions de mélange de trois différents types de masse d'eau maximum. Un diagramme θ-S seul, ne peut pas fournir d'information sur les processus de consolidation ou du vieillissement d'une masse d'eau ni même d'étudier la circulation des masses d'eau dans l'océan global.

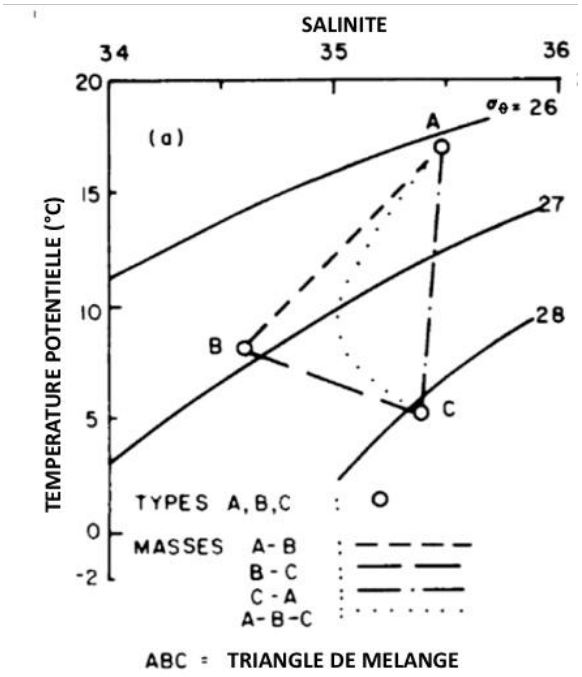

Figure 12 : Diagramme théorique θ-S montrant trois types d'eaux et quatre masses d'eau (adapté de Pickard & Emery, 2016).

Cette limitation a conduit à l'émergence de l'utilisation des outils géochimiques et des modèles numériques pour l'étude des masses d'eau.

Parmi les outils géochimiques, on citera notamment l'apport des traceurs transitoires (ex chlorofluorocarbures, le tritium, le ^{3}He tritiugénique et le carbone 14) qui sont des traceurs de la circulation thermohaline de l'océan et des mélanges à l'intérieur de l'océan (Roether, 1994). Ces traceurs permettent notamment de déterminer « l'âge » des masses d'eau i.e. le temps écoulé depuis qu'une masse d'eau a eu son dernier contact avec l'atmosphère. Ils renseigneront donc sur le processus de consolidation des masses d'eau.

Un autre exemple de l'utilisation des outils géochimiques est l'introduction des données de nutriments et d'oxygène, en plus de la température et de la salinité, pour l'étude et la quantification des mélanges de masses d'eau. Cela permet de quantifier le mélange de plus de trois masses d'eau. Les nutriments (nitrate et phosphate) et l'oxygène, étant impactés par les processus de reminéralisation, sont, contrairement à la température et à la salinité, des traceurs non-conservatifs. Le rapport de Redfield permet d'estimer le nombre de moles d'oxygène consommées pour une mole de phosphate et nitrate libérée lors de la reminéralisation. L'utilisation des mesures de nitrate et phosphate corrigées de la reminéralisation (N*, P* ou NO, PO) est aujourd'hui largement répandue. Pour permettre d'optimiser le calcul du mélange de plusieurs masses d'eau à de nombreux échantillons, Tomczak (1981) a introduit l'utilisation de la méthode des moindres carrés au sein d'une technique par la suite nommée Optimum Multiparameter Analysis (OMPA).

Il est important de noter que l'analyse de masses d'eau connaît ses limites à la surface de l'océan. Elle ne peut pas s'appliquer à la profondeur de la couche de mélange, où la température et la salinité ne sont pas conservatives. Or comprendre la dynamique de surface

de l’océan est essentiel car c’est le principal lieu d’échange entre les réservoirs océan et atmosphère (échange d’énergie, d’éléments chimique…).

2.1.3 Analyse des masses d'eau dans l'Atlantique Nord subtropical

Le transect de la campagne GEOTRACES GApr08 “Zinc, Iron and Phosphorus co-Limitation” est situé à l'extrémité sud du gyre de l'Atlantique Nord subtropical des deux côtés de la dorsale médio-atlantique (~22 °N, ~58-31 °W). L’objectif de cette campagne est de comprendre comment un environnement limité en phosphate peut conduire à une co-limitation zinc-phosphore et fer-phosphore sur la fixation de l'azote. Dans ce contexte, les métaux traces fer, zinc et aluminium ont été mesurés. Avant d’interpréter les distributions de ces métaux traces, il est nécessaire de réaliser une analyse de masse d’eau de la région d’étude. C’est l’objectif de l’article présenté dans ce chapitre qui propose une analyse de masse d’eau dans l'Atlantique Nord subtropical, le long de la section GEOTRACES GApr08.

2.2 Article publié : *Water mass analysis along 22 °N in the subtropical North Atlantic for the JC150 cruise (GEOTRACES, GApr08)*

2.2.1 Résumé

Ce papier présente une analyse de masse d'eau basée sur des données de température, salinité, oxygène et de nutriments, qui combine pour la première fois une OMPA étendue (eOMPA) à l'outil Lagrangien. L'outil Lagrangien nous a permis (i) de déterminer l'origine des particules d'eau impactant notre section et ainsi de mieux choisir les masses d'eau à intégrer dans l'eOMPA, (ii) de fournir des informations sur les trajectoires de ces masses d'eau entre leur zone de formation et la section, (iii) et de fournir des informations sur la dynamique dans les couches de surface où (en raison de la non conservativité des paramètres hydrographiques) une eOMPA ne peut être réalisée. L'eOMPA nous a permis d'estimer le pourcentage de contribution des différentes masses d'eau présentes le long de la section GApr08. Ces deux outils complémentaires nous ont permis d'obtenir les résultats suivants. Les couches de surface sont occupées par un type peu profond de *Eastern South Atlantic Central Water*, avec des traces du panache amazonien à l'ouest de la section. La *Western North Atlantic Central Water* domine entre 100 et 500 m avec une contribution supérieure à 90 % à 300 m. Légèrement plus profond, on trouve une variété à 13°C de *Eastern South Atlantic Central Water* avec une contribution de plus de 40 % à environ 600 m. Aux alentours de 700 m, l'*Antarctic Intermediate Water* domine à l'ouest de la dorsale médio-atlantique avec une contribution de plus de 30 %, tandis que la *Mediterranean Water* domine à l'est de celle-ci, avec une contribution maximale de 40 %. Nous avons constaté que, bien qu'en petite quantité (de l'ordre de 5 %), la contribution de la *Mediterranean Water* est nécessaire jusqu'à une profondeur de 3500 m. En dessous de l'*Antarctic Intermediate Water*, on retrouve l'*Upper Circumpolar Deep Water* avec une contribution de plus de 25 % à environ 1000 m de profondeur. En dessous, la *Labrador Sea Water* est présente entre 900 et 2000 m de profondeur avec un maximum de contribution de plus de 70 % à ~ 1500 m sur toute la section. De manière inattendue, l'outil lagrangien nous a permis de constater que la *Labrador Sea Water* coule vers le sud depuis l'est de l'Atlantique Nord jusqu'à l'est de l'Atlantique subtropical. Nous n'avons pas pu trouver de précédents travaux présentant cette trajectoire en dessous de 40°N. En dessous de la *Labrador Sea Water*, on trouve la *North East Atlantic Deep Water* qui est présente à environ 2500 m sur toute la section avec une contribution de plus de 70 %, tandis que la *North West Atlantic Bottom Water* est principalement localisée à l'ouest de la dorsale avec une contribution de plus de 45 % à environ 4500 m. La *North West Atlantic Bottom Water* est également présente dans des proportions significatives (> 25 %) à l'est de la dorsale, ce qui suggère que cette eau la traverse possiblement par la zone de fracture de Kane. Là encore cette trajectoire à travers la zone de fracture de Kane et cette présence de *North West Atlantic Bottom Water* à l'est de la dorsale ne semblent pas avoir été documentées précédemment. Enfin, l'*Antarctic Bottom Water* est présente dans les profondeurs de la section, principalement à l'ouest de la dorsale où sa contribution dépasse 35 % à plus de 5000 m. Pour valider la fiabilité et la robustesse de ces résultats, nous avons effectué une série de tests de perturbation (analyse de Monte Carlo).

2.2.2 Article

Deep–Sea Research I xxx (xxxx) xxx

Contents lists available at ScienceDirect

Deep-Sea Research Part I

journal homepage: http://www.elsevier.com/locate/dsri

Water mass analysis along 22 °N in the subtropical North Atlantic for the JC150 cruise (GEOTRACES, GApr08)

Lise Artigue [a,*], François Lacan [a], Simon van Gennip [b], Maeve C. Lohan [c], Neil J. Wyatt [c], E. Malcolm S. Woodward [d], Claire Mahaffey [e], Joanne Hopkins [f], Yann Drillet [b]

[a] LEGOS, University of Toulouse, CNRS, CNES, IRD, UPS, 31400, Toulouse, France
[b] Mercator Ocean International, Ramonville Saint-Agne, France
[c] Ocean and Earth Science, University of Southampton, National Oceanographic Center, Southampton, SO14 3ZH, UK
[d] Plymouth Marine Laboratory, Plymouth, PL1 3DH, UK
[e] Department of Earth, Ocean and Ecological Sciences, School of Environmental Sciences, 4 Brownlow Street, University of Liverpool, Liverpool, L69 3GP, UK
[f] National Oceanography Centre, Liverpool, L3 5DA, UK

ARTICLE INFO

Keywords:
Water mass
Optimum multiparameter analysis (OMPA)
Lagrangian particle tracking experiment
Subtropical north Atlantic
JC150
GEOTRACES

ABSTRACT

This study presents a water mass analysis along the JC150 section in the subtropical North Atlantic, based on hydrographic and nutrient data, by combining an extended optimum multiparameter analysis (OMPA) with a Lagrangian particle tracking experiment (LPTE). This combination, which was proposed for the first time, aided in better constraining the OMPA end-member choice and providing information about their trajectories. It also enabled tracing the water mass origins in surface layers, which cannot be achieved with an OMPA. The surface layers were occupied by a shallow type of Eastern South Atlantic Central Water (ESACW) with traces of the Amazon plume in the west. Western North Atlantic Central Water dominates from 100 to 500 m, while the 13 °C-ESACW contribution occurs marginally deeper (500–900 m). At approximately 700 m, Antarctic Intermediate Water (AAIW) dominates the west of the Mid-Atlantic Ridge (MAR), while Mediterranean Water dominates the east with a small but non-negligible contribution down to 3500 m. Below AAIW, Upper Circumpolar Deep Water (UCDW) is observed throughout section (900–1250 m). Labrador Sea Water (LSW) is found centered at 1500 m, where the LPTE highlights an eastern LSW route from the eastern North Atlantic to the eastern subtropical Atlantic, which was not previously reported. North East Atlantic Deep Water (encompassing a contribution of Iceland-Scotland Overflow Water) is centered at ~2500 m, while North West Atlantic Bottom Water (NWABW, encompassing a contribution of Denmark Strait Overflow Water) is principally localized in the west of the MAR in the range of 3500–5000 m. NWABW is also present in significant proportions (>25%) in the east of the MAR, suggesting a crossing of the MAR possibly through the Kane fracture zone. This feature has not been investigated so far. Finally, Antarctic Bottom Water is present in deep waters throughout the section, mainly in the west of the MAR. Source waters have been characterized from GEOTRACES sections, which enables estimations of trace elements and isotope transport within water masses in the subtropical North Atlantic.

1. Introduction

Oceanic water masses store and transport considerable amounts of energy, water and chemical elements in the earth's surface. These water masses impact the atmosphere through interactions at the air/sea interface. Water mass analysis, which consist in studying the formation, spreading, and mixing of water masses, is therefore essential to understand the role of oceans in climate processes. The methods used for water mass analysis have evolved from classical descriptions of oceanic circulation based on hydrographic properties to the determination of water mass formation regions, transport pathways, and mixing length scales from numerical models and novel tracer data (Tomczak, 1999). An example of such development is the introduction of the optimum multiparameter analysis (OMPA, Tomczak, 1981). This method enables estimating the contributions of different water masses defined in specific locations (end-members) to a measured ocean section based on a range

Abbreviations: LPTE, Lagrangian Particle Tracking Experiment.

* Corresponding author. LEGOS/CNES, 18, avenue Edouard Belin, 31401, Toulouse Cedex 9, France.
E-mail address: lise.artigue@legos.obs-mip.fr (L. Artigue).

https://doi.org/10.1016/j.dsr.2020.103230
Received 29 June 2019; Received in revised form 26 January 2020; Accepted 27 January 2020
Available online 30 January 2020

of hydrographic parameters. This method demonstrates a significant amount of improvement compared to previous methods and has been widely used (Álvarez et al., 2014; García-Ibáñez et al., 2018; Jenkins et al., 2015; Pardo et al., 2012; Peters et al., 2018). However, the results of OMPA are strongly dependent on the choice of water mass end-members that possibly impact the ocean section, and OMPA cannot provide any information related to surface layers. Moreover, a water mass analysis conducted only with OMPA does not provide direct information on the water mass pathways between their formation region and the measured section. Therefore, the water mass analysis proposed in this study combines, for the first time to the best of our knowledge, an extended OMPA with a Lagrangian particle tracking experiment (LPTE) to better constrain the end-members and provide information on water mass pathways. LPTEs are widely used in recent times to investigate several aspects of ocean sciences, such as oceanic circulation (eg. Spence et al., 2014) or biogeochemistry (eg. Cetina-Heredia et al., 2016).

The present water mass analysis was conducted for the JC150 "Zinc, Iron and Phosphorus co-Limitation" GEOTRACES process study (GApr08). This cruise departed Point-à-Pitre, Guadeloupe on June 27, 2017 and arrived at Santa Cruz, Tenerife on August 12, 2017. The transect is located at the southern end of the North Atlantic Subtropical gyre (Fig. 1) on both sides of the Mid-Atlantic Ridge (MAR, ~22 °N, ~58–31 °W). The JC150 section was specifically studied to understand how a low phosphate environment could lead to zinc-phosphorus and iron-phosphorus co-limitation on nitrogen fixation (Browning et al., 2017; Mahaffey et al., 2014; Moore et al., 2009; Snow et al., 2015; Wu et al., 2000). In this context, the trace metals iron, zinc and aluminum, were measured. The aim of the present water mass analysis is two-fold. Firstly, it aims to provide a detailed understanding of the contribution and distributions of the water masses that exist along the zonal section as well as new constraints in water mass circulation in the subtropical North Atlantic that might be of general interest. Secondly, it aims to

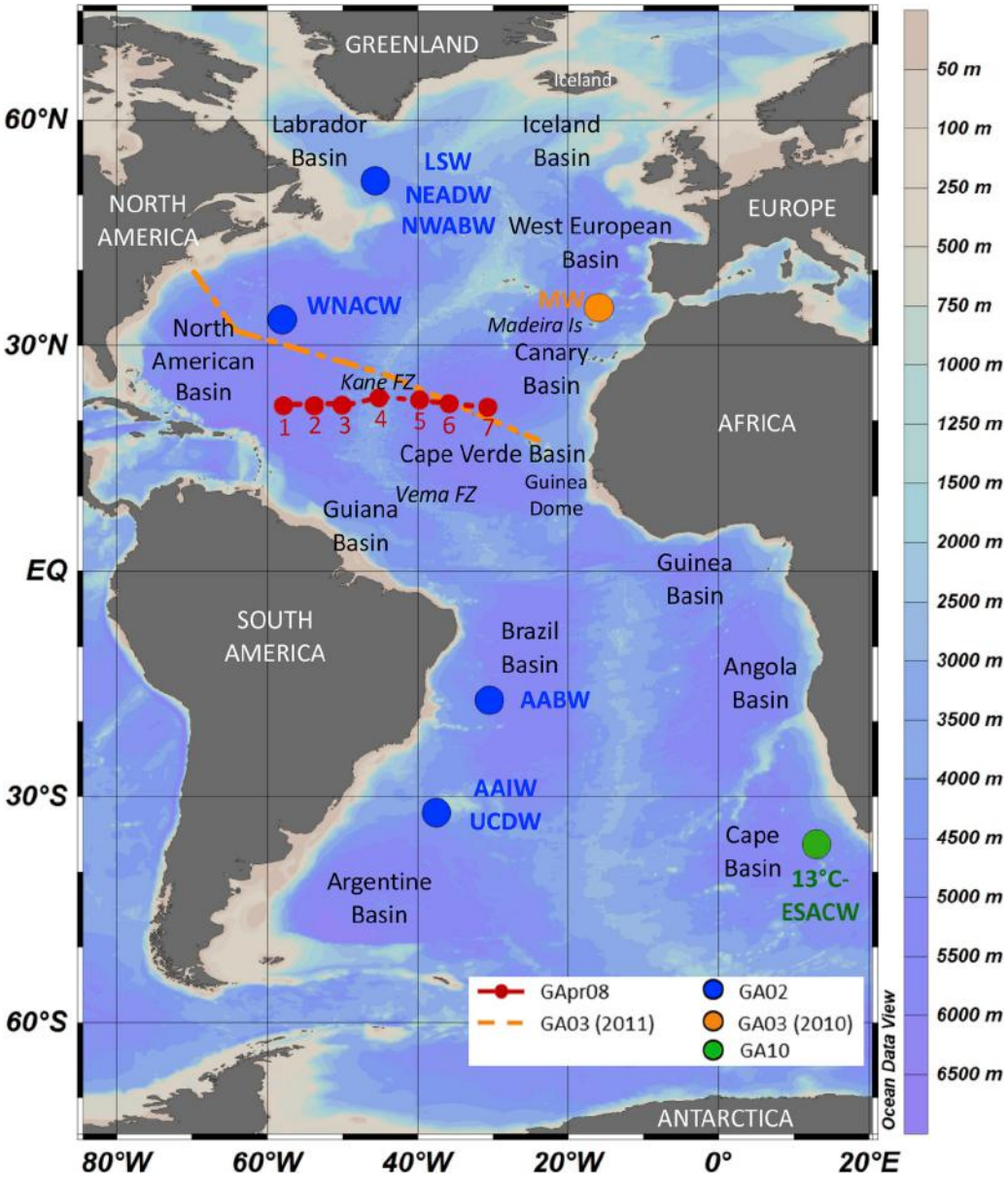

Fig. 1. Map of the JC150 cruise (red dots); locations where the end-members are defined (blue dots - GA02, orange dot - 2010 GA03, and green dot - GA10), and track of the 2011 GA03 cruise (orange dashed line). Refer to Table 1 for water mass acronyms. (For interpretation of the references to color in this figure legend, the reader is referred to the Web version of this article.)

provide the tools to efficiently combine this hydrodynamic knowledge with the biogeochemical knowledge from the GEOTRACES program. To achieve this objective, all the OMPA end-members were chosen from GEOTRACES cruises with available zinc, iron, and aluminum concentrations. This enables the estimation of transport and mixing of these elements. Such a choice is a first to the best of our knowledge, and it is now possible thanks to the great extent of the GEOTRACES program.

This study presents the hydrographic properties measured during JC150, including potential temperature, salinity, and the concentration of oxygen and nutrients (θ, S, O_2, NO_{3^-}, PO_4^{3-}, and $Si(OH)_4$) along with a water mass analysis based on an OMPA and a LPTE.

2. Materials and methods

2.1. Hydrography and nutrients

The samples for nutrients, oxygen, and salinity analyses were collected using 24, 10 L trace metal clean Teflon-coated OTE (ocean test equipment) bottles with external springs, mounted on a titanium rosette and deployed on a Kevlar-coated conducting wire. A SeaBird 911plus CTD recorded the temperature, conductivity, and pressure at 24 Hz with an accuracy of ±0,001 °C, ± 0,0003 S/m, and ±0,015%, respectively. An SBE43 oxygen sensor measured the dissolved oxygen concentration. Standard SeaBird processing routines were used to extract the raw data. The effect of thermal inertia on the conductivity was removed, and a correction was applied for deep oxygen hysteresis (https://www.bodc.ac.uk/resources/inventories/cruise_inventory/reports/jc150.pdf).

After rosette recovery, the OTE bottles were transferred into a class 1000 clean air shipboard laboratory for sampling. The samples for dissolved oxygen and salinity analyses were collected to calibrate the CTD sensors. For the measurements of dissolved oxygen, triplicate samples from 12 depths were fixed immediately and analyzed within 48 h of collection. The samples were analyzed with an automated titrator (Metrohm titrando Titrator). A platinum electrode was used for the potentiometric analysis of Winkler titration. The salinity samples were collected at 6 depths on each cast and analyzed using Guildline's Autosal 8400 B. The salinity and oxygen sensors were then calibrated using bottle derived salinity and bottle derived oxygen, which resulted in linear regressions for salinity (calibrated salinity = CTD salinity * 1.0012–0.0439) and oxygen (calibrated oxygen (μmol kg^{-1}) = CTD oxygen * 0.9768 + 5.3398). The salinity and oxygen data used in this study were the sensor calibrated data obtained with an accuracy of 0,0001 for salinity and 0,5 μmol kg^{-1} for oxygen. With measurements of calibrated oxygen, salinity, and potential temperature, we calculated the apparent oxygen utilization (AOU) (AOU (μmol kg^{-1}) = saturated oxygen (μmol kg^{-1}) - calibrated oxygen (μmol kg^{-1})). For the AOU calculation, we employed a script, which is originally part of the oceanography toolbox v1.4 compiled by R. Pawlowicz and now available on the MBARI website (https://www.mbari.org/products/research-software/matlab-scripts-oceanographic-calculations/).

The samples for nutrient analyses were collected unfiltered into acid-cleaned 60 mL HDPE Nalgene bottles from each OTE bottle. Immediately after collection, they were analyzed through colorimetric procedures (Woodward and Rees, 2001) using clean handling GO-SHIP protocols (Hydes et al., 2010). The micromolar nutrient concentrations were measured using a segmented flow colorimetric auto-analyzer: the PML 5-channel (nitrate, nitrite, phosphate, silicic acid, and ammonium) Bran and Luebbe AAIII system. The instrument was calibrated with nutrient stock standards, and the accuracy was determined using Certified Nutrient Reference Materials (batches CA and BU) obtained from KANSO Technos, Japan. The nano-molar nitrate, nitrite, and phosphate concentrations were analyzed through the segmented flow colorimetric technique that improved the analytical detection limits by using a 2-m liquid waveguide as the analytical flow cell. The same colorimetric method as for the micromolar system was used for analyzing nitrate and nitrite, while the method described in (Zhang and Chi, 2002) was used for analyzing phosphate. The nutrient data presented in this study were measured with an uncertainty of 2%.

2.2. An extended optimum multiparameter analysis (eOMPA)

An eOMPA was used to resolve the water mass structure along the JC150 section (Mackas et al., 1987; Poole and Tomczak, 1999; Tomczak, 1981; Tomczak and Large, 1989). This analysis assumes that the waters sampled along a section result from the mixing of several well-defined water masses, called the source water types or end-members. The degree of mixing and the contribution of each end-member is solved using an optimization procedure. Mathematically, an OMPA is an optimal solution to a linear system of mixing equations with the contribution of end-members as variables and the conservative hydrographic properties as the parameters of the system. This model optimizes, for each data point (sample), the end-member parameter contributions to reproduce the observational data. The OMPA is performed as an overdetermined system using non-negative least square optimization.

In OMPA, the hydrographic properties are used as parameters in the equation system. In this study, the available parameters are as follows: potential temperature (θ), salinity (S), concentration of dissolved oxygen (O_2), phosphate (PO_4^{3-}), nitrate (NO_{3^-}), and silicic acid ($Si(OH)_4$), and mass conservation (the sum of all contributions must be equal to unity). A classical OMPA resolves the system assuming that all those parameters are conservative, i.e., they have no sources or sinks in the ocean interior. This assumption was not acceptable for O_2, NO_{3^-}, and PO_4^{3-} in our case, as the end-members were defined at the Atlantic basin-wide scale and thus highly susceptible to organic matter remineralization. To consider these biogeochemical processes, we realized an eOMPA for this study. Most eOMPA studies use the quasi-conservative N* and P* parameters (García-Ibáñez et al., 2018; Jenkins et al., 2015). We preferred to adopt the parameters PO and NO defined in Broecker (1974) using the following equations, because unlike P* and N*, PO and NO do not require any assumption about initial gas equilibrium at the air/sea interface. Other recent studies have also made this choice (Álvarez et al., 2014; Peters et al., 2018).

$$PO = [O_2] + R_{O2/P} * [\ PO_4^{3-}], \quad (1)$$

$$NO = [O_2] + R_{O2/N} * [\ NO_3^-], \quad (2)$$

where $R_{O2/P}$ and $R_{O2/N}$ are Redfield ratios that estimate the number of O_2 moles consumed for 1 mol of PO_4^{3-} and NO_{3^-} released during the process of organic matter remineralization, respectively (Anderson and Sarmiento, 1994). In this manner, and under the assumption that the Redfield ratios $R_{O2/P}$ and $R_{O2/N}$ are accurate, remineralization has no impact on PO and NO. However, it is important to note that the Redfield ratios are spatiotemporally variable and have been revised since their original definition. Therefore, we qualified PO and NO as quasi-conservative. In this study, we defined $R_{O2/P} = 155$ and $R_{O2/N} = 9.69$, in the range of Anderson (1995), and similar to the values used by Peters et al. (2018).

These definitions combine the three non-conservative parameters O_2, PO_4^{3-}, and NO_{3^-} into two quasi-conservative parameters PO and NO. Transforming three parameters into two reduces the rank of the mixing equation system by one and thereby the number of end-members that can be considered.

The conservative character of the $Si(OH)_4$ parameter is also questionable. At depth, the biogenic particulate matter degradation releases $Si(OH)_4$. Unlike PO_4^{3-} and NO_{3^-}, the $Si(OH)_4$ parameter cannot be corrected using the Redfield ratio, as it is not linked to organic matter remineralization, but to biogenic opal dissolution. In the Atlantic, the magnitude of the $Si(OH)_4$ excess from opal dissolution has been estimated to represent only 5% of the difference between the $Si(OH)_4$ concentrations of the northern and southern end-members. Therefore, the opal dissolution effect on water mass properties is insignificant compared to the effect of water mass mixing at the basin scale (Broecker

et al., 1991). Thus, the $Si(OH)_4$ concentration was considered as a conservative parameter in this study.

The parameters considered to resolve the eOMPA in this work were as follows: θ, S, PO, NO, $Si(OH)_4$, and mass conservation. This led to the following system of mixing equations applied at each sample point with (n) end-members:

$$X_1\theta_1 + X_2\theta_2 + \ldots.. + X_n\theta_n = \theta_{sample} + \varepsilon_\theta, \quad (3)$$

$$X_1S_1 + X_2S_2 + \ldots.. + X_nS_n = S_{sample} + \varepsilon_S, \quad (4)$$

$$X_1PO_1 + X_2PO_2 + \ldots.. + X_nPO_n = PO_{sample} + \varepsilon_{PO}, \quad (5)$$

$$X_1NO_1 + X_2NO_2 + \ldots.. + X_nNO_n = NO_{sample} + \varepsilon_{NO}, \quad (6)$$

$$X_1\,Si(OH)_{4,1} + X_2\,Si(OH)_{4,2} + \ldots.. + X_n\,Si(OH)_{4,n} = Si(OH)_{4,sample} + \varepsilon_{Si(OH)4}, \quad (7)$$

$$X_1 + X_2 + \ldots.. + X_n = 1 + \varepsilon_x, \quad (8)$$

$$Xi \geq 0, \quad (9)$$

where the variables X_1–X_n (n = each end-member) denote the contribution of the end-members, and ε_θ, ε_S, ε_{PO}, ε_{NO}, $\varepsilon_{Si(OH)4}$, and ε_x are the residuals, i.e., the difference between the calculated and observed values. The eOMPA was performed using the OMPA V2.0 MATLAB package developed by Johannes Karstensen and Matthias Tomczak (https://omp.geomar.de).

As the OMPA should be performed as an overdetermined system, the number of end-members must be strictly lower than that of available parameters. A total of six parameters were considered in this study; however, over five end-members probably contributed to the water masses found along the JC150 section. To solve this problem, we first tried to increase the number of parameters used. However, no other conservative (or quasi-conservative) tracer was available in the JC150 cruise. We considered adding the potential vorticity as a quasi-conservative tracer. However, the profiles were observed to be excessively noisy, and despite many filtration attempts, we could not deduce an approach to obtain benefits from the use of this parameter in the eOMPA calculation. Therefore, we did not include this parameter. Another way to include over five end-members is to divide the water column into several layers, because some end-members impact only certain depth layers. The zonal section was therefore divided into three density layers with the following isopycnals: 26.50 kg m^{-3}–27.30 kg m^{-3} (thermocline layer), 27.30 kg m^{-3}–27.75 kg m^{-3} (intermediate layer) and >27.75 kg m^{-3} (deep layer). These density layers broadly corresponded to depths of 300–700 m (thermocline layer), 700–1500 m (intermediate layer), and 1500 m to seafloor (deep layer). An eOMPA was then applied independently to each of these layers. Waters above ~300 m were excluded from the eOMPA for two reasons: firstly, the hydrographic parameters, including θ and S were non-conservative in the mixed layer (mean annual maximum ~120 m at 22°N, http://mixedlayer.ucsd.edu, Holte et al., 2017); secondly, these waters were warmer and saltier than any well-defined end-member in the literature (Fig. 2). To precisely define the boundaries between the density layers (thermocline, intermediate, and deep layers), the samples located close to the layer boundaries were executed in both the overlying and underlying eOMPAs (both thermocline and intermediate eOMPAs and both intermediate and deep eOMPAs). The boundaries of the density layers were chosen where the smallest residuals were obtained. This procedure was performed, similar to those reported by Kim et al. (2013) and Peters et al. (2018). With the availability of six parameters, five end-members can be considered in each layer. We carefully selected them through an in-depth literature review, comparison of the JC150 hydrographic section properties with those of the end-member candidates, and interpretation of the LPTE results (see section 3.2). In this study, the end-member characteristics were all selected from GEOTRACES cruises in the core of the water masses and with intervals of variations established by comparison with nearby data areas (refer to Table 1). These intervals are specific to each of the properties of each end-members and reflect the natural variability of end-member characteristics (temporal, spatial). Perturbation analyses are presented below.

The eOMPA parameters were weighted according to their signal to noise ratios (measurement accuracy compared to the range of variation among end-members) and conservative character (conservative or quasi-conservative). In most studies, this led to assigning higher weights to θ, S, and mass conservation than NO_{3^-}, PO_4^{3-} (or NO, PO), and Si $(OH)_4$. The mass conservation usually receives the same weighting as the parameter with the highest weight (Poole and Tomczak, 1999; Tomczak and Large, 1989).

In this work, different weightings were tested, starting from a uniform value for all parameters to 16 times higher weighting for θ, S, and mass conservation than PO, NO, and $Si(OH)_4$. The minimum residuals were obtained for the following weightings: 24 for θ, 24 for S, 2 for PO, 2 for NO, 2 for $Si(OH)_4$, and 24 for mass conservation. To compare the residuals of different parameters (for instance, θ and S), we expressed these residuals as percentages of the parameter ranges over the entire layer (Fig. S4).

To validate the reliability and robustness of the eOMPA results obtained in this study, a series of perturbation tests (Monte Carlo analysis) were realized. These tests allowed to estimate the extent to which the eOMPA results could be affected by the variability of 1) the end-member characteristics, 2) JC150 data (including the Redfield ratio used to calculate NO and PO), and 3) the chosen weights. For each test, 100 runs were performed in each eOMPA layer. For each run, perturbations were applied to targeted parameters (end-members, JC150 data, or weights) using normal probability density functions with standard deviations scaled to the uncertainty (or variability) attributed to each parameter. For the first test, uncertainties were the end-member property definition intervals, which reflected the possible variation in the end-member characteristics (reported in Table 1). For the second test, the JC150 data uncertainties were used, i.e., the sensor uncertainties (0,001 for θ, 0,0001 for S, and 0,5 μmol kg^{-1} for O_2) and the nutrient measurement uncertainties (2% for PO_4^{3-}, NO_{3^-}, and $Si(OH)_4$). For this test, the Redfield ratios used to define NO and PO were also modified within a 10% range (155 ± 15 for $R_{O2/P}$, 9,69 ± 1 for $R_{O2/N}$), which was consistent with reported Redfield ratio variability (Anderson, 1995; Anderson and Sarmiento, 1994). For the third test, the weights were modified within the range of 24 ± 5 for θ and S and 2 ± 0,7 for PO, NO, and $Si(OH)_4$. 1000 perturbations were also performed for the first two tests, and the results obtained (not shown here) were very similar to those obtained with 100 perturbations.

2.3. LPTE

To improve the proposed water mass analysis, LPTEs were conducted to complement the eOMPA (i) to aid in identifying the origin of the water masses sampled along JC150 (and thereby contribute to the eOMPA end-member choices) and (ii) to provide information about water mass trajectories between their formation areas and the JC150 section, which cannot be achieved by a sole OMPA. The LPTE experiments were conducted in the velocity field of an eddy-resolving Ocean General Circulation Model. Through the seeding of numerous 'virtual' particles around a point and time of interest (i.e., latitude, longitude, depth, and time), the LPTE can track the particles' location through reverse time by updating the particles' position after each time step of the model. This method enables us to identify the particles' origin over timescales from tens to hundreds of years and reconstruct the trajectories of these particles from the position of origin to the point of interest. As the particles deployed are all marginally offset in space and time relative to the exact sampling position, they generate an ensemble of backward trajectories and origins that can assist in identifying likely water masses constituting the sampled seawater. The model and experiments used in this study are described below.

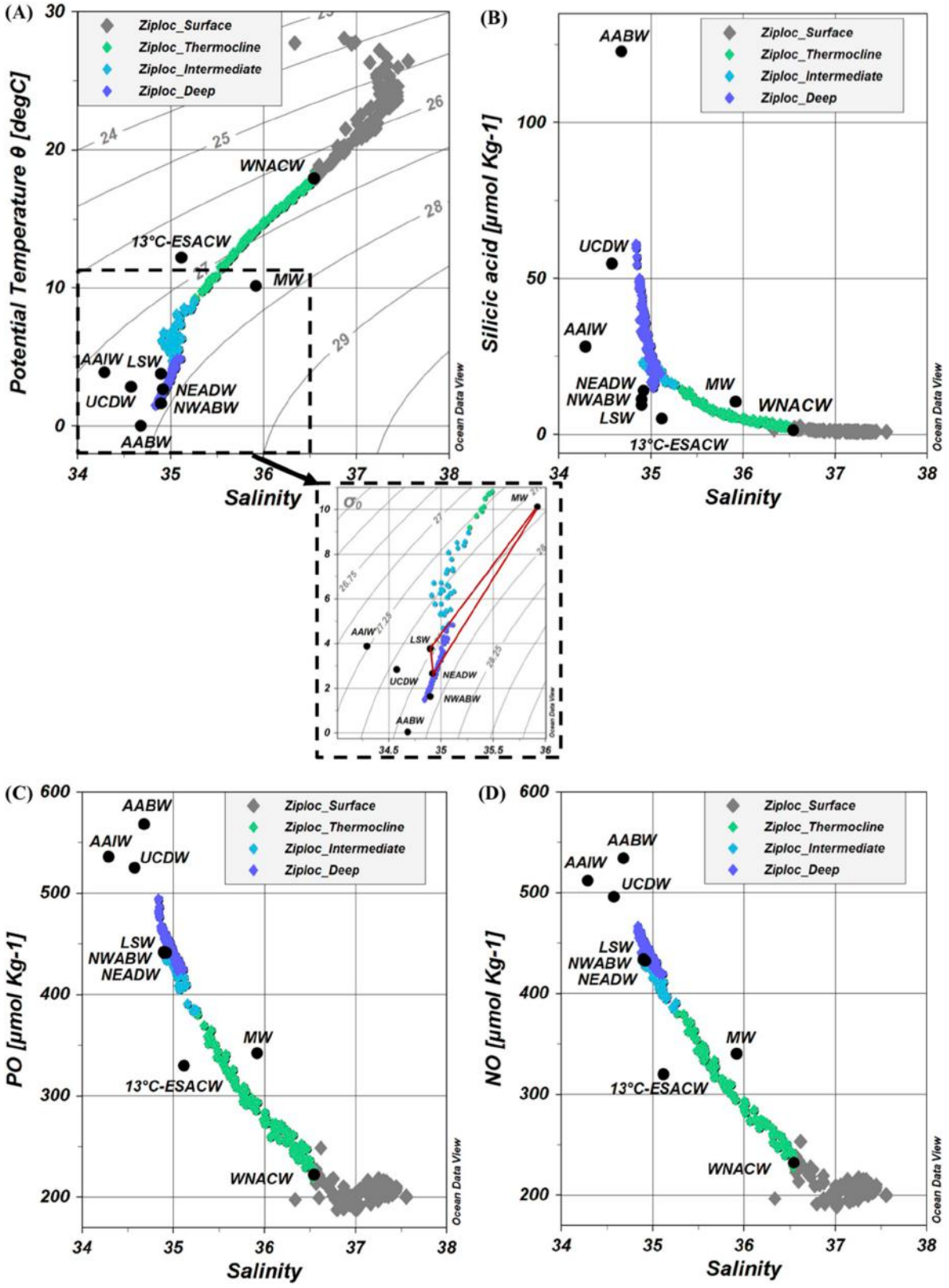

Fig. 2. Potential temperature versus salinity with isopycnals (gray lines) and a zoom on water colder than 10 °C, in which the red triangle highlights the impact of Mediterranean Water (MW) in the deep layer (A), silicic acid versus salinity (B), PO versus salinity (C), and NO versus salinity (D) for the JC150 data (color diamonds) and GEOTRACES end-members (black diamonds). PO and NO definitions are provided in section 2.2. (For interpretation of the references to color in this figure legend, the reader is referred to the Web version of this article.)

Table 1
End-member definitions (values ± uncertainties) from GEOTRACES cruises (refer to the GA03 special issue, Boyle et al., 2015; GA02 papers, Middag et al., 2015; and Rijkenberg et al., 2014). Each end-member is included into one or more of the three extended optimum multiparameter analysis (eOMPA) layers - T: Thermocline, I: Intermediate, and D: Deep. To facilitate the future use of this eOMPA for biogeochemical studies, trace elements and some isotope data are available for each end-member on the GEOTRACES Intermediate Data Product 2017 (IDP, 2017 v2, Schlitzer et al., 2018).

Acronym	Name	Θ (°C)	S	O2 (μmol Kg-1)	$[PO_4^{3-}]$ (μmol Kg-1)	$[NO_{3^-}]$ (μmol Kg-1)	Si (μmol Kg-1)	'PO' (μmol Kg-1)	'NO' (μmol Kg-1)	Data sources	eOMPA layer
WNACW	West North Atlantic Central Water	17.94 ± 0.1	36.545 ± 0.02	202.30 ± 11	0.13 ± 0.04	3.10 ± 1.2	1.40 ± 0.6	222 ± 16	232 ± 16	GA02 station 18, May 22, 2010, 33.433°N, 58.05°W, 251 m	T
ESACW	East South Atlantic Central Water	12.20 ± 0.2	35.117 ± 0.15	205.20 ± 1	0.80 ± 0.04	11.89 ± 2	5.01 ± 1	330 ± 3	320 ± 28	GA10 station 3, December 29, 2011, 36.348°S, 13.140°E, 497 m	T&I
MW	Mediterranean Water	10.13 ± 0.4	35.920 ± 0.1	178.10 ± 8	1.06 ± 0.01	16.67 ± 0.2	10.43 ± 0.5	342 ± 3	340 ± 3	GA03 station 3, October 19, 2010, 35.201°N, 16°W, 986 m	T&I&D
AAIW	Antartic Intermediate Water	3.89 ± 0.3	34.290 ± 0.05	218.30 ± 10	2.05 ± 0.12	30.29 ± 1.5	28.08 ± 8	536 ± 8	512 ± 6	GA02 station 9, March 14, 2011, 32.089°S, 37.459°W, 1001 m	T&I
UCDW	Upper Circumpolar Deep Water	2.84 ± 0.03	34.576 ± 0.08	186.90 ± 5	2.18 ± 0.05	31.93 ± 0.7	54.78 ± 1.7	525 ± 16	496 ± 10	GA02 station 9, March 14, 2011, 32.089°S, 37.459°W, 1501 m	T&I
LSW	Labrador Sea Water	3.76 ± 0.15	34.896 ± 0.04	272.30 ± 6	1.09 ± 0.05	16.70 ± 0.3	9.40 ± 0.8	441 ± 3	434 ± 64	GA02 station 9, May 09, 2010, 51.821°N, 45.732°W, 996 m	I&D
NEADW	North East Atlantic Deep Water	2.66 ± 0.09	34.917 ± 0.003	273.20 ± 5	1.08 ± 0.02	16.40 ± 0.2	14.00 ± 1.9	441 ± 2	432 ± 3	GA02 station 9, May 09, 2010, 51.821°N, 45.732°W, 2512 m	D
NWABW	North West Atlantic Bottom Water	1.63 ± 0.02	34.896 ± 0.09	290.50 ± 0.2	0.98 ± 0.01	14.70 ± 0.1	11.20 ± 0.1	442 ± 0.6	433 ± 0.8	GA02 station 9, May 09, 2010, 51.821°N, 45.732°W, 4041 m	D
AABW	Antartic Bottom Water	0.04 ± 0.06	34.680 ± 0.01	217.40 ± 1.9	2.26 ± 0.07	32.72 ± 0.7	122.80 ± 4.5	568 ± 9	534 ± 4	GA02 station 13, March 20, 2011, 17.017°S, 30.599°W, 4889 m	D

The velocity fields of the Operational Mercator global ocean analysis and forecast system (http://marine.copernicus.eu) were used in this study. This system uses the Ocean General Circulation Model from the Nucleus for European Modelling of the Ocean (NEMO) framework (Madec & the NEMO team, 2008) with a horizontal resolution of 1/12° and 50 vertical layers. The thickness of each vertical layer increases with depth from 1 m at the surface to 450 m at the bottom (5500 m depth). Partial steps were used for the bottom grid cell of the water column to better represent the bottom topography within the model. The model topography was generated with the bathymetric databases ETOPO2 (Amante and Eakins, 2009) and GEBCO8 (Becker et al., 2009) for open ocean and continental shelves, respectively. For further details on the model product and the validity of its velocity fields, the reader can refer to Lellouche et al. (2018a) and Lellouche et al. (2018b). The velocity fields are available as daily and monthly mean values from December 26, 2006 to present.

The Lagrangian experiments were conducted for each sample obtained from the seven stations (total of 302 samples) occupied during the 40-day JC150 cruise (Fig. 1) using the Lagrangian particle tracking tool ARIANE (Blanke and Raynaud, 1997).

As currents are faster in the upper ocean (defined here as the top 800 m), and capturing their behavior requires a finer time resolution, different experimental configurations were defined for each sample based on its sampling depth. Firstly, for depths shallower than 800 m, we employed daily mean velocity fields to track the deployed particles, whereas for depths deeper than 800 m, we used monthly mean values. Secondly, the particles were advected backward in time for varied periods depending on the depth: up to 10 years for the upper ocean samples and up to 300 years for the deep ocean ones.

In all cases, an ensemble of particles (or particle clouds) was uniformly distributed around the sampling location and repeatedly deployed across a period that was centered on the sampling time. This ensemble was organized as a vertical cylinder, made of equally spaced disks of particles spaced at 1/12° resolution radially.

The height of the cylinder, number of disks inside each cylinder, and the number of repeated releases around the sampling time varied between the samples taken within the upper or deep ocean. For example, for the upper ocean, we used a cylinder with a height of 10 m and radius of ¼° and 12-hourly release of particles within a five-day window (nine releases). More details about this experimental setup are provided in S1, while several examples of particle trajectory ensembles for different depths and advection times are shown in Figure S2.

3. Water mass analysis: results and discussion

The hydrographic properties measured during JC150, θ, S, AOU, and concentrations of O_2, PO_4^{3-}, NO_{3-}, and $Si(OH)_4$, are presented in this study for the first time. They are shown as property/property plots in Fig. 2, and as section in Fig. 3.

The discussion is organized in three parts. Firstly, the surface waters shallower than 200–300 m (where an eOMPA cannot be performed, because water properties are constantly changing due to ocean-atmosphere exchange) are discussed using satellite data and LPTE results. Secondly, the end-member choice for the three eOMPA layers is extensively discussed using a thorough literature review, meticulous comparison of the JC150 hydrographic section properties with those of the end-member candidates, and the LPTE results. Finally, the results of the eOMPA are presented (end-members contributions) and discussed.

The LPTE results are presented in Fig. 4. It is beyond the scope of this study to present the LPTE results across all stations and depths. Therefore, for discussion, we selected results at specific depths and from stations 1 and 7, representing the westernmost and easternmost stations, respectively. Finally, the results from the eOMPA are presented in Fig. 5.

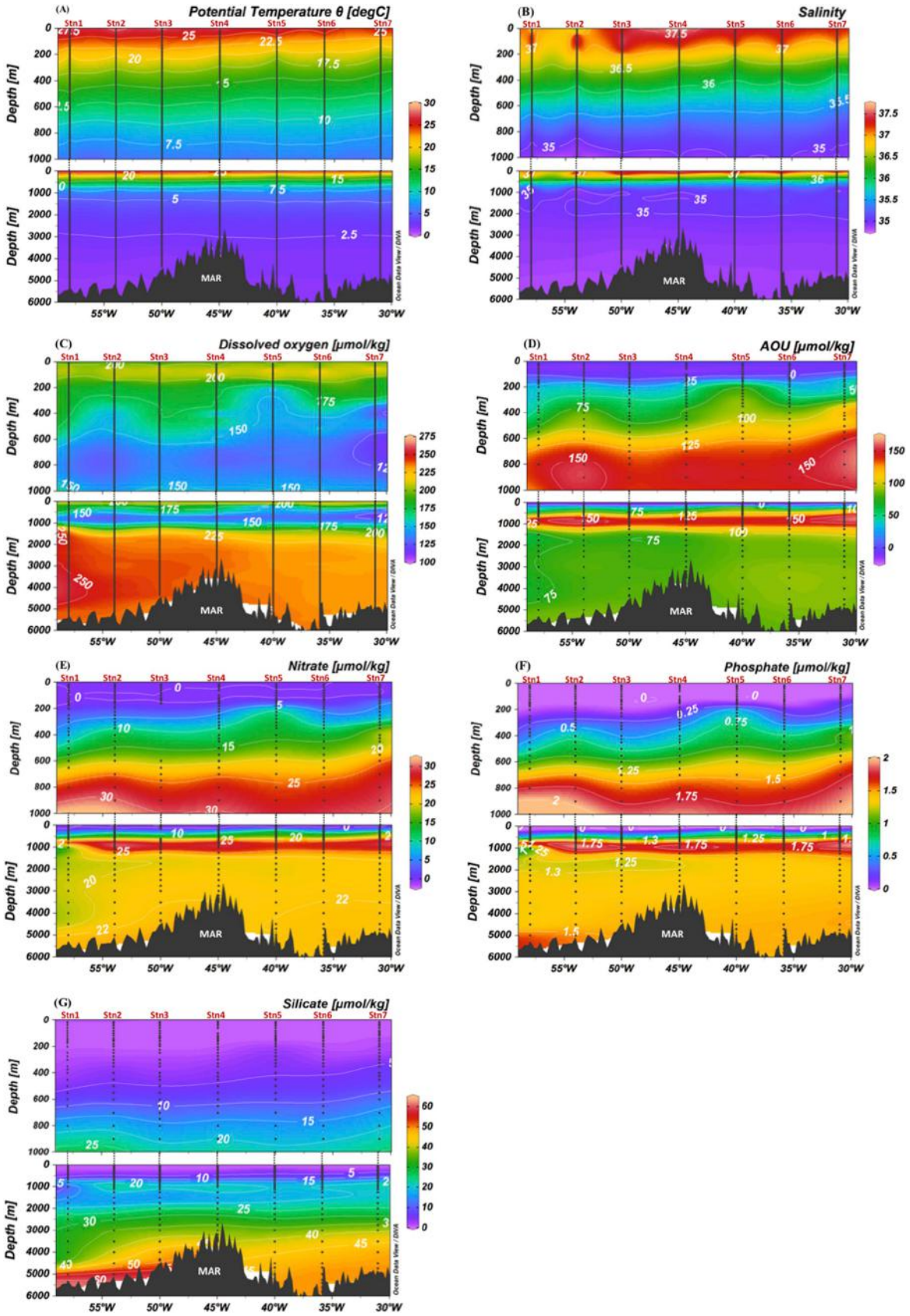

Fig. 3. Observed section of potential temperature (A), salinity (B), dissolved oxygen (C), apparent oxygen utilization (AOU, D), and concentrations of nitrate (E), phosphate (F), and silicic acid (G) from the JC150 cruise. The upper figures show zooms on the upper 1000 m, while the lower figures show the full depth range. Data points are represented by black dots.

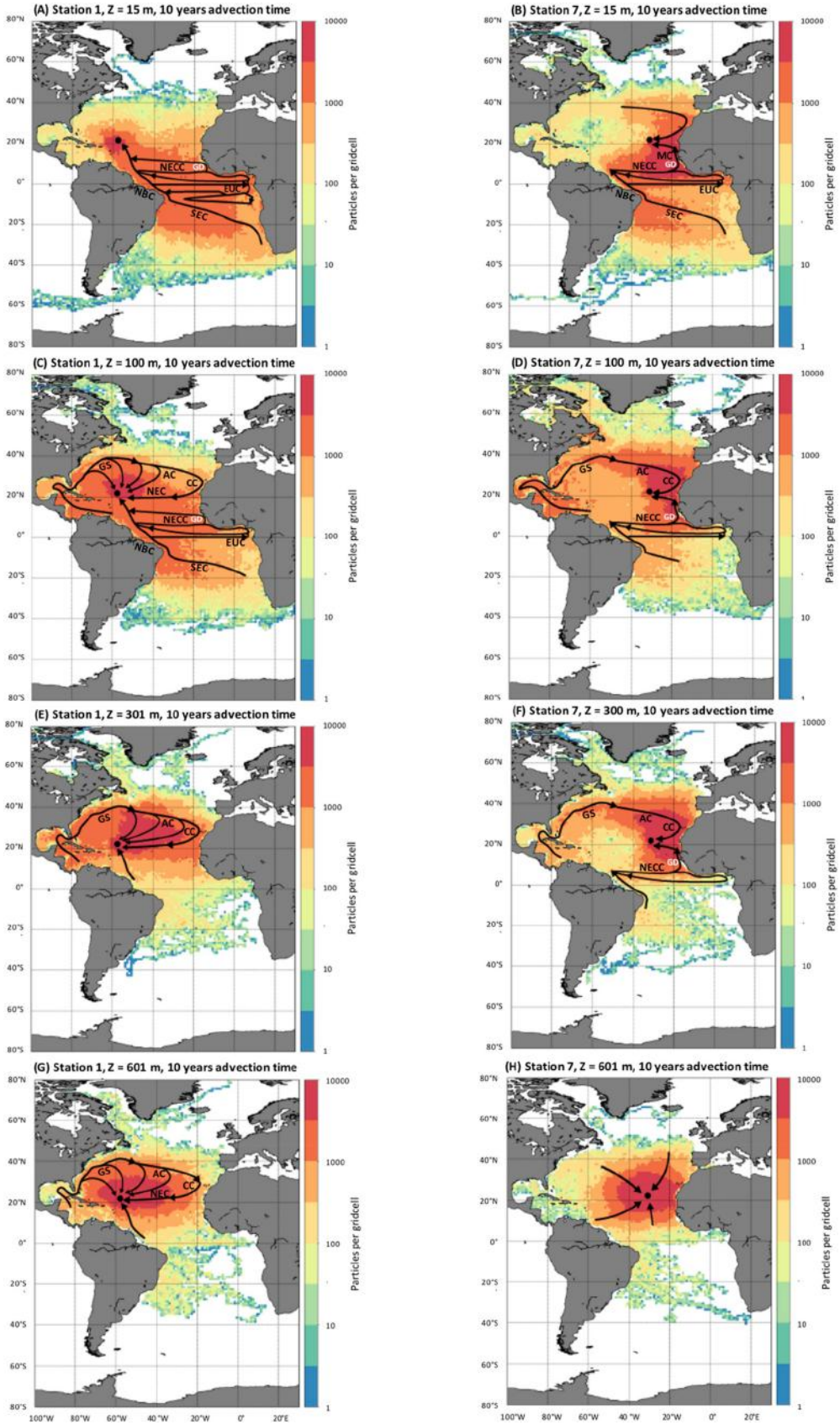

Fig. 4. Particle counts per 2° × 2° grid cells computed by the Lagrangian particle tracking experiment (LPTE), indicating particle origins and particles' most-used pathways to attain the sampling locations. Results are presented for two JC150 stations (westernmost station 1, 22 °N, 58 °W, left panels and easternmost station 7, 22 °N, 31 °W, right panels) and different depths. Particles are advected backward in time with an advection time varying with depth. Arrows highlight the main particle paths obtained from the LPTE results and literature general knowledge. The following currents and location are presented in the figures: Gulf Stream (GS), Azores Current (AC), Canary Current (CC), North Equatorial Current (NEC), South Equatorial Current (SEC), North Brazil Current (NBC), Equatorial Undercurrent (EUC), North Equatorial Countercurrent (NECC), Mauritania Current (MC), Deep Western Boundary Current (DWBC) and Guinea Dome (GD). Refer to Fig. S2 for corresponding raw trajectories.

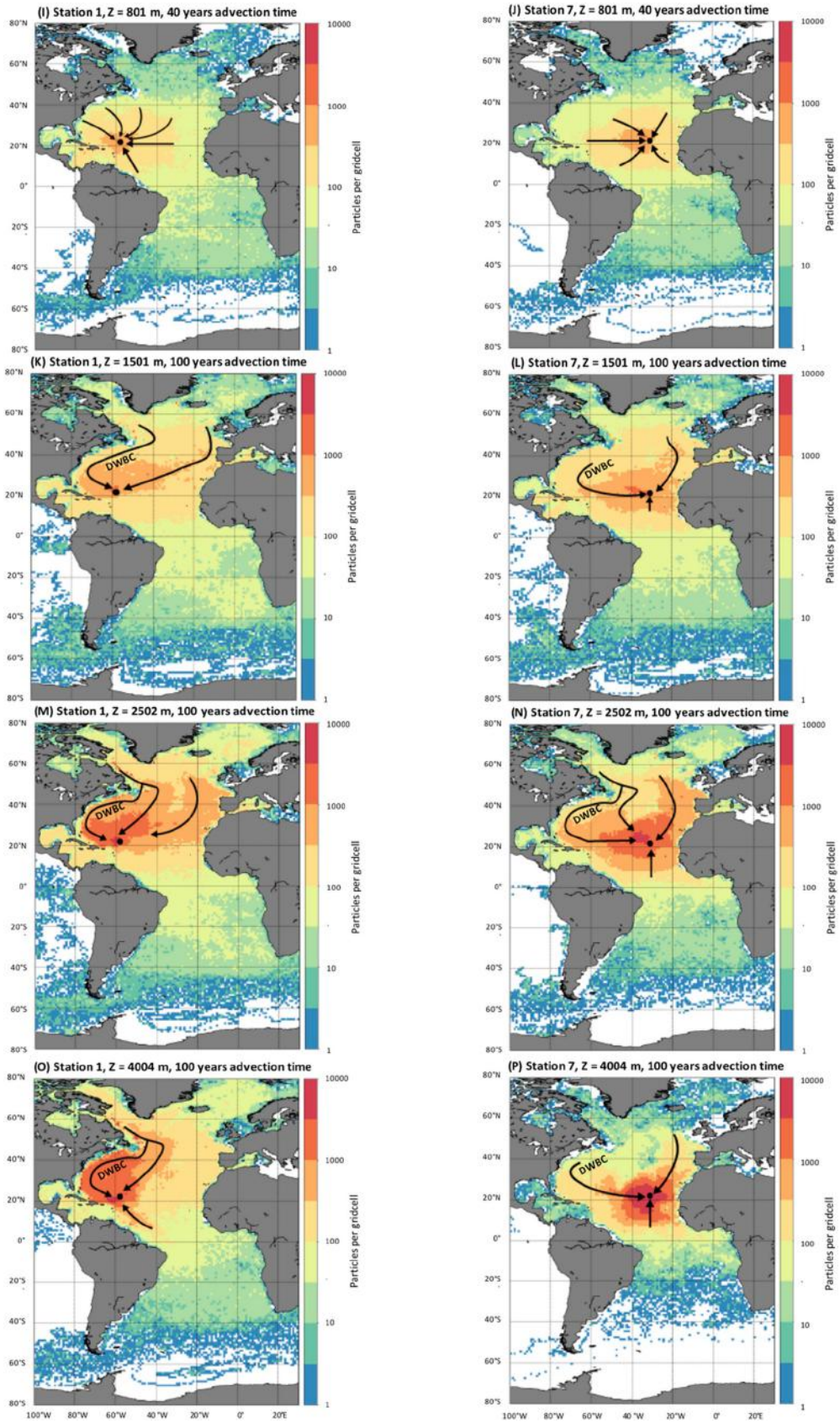

Fig. 4. (*continued*).

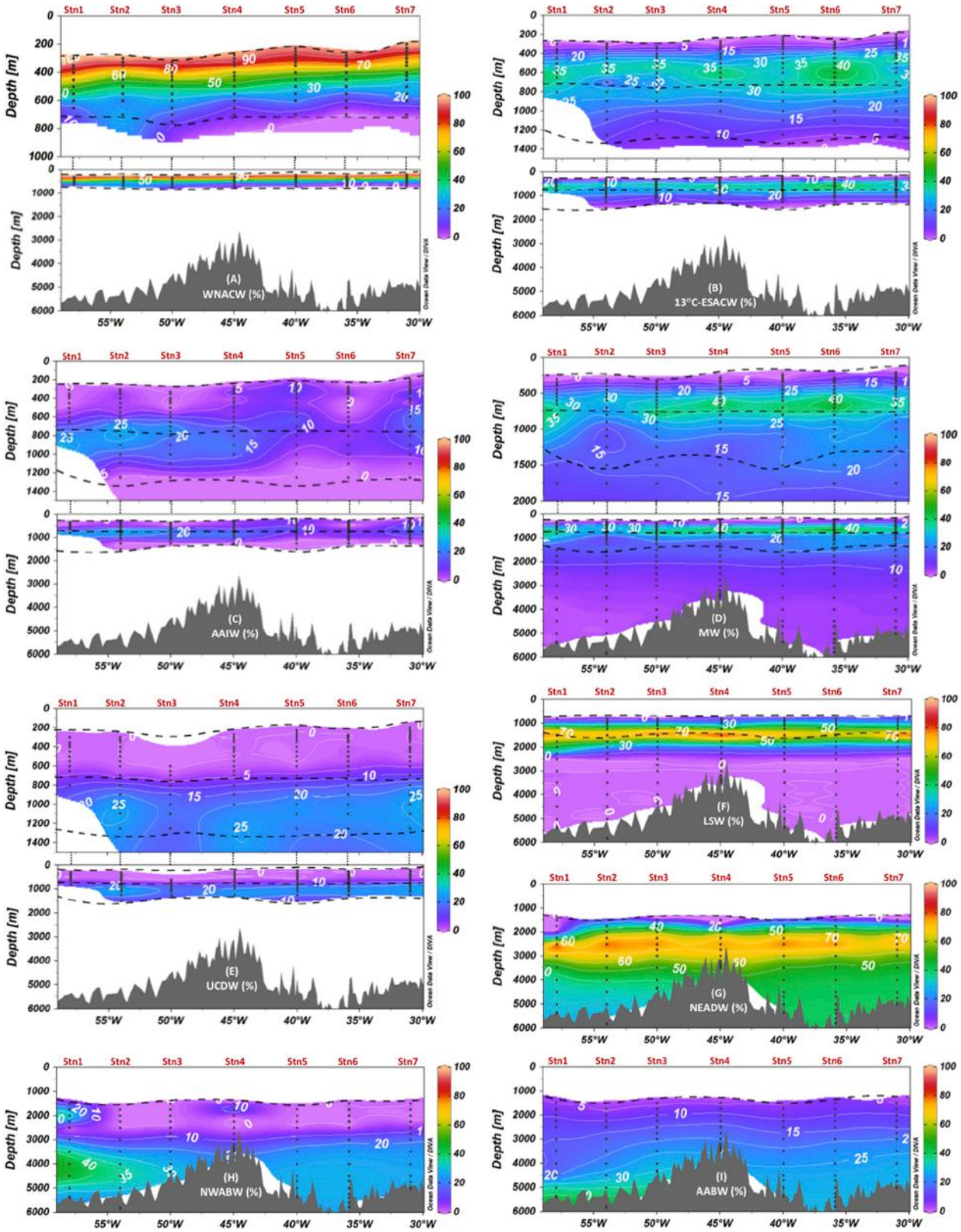

Fig. 5. Contributions (%) of the different end-members to the JC150 section according to the extended optimum multiparameter analysis (eOMPA) of West North Atlantic Central Water (WNACW) (A), 13°C- East South Atlantic Central Water (ESACW) (B), Antarctic Intermediate Water (AAIW) (C), Mediterranean Water (MW) (D), Upper Circumpolar Deep Water (UCDW) (E), Labrador Sea Water (LSW) (F), North East Atlantic Deep Water (NEADW) (G), North West Atlantic Bottom Water (NWABW) (H), and Antarctic Bottom Water (AABW) (I). Sampling points and eOMPA layer boundaries are represented by black dots and horizontal black dashed lines, respectively.

3.1. Surface waters

At the western edge of the section, a near surface tongue of low salinity water (36.3–37) is observed shallower than 27 m at stations 1 and 2 (Fig. 3b). Using a surface satellite salinity map (SMOS, July 2017, Fig. S3), this feature can clearly be attributed to Amazon River plume. This is supported by the LPTE results that show the particle trajectories from near the Amazon River mouth reaching the west of the zonal section (at depths of 15 m and 100 m, as shown in Fig. 4a and c, respectively). This feature is constrained to the very surface and does not impact the eOMPA results discussed below.

Two well-defined central water masses dominate the tropical Atlantic thermocline layer: the North Atlantic Central Water (NACW) and the South Atlantic Central Water (SACW). The sampled section extends along 22 °N, 58–31 °W, while the transition from NACW into SACW occurs at approximately 15 °N at the Cape Verde Frontal Zone (Fieux, 2010; Tomczak and Godfrey, 1994). Therefore, the impact of NACW and SACW on the sampled waters was investigated.

SACW encompasses two main water masses, including the Western SACW (WSACW) and the Eastern SACW (ESACW) (Poole and Tomczak, 1999). WSACW is formed in the confluence zone of Brazil and Malvinas Currents (Fieux, 2010) and recirculates within the southern subtropical gyre. Therefore, it is mostly restricted to the western South Atlantic Ocean (Fieux, 2010; Tomczak and Godfrey, 1994). In contrast, ESACW mainly comprises Indian Central Water transferred into the Atlantic Ocean through Agulhas Current rings and is known to cross the Atlantic basin several times during its northwards transit (Fieux, 2010; Tomczak and Godfrey, 1994; Tsuchiya, 1986). Our LPTE trajectories are in good agreement with the current understanding of the ESACW northward transit (Fig. 4a–d): ESACW is transported northwestwards from the Cape Basin to the equator through the southern branch of the South Equatorial Current and North Brazil Current. Here, the trajectories show a portion of ESACW continuing northward toward the western stations (Fig. 4a and c), while a portion retroflects eastward toward the Guinea Dome within components of the equatorial current system (Fig. 4a–d).

In addition to what has been previously described, the LPTE suggested that this shallow ESACW reached the JC150 zonal section from the Guinea Dome by two trajectories: a portion flows northwards within the Mauritania Current to the easternmost stations (Fig. 4b and d), while another portion crosses the Atlantic basin westward once more and then flows northward to join the westernmost stations (Fig. 4a and c).

NACW also comprises several waters masses. More than half of its volume comprises subtropical mode water (Tomczak and Godfrey, 1994). The principal North Atlantic's subtropical mode water is the Western NACW (WNACW, Talley et al., 2011), also called '18 °C water'. WNACW is formed in the Sargasso Sea and identified by a permanent thermostat between 300 and 500 m at approximately 17–18 °C (Fieux, 2010; Tomczak and Godfrey, 1994).

Between 100 and 300 m, the LPTE analysis shows waters following the North Atlantic anticyclonic subtropical gyre circulation, i.e., waters originate from the Gulf of Mexico and the Caribbean Sea, flow through the Sargasso Sea and the Gulf Stream and then the Azores and Canary currents, and finally the North Equatorial Current flowing westward redistributes these waters from the eastern to the western JC150 stations. In addition, the LPTE trajectories show a direct transfer from the Gulf Stream to the sampled stations (Fig. 4c–f). These trajectories correspond very well to the circulation pattern of WNACW. This suggests that this 100–300 m depth layer, below the layer mainly occupied by ESACW, is dominated by WNACW.

In summary, above ~300 m, the salinity data from JC150, SMOS, and LPTE show an Amazon influence in the west of the section, which is restricted to the near-surface. The LPTE results highlight the dominant influence of a shallow variety of ESACW in the upper 100 m and an increasing WNACW impact below 100 m.

3.2. Analysis of end-members for thermocline, intermediate, and deep eOMPA layers

This section discusses the end-member choice for the thermocline (main thermocline from 300 to 700 m), intermediate (700–1500 m) and deep eOMPA layers (1500 m to seafloor).

All end-members of the present eOMPA were selected from GEOTRACES cruises, where numerous parameters, including trace elements and isotopes, are available to facilitate further use of this eOMPA results (these locations are not necessarily in the water mass formation regions).

3.2.1. Thermocline waters

The two central waters discussed above (ESACW and WNACW) are also present below 300 m. WNACW is the only water mass that can account for the warm, salty, and low PO and NO concentration waters found in the thermocline layer (Fig. 2). In addition to supporting the presence of WNACW in surface waters (section 3.1), the LPTE analysis supports the large contribution of WNACW to the thermocline layer (Fig. 4e–h) with particles following the anticyclonic North Atlantic Subtropical gyre circulation between 300 and 600 m (refer to WNACW circulation details in section 3.1). Although the surface gyre circulation pattern appears weaker by 800 m (Fig. 4i and j), WNACW is ultimately an important end-member to be included in the thermocline layer. We used θ, S, concentrations of O_2, PO_4^{3-}, NO_{3-}, and $Si(OH)_4$ data from the GEOTRACES GA02 cruise station 18 at ~250 m to define WNACW (Fig. 1). These end-member hydrographic and nutrient values are in agreement with those reported in literature (Hinrichsen and Tomczak, 1993; Talley et al., 2011, cf. Table .1 for detailed properties). As stated earlier (section 3.1), WNACW is the main type of NACW. Other types of NACW, such as the Madeira Mode Water or the East NACW, exist (Harvey, 1982; Talley et al., 2011; Tomczak and Godfrey, 1994). However, the Madeira Mode Water presents a formation rate and volume, which are much lower than those of WNACW. The East NACW is considered in this study as partly included in the Mediterranean Water (MW) definition (refer below, Carracedo et al., 2016; Talley et al., 2011). Therefore, Madeira Mode Water and East NACW were not included as an end-member in the present eOMPA.

A type of ESACW, namely the 13 °C-ESACW, is an important contributor to the thermocline of the Atlantic Ocean (Tomczak and Godfrey, 1994; Tsuchiya, 1986). 13 °C-ESACW is needed to account for the warm, low salinity, and low PO, NO, and $Si(OH)_4$ waters in the thermocline layer, as well as the warm, low salinity, and low PO and NO waters in the intermediate layer (Fig. 2). Even though the LPTE results do not show a dominance of ESACW trajectories below 300 m along the JC150 zonal section (WNACW dominates at 300–800 m), they still show a non-negligible influence from south Atlantic origin waters to depths of 800 m (Fig. 4i and j) and 1000 m (data not shown). Therefore, 13 °C-ESACW was chosen as an end-member to be considered in both thermocline and intermediate layers. We used θ, S, concentrations of O_2, PO_4^{3-}, NO_{3-}, and $Si(OH)_4$ data from the GEOTRACES GA10 cruise station 3 at ~500 m to define 13 °C-ESACW (Fig. 1). These end-member hydrographic and nutrient values are in agreement with those reported in literature (Poole and Tomczak, 1999, refer to Table 1 for detailed properties).

As stated earlier (section 3.1), the other major SACW, which is WSACW, is restricted to the southwest Atlantic (south of 30 °S, Fieux, 2010; Tomczak and Godfrey, 1994). This restriction was underlined by a previous OMPA study, in which almost no contribution of WSACW was observed at 22 °N (Poole and Tomczak, 1999). The LPTE results support these conclusions, as they show no significant particles originating from the West South Atlantic, south of 30 °S, at the thermocline depths (Fig. 4e–h). Therefore, WSACW was not included in the thermocline eOMPA. Note that the Guinea Dome Water was not explicitly included as an end-member in the present eOMPA; however, it was implicitly included, as it could be considered as ESACW significantly modified by

the remineralization processes (Stramma and Schott, 1999).

3.2.2. Intermediate waters

At intermediate depths (~700–1500 m), the hydrographic atlases clearly show a high salinity layer, which is attributed to the MW (World Ocean Atlas, 2018, Zweng et al., 2019; Fieux, 2010). MW is formed by the mixing of the Mediterranean Outflow water, entering the Atlantic through the Gibraltar Strait, with the subsurface and intermediate waters of the northeast Atlantic (Baringer, 1997; Carracedo et al., 2016). MW extends northward to the Iceland-Scotland Ridge and westward to the Gulf Stream (core at ~1000 m, Fieux, 2010), thereby presenting an important contribution to intermediate depths across the North Atlantic. However, high salinity MW is not visible along the JC150 section (Fig. 3b). This is because, at ~20 °N, the MW salinity maximum is located at the same depth as low salinity Antarctic Intermediate Water (AAIW), where mixing reduces the salinity (Fieux, 2010; Talley et al., 2011). AAIW is the densest and less salty of the subantarctic mode water. Formed along the subantarctic and mostly in the southeast Pacific, AAIW enters into the Atlantic Ocean mainly via the Drake Passage and the Malvinas Current (Pacific type of AAIW) and expands northward (Fieux, 2010 and references therein; Talley, 1996; Tomczak and Godfrey, 1994). This northward expansion of low salinity AAIW is traced as far as 20 °N between 800 and 1000 m (Fieux, 2010; Hinrichsen and Tomczak, 1993; Talley et al., 2011). This observation possibly explains the lower salinity (<35) centered at ~1000 m, mainly observed in the west of the MAR during the JC150 cruise (Fig. 3b). Nevertheless, the θ-S diagram (Fig. 2a) shows that MW is the only intermediate water mass that can explain the cold and saline waters in the thermocline layer and the saltiest waters in both intermediate and deep layers (as previously suggested by Reid, 1979).

Furthermore, a strong O_2 minimum ($O_2 < 150$ μmol kg^{-1}), which is coincident with a layer of high AOU (AOU > 125 μmol kg^{-1}), is visible across the entire JC150 zonal section centered at ~800 m (Fig. 3c and d). This O_2 minimum is also nearly coincident with a layer of maximum NO_{3^-} and PO_4^{3-} concentrations centered at ~900 m (>25 μmol kg^{-1} and >1.5 μmol kg^{-1}, respectively, Fig. 3e and f, respectively) and relatively high $Si(OH)_4$ concentration (>20 μmol kg^{-1}, ~1000 m, Fig. 3g). All these properties reflect the remineralization processes known to characterize the Upper Circumpolar Deep Water (UCDW) originating from the Southern Ocean and flowing northward into the Atlantic just below AAIW (Broecker et al., 1985). In the tropics, AAIW joins vertically with UCDW (Talley et al., 2011; Tsuchiya et al., 1994). The resulting AAIW/UCDW complex, traceable by high nutrients rather than low salinity, moves northward into the Gulf Stream system and North Atlantic Current as far as 60 °N just south of Iceland (Talley et al., 2011; Tsuchiya, 1989; Tsuchiya et al., 1994). This is consistent with the low O_2, high NO_{3^-}, PO_4^{3-}, and $Si(OH)_4$ layers described above along the JC150 section. In addition, inclusion of AAIW and UCDW are necessary to explain the coldest and highest PO and NO values in both thermocline and intermediate layers (Fig. 2). UCDW is also specifically needed to explain the highest $Si(OH)_4$ values of the intermediate layer.

Although, the LPTE results did not aid us in clearly confirming (nor reject) the contributions of MW, AAIW, and UCDW along the JC150 section, the above discussion is sufficient to conclude that MW was an essential end-member to include in the three eOMPA layers, while AAIW and UCDW were essential end-members in the thermocline and intermediate layers. We used θ, S, concentrations of O_2, PO_4^{3-}, NO_{3^-}, and $Si(OH)_4$ data from GEOTRACES GA03 cruise station 3 at ~1000 m to define MW and GEOTRACES GA02 cruise station 9 at ~1000 m to define AAIW and those at ~1500 m to define UCDW (Fig. 1). These end-member properties were in agreement with those reported in literature (Talley et al., 2011; Tsuchiya et al., 1994, refer to Table 1 for detailed properties).

3.2.3. Deep and bottom waters

In the west of the section, high O_2, and relatively low NO_{3^-} and PO_4^{3-} waters are observed from ~1500 to 4500 m (Fig. 3c, e, and 3f). This feature progressively decreases eastwards, but is still visible east of the MAR. It is well established that these distributions are associated with low nutrients and recently ventilated waters from the North Atlantic, mainly leading to the formation of North Atlantic Deep Water: Labrador Sea Water (LSW), North East Atlantic Deep Water (NEADW), and North West Atlantic Bottom Water (NWABW) (Swift, 1984; Talley et al., 2011).

LSW is formed in the Labrador Sea by winter convection leading to a homogenous water mass from the surface to a depth of 1500–2000 m depending on the winter severity (Fieux, 2010; Lazier et al., 2002). From the Labrador Sea, LSW is transported in three main directions, including northward in the Irminger Sea, eastward crossing the MAR, and southward within the Deep Western Boundary Current (DWBC, Fieux, 2010; Talley and McCartney, 1982). At 1500 m, the LPTE results show two main flows that transport LSW to the JC150 section (Fig. 4k and l): west of the MAR from the Labrador basin within the DWBC, and east of the MAR from the Iceland basin. The first path within the DWBC has been well documented (Fieux, 2010; Talley et al., 2011; Talley and McCartney, 1982). The presence of LSW in the eastern North Atlantic (the eastern subpolar gyre, Iceland Basin, and the Rockall Trough) has also been well documented (Talley et al., 2011). However, we could not find previous works presenting an evidence of the second LSW pathway, east of the MAR and below 40 °N, from the eastern North Atlantic to the eastern tropical Atlantic.

Below the LSW layer, NEADW is formed by the mixing of dense Iceland-Scotland Overflow Water (ISOW) with southern origin Lower Deep Water (modified Antarctic Bottom Water), entrained LSW, and subpolar mode water (Lacan and Jeandel, 2005; McCartney, 1992; Read, 2001). NEADW flows in the recirculation cells in the western and eastern parts of the Subpolar North Atlantic Gyre, which are connected to each other through the Charlie-Gibbs Fracture Zone (van Aken, 2007; Fieux, 2010; McCartney and Talley, 1984; Read, 2001; Swift, 1984; Talley et al., 2011). This water mass is known to be transported southward within the DWBC and east of the MAR (Fieux, 2010). The LPTE results (at 2500 m, Fig. 4m and n) confirm both pathways.

NWABW is the densest water found near the bottom of the northwest Atlantic (Swift, 1984). It originates from the dense, cold, and ventilated Denmark Strait Overflow Water (DSOW) which, descending over the East Greenland continental slope to the bottom of the North Atlantic Subpolar gyre, mixes with Irminger water, LSW, and ISOW (Fieux, 2010). Contrary to LSW and NEADW, NWABW is too deep to cross the MAR and is therefore restricted to the western basin of the North Atlantic Subpolar Gyre. From there, NWABW flows equatorward within the DWBC along the western margin of the North Atlantic (Fieux, 2010). At 3000 m (data not shown) and 4000 m (Fig. 4o and p), the LPTE results confirm the NWABW transport from the Labrador Sea in the DWBC.

The above discussion confirms that LSW, NEADW, and NWABW, which are the main contributors along with the MW to the North Atlantic Deep Water, should be considered as end-members for the JC150 section. The contribution of LSW is specifically required to explain the cold and slightly saline waters of the intermediate layer as well as the warm and low salinity waters of the deep layer (Fig. 2). Therefore, LSW was included in both intermediate and deep layers. LSW, NEADW, and NWABW are needed to explain the $Si(OH)_4$, PO, and NO values at low salinity of the deep layer (Fig. 2b–d). Therefore, NEADW and NWABW were included in the deep layer. We used θ, S, concentrations of O_2, PO_4^{3-}, $NO_{3^-, \text{ and } Si(OH)4}$ data from the GEOTRACES GA02 cruise station 9 at ~1000 m to define LSW, ~2500 m to define NEADW, and ~4000 m to define NWABW (Fig. 1). These chosen end-member properties are in agreement with those reported in literature (van Aken, 2007, refer to Table 1 for detailed properties; Fieux, 2010).

A marked increase in the $Si(OH)_4$ concentration is observed in the range of 2500 m to the bottom, which attains a maximum value (>60 μmol kg^{-1}) in the west of the MAR. This feature reflects the influence of Antarctic Bottom Water (AABW) originating from the Weddell Sea with a $Si(OH)_4$ maximum that can be traced to the North Atlantic (Word

Ocean Atlas, 2018, Garcia et al., 2019). Its characteristics and northward expansion are influenced by its mixing with overlying water masses and the complex topography (van Aken, 2007; McCartney, 1992; Talley et al., 2011). AABW is the only water mass that can explain the coldest waters as well as the highest $Si(OH)_4$, NO, and PO waters of the deep layer (Fig. 2). The presence of this water mass in the deep layer is indisputable and was therefore included. We used θ, S, concentrations of O_2, PO_4^{3-}, NO_{3-}, and $Si(OH)_4$ data from the GEOTRACES GA02 cruise station 13 at ~4900 m to define AABW (Fig. 1). These chosen end-member properties are in agreement with those reported in literature (van Aken, 2007; McCartney, 1992; Talley et al., 2011).

In summary, the eOMPA thermocline layer includes WNACW, 13 °C-ESACW, AAIW, UCDW, and MW. The eOMPA intermediate layer includes 13 °C-ESACW, AAIW, UCDW, MW, and LSW. The eOMPA deep layer includes MW, LSW, NEADW, NWABW, and AABW. These end-member properties are summarized in Table 1.

3.3. eOMPA

The eOMPA MATLAB routine was executed with the section data, end-members, weightings, and the Redfield ratios determined earlier. The results from the eOMPA are presented in Fig. 5 as sections of end-member contributions. These results are discussed in detail in this section.

3.3.1. Residuals and perturbation tests

The validity of the eOMPA results is discussed in this section. Firstly, to verify that the eOMPA reproduces the observed values well, the residuals were closely observed. This aided in determining whether the end-members were accurately selected. Secondly, to evaluate whether the eOMPA results were robust, we discuss the results of the perturbation analysis. This aids in quantifying the sensitivity of the results to our initial choices.

The residuals are presented as sections in Fig. S4. The residual values are similar for the three eOMPA layers and their average values are as follows: ~0% for θ, < 1% for S, < 7% for PO, < 9% for NO, < 5% for Si, and ~0% for mass conservation. These average values include one outlier at 1500 m (over 199 samples, station 5). Except for this sample, that does not change the features of the results, the low residue values indicate that the eOMPA well reproduces the observed values. This a posteriori validates the initial choices about the end-members and Redfield ratios.

The results of the three perturbation tests (end-member characteristics, JC150 section data, and parameters weights) enable us to assign an uncertainty/variability (two standard deviation) to each water mass contribution (the section mean values of these uncertainties are reported in Table. S5 and presented on sections in Figs. S6, S7, and S8). Overall, the perturbation of both the end-members' properties and the JC150 data result in uncertainties/variabilities of approximately 8% each on average on the water mass percentage results (mean standard deviation over the three eOMPA layers, 2 SD, %). The perturbation of the weights attributed to the eOMPA properties only perturbs the water mass percentage results up to 2% (mean standard deviation over the three eOMPA layers, 2SD, %). Overall, these perturbation analyses show that the main results of the OMPA are robust, i.e., the water mass spatial distribution and their main characteristics (such as dominant water masses) remain unchanged.

3.3.2. Thermocline waters

WNACW strongly dominates the thermocline layer (Fig. 5a) with a contribution exceeding 90% at ~300 m. This contribution quickly decreases with depth and declines to 50% between 400 and 500 m and under 10% at the depth of ~700 m. The presence of WNACW extends marginally deeper in the west of the section (~100 m deeper than in the east), which is consistent with a stronger WNACW penetration closer to its formation area in the Sargasso Sea (Fieux, 2010; Tomczak and Godfrey, 1994). The dominance of WNACW in this layer was expected based on the two previous basin scale **e**OMPA studies conducted in the Atlantic Ocean thermocline (Poole and Tomczak, 1999) and along the GA03 2011 GEOTRACES section (Jenkins et al., 2015) located close to the JC150 section (refer to Fig. 1). Both studies obtained large NACW contributions at depths above 600/800 m and the latitude of JC150. The dominance of WNACW in the thermocline layer is also consistent with the LPTE results, indicating that the density of particles coming from the North Atlantic Subtropical Gyre is dominant in the range of 300–600 m (Fig. 4e–h).

Below the WNACW, a core of 13 °C-ESACW is found across the section with contributions higher than ~30% in the range of 500–800 m, which attains the maximum at ~600 m depth (35%, Fig. 5b). This result remarkably agrees with a previous eOMPA that estimates a contribution of ~25% at 22 °N:25 °W in the range 400–800 m (Poole and Tomczak, 1999). Below 850 m, the 13 °C-ESACW contribution decreases with depth to under 10% at ~1250 m. No previous eOMPA study included 13 °C-ESACW as an end-member deeper than 800 m in the Atlantic. However, no other water mass could explain the warm, low salinity, and low PO and NO waters observed in the intermediate layer of the JC150 section (Fig. 3).

3.3.3. Intermediate waters

AAIW is present at depths of 550–1100 m, thereby contributing to both thermocline and intermediate layers. Its contribution is higher west of the MAR, where it attains a maximum at ~700 m (>30%) (Fig. 5c). UCDW is present over a similar depth range of 700–1500 m just below the AAIW and attains a maximum (>25%) at ~1000 m depth. The presence of AAIW and, just below, UCDW in the subtropical Atlantic is consistent with what was reported in previous hydrodynamic studies (Talley et al., 2011; Tsuchiya, 1989; Tsuchiya et al., 1994). This is also supported by two other OMPA studies reporting an AAIW contribution at ~750–900 m immediately above UCDW (Álvarez et al., 2014; Jenkins et al., 2015).

The MW contribution exceeds 25% in the depth range of 500–1000 m across the section with a maximum contribution (>40%) centered at ~700 m depth (Fig. 5d). The MW contribution is higher and deeper in the east of the MAR (>20% at 1500 m) than in the west of the MAR (>20% at ~1000 m), suggesting a westward expansion of this water mass, which is consistent with the MW propagation in the North Atlantic (Fieux, 2010). The MW contribution results are also comparable with the GA03 OMPA study (Jenkins et al., 2015), according to which the MW contribution extended westward across the MAR at approximately 500–1000 m depth. However, our MW contributions are larger than those reported in other OMPA analyses (Bashmachnikov et al., 2015; Louarn and Morin, 2011). This might be explained by the fact that our MW end-member was defined further away from the Strait of Gibraltar and included a contribution of subsurface and intermediate waters of the Northeast Atlantic (refer to section 3.2.2). The MW maximum contribution is in the same depth range as that of AAIW; however, MW is more pronounced in the east, whereas AAIW is more pronounced in the west. This is consistent with the mixing of MW with AAIW at approximately 20 °N (Fieux, 2010; Talley et al., 2011). In the deep eOMPA layer, the MW contribution is under 10% deeper than 2300 m and under 5% deeper than 3500 m. This is consistent with the GA03 OMPA study that reported an MW contribution of ~10% in the range of 2000–3600 m (Jenkins et al., 2015). Though this contribution in our deep layer eOMPA is low, it is not zero. It is absolutely necessary to account for the deep layer saltiest waters (refer to the red triangle in Fig. 2a), which is in agreement with initial findings of Reid (1979).

3.3.4. Deep waters

LSW is included in both intermediate and deep eOMPA layers. This water mass is present across the section and exceeds a contribution of over 20% in the depth range of 900–2000 m. Its contribution exceeds 50% in the depth range of 1250–1750 m and attains a maximum (>70%)

at ~1500 m depth (Fig. 5f). This is consistent with the GA01 (Subpolar Gyre) eOMPA study, that found LSW centered at 1500 m in the Iceland and west European Basins (García-Ibáñez et al., 2018). It is also consistent with the GA03 OMPA study that found the Upper LSW centered at 1500 m across the MAR (Jenkins et al., 2015).

The NEADW contribution exceeds 30% from ~2000 m to the bottom across the section (Fig. 5g). Its maximum (>70%) is attained at ~2500 m. The NEADW contribution is under 40% at a depth of over 4000 m and in the west of the MAR, while the contribution in the east of the MAR is over 40% down to the bottom. This is consistent with the LPTE results and previous studies that suggest that the NEADW contribution is achieved not only from the DWBC, but also directly from the eastern part of the Subpolar North Atlantic Gyre east of the MAR (van Aken, 2007; Fieux, 2010; McCartney, 1992; Read, 2001; Talley et al., 2011).

Below the NEADW, NWABW appears from 3000 m (>10%) to the bottom and attains its maximum (>45%) at approximately 4000–4500 m at the section's western end (Fig. 5h). This maximum seems to expand eastward to the MAR. East of the MAR, the NWABW contribution exceeds 25% from 4000 m to the bottom. Four data points located shallower than 2500 m present an unrealistic high NWABW contribution of over 19% and are clear outliers (Station 1 1750 m, 2000 m, and 2251 m and Station 4 1750 m), as a previous work has reported that this water mass is absent at such shallow depths (García-Ibáñez et al., 2018). The lack of continuity between the calculated NWABW core (observed here at 4000–4500 m) and these points is also an argument for excluding these four data points. These four outliers should correspond to a predominance of LSW and NEADW. LSW, NEADW, and NWABW have very close properties (almost undistinguishable in terms of S, PO, NO, and Si $(OH)_4$ and temperature differences in the order of 1 °C, refer to Fig. 2). These similitudes explain that the deep eOMPA did not accurately distinguish the three end-members for these four outliers. However, for the other 84 data points of the deep layer (88 data points in total), the eOMPA appropriately distinguished between LSW, NEADW, and NWABW and provided results, which are consistent with the literature (notably LSW above NEADW above NWABW, Lacan and Jeandel, 2005; Swift, 1984). The maximum NWABW contribution in the west is consistent with what was reported in previous studies on NWABW flowing equatorward from the Labrador basin with DWBC along the western margin of the North Atlantic (Fieux, 2010). However, the significant NWABW contribution east of the MAR (up to ~20%) is unexpected or at least unreported so far. This water mass, which is formed in the Labrador and Irminger Basins, is too dense to cross the MAR through the Charlie-Gibbs Fracture Zone and was therefore never observed east of the MAR in the North Atlantic Subpolar Gyre. Flowing southward from there, the first passage sufficiently deep for the NWABW to cross the MAR is the Kane fracture zone, which is localized at 24 °N (just north of the JC150 section at 22 °N, Fig. 1) with a sill depth of ~4350 m (Morozov et al., 2017). The next passage that is sufficiently deep is the Vema Fracture Zone with a sill depth of ~5000 m; however, it is located much further south (10–11 °N, Kastens et al., 1998). Therefore, our results suggest that NWABW enters the eastern Atlantic through the Kane fracture zone. This eastern trajectory is confirmed by the LPTE results, which indicates particles originating directly from the eastern part of the Subpolar North Atlantic Gyre east of the MAR at 4000 m (Fig. 4p). We could not find any previous study describing this aspect.

Note that our results about the localization of NEADW above NWABW contradicts with those of the GA03 OMPA, which found DSOW (that significantly contributes to the formation of NWABW) lying above ISOW (that significantly contributes to the formation of NEADW) (Jenkins et al., 2015). Our results confirm that NWABW (including DSOW) lies below NEADW (including ISOW) in the subtropical North Atlantic. In addition, our results are consistent in terms of the densities of NWABW and DSOW being higher than those of NEADW and ISOW, respectively. It is generally consistent with the current understanding of deep water mass dynamics in the North Atlantic as well (Fieux, 2010; Lacan and Jeandel, 2005; Middag et al., 2015; Swift, 1984).

Deeper than 3000 m, the AABW contribution exceeds 15% across the section. West of the MAR, AABW attains its maximum contribution (>35%) from 5000 m to the bottom. East of the MAR, the AABW contribution stays relatively high (>20%) at a depth of over 3500 m. This AABW contribution to bottom waters of the section and across the MAR is consistent with the findings reported in previous studies, which describe AABW as the densest water in the majority of the Atlantic, moving northward from its formation zone and crossing the MAR at 11 °N through the Vema fracture zone (van Aken, 2007; McCartney, 1992; Talley et al., 2011). This AABW contribution is also consistent with the GA03 OMPA study, in which a contribution of AABW is observed across the MAR in the deepest parts of both the western and eastern basins (Jenkins et al., 2015).

4. Conclusions

Based on i) the hydrographic data (θ, S, concentrations of O_2, NO_3^-, PO_4^{3-}, and $Si(OH)_4$), ii) an eOMPA, and iii) an LPTE conducted in an eddy-resolving ocean circulation model, a water mass analysis has been presented for the 2017 JC150 GEOTRACES process study (GApr08) in the subtropical North Atlantic along 22 °N.

This is the first time to the best of our knowledge that a water mass analysis combined an eOMPA with an LPTE. This approach demonstrated several advantages:

- In addition to a thorough literature review and a meticulous analysis of the hydrographic data, the LPTE helped select the eOMPA end-members. This is important, because the eOMPA results are very sensitive to end-member choice. This meticulous end-member's choice enabled the eOMPA to reproduce the observations (small residuals) and provide results, which were in good agreement with the current knowledge (notably other Atlantic OMPA studies).
- LPTE provided information about water mass trajectories between their formation areas and the studied location, which could not be achieved with a sole eOMPA.
- Finally, LPTE was effective in tracing water mass origins in surface layers, where an eOMPA could not be performed due to the non-conservative hydrographic parameters.

The following conclusions were drawn from our study. The upper 100 m is occupied by a shallow type of ESACW with impacts of the Amazon River plume in the west of the section. The WNACW contribution dominates the upper part of the transect (mainly between 100 and 500 m) with a contribution exceeding 90% at approximately 300 m. The 13 °C-ESACW contribution appears marginally deeper with a contribution exceeding 40% at approximately 600 m depth. The AAIW presents a maximum contribution of over 30% in the west of the MAR at ~700 m. At approximately the same depth, MW, whose high salinity signal is lost because of mixing with AAIW, attains its maximum contribution of over 40% in the east of the MAR. We found that MW's contribution, although in small quantities (in the order of 5%), is required down to 3500 m. Just below AAIW, the UCDW maximum contribution of over 25% is observed at ~1000 m depth. The LSW contribution is present in the depth of 900–2000 m with a maximum of over 70% at ~1500 m depth all across the section. Unpredictably, at this depth, we found through the LPTE that the LSW present in the eastern North Atlantic flows southward to the eastern subtropical Atlantic. We could not find previous works presenting this evidence below 40 °N. Below LSW, the NEADW contribution, which includes the ISOW contribution, exceeds 70% at approximately 2500 m all across the section. Below NEADW, the NWABW maximum contribution of over 45% is attained at ~4500 m west of the MAR. The NWABW contribution is also found in the east of the MAR in significant proportions (>25%). Crossing of the MAR by this water mass has not been investigated so far. As this water is too dense to cross the MAR in the Subpolar Gyre (through the Charlie-Gibbs Fracture Zone), we suggest that it crosses the MAR

through the Kane fracture zone (sill depth of 4350 m) at ~24 °N. The occurrence of NWABW (including DSOW) below NEADW (including ISOW) is consistent with the current knowledge about these water masses and notably their densities. This contradicts a recent OMPA result obtained in a nearby area, where ISOW was found below DSOW (GA03, Jenkins et al., 2015). The deeper water mass contributing to our section is AABW with a maximum contribution of over 35% deeper than 5000 m in the west of the MAR.

These results will be useful to interpret the biogeochemical datasets from the subtropical North Atlantic, notably those with respect to trace elements and isotope distributions (which can be facilitated by the end-member choices at GEOTRACES stations).

Author contributions

CM was the chief scientist of the cruise. CM, MCL, NJW, and EMSW participated in the sampling on board. They participated in the temperature, salinity, dissolved oxygen, and nutrient concentration data production along with JH. SvG produced the Lagrangian particle tracking experiment under the supervision of YD with the contribution of LA and FL. LA and FL produced the optimum multiparameter analysis and conducted the interpretation work. LA drafted the manuscript under the supervision of FL with contributions from SvG, NJW, and all other authors.

Funding source

French Ministry of Higher Education, Research and Innovation (MESRI) public funding awarded to Lise Artigue (University of Toulouse).

French National Centre for Scientific Research (CNRS) public funding awarded to François Lacan (LEGOS).

NERC with reference NE/N001979/1 awarded to Claire Mahaffey (University of Liverpool) and Malcolm Woodward (PML) and NE/N001125/1 awarded to Maeve Lohan (University of Southampton).

Mercator Ocean International for Simon van Gennip and Yann Drillet.

Declaration of competing interest

The authors declare that they have no known competing financial interests or personal relationships that could have appeared to influence the work reported in this paper.

Acknowledgments

We dedicate this work to Pr. Matthias Tomczack for his invaluable contributions to the Oceanographic community. As part of his large body of work, Matthias Tomczack introduced and developed the optimum multiparameter analysis. We particularly thank him for his thoughtful answers to our questions and his helpful explanations of his work.

We sincerely thank Dr. Johannes Karstensen for providing the OMP Analysis Package for MATLAB Version 2.0 with a clear manual of utilization on the website: https://omp.geomar.de/

We sincerely thank Dr. Gael Alory for providing the July 2017 salinity map from the SMOS satellite and Dr. Julien Jouanno for his helpful comments on the Amazon River plume. We thank Dr. Elodie Kestenar and Manon Gevaudan for their help with MATLAB.

Last, but not the least, we would like to thank the captain and crew of RRS James Cook for their help at sea as well as all of the scientists involved in JC150.

Appendix A. Supplementary data

Supplementary data to this article can be found online at https://doi.org/10.1016/j.dsr.2020.103230.

References

van Aken, H. M. van, 2007. The Oceanic Thermohaline Circulation: an Introduction. Springer, New York.

Álvarez, M., Brea, S., Mercier, H., Álvarez-Salgado, X.A., 2014. Mineralization of biogenic materials in the water masses of the South Atlantic Ocean. I: assessment and results of an optimum multiparameter analysis. Prog. Oceanogr. 123, 1–23. https://doi.org/10.1016/j.pocean.2013.12.007.

Amante, C., Eakins, B.W., 2009. ETOPO1 1 Arc-Minute Global Relief Model: Procedures, Data Sources and Analysis. NOAA Technical Memorandum NESDIS NGDC-24, Marine Geology and Geophysics Division, Boulder, Colorado, p. 25.

Anderson, L.A., 1995. On the hydrogen and oxygen content of marine phytoplankton. Deep Sea Res. Oceanogr. Res. Pap. 42 (9), 1675–1680. https://doi.org/10.1016/0967-0637(95)00072-E.

Anderson, L.A., Sarmiento, J.L., 1994. Redfield ratios of remineralization determined by nutrient data analysis. Global Biogeochem. Cycles 8 (1), 65–80. https://doi.org/10.1029/93GB03318.

Baringer, M.O., 1997. Mixing and spreading of the Mediterranean outflow. J. Phys. Oceanogr. 27, 24.

Bashmachnikov, I., Nascimento, Â., Neves, F., Menezes, T., Koldunov, N.V., 2015. Distribution of intermediate water masses in the subtropical northeast Atlantic. Ocean Sci. 11 (5), 803–827. https://doi.org/10.5194/os-11-803-2015.

Becker, J.J., Sandwell, D.T., Smith, W.H.F., Braud, J., Binder, B., Depner, J., et al., 2009. Global bathymetry and elevation data at 30 arc seconds resolution: SRTM30_PLUS. Mar. Geodes. 32 (4), 355–371. https://doi.org/10.1080/01490410903297766.

Blanke, B., Raynaud, S., 1997. Kinematics of the Pacific equatorial undercurrent: an Eulerian and Lagrangian approach from GCM results. J. Phys. Oceanogr. 27 (6), 1038–1053. https://doi.org/10.1175/1520-0485(1997)027<1038:KOTPEU>2.0.CO;2.

Boyle, E.A., Anderson, R.F., Cutter, G.A., Fine, R., Jenkins, W.J., Saito, M., 2015. Geotraces GA-03 - the U.S. GEOTRACES North Atlantic transect. Deep Sea Res. Part II Top. Stud. Oceanogr. 116, 1–342.

Broecker, W.S., 1974. "NO", a conservative water-mass tracer. Earth Planet Sci. Lett. 23 (1), 100–107. https://doi.org/10.1016/0012-821X(74)90036-3.

Broecker, W.S., Takahashi, T., Takahashi, T., 1985. Sources and flow patterns of deep-ocean waters as deduced from potential temperature, salinity, and initial phosphate concentration. J. Geophys. Res. 90 (C4), 6925. https://doi.org/10.1029/JC090iC04p06925.

Broecker, W.S., Blanton, S., Smethie, W.M., Ostlund, G., 1991. Radiocarbon decay and oxygen utilization in the deep Atlantic Ocean. Global Biogeochem. Cycles 5 (1), 87–117. https://doi.org/10.1029/90GB02279.

Browning, T.J., Achterberg, E.P., Yong, J.C., Rapp, I., Utermann, C., Engel, A., Moore, C. M., 2017. Iron limitation of microbial phosphorus acquisition in the tropical North Atlantic. Nat. Commun. 8 https://doi.org/10.1038/ncomms15465.

Carracedo, L.I., Pardo, P.C., Flecha, S., Pérez, F.F., 2016. On the Mediterranean water composition. J. Phys. Oceanogr. 46 (4), 1339–1358. https://doi.org/10.1175/JPO-D-15-0095.1.

Cetina-Heredia, P., van Sebille, E., Matear, R., Roughan, M., 2016. Lagrangian characterization of nitrate supply and episodes of extreme phytoplankton blooms in the Great Australian Bight. Biogeosci. Discuss. 1–15. https://doi.org/10.5194/bg-2016-53.

Fieux, M., 2010. L'océan Planétaire. Les Presses de l'ENSTA.

Garcia, H.E., Weathers, K., Paver, C.R., Smolyar, I., Boyer, T.P., Locarnini, R.A., Zweng, M.M., Mishonov, A.V., Baranova, O.K., Seidov, D., Reagan, J.R., 2019. World Ocean Atlas 2018, Volume 4: Dissolved Inorganic Nutrients (phosphate, nitrate and nitrate+nitrite, silicate). A. Mishonov Technical Editor, NOAA Atlas NESDIS 84.

García-Ibáñez, M.I., Pérez, F.F., Lherminier, P., Zunino, P., Mercier, H., Tréguer, P., 2018. Water mass distributions and transports for the 2014 GEOVIDE cruise in the North Atlantic. Biogeosciences 15 (7), 2075–2090. https://doi.org/10.5194/bg-15-2075-2018.

Harvey, J., 1982. θ-S relationships and water masses in the eastern North Atlantic. Deep-Sea Res. Part A Oceanogr. Res. Pap. 29 (8), 1021–1033. https://doi.org/10.1016/0198-0149(82)90025-5.

Hinrichsen, H.-H., Tomczak, M., 1993. Optimum multiparameter analysis of the water mass structure in the western North Atlantic Ocean. J. Geophys. Res.: Oceans 98 (C6), 10155–10169. https://doi.org/10.1029/93JC00180.

Holte, J., Talley, L.D., Gilson, J., Roemmich, D., 2017. An Argo mixed layer climatology and database: ARGO MLD climatology. Geophys. Res. Lett. 44 (11), 5618–5626. https://doi.org/10.1002/2017GL073426.

Hydes, D., Aoyama, M., Aminot, A., Bakker, K., Becker, S., Coverly, S., Daniel, A., Dickson, A.G., Grosso, O., Kerouel, R., van Ooijen, J., Sato, K., Tanhua, T., Woodward, E.M.S., Zhang, J.Z., 2010. Determination of dissolved nutrients (N, P, Si) in seawater with high precision and inter-comparability using gas-segmented continuous flow analysers. *The GO-SHIP Repeat Hydrography Manual: A Collection of Expert Reports and guidelines.* IOCCP Report No. 14. ICPO Publication Series No. 134.

Jenkins, W.J., Smethie, W.M., Boyle, E.A., Cutter, G.A., 2015. Water mass analysis for the U.S. GEOTRACES (GA03) North Atlantic sections. Deep Sea Res. Part II Top. Stud. Oceanogr. 116, 6–20. https://doi.org/10.1016/j.dsr2.2014.11.018.

Kastens, K., Bonatti, E., Caress, D., Carrara, G., Dauteuil, O., Frueh-Green, G., et al., 1998. The Vema Transverse Ridge (Central Atlantic), vol. 2.

Kim, I.-N., Min, D.-H., Macdonald, A.M., 2013. Water column denitrification rates in the oxygen minimum layer of the Pacific Ocean along 32°S. Global Biogeochem. Cycles 27 (3), 816–827. https://doi.org/10.1002/gbc.20070.

Lacan, F., Jeandel, C., 2005. Acquisition of the neodymium isotopic composition of the North Atlantic deep water. G-cubed 6 (12). https://doi.org/10.1029/2005GC000956 n/a-n/a.

Lazier, J., Hendry, R., Clarke, A., Yashayaev, I., Rhines, P., 2002. Convection and restratification in the Labrador Sea, 1990–2000. Deep Sea Res. Oceanogr. Res. Pap. 49 (10), 1819–1835. https://doi.org/10.1016/S0967-0637(02)00064-X.

Lellouche, J.-M., Le Galloudec, O., Greiner, E., Garric, G., Régnier, C., Clavier, M., et al., 2018b. Performance and quality assessment of the current Copernicus Marine Service global ocean monitoring and forecasting real-time system. In: Operational Oceanography Serving Sustainable Marine Development. EuroGOOS, Brussels, Belgium, pp. 251–260.

Lellouche, J.-M., Greiner, E., Le Galloudec, O., Garric, G., Regnier, C., Drevillon, M., et al., 2018a. Recent updates to the Copernicus Marine Service global ocean monitoring and forecasting real-time 1/12° high-resolution system. Ocean Sci. 14 (5), 1093–1126. https://doi.org/10.5194/os-14-1093-2018.

Louarn, E., Morin, P., 2011. Antarctic intermediate water influence on Mediterranean Sea Water outflow. Deep Sea Res. Oceanogr. Res. Pap. 58 (9), 932–942. https://doi.org/10.1016/j.dsr.2011.05.009.

Mackas, D.L., Denman, K.L., Bennett, A.F., 1987. Least squares multiple tracer analysis of water mass composition. J. Geophys. Res. 92 (C3), 2907. https://doi.org/10.1029/JC092iC03p02907.

Madec, G., the NEMO team, 2008. NEMO ocean engine, Note du Pôle de modélisation. Institut Pierre-Simon Laplace (IPSL), pp. 1288–1619.

Mahaffey, C., Reynolds, S., Davis, C.E., Lohan, M.C., 2014. Alkaline phosphatase activity in the subtropical ocean: insights from nutrient, dust and trace metal addition experiments. Front. Mar. Sci. 1 https://doi.org/10.3389/fmars.2014.00073.

McCartney, M.S., 1992. Recirculating components to the deep boundary current of the northern North Atlantic. Prog. Oceanogr. 29 (4), 283–383. https://doi.org/10.1016/0079-6611(92)90006-L.

McCartney, M.S., Talley, L.D., 1984. Warm-to-Cold water conversion in the Northern North Atlantic ocean. J. Phys. Oceanogr. 14 (5), 922–935. https://doi.org/10.1175/1520-0485(1984)014<0922:WTCWCI>2.0.CO;2.

Middag, R., van Hulten, M.M.P., Van Aken, H.M., Rijkenberg, M.J.A., Gerringa, L.J.A., Laan, P., de Baar, H.J.W., 2015. Dissolved aluminium in the ocean conveyor of the West Atlantic Ocean: effects of the biological cycle, scavenging, sediment resuspension and hydrography. Mar. Chem. 177, 69–86. https://doi.org/10.1016/j.marchem.2015.02.015.

Moore, C.M., Mills, M.M., Achterberg, E.P., Geider, R.J., LaRoche, J., Lucas, M., et al., 2009. Large-scale distribution of Atlantic nitrogen fixation controlled by iron availability. https://doi.org/10.1038/NGEO667.

Morozov, E.G., Tarakanov, R. Yu, Demidova, T.A., Makarenko, N.I., 2017. Flows of bottom water in fractures of the North Mid-Atlantic Ridge. Dokl. Earth Sci. 474 (2), 653–656. https://doi.org/10.1134/S1028334X17060058.

Pardo, P.C., Pérez, F.F., Velo, A., Gilcoto, M., 2012. Water masses distribution in the Southern Ocean: improvement of an extended OMP (eOMP) analysis. Prog. Oceanogr. 103, 92–105. https://doi.org/10.1016/j.pocean.2012.06.002.

Peters, B.D., Jenkins, W.J., Swift, J.H., German, C.R., Moffett, J.W., Cutter, G.A., et al., 2018. Water mass analysis of the 2013 US GEOTRACES eastern Pacific zonal transect (GP16). Mar. Chem. 201, 6–19. https://doi.org/10.1016/j.marchem.2017.09.007.

Poole, R., Tomczak, M., 1999. Optimum multiparameter analysis of the water mass structure in the Atlantic Ocean thermocline. Deep Sea Res. Oceanogr. Res. Pap. 46 (11), 1895–1921. https://doi.org/10.1016/S0967-0637(99)00025-4.

Read, J.F., 2001. CONVEX-91: water masses and circulation of the Northeast Atlantic subpolar gyre. Prog. Oceanogr. 48 (4), 461–510. https://doi.org/10.1016/S0079-6611(01)00011-8.

Reid, J.L., 1979. On the contribution of the Mediterranean sea outflow to the Norwegian-Greenland sea. Deep-Sea Res. Part A Oceanogr. Res. Pap. 26 (11), 1199–1223. https://doi.org/10.1016/0198-0149(79)90064-5.

Rijkenberg, M.J.A., Middag, R., Laan, P., Gerringa, L.J.A., van Aken, H.M., Schoemann, V., et al., 2014. The distribution of dissolved iron in the west Atlantic Ocean. PloS One 9 (6), e101323. https://doi.org/10.1371/journal.pone.0101323.

Schlitzer, R., Anderson, R.F., Dodas, E.M., Lohan, M., Geibert, W., Tagliabue, A., et al., 2018. The GEOTRACES intermediate data product 2017. Chem. Geol. 493, 210–223. https://doi.org/10.1016/j.chemgeo.2018.05.040.

Snow, J.T., Schlosser, C., Woodward, E.M.S., Mills, M.M., Achterberg, E.P., Mahaffey, C., et al., 2015. Environmental controls on the biogeography of diazotrophy and trichodesmium in the Atlantic Ocean. Global Biogeochem. Cycles 29 (6), 865–884. https://doi.org/10.1002/2015GB005090.

Spence, P., van Sebille, E., Saenko, O.A., England, M.H., 2014. Using Eulerian and Lagrangian approaches to investigate wind-driven changes in the Southern Ocean abyssal circulation. J. Phys. Oceanogr. 44 (2), 662–675. https://doi.org/10.1175/JPO-D-13-0108.1.

Stramma, L., Schott, F., 1999. The mean flow field of the tropical Atlantic Ocean. Deep Sea Res. Part II Top. Stud. Oceanogr. 46 (1–2), 279–303. https://doi.org/10.1016/S0967-0645(98)00109-X.

Swift, J.H., 1984. The circulation of the Denmark strait and Iceland-Scotland overflow waters in the North Atlantic. Deep-Sea Res. Part A Oceanogr. Res. Pap. 31 (11), 1339–1355. https://doi.org/10.1016/0198-0149(84)90005-0.

Talley, L.D., 1996. Antarctic intermediate water in the south Atlantic. In: The South Atlantic. Springer Berlin Heidelberg, Berlin, Heidelberg, pp. 219–238. https://doi.org/10.1007/978-3-642-80353-6.

Talley, L.D., McCartney, M.S., 1982. Distribution and circulation of Labrador Sea water. J. Phys. Oceanogr. 12, 1189–1205.

Talley, L.D., Pickard, G.L., Emery, W.J., Swift, J.H. (Eds.), 2011. Descriptive Physical Oceanography: an Introduction, 6. Elsevier, Amsterdam.

Tomczak, M., 1981. A multi-parameter extension of temperature/salinity diagram techniques for the analysis of non-isopycnal mixing. Prog. Oceanogr. 10 (3), 147–171. https://doi.org/10.1016/0079-6611(81)90010-0.

Tomczak, M., 1999. Some historical, theoretical and applied aspects of quantitative water mass analysis. J. Mar. Res. 57 (2), 275–303. https://doi.org/10.1357/002224099321618227.

Tomczak, M., Godfrey, J.S., 1994. Regional-Oceanography-An-Introduction.pdf.

Tomczak, M., Large, D.G.B., 1989. Optimum multiparameter analysis of mixing in the thermocline of the eastern Indian Ocean. J. Geophys. Res. 94 (C11), 16141. https://doi.org/10.1029/JC094iC11p16141.

Tsuchiya, M., 1986. Thermostads and circulation in the upper layer of the Atlantic Ocean. Prog. Oceanogr 16, 235–267.

Tsuchiya, M., 1989. Circulation of the Antarctic intermediate water in the North Atlantic Ocean. J. Mar. Res. 47 (4), 747–755. https://doi.org/10.1357/002224089785076136.

Tsuchiya, M., Talley, L.D., McCartney, M.S., 1994. Water-mass distributions in the western South Atlantic; A section from South Georgia Island (54S) northward across the equator. J. Mar. Res. 52 (1), 55–81. https://doi.org/10.1357/0022240943076759.

Woodward, E.M.S., Rees, A.P., 2001. Nutrient distributions in an anticyclonic eddy in the northeast Atlantic Ocean, with reference to nanomolar ammonium concentrations. Deep Sea Research Part II: Topical Studies in Oceanography 48, 775–793. https://doi.org/10.1016/S0967-0645(00)00097-7.

Wu, J., Sunda, W., Boyle, E.A., Karl, D.M., 2000. Phosphate depletion in the western North Atlantic. Ocean 289, 4.

Zhang, J.-Z., Chi, J., 2002. Automated analysis of nanomolar concentrations of phosphate in Natural waters with liquid waveguide. Environ. Sci. Technol. 36 (5), 1048–1053. https://doi.org/10.1021/es011094v.

Zweng, M.M., Reagan, J.R., Seidov, D., Boyer, T.P., Locarnini, R.A., Garcia, H.E., Mishonov, A.V., Baranova, O.K., Weathers, K., Paver, C.R., Smolyar, I., 2019. World Ocean Atlas 2018, Volume 2: Salinity. A. Mishonov Technical Editor, NOAA Atlas NESDIS 82.

2.2.3 Matériel complémentaire

Supplementary material

S1. Details of the Lagrangian Particle Tracking Experiment (LPTE)

Particles are advected backwards in time using the three-dimensional velocity output of the model. The particles' positions are recorded after each time step.
In all cases, an ensemble of particles (or particle clouds) was uniformly distributed around the sampling location and repeatedly deployed across a period centered on the sampling time. This ensemble was organized as a vertical-cylinder made of equally spaced disks of particles spaced at 1/12° resolution radially.
The height of the cylinder, the number of disks inside each cyclinder and the number of repeated releases around the sampling time differed based on the sampling depth.

- Surface experiment setup, depth shallower than 800 m

- Horizontal layout: horizontal disk with radius ¼° centred on sampling point; particle deployed at 1/12° horizontal resolution; 32 particle release points per layer generated.
- Vertical layout: 10 m cylinder height (centred on the sampling depth) made of 5 super-imposed horizontal disks (every 2.5 m); generating 160 release points (See Figure S1).
- Temporal resolution: 9 releases over 5 days (from 2 days before, to 2 days after the sampling date, with 12 hours resolution), equivalent in total to 1440 particles deployed for each sampling depth.
- Duration of the experiment back in time: 10 years using daily velocity outputs.

- Deep-water experiment, 800 to 2000m

- Horizontal layout: No changes from the surface experiment setup shallower than 800 m.
- Vertical layout: 20 m cylinder height (centred on the sampling depth); 9 horizontal disks (every 5 m); generating 288 particle release points.
- Temporal resolution: 3 releases over 1 month (2 weeks before, at, and 2 weeks after the sampling date), equivalent to 864 particles deployed for each sampling depth.
- Duration of the experiment back in time: up to 100 years; monthly-mean velocities outputs.

- Deep-water experiment, deeper than 2000m

- Horizontal layout: horizontal disk with radius ¼° centred on sampling point; 1/12° horizontal resolution; 112 particles per layer generated.
- Vertical layout: 200m-high cylinder (centred on the sampling depth); 5 horizontal disks (every 50 m); 560 particles per time released.
- Temporal resolution: 3 releases over 4 weeks (2 weeks before, at and 2 weeks after the sampling date), 1680 particles deployed for each sampling depth.
- Duration of the experiment back in time: up to 300 years using monthly-mean velocities outputs.

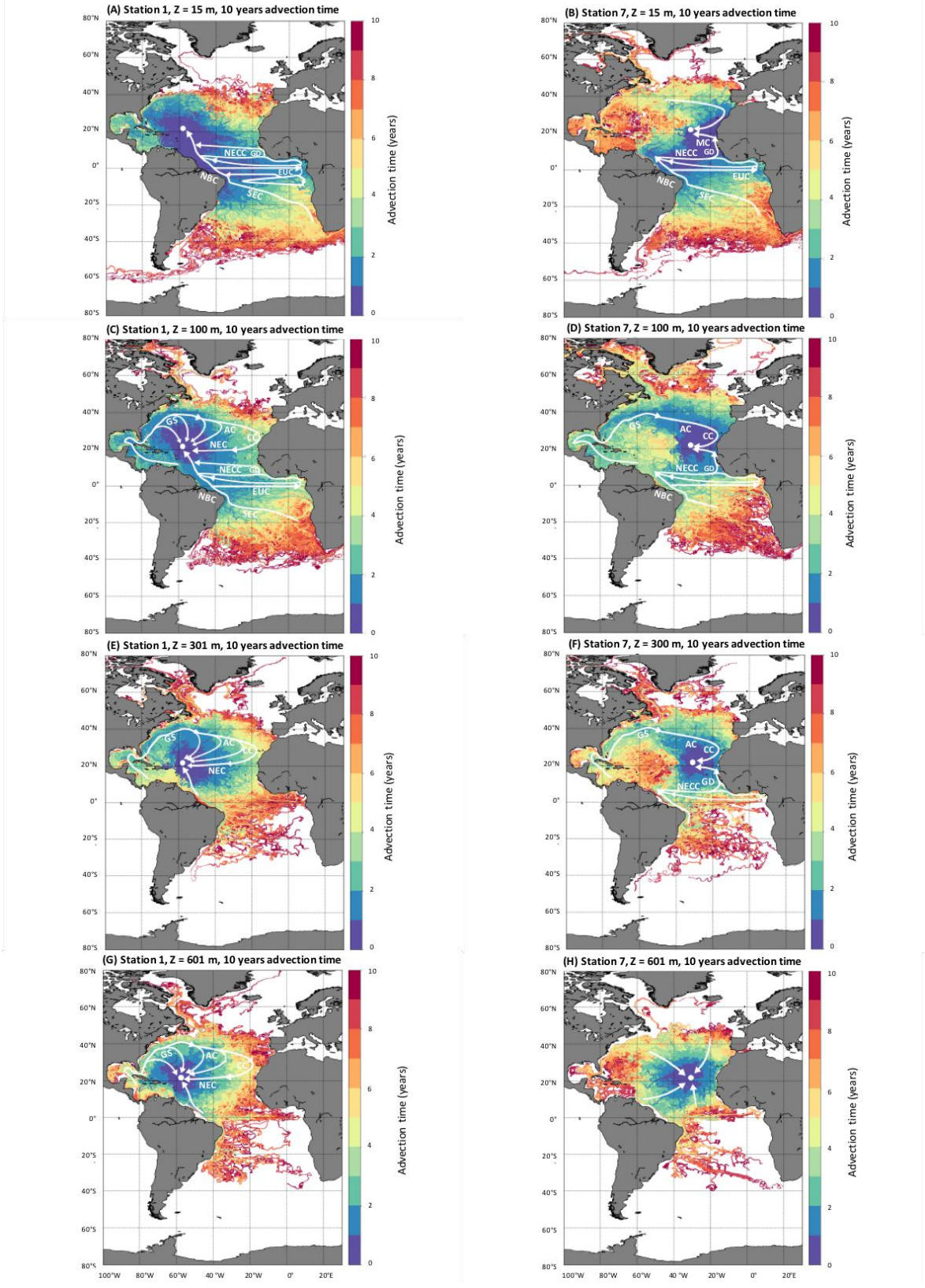
(A) Station 1, Z = 15 m, 10 years advection time
(B) Station 7, Z = 15 m, 10 years advection time
(C) Station 1, Z = 100 m, 10 years advection time
(D) Station 7, Z = 100 m, 10 years advection time
(E) Station 1, Z = 301 m, 10 years advection time
(F) Station 7, Z = 300 m, 10 years advection time
(G) Station 1, Z = 601 m, 10 years advection time
(H) Station 7, Z = 601 m, 10 years advection time
Advection time (years)
NECC
GD
EUC
NBC
SEC
MC
GS
AC
CC
NEC
80°N
60°N
40°N
20°N
0°
20°S
40°S
60°S
80°S
100°W
80°W
60°W
40°W
20°W
0°
20°E

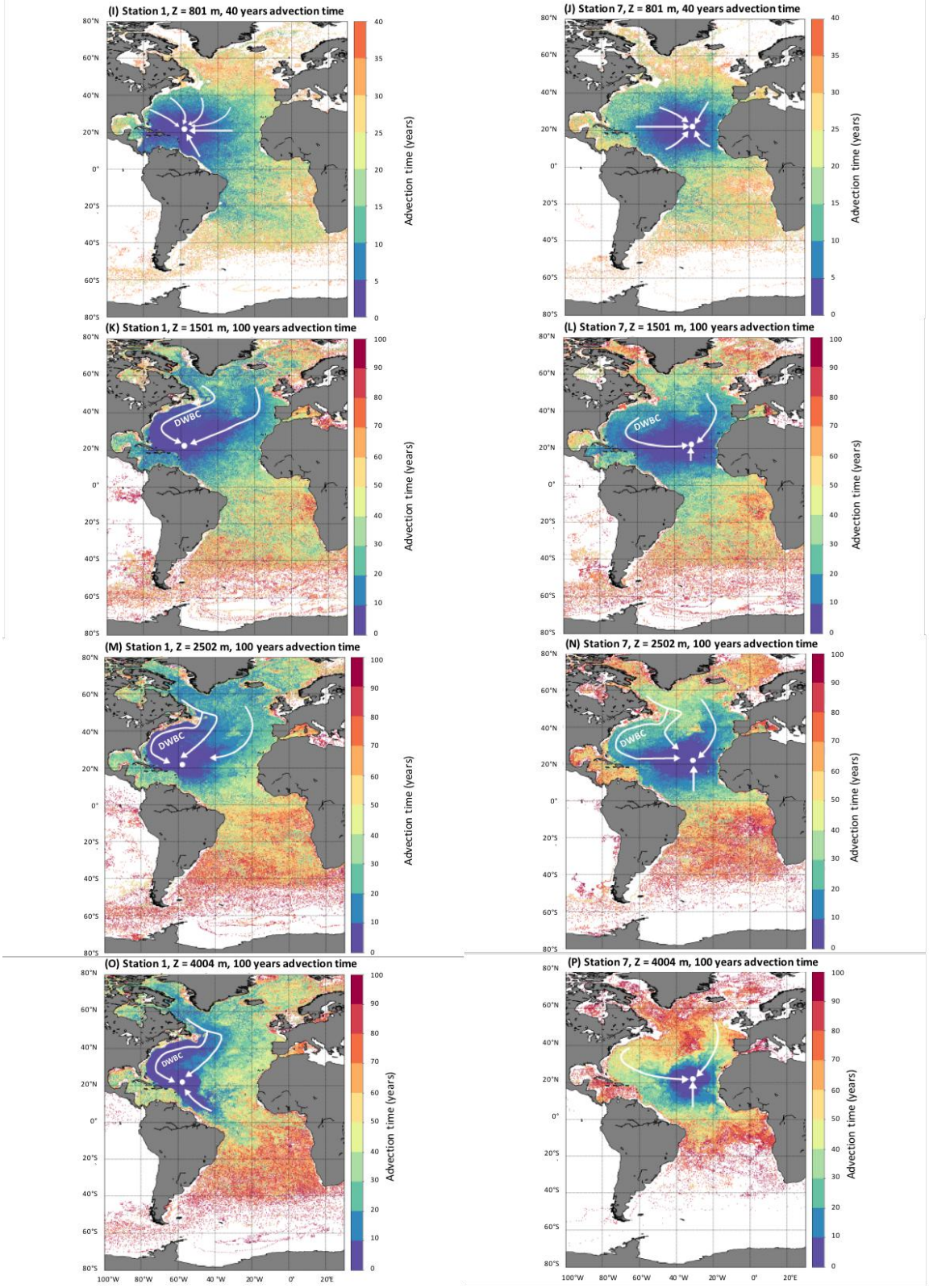
(I) Station 1, Z = 801 m, 40 years advection time
(J) Station 7, Z = 801 m, 40 years advection time
(K) Station 1, Z = 1501 m, 100 years advection time
(L) Station 7, Z = 1501 m, 100 years advection time
(M) Station 1, Z = 2502 m, 100 years advection time
(N) Station 7, Z = 2502 m, 100 years advection time
(O) Station 1, Z = 4004 m, 100 years advection time
(P) Station 7, Z = 4004 m, 100 years advection time
DWBC
Advection time (years)

Fig. S2. Trajectories of the water that reach the JC150 stations, obtained from particles deployed in the Lagrangian Particle Tracking Experiment. Results are presented for two JC150 stations (westernmost station 1, 22°N, 58°W, left panels and easternmost station 7, 22°N, 31°W, right panels) at different depths and advection times. Each particle trajectory is multicolored, with each colored portion corresponding to the section travelled over one to ten (or hundred) years. Note that particle year sections are superimposed, and therefore colors only show the maximum extend covered in each year. The following currents and location are presented in the figures: Gulf Stream (GS), Azores Current (AC), Canary Current (CC), North Equatorial Current (NEC), South Equatorial Current (SEC), North Brazil Current (NBC), Equatorial Undercurrent (EUC), North Equatorial Countercurrent (NECC), Mauritania Current (MC), Deep Western Boundary Current (DWBC) and Guinea Dome (GD).

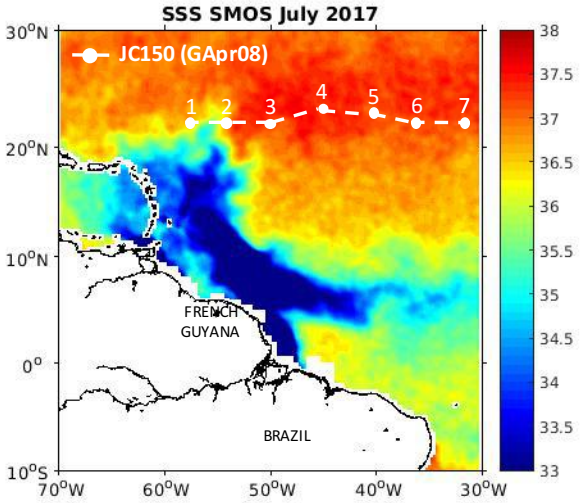

Fig. S3. Salinity map on July 2017 from SMOS satellite (Boutin et al., 2018).

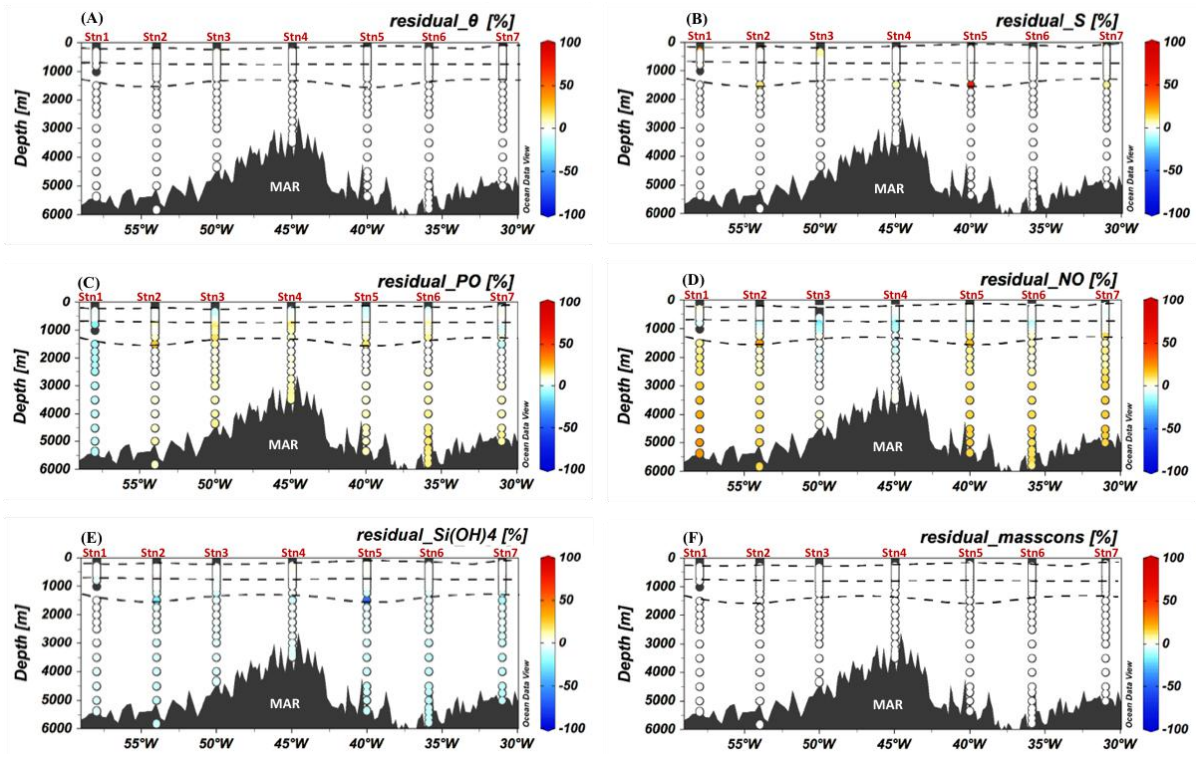

Fig. S4. Residuals of the Potential temperature (A), Salinity (B), PO (C), NO (D), Silicic acid (E) and, Mass conservation (F), expressed as percentages of the parameter ranges over the section. Positive residue values mean higher OMPA calculated hydrographic properties compared to the observed ones and vice versa for negative residue values. Sampling points are represented by black empty dots and eOMPA layer boundaries by horizontal black dashed lines. The full black dots represents samples where no eOMPA could be performed.

eOMPA Layer	Acronym	Test 1: End-member properties (2SD, %)	Test 2: JC150 measured properties (2SD, %)	Test 3: weights (2SD, %)
Thermocline	WNACW	5	6	2
	ESACW	7	6	2
	MOW	7	5	2
	AAIW	5	6	2
	UCDW	1	1	1
Intermediate	ESACW	6	7	1
	MOW	7	8	1
	AAIW	9	14	2
	UCDW	7	6	2
	LSW	7	10	2
Deep	MOW	3	2	0
	LSW	8	9	1
	NEADW	23	23	3
	NWABW	17	9	3
	AABW	3	7	2
Mean		8	8	2

Table. S5. Results of the three Monte Carlo tests applied to each of the three eOMPA layers. The results represent the water mass percentage uncertainties (two standard deviation, %).

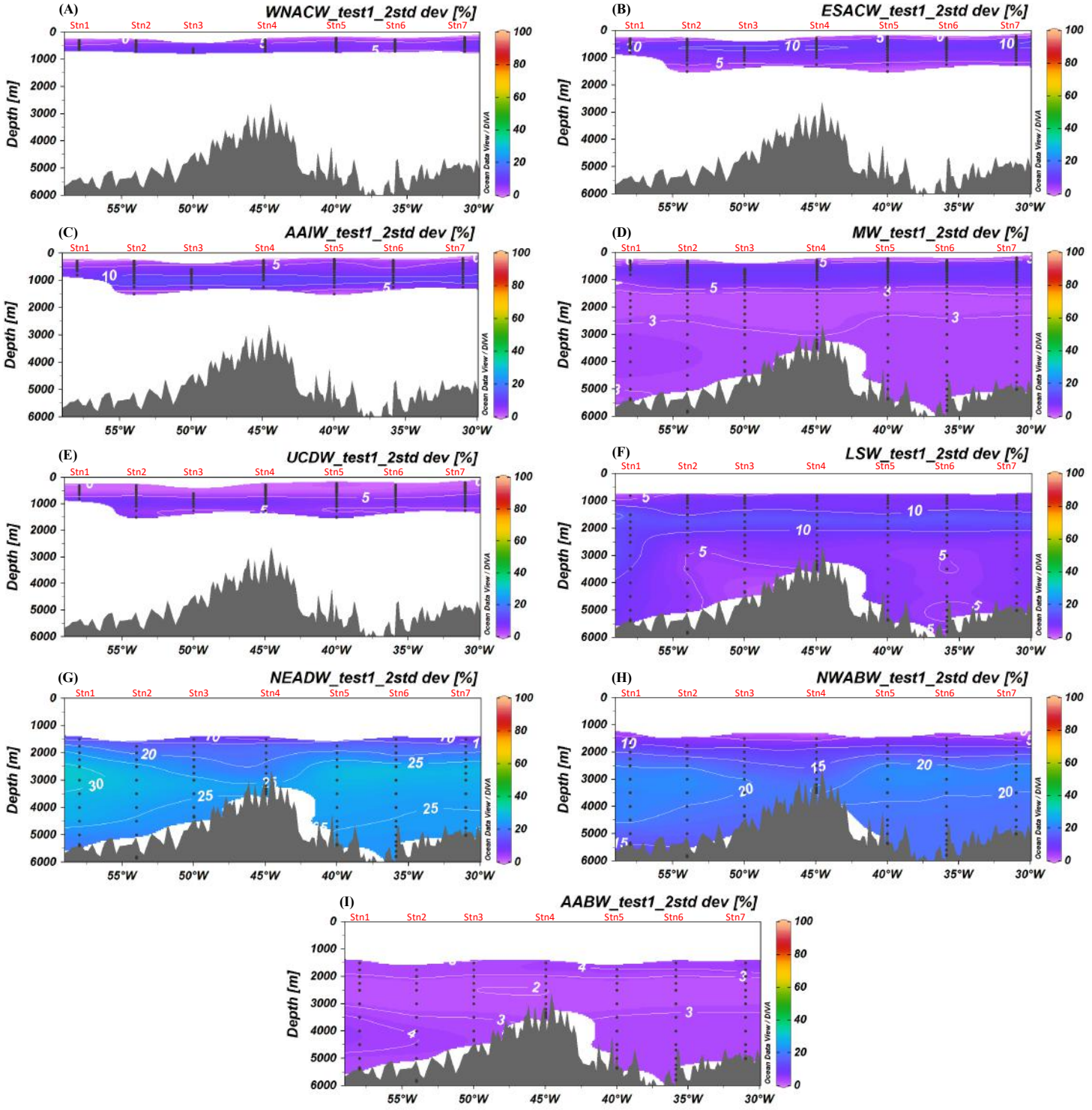

Fig. S6. Two standard deviation (%) of WNACW (A), 13°C-ESACW (B), AAIW (C), MW (D), UCDW (E), LSW (F), NEADW (G), NWABW (H), AABW (I) according to the Monte Carlo test1 on end-members characteristics. Sampling points are represented by black dots and eOMPA layer boundaries by horizontal black dashed lines.

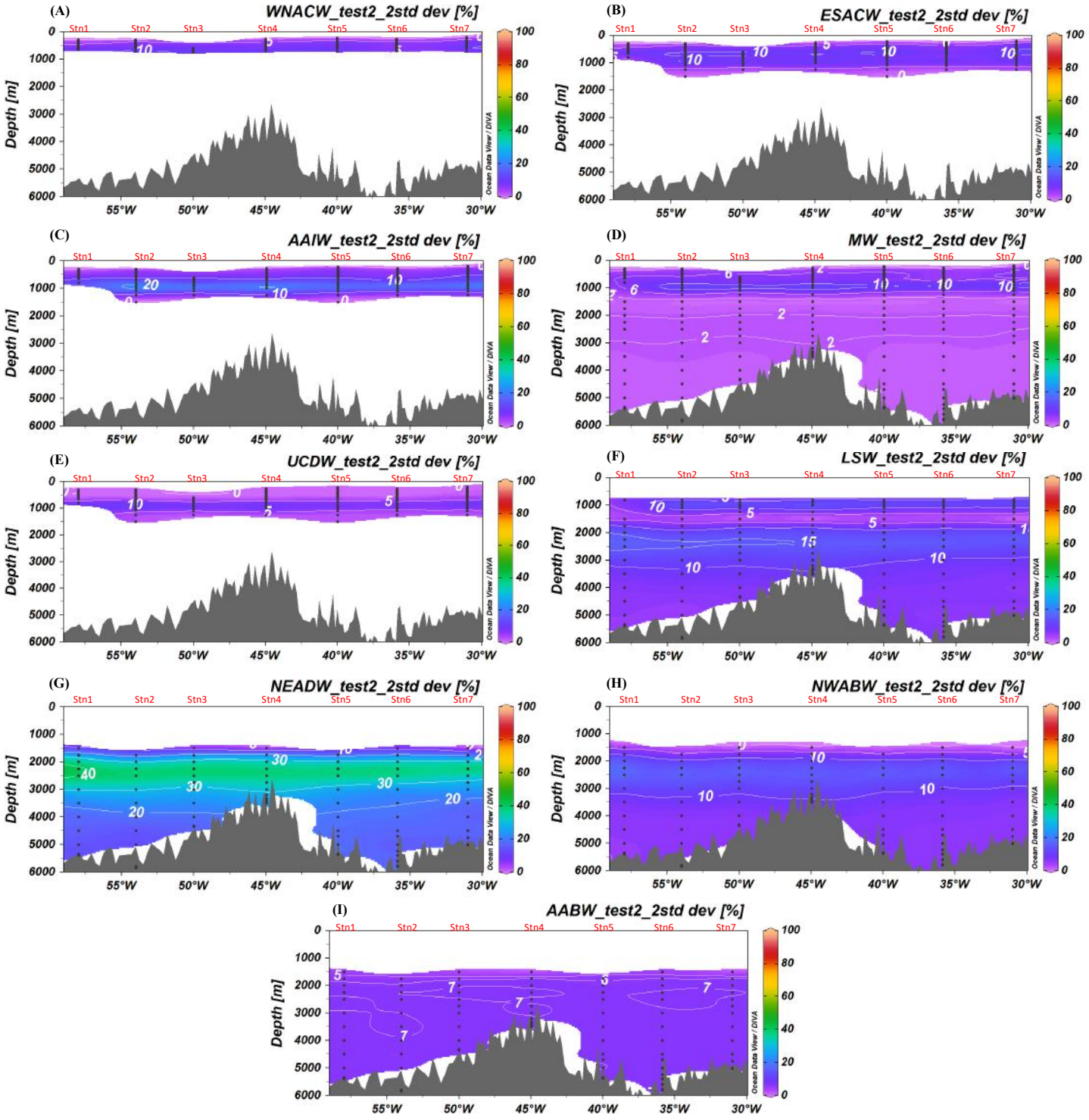

Fig. S7. Two standard deviation (%) of WNACW (A), 13°C-ESACW (B), AAIW (C), MW (D), UCDW (E), LSW (F), NEADW (G), NWABW (H), AABW (I) according to the Monte Carlo test2 on the JC150 data. Sampling points are represented by black dots and eOMPA layer boundaries by horizontal black dashed lines.

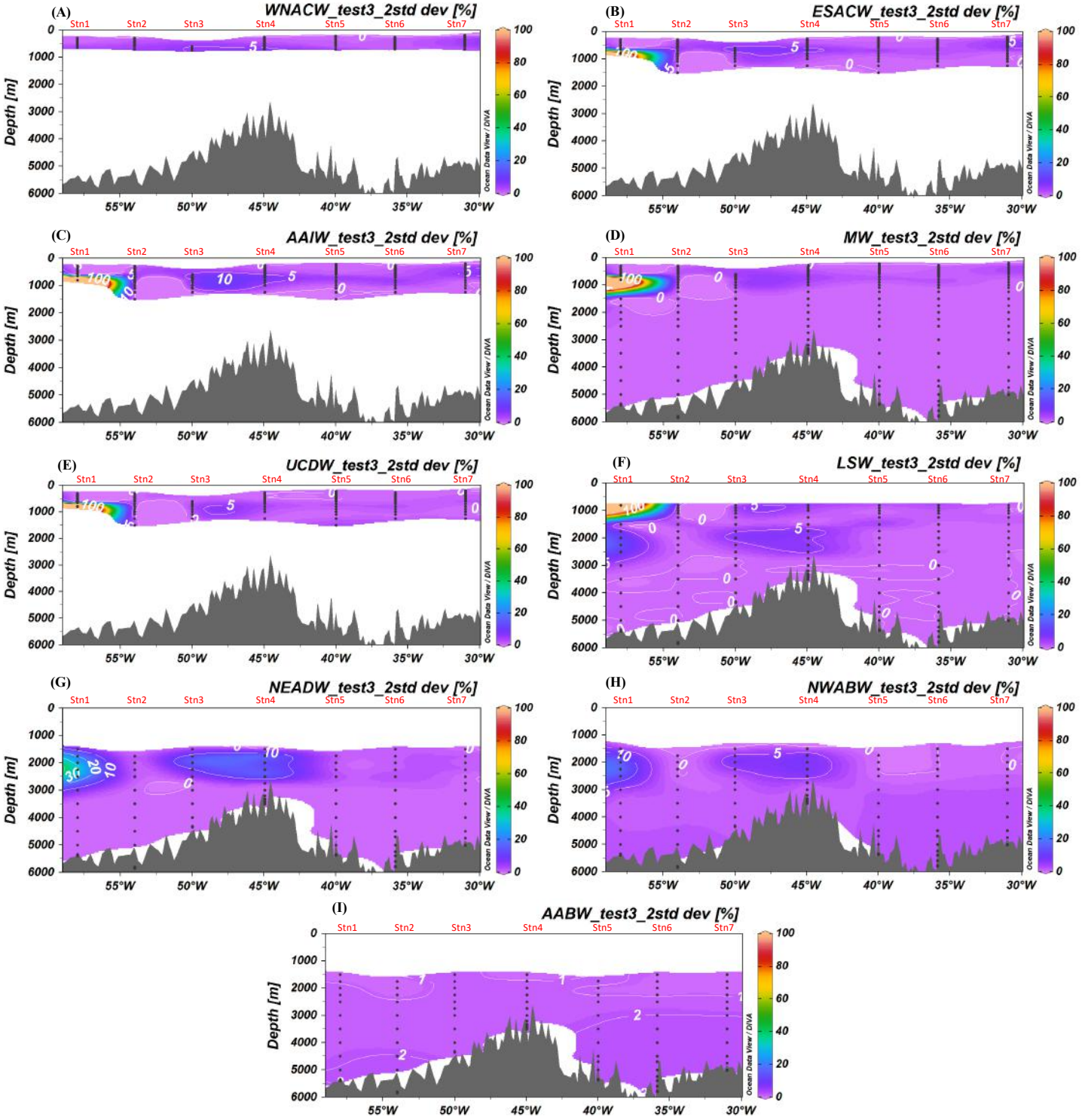

Fig. S8. Two standard deviation (%) of WNACW (A), 13°C-ESACW (B), AAIW (C), MW (D), UCDW (E), LSW (F), NEADW (G), NWABW (H), AABW (I) according to the Monte Carlo test2 on the chosen weights. Sampling points are represented by black dots and eOMPA layer boundaries by horizontal black dashed lines.

2.3 Conclusion

L'évolution des méthodes d'analyse des masses d'eau nous a permis de combiner une eOMPA à l'outil lagrangien afin d'améliorer nos connaissances sur la contribution et la circulation des masses d'eau de l'Atlantic Nord subtropical. Dans le futur, nous suggérons de combiner ces deux outils complémentaires pour l'analyse de masses d'eau d'autres régions océaniques. Comme expliqué dans l'introduction générale, connaître la contribution des masses d'eau, nous permet également de mieux comprendre les cycles des éléments biogéochimiques dans l'océan. Ainsi notre eOMPA pourra être utilisée pour isoler le signal « conservatif » associé à la circulation des masses d'eau du signal « non-conservatif » associé aux processus biogéochimiques des éléments de l'Atlantique subtropical. Le chapitre suivant propose une application directe des informations récoltées sur l'analyse des masses d'eau de l'Atlantique subtropical pour comprendre la distribution du traceur lithogénique aluminium mesuré dans la même zone d'étude.

3 Importance du transport des masses d'eau et des interactions dissous-particules sur le cycle de l'aluminium

3.1 Introduction

3.1.1 Le cycle de l'aluminium dissous, de nombreuses questions en suspens

L'aluminium (Al) est le troisième élément le plus abondant de la croûte terrestre (8,15 % en masse, Rudnick & Gao, 2014). Cependant il est présent à des concentrations de l'ordre du nanomolaire dans l'eau de mer (i.e. 10^{-9} mol/L).
La Figure 13 présente une vision schématique de nos connaissances actuelles sur le cycle de l'aluminium dissous (dAl). Les poussières atmosphériques sont considérées comme étant la source principale de dAl à l'océan (Jickells et al., 1994; Maring & Duce, 1987; Measures et al., 2005, 2010). Le principal puits de dAl est le scavenging (adsorption suivi de sédimentation, Hydes, 1979; Orians & Bruland, 1986a; Stoffyn & Mackenzie, 1982). Comme expliqué dans l'introduction générale, l'aluminium n'ayant pas de fonction biologique connue dans la cellule et n'étant pas impliqué dans les réactions d'oxydoréduction, cela en fait un bon traceur de sources lithogéniques. En surface, les concentrations de dAl sont largement utilisées pour tracer et quantifier les apports de poussières atmosphériques (Han et al., 2008; Measures et al., 2005; Measures & Vink, 2000). En profondeur, les concentrations servent à tracer la resuspension sédimentaire ou des sources hydrothermales (Measures et al., 2015; Middag et al., 2009, 2012, 2015; Resing et al., 2015; van Hulten et al., 2013).

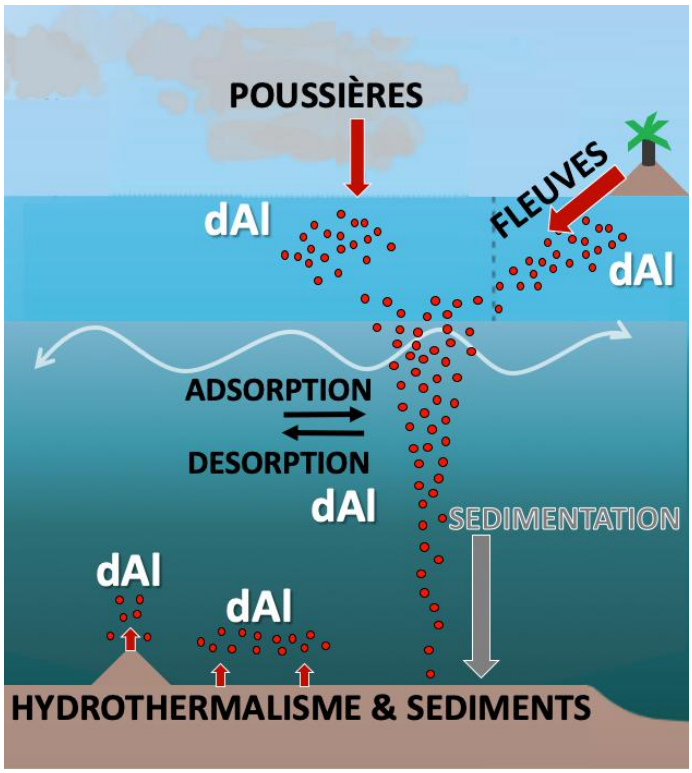

Figure 13 : Cycle de l'aluminium dissous. Les sources externes (flèches rouges), les processus physiques (flèches noires) et le puit dominant (flèche grise) sont indiqués.

Du fait de cette caractéristique de traceur de sources lithogéniques, la connaissance de la distribution des concentrations de dAl contribue à contraindre le cycle océanique d'autres éléments d'origine lithogénique, y compris ceux qui sont directement impliqués dans la production primaire (ex. le fer). Comme présenté dans l'introduction, de nombreuses incertitudes sur les sources externes et les cycles internes des éléments traces demeurent. L'aluminium ne fait pas exception à ces incertitudes et de nombreuses questions demeurent tant sur ses sources externes que sur son cycle interne.

1- Les dépôts de poussières à l'océan, aujourd'hui considérés comme la source majeure de dAl dans l'océan, peuvent-ils à eux seuls expliquer la distribution de dAl à la surface de l'océan?
2- Peut-on réellement considérer que les apports de dAl d'origine fluviale n'atteignent pas l'océan ouvert en quantité significatives (comme suggérés par Hydes & Liss, 1977; Mackin & Aller, 1984; Maring & Duce, 1987) ?
3- Quelles sources hydrothermales constituent une source importante de dAl dans l'océan profond et sur quelle distance l'aluminium apporté est-il transporté ?
4- Dans quelles régions océaniques et dans quelle proportion la biologie impacte-t-elle le cycle de l'aluminium dissous ?
5- Le scavenging réversible, déjà observé comme un processus important pour le cycle du thorium, des terres rares, du cuivre, du fer et du zinc dans l'océan profond, joue-t-il également un rôle significatif dans le cycle du dAl ?

Pour répondre à ces questions nous avons décidé de prendre en compte et d'isoler l'impact du transport physique et du mélange des masses d'eau sur la distribution de dAl dans le but d'étudier plus précisément les processus biogéochimiques. L'objectif de ce chapitre est d'apporter des éléments de réponse aux questions précédemment exposées en prenant en compte l'impact de la circulation océanique sur la distribution de dAl dans le contexte de la campagne GApr08, une section zonale représentée sur la Figure 14 ci-dessous.

3.1.2 L'aluminium dissous dans le contexte de la campagne GApr08

Nous avons mesuré les concentrations de dAl le long de la campagne GApr08 (~ 22 °N, ~ 58–31 °W) se situant à l'extrémité sud du gyre subtropical de l'Atlantique Nord (Figure 14). Cette section se situe dans une zone caractérisée par une faible production primaire (Figure 14a). Cela est surprenant car cette zone se situe sous un panache de fort dépôt de poussières atmosphériques, où les apports de matière sont donc importants (Figure 14b, Jickells et al., 2005). L'objectif de la campagne GApr08 est l'étude de la co-limitation zinc-phosphore et fer-phosphore. Il est donc important d'estimer les apports lithogéniques de ces éléments et en particulier ceux du fer. C'est pour cela qu'il a été choisi de mesurer le traceur lithogénique dAl le long de cette section.

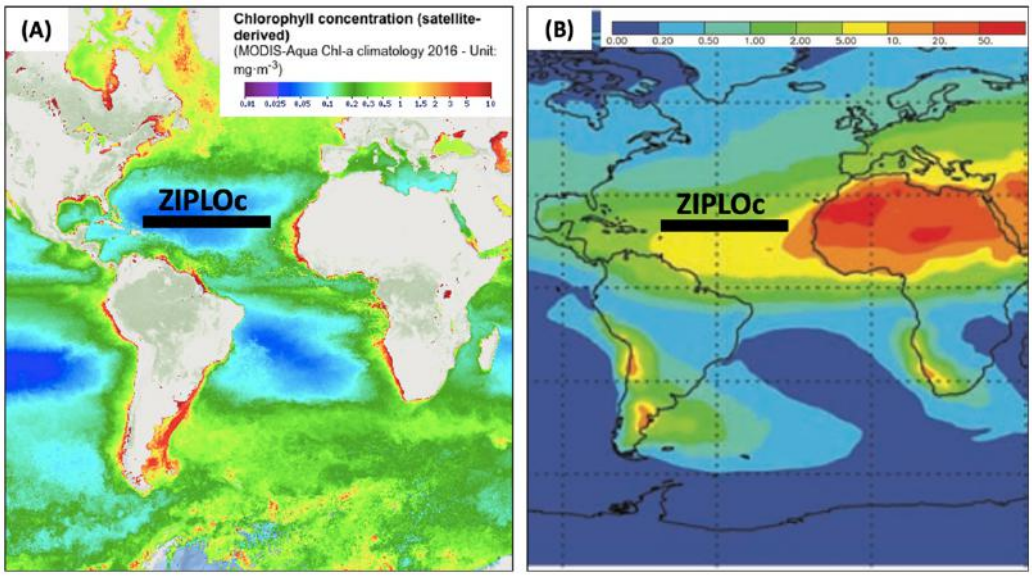

Figure 14 : (A) Concentration en chlorophylle (https://ec.europa.eu/), (B) Flux de poussière moyenné (g/m2/an, adapté de Jickells et al., 2005). Le transect de la campagne GApr08 est indiqué en noir.

3.1.3 Méthode de mesure des concentrations d'aluminium dissous

Les concentrations de dAl présentées dans ce chapitre ont été mesurées, au cours de cette thèse, dans le cadre d'une mobilité à l'Université de Southampton (National Oceanographic Center, UK) financée par l'école des docteurs de Toulouse (Annexe 7.2). Les étapes d'analyses, du prélèvement en mer à la mesure par flow injection analysis (FIA), sont représentées Figure 15. Une étape de développement analytique a été nécessaire pour mettre en place le système de FIA à l'Université de Southampton, elle est décrite en Annexe 7.3. La justesse des mesures a été vérifiée avec un standard international (SAFe, www.geotraces.org), la précision des mesures est de 2% et la limite de détection est 70 fois inférieure à la concentration la plus faible de dAl mesurée.

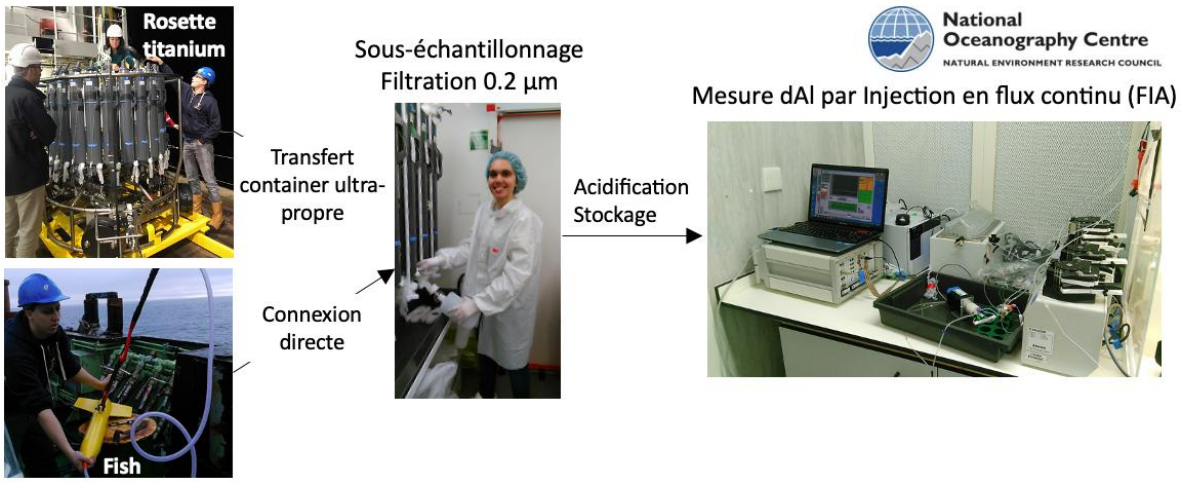

Figure 15 : Méthode de prélèvement et de mesure de l'aluminium dissous de l'échantillonnage en mer à la mesure par flow injection analysis.

3.2 Article soumis: *The importance of water mass transport and dissolved-particle interactions on the dissolved aluminum cycle in the subtropical North Atlantic*

3.2.1 Résumé

Les concentrations de dAl en surface, ont montré un gradient marqué augmentant vers l'ouest. Ce résultat est contre-intuitif étant donné que les plus forts flux de dépôt de poussière atmosphérique (g/m^2/an) se trouvent à l'est. À l'aide d'un modèle 1D d'advection-dépôt de poussière, nous avons montré que l'augmentation des concentrations de dAl n'est pas seulement due aux dépôts de poussière, mais aussi à l'advection qui est essentielle pour conduire ce gradient de dAl. En outre, à l'ouest de la section GApr08, un flux supplémentaire de dAl d'environ 3 10^5 mol/jour est nécessaire pour expliquer les concentrations de dAl. Nous suggérons que la source la plus probable est la dissolution des particules érodées des continents et amenées aux marges depuis les petites Antilles et/ou le fleuve Amazone.
Pour les eaux plus profondes (> 300 m), les résultats de l'eOMPA présentés dans le chapitre précédent, nous ont permis d'estimer que la composante « conservative » associée au transport des masses d'eau domine la distribution de dAl le long de la section. La composante biogéochimique « non-conservative » a quant à elle révélée que la section GApr08 est fortement influencée par (i) une soustraction nette de dAl entre 200 et 800 m, attribuée au scavenging à l'échelle de l'Atlantique Nord subtropical, et (ii) des apports internes de dAl entre 800 m et le fond, attribués à une libération d'aluminium dissous depuis les particules, via des processus de scavenging réversibles. Ce travail a également permis de mettre en évidence un enrichissement de dAl provenant de la source hydrothermale Snakepit, sans néanmoins pouvoir suivre un éventuel panache sur une longue distance.

3.2.2 Article en révision

L'article suivant a été soumis le 05 février 2020 à la revue Global Biogeochemical Cycles.

The importance of water mass transport and dissolved-particle interactions on the aluminum cycle in the subtropical North Atlantic.

L. Artigue[1], N. J. Wyatt[2], F. Lacan[1], C. Mahaffey[3], and M.C. Lohan[2]

[1] LEGOS, University of Toulouse, CNRS, CNES, IRD, UPS, 31400 Toulouse, France.

[2] Ocean and Earth Science, University of Southampton, National Oceanographic Center, Southampton, SO14 3ZH, U.K.

[3] Department of Earth, Ocean and Ecological Sciences, 4 Brownlow Street, University of Liverpool, Liverpool L69 3 GP, U.K.

Corresponding author: Lise Artigue* (lise.artigue@gmail.com)

* LEGOS/CNES, 18, avenue Edouard Belin – 31401 Toulouse Cedex 9, France

Key Points:

- Advection and dust deposition are the main processes driving the surface gradient of dissolved aluminum in the subtropical North Atlantic.
- Lesser Antilles erosion products are a possible source of dissolved aluminum to the western subtropical North Atlantic.
- Dissolved-particle interactions play a major role in the dissolved aluminum distribution in the subtropical North Atlantic.

Abstract

New dissolved aluminum (dAl) data from the 2017 GEOTRACES process study GApr08 along 22°N in the subtropical North Atlantic are presented. They show an east to west increase in dAl concentration in the surface waters. Simulation of these data with a 1D advection-dust deposition -scavenging model revealed that, (i) advection and dust dissolution are equally important dAl sources, (ii) scavenging plays a minor role compared to advection in dAl removal, and (iii) in addition to dust dissolution, another dAl source is required at the westernmost stations to fully explain our observations. We attribute this additional source to the dissolution of erosion products delivered to the western subtropical North Atlantic by the Lesser Antilles.

For waters deeper than ~200 – 300 m, an optimum multiparameter analysis allowed to separate the component of the dAl signal derived from water mass transport from its biogeochemical component. This revealed (i) a major role played by water mass transport, (ii) a net dAl removal between 200 and 800 m, attributed to scavenging at the subtropical North Atlantic scale, and (iii) internal dAl inputs between 800 m and the seafloor, attributed to reversible scavenging.

While the dAl oceanic distribution is usually considered to be dominated by atmospheric dust input and removal by particle scavenging, this paper highlights the important role played by advection and the need to explicitly take this into account in order to quantitatively reveal the impact of external sources and dissolved-particulate interactions on the Al cycle in the North Atlantic Ocean.

1 Introduction

Aluminum (Al) is the 3rd most abundant element in the Earth's crust (8.15 % by weight, Rudnick & Gao, 2014) and is widely used as a tracer of lithogenic material to the oceans, particularly the delivery of atmospheric dust to the open ocean (Han et al., 2008; Measures et al., 2005; Measures & Vink, 2000). Knowledge of the distribution and concentration of Al therefore helps to constrain the oceanic cycle of other crustal-derived elements, including those directly involved in primary production (e.g. iron). The cycling of Al in the marine environment has been hotly debated throughout the years (Measures et al., 2015). Initially, fluvial inputs were considered as the major source of dissolved Al (dAl) to the surface ocean (Stoffyn & Mackenzie, 1982). It has been since shown that dAl is heavily scavenged in estuarine and coastal environments and therefore fluvial inputs constitute a negligible flux of dAl to the remote open ocean (Brown et al., 2010; Hydes & Liss, 1977; Mackin & Aller, 1984; Orians & Bruland, 1986). The dissolution of atmospheric aerosols is now considered to be the major source of dAl to open ocean surface waters (Jickells et al., 1994; Maring & Duce, 1987; Measures et al., 2005, 2010; Tria et al., 2007). At the sea floor, sediment resuspension also acts as a source of dAl, especially in regions with strong boundary currents and nepheloid layers (Middag et al., 2009, 2012, 2015a; Moran & Moore, 1991; van Hulten et al., 2013). Finally, hydrothermal vents can provide significant dAl inputs that can be transported over local to basin scales in the abyssal ocean (Hydes et al., 1986; Lupton et al., 1993; Measures et al., 2015; Resing et al., 2015). Dissolved Al is removed from the water column by particle scavenging, i.e. surface adsorption and particle settling (Hydes, 1979; Orians & Bruland, 1986; Stoffyn & Mackenzie, 1982), and can be removed by incorporation into diatomaceous material in some ocean regions (Gehlen et al., 2002; Hydes et al., 1988; Middag et

al., 2009, 2015a). Model results suggested that, during sinking, desorption and dissolution of particulate Al (pAl) constitute a source of dAl to the water column (van Hulten et al., 2013).

The present work provides a detailed study of the factors driving the distribution and concentration of dAl in the subtropical North Atlantic. To constrain the processes driving the observed east to west gradient in surface dAl, we utilized a 1D model that included both dust and advection as sources of dAl, and both advection, and scavenging as sinks of dAl. In deeper waters, an extended optimum multiparameter analysis (eOMPA, Artigue et al., 2020) is used to estimate how water mass transport and biogeochemical cycling (i.e. external inputs, dissolved/particulate interactions) impact the dAl distribution at the basin scale. In this study, the application of the surface model and the eOMPA provides new insights on the processes controlling the dAl distribution in the subtropical North Atlantic.

2 Materials and Methods

2.1 Sampling and processing

Seawater samples were collected during the GEOTRACES process cruise (GApr08, Fig. 1) in the sub-tropical North Atlantic along ~ 22 °N, ~ 58–31 °W on-board the *R.R.S. James Cook*. This cruise departed Point-à-Pitre, Guadeloupe on the 27th June 2017 and ended in Santa Cruz, Tenerife, on 12th August 2017. Seawater samples were collected from seven full depth stations using 24 trace metal clean 10 L Teflon-coated OTE (Ocean Test Equipment) externally closing bottles and mounted on a titanium CTD rosette deployed on a Kevlar coated conducting wire. At each station a shallow (< 700 m) and deep (> 600 m) CTD cast was sampled resulting in seven high resolution, full depth vertical dAl profiles. Upon recovery, the OTE bottles were transferred into a class ISO 6 clean air container and pressurised with compressed air (1.7 bar) filtered in-line through a 0.2 µm PTFE filter capsule (Millex-FG 50, Millipore). All samples for trace metals were filtered through 0.2 µm membrane cartridge filters (Sartobran-300, Sartorious) into 125 mL low density polyethylene bottles (LDPE, Nalgene). Each sub-sample was acidified to pH 1.7 (0.024 M) with ultra-pure hydrochloric acid (HCl, UPA, Romil). In total, 201 samples were analyzed for dAl from the vertical profiles. Surface seawater samples (130 total) were collected underway using a towed fish positioned at approximately 5 m depth. Seawater was pumped from the fish into the trace metal clean container through acid–cleaned, braided PVC tubing

connected to a Teflon diaphragm pump (Almatec A-15). Sub-samples were filtered in-line through a 0.8/0.2 µm polyethersulfone membrane filter capsule (Sartobran, Sartorius).

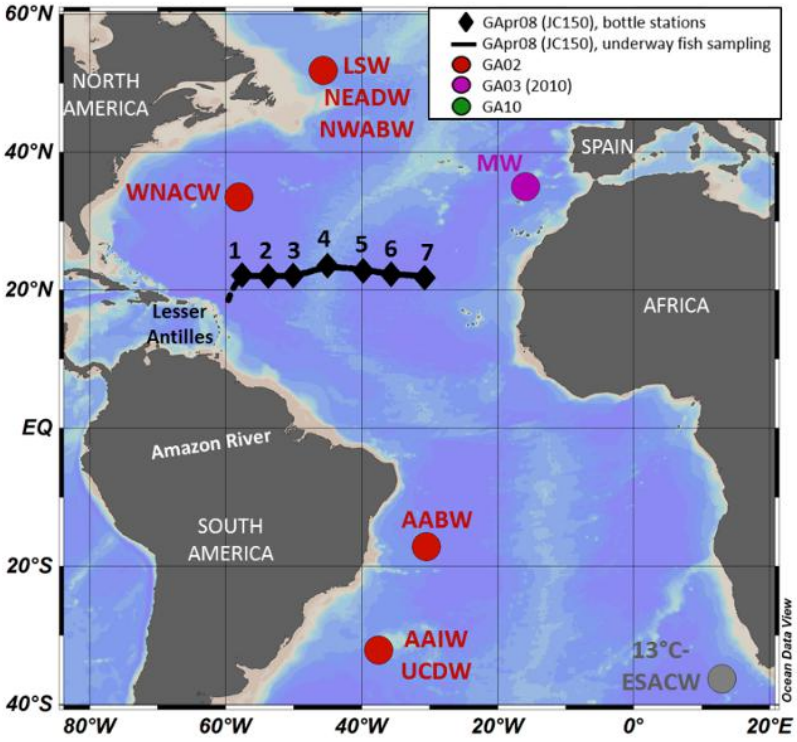

Figure 1. Cruise track of the GApr08 North Atlantic transect. Also shown are the locations where the extended optimum multiparameter analysis end-members of Artigue et al. (2020) were defined : West North Atlantic Central Water (WNACW), Antarctic Intermediate Water (AAIW), Upper Circumpolar Deep Water (UCDW), Labrador Sea Water (LSW), North East Atlantic Deep Water (NEADW), North West Atlantic Bottom Water (NWABW), Antarctic Bottom Water (AABW).

2.2 Dissolved Al analysis

Samples were analyzed for dAl at the University of Southampton Waterfront Campus, National Oceanography Centre using flow injection analysis (FIA) with fluorescence detection (Fig. S1) based on the protocol of Resing and Measures (1994) and modified by Brown and Bruland (2008).

Briefly, the cation exchange resin Toyopeal-AF-Chelate 650 M (Tosohass) was preconditioned with a 0.1 M ammonium acetate solution (Romil, SpA) for 15 s. Seawater samples were buffered in-line to pH 5.75 using a 0.3 M ammonium acetate solution before dAl was preconcentrated onto the resin for 60 s at a flow rate of 1.5 ml/min. Dissolved Al was eluted from the resin using 0.1 M HCl (Romil, SpA) for 2.5 min, entering the reaction stream where it mixed with a lumogallion/ammonium acetate buffer solution. The resulting

fluorescent lumogallion-Al complex formed as the reaction stream passed through a water bath set to 50 °C. The stream was then mixed with the non-ionic surfactant 5% Brij-35 solution (Merck) to enhance the fluorescence quantum yield (Resing & Measures, 1994). Fluorescence was detected using a Shimadzu RF20Axs fluorometer with excitation and emission wavelengths set to 489 nm and 559 nm respectively. Dissolved Al concentration was quantified by the method of standard addition (TraceCERT, Fluka Analytical, Al concentration of 0.037 mol/kg) to column cleaned (Chelex-100, Sigma-Aldrich) seawaters with a dAl concentration ranging from 0.893 nmol/kg to 2.891 nmol/kg. Except when explicitly mentioned, all uncertainties presented in this paper will be expressed at a confidence level of 95 % (e.g. two standard deviation of repeated measurement). Accuracy was quantified through repeat measurement of the SAFe S reference seawater yielding an average concentration of 1.75 ± 0.33 nmol/kg (n = 9), in good agreement with the consensus value of 1.67 ± 0.20 nmol/kg (www.geotraces.org). Measurements of the GSP and GSC reference seawater yielded concentrations of 1.32 ± 0.14 nmol/kg (n = 13) and 0.61 ± 0.16 nmol/kg (n = 13), respectively. Consensus values for GSP and GSC dAl concentration have yet to be published. However, GSP and GSC data confirmed the measurement precision. Surface water collected from the towed fish was used as an internal standard (fish sample 130) as its concentration was representative of that in most of our samples. Its repeat measurement yielded a dAl concentration of 15.29 ± 0.38 nmol/kg (n = 8). This corresponds to a relative precision of 2.5 %, similar to the precision determined from triplicate analysis of each sample (< 5 %). The limit of detection (3x the standard deviation of the lowest standard) was 0.15 ± 0.22 nmol/kg (n = 60).

Possible dAl contamination due to batch-to-batch variability in the polypropylene (PP) caps of LDPE bottles has been previously reported (Brown & Bruland, 2008). This was investigated during this study following the protocol described by Brown & Bruland (2008). Ten acid-cleaned 125 mL LDPE bottles with PP caps were filled with 90 ml of column-cleaned and acidified (0.024 M HCl) seawater. Five bottles were placed upright and five inverted on their caps. All samples were measured before and after one week. We observed no significant increase in dAl in the upright bottles (0.22 ± 0.30 nmol/kg) but an increase in dAl in the inverted bottles (0.43 ± 0.39 nmol/kg). Although caps may be an important source of contamination in low dAl waters, the contamination represented only ~ 2 % of the lowest concentration measured during this study.

3 Results

Along section GApr08, dAl concentration ranged from 10 to 50 nmol/kg (Figs. 2a and 2b). This is in good agreement with the range of dAl values previously reported for the North Atlantic (~ 5–

50 nmol/kg, Barrett et al., 2015; Hydes, 1979; Measures et al., 1986, 2015; Menzel Barraqueta et al., 2018; Middag et al., 2015a; Moran & Moore, 1991; Orians & Bruland, 1986).

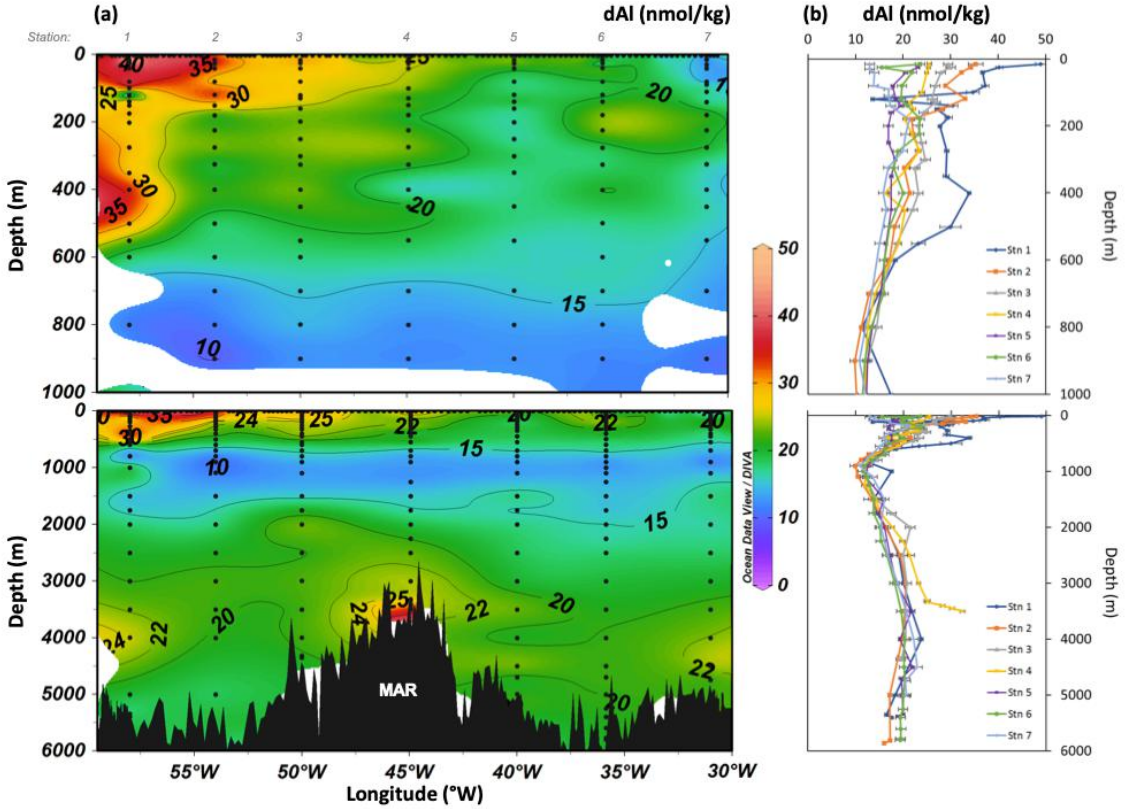

Figure 2. Dissolved aluminum concentrations presented (a) as colour contour plots along the GApr08 section, including both bottle and towed fish data, and (b) by vertical profile for each of the seven stations. The upper figures show zooms on the upper 1000 m, while the lower figures show the full depth range.

Specifically, four main features are notable in the GApr08 dAl distributions (Fig. 2). First, dAl in the upper 100 m displays a strong concentration gradient with values increasing westward from 13 to 49 nmol/kg between 31 and 58 °W. This concentration gradient correlates well with that of dissolved iron from the same study (Kunde et al., 2019). Second, a marked dAl minimum (< 15 nmol/kg) was observed across the entire GApr08 zonal section between 700 and 1500 m depth. Third, below this dAl minimum, dAl concentrations increase and stabilize at around 20 nmol/kg. Finally, elevated dAl concentrations to a maximum 33 nmol/kg were observed at station 4 at depths below 3340 m associated with the Snakepit hydrothermal site.

Figure 3 compares the GApr08 dAl data with that of other North Atlantic section cruises. At 50 m (Fig. 3a), the gradient from low dAl concentrations in the east to higher concentrations in the west during GApr08 is consistent with the basin scale distribution of dAl. West of the mid-Atlantic ridge (MAR), the GA03 section (Measures et al., 2015), displays higher dAl values than GApr08. These discrepancies may be attributed to temporal variation (variable flows and/or dust deposition), and/or to the fact that GA03 is located north of GApr08. East of the MAR, where

GA03 crosses GApr08 the dAl data are in good agreement. At 1000 m depth (Fig. 3b), the dAl minimum was visible across the subtropical North Atlantic with concentrations lower than ~ 15 nmol/kg. At 4000 m depth (Fig. 3c), elevated dAl concentrations (> 20 nmol/kg) compared with intermediate depths were visible across the North Atlantic.

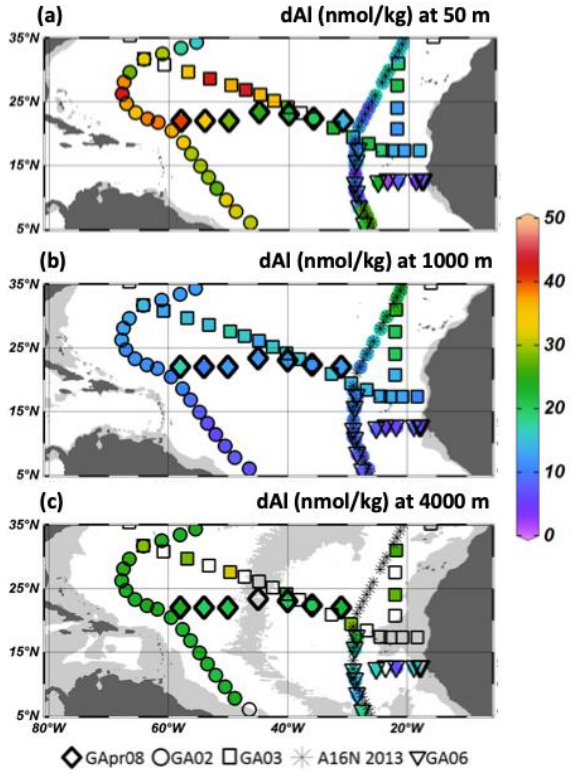

Figure 3. Depth horizon maps of dissolved aluminum (dAl) in the North Atlantic at (a) 50 m, (b) 1000 m, and (c) 4000 m. The data originate from several cruises: GApr08 (July 2017, this study); GA02 (May to July 2010, Middag et al., 2015a); GA03 (November to December 2011, Measures et al., 2015); A16 N (August to September 2013, Barrett et al., 2015); GA06 (March 2011, J.K. Klar, IDP 2017). Dissolved Al data was extracted from the GEOTRACES IDP 2017 (Schlitzer et al., 2018). Empty symbols indicate no dAl data were available.

Figure 4 compares dAl profiles from GApr08 stations 1, 6 and 7 with profiles from closely located stations previously occupied; GApr08 station 1 with GA02 station 29 (~ 234 km distance, Fig. 4a), GApr08 station 6 with GA03 station 20 (crossover station, Fig. 4b), and GApr08 station 7 with A16N station 90 (~ 288 km away, Fig. 4c). In the west Atlantic (Fig. 4a), there is an excellent agreement in the dAl profiles below 800 m (except for one data point at 1000 m). In the upper 1000 m, the dAl concentrations during both cruises are within the same range with differences likely due to temporal variation in dAl supply. In the east Atlantic, the dAl profiles of GApr08 and GA03 (Fig. 4b) are offset in waters deeper than 1000 m. Here, GA03 dAl concentrations are higher than GApr08 with the difference increasing with depth (i.e. 28 % at 1000 m to 42 % at 5800 m). A similar dAl concentration offset for waters deeper than 1000 m was observed at the GA02/GA03 crossover station in the western Atlantic, the reason for which remains unresolved (Measures et al., 2015; Middag et al., 2015a, 2015b), whilst the GApr08 and GA02 data are in close agreement

for the western North Atlantic. At the easternmost stations (Fig. 4c), the dAl profiles are similar in the upper 1000 m (no A16 N data are available deeper than 1000 m). Overall, in addition to the good agreement we obtained with the SAFe S reference standard, this inter-comparison provides great confidence in the data presented in this work.

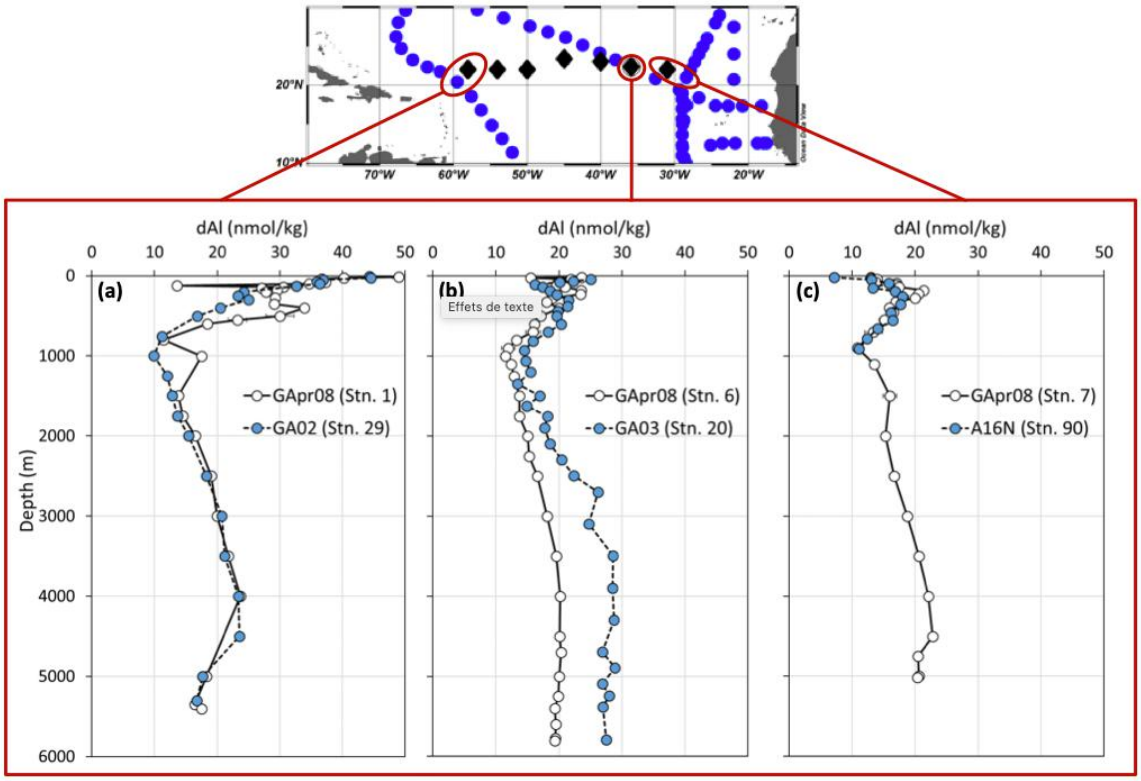

Figure 4. Dissolved aluminum profiles for three stations pairs in the subtropical North Atlantic Ocean: (a) GApr08 station 1 vs. GA02 station 29 (Middag et al., 2015a); (b) GApr08 station 6 vs. GA03 station 20 (Measures et al., 2015); (c) GApr08 station 7 vs. A16N station 90 (Barrett et al., 2015).

4 Discussion

To interpret our results the following discussion is organized in two main parts. First, we discuss the westward increase in surface dAl concentration using a model of advective transport, atmospheric sources and scavenging. Second, we investigate the distribution of dAl in intermediate and deep waters using an eOMPA (Artigue et al., 2020) in order to determine if the dAl distribution is driven by water mass transport and/or biogeochemical processes.

4.1 dAl in surface waters

4.1.1 Modelling of the westward transport and dust deposition in surface waters

Surface dAl concentration in the upper 100 m increases westward along GApr08. At 22 °N, surface waters are transported westwards within the North Equatorial current (NEC;

Arnault, 1987; Fieux, 2010; Richardson & Walsh, 1986), likely impacting on the surface dAl distributions. In addition, large quantities of dust, mainly derived from North Africa deserts, are transported all year long across the subtropical North Atlantic (Prospero, 1996; Prospero et al., 2014; Prospero & Carlson, 1972). The dissolution of dust is considered to be the major source of dAl to open ocean surface waters (Maring & Duce, 1987). Along 22 °N, the maximum winter mixed layer depth is estimated to be ~ 100 m, and therefore the effect of dust dissolution is expected to impact this depth layer (de Boyer Montégut, 2004).

A simple model inspired from Roy-Barman and Jeandel (2016) is constructed below to simulate the evolution of the dAl concentration westward in the upper 100 m, (x coordinate oriented west) considering the two processes of advection, and atmospheric deposition (Fig. 5). Consequently the model neglects in a first approximation all other processes, notably dAl removal onto particles (e.g. scavenging) or additional external sources. This will be discussed below.

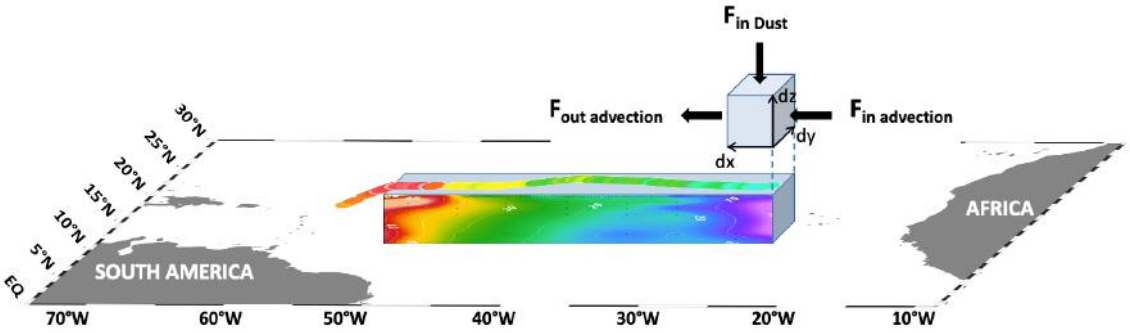

Figure 5. Schematic representation of how modelled advection, and dust deposition fluxes have been applied to the upper 100 m dissolved aluminum (dAl) data for GApr08. Input/output fluxes are designated by black arrows. The GApr08 upper 100 m dAl section as well as the towed fish dAl data are displayed on the map.

Mass conservation implies that, within a volume (V), the dAl concentration (C) variation with time equals the net dAl flux into the volume:

$$\frac{d(CV)}{dt} = \underbrace{F_{adv}(x).dy\,dz}_{\text{F in advection}} - \underbrace{F_{adv}(x+dx)dy\,dz}_{\text{F out advection}} + \underbrace{F_{dust}(x).dx\,dy}_{\text{F in dust}} \quad (1)$$

The volume V does not change with time, so we can divide the equation (1) by dV=dx dy dz. After a first order Taylor expansion of the $F_{\text{out advection}}$ term, this leads to the following net flux equation:

$$\frac{dC}{dt} = -\frac{\partial F_{adv}(x)}{\partial x} + \frac{F_{dust}(x)}{dz} \quad (2)$$

Despite recent studies indicating that advection can be important for dAl distribution in the subtropical North Atlantic (Middag et al., 2015a), this process has been largely neglected and to our knowledge, not quantified when estimating dust fluxes based on surface dAl

measurement (Measures et al., 2005; Measures & Brown, 1996; Menzel Barraqueta et al., 2018b). However, in the case of strong horizontal gradients, such as dAl surface concentration along GApr08, advection cannot be neglected. The quantity of dAl (dq) flowing through a surface (dy. dz) at a velocity (u), and during a time (dt) is:

$$dq = C.u.dy.dz.dt \quad (3)$$

As the advected flux is the quantity of dAl (dq, refer to equation (3)) by unit of time (dt) and surface (dy. dz), this leads to the following advected flux:

$$F_{adv}(x) = \frac{dq/dt}{dy.dz} = C(x).u \quad (4)$$

where u is the NEC velocity. The NEC velocity is modelled here as a constant (in time and space). The NEC velocity was established through a literature review (Arnault, 1987; Fieux, 2010; Richardson & Walsh, 1986), the results from a Lagrangian particle tracking experiment carried out along GApr08 (Artigue et al., 2020), and finally, extracted from the global reanalysis GLORYS12V1 of the Copernicus Marine Environment Monitoring Service (CMEMS, Global_Reanalysis_Phy_001_030, http://marine.copernicus.eu/). We calculate value of 2.8 cm/s as the mean current velocity for the upper 100 m, over the three years prior to GApr08 for the latitude range 21 to 24 °N.

The total dust flux values used in this model were extracted from the Modern-Era Retrospective Analysis for Research and Applications version 2 (MERRA-2, Gelaro et al., 2017), using the database provided by the Global Modeling and Assimilation Office (GMAO, 2015, https://doi.org/10.5067/RZIK2TV7PP38). This atmospheric reanalysis dataset developed by the NASA, includes both satellite data and conventional weather observations (Gelaro et al., 2017). For the model, we determined the mean total (wet + dry) dust deposition for the three years prior to GApr08 over the latitude range 21 to 24 °N, as for the NEC velocity. Modelled deposition to surface waters along GApr08 (Fig. 6) were consistent with previous estimates for the subtropical North Atlantic (Jickells et al., 2005). A strong negative relationship was found between dust flux and distance between station 7 and 1 that we modelled by linear regression (ax + b in equation 5).

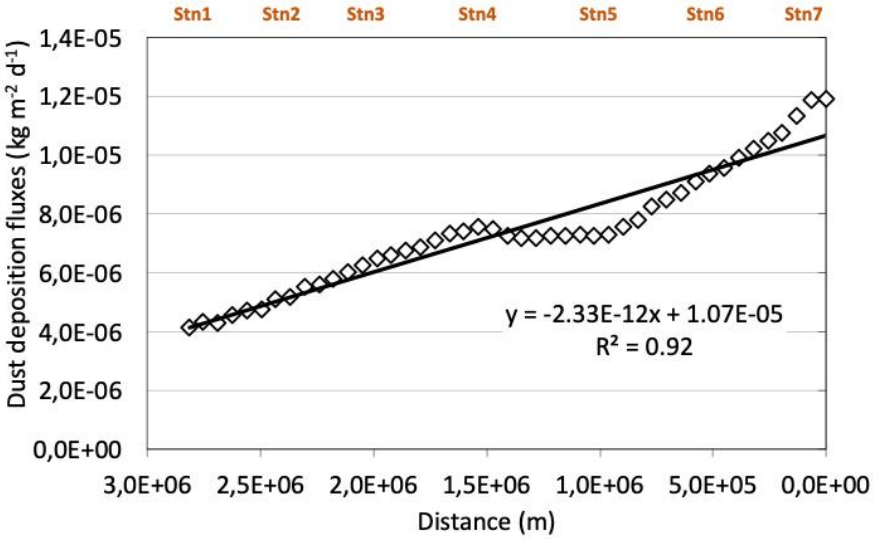

Figure 6. Mean total (wet+dry) dust deposition (white diamonds) for the latitude range 21 to 24 °N over three years prior to GApr08 (1/7/2014 to 30/6/2017) extracted from the Modern-Era Retrospective Analysis for Research and Applications version 2 (MERRA-2, Gelaro et al., 2017). The x-axis denotes the distance between station 7 (x = 0 m) and station 1 (x = 2.82 E+6 m). The linear regression line (black line), its equation and regression number are displayed.

The dust derived dAl flux, F_{dust} (mol m^{-2} day^{-1}), was obtained by multiplying the total dust flux (ax + b) with the Al concentration in the upper continental crust (D_{Al}) and the solubility of Al in aerosols (S_{Al}):

$$F_{dust}(x) = D_{Al}S_{Al} \,.\, (ax + b) \quad (5)$$

with a = -2.33 E-12 kg m^{-3} day^{-1}, b = 1.07 E-5 kg m^{-2} day^{-1}, D_{Al} = 3.02 mol kg^{-1} (Rudnick & Gao, 2014), and S_{Al} = 6.8 % (Baker et al., 2013).

Replacing the F_{adv} and F_{dust} terms, defined in equation (4) and (5) respectively, in equation (2), leads to the net flux equation:

$$\frac{dC}{dt} = -u\frac{dC(x)}{dx} + \frac{D_{Al}S_{Al}(ax+b)}{dz} \quad (6)$$

We assumed that the dAl concentration was in steady state, and that the height of the box was fixed at dz = h = 100 m. Using these assumptions and after integration of equation (6), we obtained the following polynomial function modelling dAl concentration C_{model} in surface water along the transect from station 7 (31 °W, x = 0 m) to station 1 (58 °W, x = 2.82 E6 m):

$$C_{model}(x) = \frac{a\,D_{Al}S_{Al}}{2hu}x^2 + \frac{b\,D_{Al}S_{Al}}{hu}x + c \quad (7)$$

where c is the dAl concentration at x = 0 m, i.e. at station 7.

C_{model} with the parameters set above is shown in Figure 7 (red line) and is compared with the measured GApr08 dAl data. At each station, the average dAl bottle value was calculated by integration over the upper 100 m ($C_{bottles}$). Towed fish surface data (C_{fish}) are also shown for comparison with the modelled dAl distribution. As shown in Figure 7a, the model re-constructed the measured dAl distribution between station 7 and 2 reasonably well. Between stations 2 and 1, the modelled concentrations are lower than both the bottle and towed fish data. The following discussion will address the model/data comparison, firstly between stations 7 and 2 and then between stations 2 and 1.

Despite a good fit between the modelled and measured dAl distribution between stations 7 and 2, the absence of dAl removal associated with particle settling is inconsistent with our knowledge of the Al cycle, dAl being known to be removed from the water column by particle scavenging (Hydes, 1979; Orians & Bruland, 1986; Stoffyn & Mackenzie, 1982). Before discussing this scavenging flux, we first discuss the robustness of the different parameters in the present simplified model.

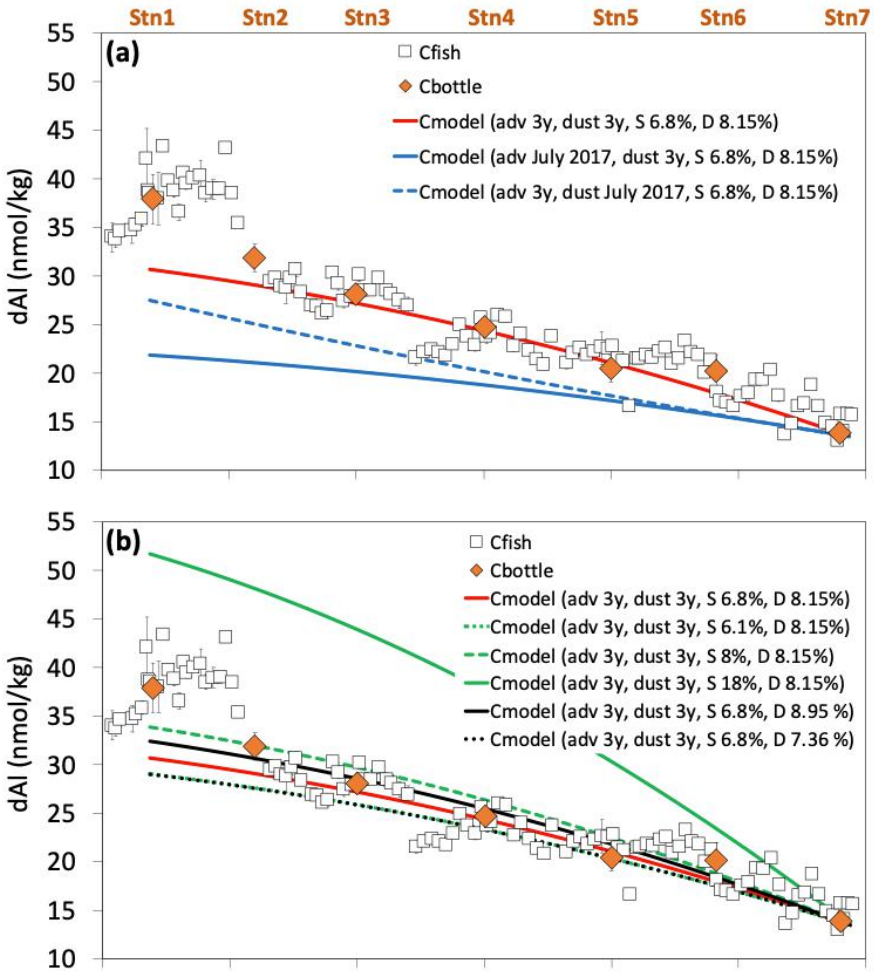

Figure 7. Measured versus modelled dissolved aluminum (dAl) distribution in the upper 100 m along GApr08. (a, b) Modelled dAl distribution from advection and dust deposition (C_{model}, red line) compared with measured dAl from the bottles (average dAl bottle value calculated by integration over the upper 100 m, $C_{bottles}$, orange diamonds) and from the towed fish (C_{fish}, white squares). The bottle and towed fish data are plotted with their respective uncertainties: 2 standard deviation of triplicate peaks for fish values and an estimate of the 95 % error interval for the average bottle values. Different parameters settings for C_{model} were tested by variation of (a) NEC velocity and dust flux independently to that of July 2017 (blue solid and dashed lines, respectively), and (b) aluminum solubility (green solid and dashed lines) and the aluminum content of dust (black solid and dotted lines).

4.1.2 Assumptions and limitation of the model

Several assumptions were made for the dAl distribution model. Here we describe these and discuss how they could affect our results.

We assumed that the concentration of dAl was in steady state (refer to equation 6). This assumption was made because there was no dAl concentration time series data along 22 °N. This type of assumption is very common in the context of projects based on a single cruise. There is excellent agreement in dAl concentrations over the upper 100 m between the three inter-comparison stations discussed above (GA02 2010, GA03 2011, and A16N 2013, refer to Fig. 4) and GApr08, which supports the assumption of a steady state in this layer in the subtropical North Atlantic.

NEC velocity was estimated from the global reanalysis GLORYS12V1 (1/12° horizontal resolution, 50 vertical levels), a product of the CMEMS that provides currents velocity based on altimeter and other observed satellite data (temperature, salinity etc). NEC velocity is highly dependent on the season with higher values in boreal summer (July/August) than in spring and fall (Arnault, 1987). This seasonality was visible within GLORYS12V1 extracted NEC velocity values with higher velocity during the time of the cruise (June to August 2017, ~6 cm s^{-1}) compared with a one, two or three-year mean (~3 cm s^{-1}). To estimate the time the water took to travel from GApr08 station 7 to station 1, we used results from Lagrangian particle tracking experiments carried out in a previous study along GApr08 (Artigue et al., 2020). These experiments tracked the origin of the water sampled during GApr08 backward in time and indicated a transit time of ~2 years from station 7 to 1 at 100 m depth. Therefore, it seems more realistic to extract a two-year NEC velocity rather than a value for the time period of the cruise (June to August 2017). Moreover, this choice removed any seasonality in the current velocity estimate. The extracted mean NEC velocity over the upper 100 m, over the latitude range 21-24 °N, and over a two-year period was 3.0 cm/s. However, given the distance between station 7 and 1 (2.82 E6 m), this results in a transit time of three years. Over a three-year period, the mean NEC velocity was 2.8 cm/s. The difference in the average NEC velocity value over a two or a three-year period is not significant, however, for consistency, we chose a NEC velocity of 2.8 cm/s obtained over a three-year period (August 16th, 2014 to August 16th, 2017). Figure 7a presents how the NEC velocity impacts C_{model}. By applying the NEC velocity

estimated for the period of our cruise (July 2017, blue solid line in Fig. 7a), we find much lower dAl concentrations along GApr08 compared with C_{model} applying a three-year mean NEC velocity (red line in Fig 7a). This supports our NEC velocity choice.

Similar to the NEC velocity, we chose an average dust deposition flux over a three-year period (July 1st, 2014 to June 30th, 2017) as this was the estimated time for the water to travel from station 7 to 1. Dust transport and deposition is also seasonally dependent (Prospero et al., 2014). In summer, dust transport occurs at higher altitudes leading to relatively low dust deposition in the eastern tropical Atlantic but maximum dust deposition in the western tropical Atlantic (Jickells et al., 2016; Kunde et al., 2019; Powell et al., 2015; Prospero et al., 2014). The MERRA-2 model also showed a higher dust deposition flux to surface waters of the western Atlantic compared with the east for July 2017 (Fig. S2), while over three years the trend is reversed (Fig. 6). Figure 7a presents how the dust deposition impacts C_{model}. When applying the July 2017 dust flux to C_{model} (blue dashed line), we find lower dAl concentrations along GApr08 compared with C_{model} using a three-year mean dust flux (red line). This supports our choice of a three-year mean dust flux for our model.

In the model, the Al content in dust was assumed to be that of upper continental crust (Al = 8.2 ± 0.8 % by mass, Rudnick & Gao, 2014). This is a common assumption (Han et al., 2008; Measures & Vink, 2000). The uncertainty of this estimate (± 0.8 %) results in negligible variations in C_{model} (Fig. 7b, black solid and dotted lines).

Another assumption in the model was the solubility of Al from aerosols, which can vary depending on the nature of the deposition (wet or dry), on the source region (Saharan dust, North American dust, etc.), which will further depend upon the season of collection (Baker et al., 2006, 2013; Shelley et al., 2018). In the above simulations, we used the Al solubility value of 6.8 % from Baker et al. (2013) who report Al solubility variability across several oceanographic regions in the Atlantic. Their calculations account for both wet and dry deposition from ten large-scale research cruises and include the contribution from different aerosol sources over two three-month periods. This led to an estimated range of Al solubility from 6.1 to 18 % for the Atlantic with a median value of 8.0 %, and a value of ~6.8 % for the eastern and subtropical North Atlantic regions, including most of GApr08 section. Figure 7b presents how the variability in aerosol Al solubility could impact C_{model} (green solid and dashed lines).

From the above discussion, it appears that the largest uncertainty results from the Al solubility in dust. This will be extensively discussed in the following section.

4.1.3 dAl removal by scavenging

We estimated the dAl removal flux by scavenging, using mass conservation assuming steady state, i.e. calculated as the difference between dAl input from dust and advection, and dAl removal by advection. Given the uncertainties on the processes involved at station 1 (see section 4.1.4), the mass balance calculation was performed on a single large box

extending from station 7 to 2. The dAl scavenging flux was calculated as an average value (hereafter F_{scav_avg}) over the length of the box, considering that F_{scav_avg} must balance the average input and output fluxes of the box, which leads to :

$$F_{scav\_avg} = \big(C(\text{station 7}) - C(station\ 2)\big).\frac{u.h}{\Delta x} + D_{Al}S_{Al}\,F_{dust\_\text{avg}} \qquad (8)$$

Where Δx = 2.37 E6 (distance between station 7 and 2), h = 100 m, C(station 7) = 1.39 E-5 mol m^{-3} and C(station 2) = 3.19 E-5 mol m^{-3}. With an average dust flux value (F_{dust_avg}) between stations 7 and 2 (8 E-3 g m^{-2} d^{-1}), and unchanged D_{Al} and u values (3.02 mol kg^{-1} and 2.8 cm/s), this leads to :

$$\underbrace{F_{scav\_avg}}_{\text{F out scavenging avg}} = \underbrace{1.42\ 10^{-6}}_{\text{F in advection}} - \underbrace{3.25\ 10^{-6}}_{\text{F out advection}} + \underbrace{S_{Al}\ 6.46\ 10^{-4}}_{\text{F in dust avg}} \qquad (9)$$

Be aware that equation (9) does not imply a mechanistic link between scavenging flux and solubility. It implies that the input and output flux values are linked through a non-mechanistic mass balance approach at steady state and over the box length.
As stated above (section 4.1.2), the equation (9) parameters u, D_{Al}, and F_{dust_avg} are well constrained, but Al solubility is more uncertain. The following discussion concentrate on the influence of aerosol dAl solubility on the mass balance.

Equilibrating advection and dust fluxes, i.e. $F_{scav\_avg} = 0$, requires a dAl solubility of ~7.7 %. A lower solubility would imply a negative F_{scav_avg} value, which is impossible. In other words, our model suggests that S is ≥ 7.7 %. Baker et al (2013) report Al solubility from 6.1 to 18 % for the Atlantic, with a median value of 8 %. Our results are in excellent agreement with Baker et al (2013).

Figure 8a displays the dAl input output fluxes for GApr08 obtained with solubility ranging between 8 and 18 %. With the median solubility of 8 %, F_{scav_avg} is 7.7 E-8 mol m^{-2} d^{-1} , which is only 4 % of the 1.9 E-6 mol m^{-2} d^{-1} dust flux; the remaining 96 % dAl was removed from the box by advection. This illustrates the major role advection plays as a dAl sink in the upper 100 m of the subtropical North Atlantic, compared with scavenging.

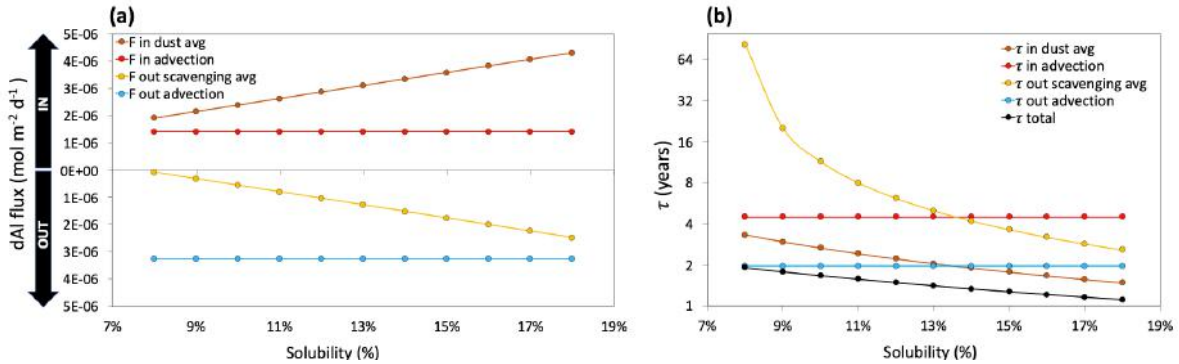

Figure 8. Dissolved Al fluxes (a) and partial residence times (b) obtained with solubilities varying from 8 to 18 % in equation (9). Note the log10 y-axis scale in (b).

Processes that control the Al cycle are often discussed in terms of their residence times (τ). Residence time is defined, assuming steady state, as follows:

$$\tau = \frac{Q}{\sum F_{in}} = \frac{Q}{\sum F_{out}} \quad (10)$$

Where Q, F_{in} and F_{out}, are the content and the fluxes in and out of a given reservoir, respectively.

This leads here to:

$$\tau_{total} = \frac{Q_{Al}}{F_{in\ dust\ avg} + F_{in\ advection}} = \frac{Q_{Al}}{F_{out\ scavenging\ avg} + F_{out\ advection}} \quad (11)$$

Here Q_{Al} is expressed as the dAl concentration mean in our box in mol m^{-2}, whilst the fluxes are in units of mol m^{-2} d^{-1}.

As there are several sources and sinks in our box model, we can also define partial residence time relative to each source and sink. Figure 8b displays the partial residence time (e.g. τ in dust avg, τ out scavenging avg) and the total residence time (τ_{total}) obtained with aerosol Al solubility ranging from 8 to 18 %. It shows that the total residence time ranged between 2 and 1 years for S between 8 and 18 %, respectively. This is consistent with previous estimates of dAl residence time between 1 and 8 years for the ~22 °N in the Atlantic when including dust, advection, and mixing as dAl inputs (Han et al., 2008). The partial residence times for advection input (4.5 years) and dust input (1.5 – 3.0 years) were similar along GApr08, irrespective of solubility. For the output terms, however, whilst the partial residence time for advection was a constant 2 years, the scavenging residence time ranged between 2.6 years for an extreme 18% solubility to 82.4 years for a more realistic 8% solubility. Again, these results highlight the major control advection has on the dAl distribution compared to scavenging.

Overall, these results suggest that advection and dust deposition are the two main processes driving the increase in dAl from station 7 to 2, scavenging playing a secondary role. They show that at a realistic 8 % solubility we can neglect dAl removal by scavenging in our model. In the unlikely case of an extreme 18% solubility the scavenging flux should be included in the model (Fig. 8).

We recognize that assuming a constant scavenging rate across the transect is a crude approximation. Scavenging fluxes are usually parameterized as a function of dissolved trace metal concentrations and/or particle concentrations and/or export (e.g. van Hulten et al., 2013), and therefore are likely to be variable across the transect. However, this simplified approach allows an estimation of its order of magnitude and therefore of its importance relative to the other processes involved in the Al cycle in this area.

492
493 4.1.4 Origin of the dAl enrichment in the western subtropical North Atlantic

494 For a realistic North Atlantic solubility range, the model reproduces the progressive dAl
495 concentration increase from stations 7 to 2, but did not capture the steep increase in dAl
496 concentration between stations 2 and 1. For C_{model} with a solubility of 8% (Fig. 7b, green
497 dashed line), there was up to a ~4 nmol/kg difference between the modelled and measured
498 dAl values. Considering that these dAl observations are representative of a 3° meridional
499 band between 21 °N and 24 °N (Δy = 3.33 E5 m distance), where dust deposition and the
500 NEC are relatively homogeneous, this offset corresponds to an additional flux of 3 E5
501 mol/d at station 1 calculated following equation (15) .
502
503 $$F_{additional\ source} = (C_{bottle}(stn.1).u - C_{model-scav}(stn.1).u)(\Delta y.h) \quad (12)$$
504
505 This missing input flux implies a source of dAl that is either not included or not correctly
506 parametrized in our model. In the following discussion, we will refer to this difference of
507 3 E5 mol/day as the "additional source" of dAl needed to explain the dAl distribution in
508 the western subtropical North Atlantic along GApr08.

509 MERRA-2 includes most species of aerosol from both natural and anthropogenic sources
510 (dust, sea salt, black carbon, organic carbon, and sulfate, Gelaro et al., 2017). The increase
511 in dAl between stations 2 and 1 could reflect the impact of another aerosol type, not
512 included in MERRA-2, with a higher solubility and/or with an Al concentration in excess
513 of typical crustal material. With increased aerosol Al solubility and/or concentration, the
514 modelled concentrations along GApr08 would gradually increase between stations 2 and
515 1, as the westward advection term should provide a continuous increase in the model, which
516 does not correspond to the observations i.e. a sharp increase in dAl concentration west of
517 station 2. This dAl increase rather suggests a disturbance in the westward advection flux,
518 most probably current branches joining the NEC from the west or the south, as shown in
519 Fig. S3.
520
521 A tongue of lower salinity surface water was observed at the western edge of the GApr08
522 section (salinity < 35 for the westernmost towed fish samples and salinity < 37 shallower
523 than 27 m at station 1 and 2, Fig. S4). Surface salinity maps allowed us to attribute this low
524 salinity to the Amazon River plume (Artigue et al., 2020). With a dAl concentration of 3E-
525 4 mol/m^3 and a mean flow rate estimated at 2 E10 m^3/day (Gaillardet et al., 2003), the
526 Amazon River delivers approximately 5 E6 mol/day of dAl to the Atlantic. In order to
527 explain the additional source of dAl to the upper 100 m of the western subtropical North
528 Atlantic (Fig. 7), 5 % of this flux would have to pass through estuaries and reach the
529 western part of the GApr08 transect some 2500 km away, which represents approximately
530 two years transit time (Julien Jouanno, personal communication). This seems unrealistic as
531 much of the riverine dAl inputs is known to be quickly scavenged in estuaries and is
532 considered to not represent a significant source of dAl to the open ocean (Brown et al.,
533 2010; Hydes & Liss, 1977; Mackin & Aller, 1984; Orians & Bruland, 1986). Moreover, no
534 increase in dAl concentration was recorded within the Amazon River plume during GA02
535 (Middag et al., 2015a), during the same time of the year as GApr08, contrary to

observations of elevated dissolved iron (Rijkenberg et al., 2014), and contrary to elevated dissolved iron and dissolved 232 thorium ~1900 km from the river's mouth (AE1410, Hayes et al., 2017). Therefore, it seems unrealistic that the Amazon River explains the dAl enrichment in the west of our section.

The Amazon suspended sediment discharge is estimated at 8 E8 tons/year (Martinez et al., 2009). Assuming a concentration of Al in upper continental crust of 0.003 mol/g (Rudnick & Gao, 2014), the Amazon river delivers 7 E9 mol/day of pAl to the western North Atlantic. The dissolution of terrigenous particle material delivered by rivers to the ocean can have a large impact on the global cycling of some elements (Jeandel & Oelkers, 2015; Radic et al., 2011). Much of these particles settle onto continental margins but for several elements, a small but non-zero fraction dissolves and can be transported over long distances, for instance 3 to 5 % for neodymium (Arsouze et al., 2009; Jeandel et al., 2011; Lacan & Jeandel, 2005). pAl dissolution in the range of 1 to 5 % has been assumed by Brown and Bruland (2009) to estimate the dAl flux delivered by the Columbia River to coastal waters. In this study, the dissolution and transport of only ~ 0.004 % of the 7 E9 mol/day pAl delivered to the continental margin by the Amazon River would be sufficient to explain the dAl enrichment in the west of our section.

The Lesser Antilles, a group of mostly volcanic islands in the Caribbean Sea, are also a potential source of dAl that is close to the western part of the GApr08 cruise (less than 400 km between Guadeloupe and the GApr08 surface transect, Fig. 1). Velocity fields over the upper 100 m indeed suggest that waters impacted by the Lesser Antilles may reach the western end of GApr08 (Fig. S3). This led us to investigate erosion and chemical weathering in the Lesser Antilles as possible sources of dAl to our section, particularly as the rates for these processes are high due to the Lesser Antilles easily weathered volcanic material, pronounced relief and high runoff rates (Gaillardet et al., 2011; Rad et al., 2013).

The mean mechanical erosion rate for Guadeloupe is estimated to be 1000 t/km^2/year (Jérôme Gaillardet, personal communication, July 24, 2020). Assuming an Al concentration in the Guadeloupe bulk regolith of 0.006 mol/g (i.e. 15.25 % by weight, mean value, Buss et al., 2010), the Lesser Antilles could delivers 7 E7 mol/day of pAl to the surrounding oceans. The dissolution and transport of only 0.4 % of this pAl could explain the dAl enrichment observed west of our section.
Due to the very low content of organic matter in the rivers of the lesser Antilles, uncomplexed dAl is considered to be rapidly removed from solution by particle scavenging (Mackin & Aller, 1984, Jérôme Gaillardet, personal communication, July 24, 2020). Moreover, the ratio of pAl fluxes delivered by rivers to the corresponding dAl being estimated at 1000, a direct dAl flux from the lesser Antilles would be lower than the 3 E5 mol/day needed to explain the additional source (Gaillardet et al., 2003; Jeandel & Oelkers, 2015; Viers et al., 2009). Therefore, it seems unrealistic that a direct dAl source from the Lesser Antilles (which does not include the dAl from the dissolution of pAl from the river) could explain the dAl enrichment in the west of our section.

In addition, Lambelet et al (2016) measured a shift towards higher neodymium concentrations and radiogenic neodymium isotopic compositions along GA02 between 19 and 25 ° N compared to northern stations. They suggested this isotopic signature reflected

lithogenic inputs from the Lesser Antilles rather than from the Amazon or Orinoco river, or from volcanic ash.

Overall this suggests that dissolution of continental pAl eroded form the Lesser Antilles, or less likely delivered by the Amazon River, could explain our observations of elevated dAl in surface waters of the western subtropical Atlantic. As described below, a dAl enrichment found along the western edge of GApr08 between 400–500 m reinforces this conclusion.

4.2 Intermediate and deep dAl distributions

Along most of the section, dAl concentrations decrease from the surface to a minimum (10-15 nmol/kg) at depths between 700 and 1500 m (Figs. 2a and 2b). Concentrations then increase to ~ 20 nM by 4000 m and stabilize around this value down to the seafloor. Two local features differ from this homogeneity, (i) a clear enrichment above the Snakepit hydrothermal site (station 4, at the MAR), and (ii) an enrichment at ~ 400 m at the westernmost station 1.

To investigate if the dAl distribution was driven by water mass transport and/or biogeochemical processes, we used the results of the eOMPA specifically carried out for this cruise, for data deeper than ~200 – 300 m (Artigue et al., 2020). This eOMPA identified the mixing fractions of the major water masses along GApr08. These water masses were defined at specific locations and called end-members. All the end-members of this eOMPA were defined from GEOTRACES section cruises where dAl concentrations were available. End-member location and dAl concentration are shown in Figure 1 and Table S1, respectively. This allowed us to calculate a dAl 'conservative' GApr08 section, i.e. where the dAl distribution results from water mass transport and physical mixing (Fig. 9a).

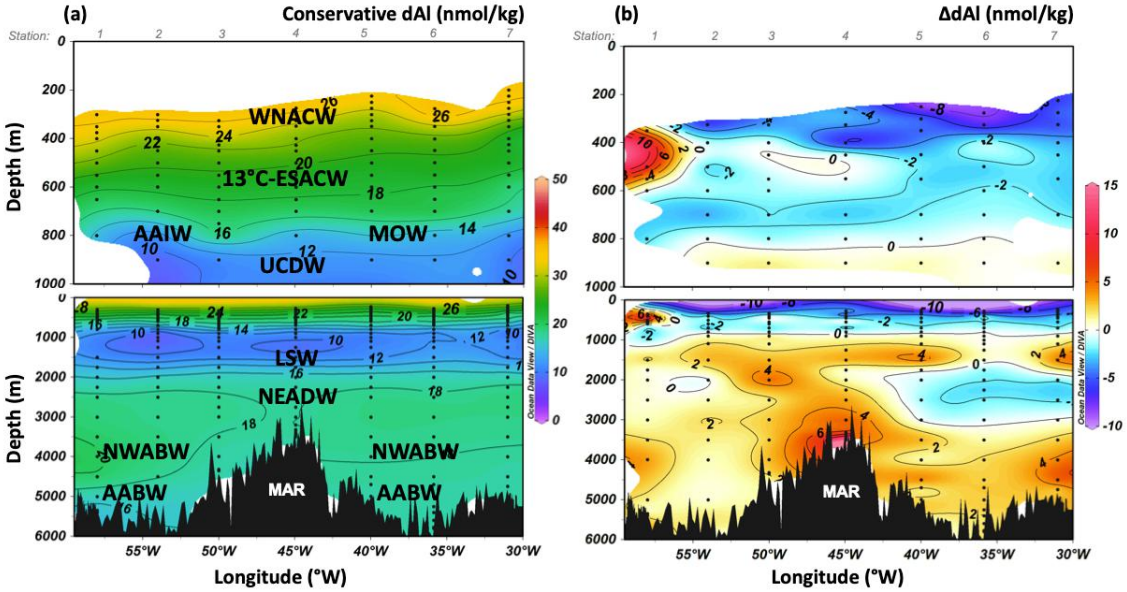

609 **Figure 9**. (a) GApr08 'conservative' dissolved aluminum (dAl) section indicating the
610 dominant water masses found along GApr08: West North Atlantic Central Water
611 (WNACW), Antarctic Intermediate Water (AAIW), Upper Circumpolar Deep Water
612 (UCDW), Labrador Sea Water (LSW), North East Atlantic Deep Water (NEADW), North
613 West Atlantic Bottom Water (NWABW), Antarctic Bottom Water (AABW). For the exact
614 distribution of these water masses see (Artigue et al., 2020). (b) GApr08 'biogeochemical'
615 ΔdAl section. Data points are represented by black dots, top panels are a zoom in the upper
616 1000 m.
617
618 The dominant water masses found along GApr08 are indicated in Figure 9a. The
619 'conservative' dAl section reflected the main features of the measured dAl section (Fig. 2a).
620 Notably, between 100–500 m, the high surface dAl carried by the West North Atlantic
621 Central Water (WNACW). Between 800–1750 m, the low dAl tongue carried by Antarctic
622 Intermediate Water (AAIW) – Upper Circumpolar Deep Water (UCDW) and Labrador Sea
623 Water (LSW). Between 2000–4000 m, the higher dAl concentrations carried by North East
624 Atlantic Deep Water (NEADW) and North West Atlantic Bottom Water (NWABW).
625 Finally, at bottom depths, the lower dAl concentrations carried by Antarctic Bottom Water
626 (AABW). These conservative dAl properties, transported within water masses, seem to
627 dominate the dAl distribution (Figs. 2a and 9a) with the exception of some local features.

628 The subtraction of the GApr08 measured dAl section data (Fig. 2a) from the 'conservative'
629 section (Fig. 9a) allowed us to calculate a residual 'biogeochemical' ΔdAl section (Fig.
630 9b). This biogeochemical ΔdAl section, represents the part of the dAl signal that does not
631 result from water mass transport and therefore results from biogeochemical processes
632 occurring between the end-member locations and the measured GApr08 section (Fig. 1).
633 These biogeochemical processes include dissolved-particulate exchange and sedimentary
634 or hydrothermal inputs. Positive and negative ΔdAl values reveal dAl input and removal,
635 respectively, due to biogeochemical processes.

636 Two local features are clearly visible in the biogeochemical ΔdAl section at stations 1 and
637 4 (Fig. 9b).

638 At station 1, a ΔdAl maximum between 400–500 m implies that 10 nmol/kg of dAl was
639 added to the dAl transported by water masses (contribution of ~66 % WNACW, ~20 %
640 13°C-ESACW, and ~13 % MW, Artigue et al., 2020). As suggested for surface waters, this
641 subsurface ΔdAl enrichment could reflect the dissolution of erosion products delivered
642 from nearby margins (e.g. Lesser Antilles and/or less likely the Amazon River).

643 Station 4 targeted the Snakepit hydrothermal site (23,367 °N, 44,95 °W, 3500 m depth,
644 Beaulieu & Szafranski, 2019, and references therein). Deeper than 3300 m, a positive
645 anomaly in the beam attenuation profile was observed at this station (Fig. S6), indicative
646 of an increased suspended particle content associated with the neutrally buoyant
647 hydrothermal plume. Deeper than 3340 m, i.e. ~ 170 m above the sea floor, ΔdAl reached
648 values of between 8–16 nmol/kg (Fig. 9b), enriching dAl to a maximum of 32.5 nmol/kg
649 at 3500 m (Fig. 2a). This would suggest that up to 50 % of the measured dAl concentration
650 at Snakepit can be attributed to the hydrothermal vent. Note that a dissolved iron

concentration maximum at 3300 m at station 4 has also been attributed to hydrothermal venting (Kunde et al., 2019). Hydrothermally derived dAl has been previously reported for the MAR (up to 53 nmol/kg at the TAG vent site, Lunel et al., 1990; Measures et al., 2015). In the Southeast Pacific Rise, hydrothermalism may explain dAl plumes extending over several thousand kilometers (Lupton et al., 1993; Resing et al., 2015). Note that we did not observe any lateral transport of high dAl concentration at GApr08 stations 3 and 5 (located ~ 500 km away from the MAR).

Except from the two specific features discussed above, the rest of the ΔdAl section is mostly zonally homogeneous. Figure 10 shows the ΔdAl profile calculated as a zonal mean of the 7 stations (excluding the 2 local features discussed above).

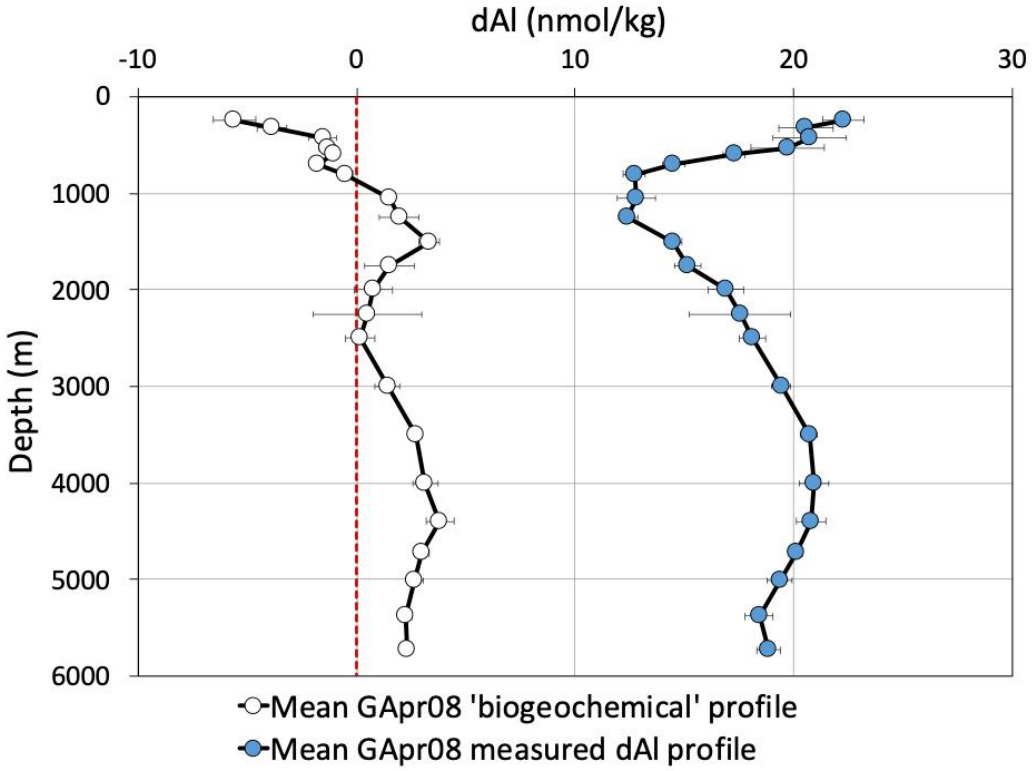

Figure 10. Mean 'biogeochemical' ΔdAl profile (white dots) and mean measured dissolved aluminum (dAl) profiles (blue dots) of the seven stations of GApr08 with their respective standard errors. Note that the two local dAl inputs were removed from the analysis (i.e. 400-500 m at station 1, and deeper than 2500 m at station 4). The profiles were calculated by including samples over a 100 m range for samples between 200 and 1100 m depth, and over 200 m range between 4000 and 5000 m.

Negative ΔdAl values between 225 m and 800 m (from -6 nmol/kg to 0 nmol/kg) revealed a clear and significant removal of dAl in this layer. The calculated ΔdAl values were well above uncertainties associated to our data and the prescribed end-member dAl

673 concentrations (~ 0.3 nmol/kg for both). This result is particularly surprising because this
674 layer, is associated with high dAl values (>20 nmol/kg), and is usually interpreted as
675 reflecting the effect of local dust dissolution (Gehlen et al., 2003; Han et al., 2008; Maring
676 & Duce, 1987; Measures et al., 2010; van Hulten et al., 2013). However, we argue that the
677 high values reflect the advection of remotely enriched waters, with significant removal
678 along their flow path. This 225–800 m layer is composed mainly of WNACW and a small
679 fraction of 13 °C-ESACW that, within the eOMPA, have their end-members located in the
680 Sargasso Sea and Cape Basin, respectively (Fig. 1). We therefore argue that between these
681 locations and the GApr08 section, the net effect of biogeochemical processes was to
682 remove dAl, rather than to add dAl as usually assumed. Most studies attribute dAl removal
683 to (i) passive adsorption onto particle surfaces followed by sinking (Bruland & Lohan,
684 2006; Orians & Bruland, 1986) or (ii) active diatom uptake (Al is incorporated during opal
685 formation as a replacement of silicium, Gehlen et al., 2002; Mackenzie et al., 1978;
686 Stoffyn, 1979). Between 225 and 800 m, diatom opal formation is not expected (below the
687 euphotic zone). Therefore, scavenging onto particles, notably mineral dust particles
688 (following partial dissolution of dust in surface waters, described in section 4.1.3 in the
689 upper 100 m), seems a more likely cause. Scavenging of dAl was further supported by the
690 fact that the negative ΔdAl values were well correlated with particle abundances as
691 indicated by the beam attenuation profiles (Fig. S5). This is not the first time that dust has
692 been postulated to act as a sink rather than a source of element. This was observed for
693 dissolved iron during a mesocosm experiment in the Mediterranean sea where the addition
694 of dust lead to a decrease of dissolved iron concentration attributed to scavenging (Wagener
695 et al., 2010; Wuttig et al., 2013; Ye et al., 2011).

696 Below 800 m, ΔdAl was positive with consistent values of ~2.5 nmol/kg down to the
697 seafloor, except between 1750 and 3000 m where ΔdAl nears zero. This latter feature was
698 the result of negative values in the east (-2.5) and positive values in the west (+2.5), which
699 cancel out (Fig. b). In fact, if the seven data points (out of 81 points below 800 m) with
700 negatives ΔdAl were not included in our calculation of the mean ΔdAl profile, we would
701 observe a homogeneous ΔdAl profile at ~2.5 nmol/kg between 800 and the seafloor.
702 Overall these data reveal that over this depth range, the dAl distribution is mostly
703 dominated by addition. Internal sources of dAl due to desorption from particles (reversible
704 scavenging) has been suggested in recent studies (Middag et al., 2015a; van Hulten et al.,
705 2013). This process, initially proposed for thorium (Bacon & Anderson, 1982; Nozaki et
706 al., 1981), has also been proposed as a significant process, notably at depth, in the internal
707 cycles of rare earth elements (Nozaki & Alibo, 2003), copper (Little et al., 2013), iron
708 (Abadie et al., 2017), and zinc (Weber et al., 2018).

709 Sediment resuspension processes can also act as a source of dAl at depth (Middag et al.,
710 2009, 2012, 2015a; Moran & Moore, 1991; van Hulten et al., 2013). The beam attenuation
711 profiles measured during GApr08 (Fig. S6) show particle increases from about 4000 m
712 down to the seafloor, consistent with sediment resuspensions. The ΔdAl results do suggest
713 a dAl source at those depths. However, this source is not larger below 4000 m than
714 elsewhere in the water column below 1000 m. Therefore, our results do not point to any
715 specific dAl source associated to particle resuspension above the bottom.

5 Conclusions

Surface dAl concentrations, measured along section GApr08 in the subtropical North Atlantic, displayed a marked westwards increasing gradient. Using an advection, dust deposition, scavenging model we showed that this increase was not just due to dust deposition, but that advection is essential in driving this gradient in the subtropical North Atlantic and therefore needs to be incorporated into future dAl studies. In this surface layer (100 m), scavenging of dAl onto particles appears to play a much smaller role than advection in driving dAl distribution.

In the westernmost part of the GApr08 section surface layer, an additional dAl flux of ~3 E5 mol/day was required to explain the dAl concentrations. We suggest that the most likely source is the dissolution of eroded continental particles delivered to the margins from the Lesser Antilles and/or less likely the Amazon River.

By utilizing the results from an eOMPA for the GApr08 cruise (Artigue et al., 2020), we estimated and separated the 'biogeochemical' from the 'conservative' component of the dAl section. The conservative component dominated the dAl distribution. However, it was insufficient to explain all features observed. The biogeochemical ΔdAl section highlighted two local features: a dAl enrichment between 400–500 m at the westernmost station and a hydrothermal enrichment from the Snakepit hydrothermal site that doubled the local dAl concentrations. Except from these two features, the ΔdAl section is mostly zonally homogeneous. Despite high dust deposition fluxes in the subtropical North Atlantic, the ΔdAl profile suggests that, between 200–800 m, removal by scavenging exceeds inputs from dust deposition and dissolution at the basin scale. From 800 m to the seafloor, the ΔdAl profile showed an addition of dAl, likely due to reversible scavenging. Just above the bottom, this profile does not provide evidence for dAl addition linked to sediment resuspension.

Overall, this study highlights the importance of quantitatively considering water mass transport processes to interpret dAl distributions throughout the water column at the local to basin scale. Firstly, in regions of significant horizontal gradients and significant flows (particularly in the surface layers) the process of advection is significant and should not be neglected. Second, by removing the portion of the dAl signal due to water mass transport we have gained new insights into the Al biogeochemical cycle of the subtropical North Atlantic.

Acknowledgments and Data

The data of this study are currently available in Table S2 and S3 and have been submitted to the British Oceanographic Data Centre as part of the GEOTRACES Intermediate Data Product 2021.

We thank K. Kunde and D. G. Santana for sampling alongside the Captain and crew of the RRS James Cook during GApr08. We thank J. Gaillardet for his help about the Lesser Antilles erosion and weathering. We thank J. K. Klar for the GA06 dAl data and for the helpful scientific discussion. We thank J. Jouanno for its helpful comments on the Amazon River plume, and A.

Carret for the help with MATLAB. We thank J. D. Milliman, R. Middag, and K. Kunde for the helpful scientific discussion.

We thank the reviewers of this paper, one anonymous, and J. Resing for constructive comments that helped improve the manuscript.

The French Ministry of Higher education, Research and Innovation (MESRI) funded through the University Toulouse III the Ph.D. fellowship of LA. The French National Centre for Scientific Research (CNRS) funded FL. NERC funded CM (NE/N001979/1) and ML (NE/ N001125/1).

Author Contributions

CM was the chief scientist of the cruise. CM, MCL, and NJW participated in the sampling on board. NJW and LA set the FIA system. LA measured the dAl concentrations with the help of NJW and under the supervision of MCL. NJW extracted the MERRA-2 dust deposition data. LA and FL produced the 1-D surface model, applied the OMPA to the dissolved aluminum section, and conducted the interpretation work. LA drafted the manuscript with the help of FL, and with contributions from NJW, MCL, and CM.

References

Abadie, C., Lacan, F., Radic, A., Pradoux, C., & Poitrasson, F. (2017). Iron isotopes reveal distinct dissolved iron sources and pathways in the intermediate versus deep Southern Ocean. *Proceedings of the National Academy of Sciences*, *114*(5), 858-863. https://doi.org/10.1073/pnas.1603107114

Arnault, S. (1987). *Tropical Atlantic geostrophic currents and ship drifts*. 13.

Arsouze, T., Dutay, J.-C., Lacan, F., & Jeandel, C. (2009). Reconstructing the Nd oceanic cycle using a coupled dynamical – biogeochemical model. *Biogeosciences*, *6*(12), 2829-2846. https://doi.org/10.5194/bg-6-2829-2009

Artigue, L., Lacan, F., van Gennip, S., Lohan, M. C., Wyatt, N. J., Woodward, E. M. S., Mahaffey, C., Hopkins, J., & Drillet, Y. (2020). Water mass analysis along 22 °N in the subtropical North Atlantic for the JC150 cruise (GEOTRACES, GApr08). *Deep Sea Research Part I: Oceanographic Research Papers*, *158*, 103230. https://doi.org/10.1016/j.dsr.2020.103230

Bacon, M. P., & Anderson, R. F. (1982). Distribution of thorium isotopes between dissolved and particulate forms in the deep sea. *Journal of Geophysical Research: Oceans*, *87*(C3), 2045-2056. https://doi.org/10.1029/JC087iC03p02045

Baker, A. R., Adams, C., Bell, T. G., Jickells, T. D., & Ganzeveld, L. (2013). Estimation of atmospheric nutrient inputs to the Atlantic Ocean from 50°N to 50°S based on large-scale field sampling : Iron and other dust-associated elements. *Global Biogeochemical Cycles*, *27*(3), 755-767. https://doi.org/10.1002/gbc.20062

Baker, A. R., Jickells, T. D., Witt, M., & Linge, K. L. (2006). Trends in the solubility of iron, aluminium, manganese and phosphorus in aerosol collected over the Atlantic Ocean. *Marine Chemistry*, *98*(1), 43-58. https://doi.org/10.1016/j.marchem.2005.06.004

Barrett, P. M., Resing, J. A., Buck, N. J., Landing, W. M., Morton, P. L., & Shelley, R. U. (2015). Changes in the distribution of Al and particulate Fe along A16N in the eastern North Atlantic Ocean between 2003 and 2013 : Implications for changes in dust deposition. *Marine Chemistry*, *177*, 57-68. https://doi.org/10.1016/j.marchem.2015.02.009

Beaulieu, S. E., & Szafranski, K. (2019). *InterRidge Global Database of Active Submarine Hydrothermal Vent Fields, Version 3.4.* https://vents-data.interridge.org/ventfields

Brown, M. T., & Bruland, K. W. (2008). An improved flow-injection analysis method for the determination of dissolved aluminum in seawater. *Limnology and Oceanography: Methods*, *6*(1), 87-95. https://doi.org/10.4319/lom.2008.6.87

Brown, M. T., & Bruland, K. W. (2009). Dissolved and particulate aluminum in the Columbia River and coastal waters of Oregon and Washington : Behavior in near-field and far-field plumes. *Estuarine, Coastal and Shelf Science*, *84*(2), 171-185. https://doi.org/10.1016/j.ecss.2009.05.031

Brown, M. T., Lippiatt, S. M., & Bruland, K. W. (2010). Dissolved aluminum, particulate aluminum, and silicic acid in northern Gulf of Alaska coastal waters : Glacial/riverine inputs and extreme reactivity. *Marine Chemistry*, *122*(1), 160-175. https://doi.org/10.1016/j.marchem.2010.04.002

Bruland, K. W., & Lohan, M. C. (2006). *6.02 Controls of Trace Metals in Seawater*. 25.

Buss, H. L., White, A. F., Dessert, C., Gaillardet, J., Blum, A. E., & Sak, P. B. (2010). *Depth profiles in a tropical, volcanic critical zone observatory : Basse- Terre, Guadeloupe*. 4.

de Boyer Montégut, C. (2004). Mixed layer depth over the global ocean : An examination of profile data and a profile-based climatology. *Journal of Geophysical Research*, *109*(C12), C12003. https://doi.org/10.1029/2004JC002378

Fieux, M. (2010). *L'océan planétaire*. Les Presses de l'ENSTA.

Gaillardet, J., Rad, S., Rive, K., Louvat, P., Gorge, C., Allegre, C. J., & Lajeunesse, E. (2011). Orography-driven chemical denudation in the Lesser Antilles : Evidence for a new feed-back mechanism stabilizing atmospheric CO2. *American Journal of Science*, *311*(10), 851-894. https://doi.org/10.2475/10.2011.02

Gaillardet, J., Viers, J., & Dupré, B. (2003). Trace Elements in River Waters. In *Surface and Ground Water, Weathering, and Soils (ed. J.I. Drever) Vol. 5 Treatise on Geochemistry (eds. H.D. Holland and K.K. Turekian)* (p. 225-272). Elsevier-Pergamon.

Gehlen, M., Beck, L., Calas, G., Flank, A.-M., Van Bennekom, A. J., & Van Beusekom, J. E. E. (2002). Unraveling the atomic structure of biogenic silica : Evidence of the structural association of Al and Si in diatom frustules. *Geochimica et Cosmochimica Acta*, *66*(9), 1601-1609. https://doi.org/10.1016/S0016-7037(01)00877-8

Gehlen, M., Heinze, C., Maier-Reimer, E., & Measures, C. I. (2003). Coupled Al-Si geochemistry in an ocean general circulation model : A tool for the validation of oceanic dust deposition fields? *Global Biogeochemical Cycles*, *17*(1). https://doi.org/10.1029/2001GB001549

Gelaro, R., McCarty, W., Suárez, M. J., Todling, R., Molod, A., Takacs, L., Randles, C. A., Darmenov, A., Bosilovich, M. G., Reichle, R., Wargan, K., Coy, L., Cullather, R., Draper, C., Akella, S., Buchard, V., Conaty, A., da Silva,

A. M., Gu, W., … Zhao, B. (2017). The Modern-Era Retrospective Analysis for Research and Applications, Version 2 (MERRA-2). *Journal of Climate*, *30*(14), 5419-5454. https://doi.org/10.1175/JCLI-D-16-0758.1

Global Modeling and Assimilation Office (GMAO). (2015). *MERRA-2 tavgM_2d_adg_Nx : 2d,Monthly mean,Time-averaged,Single-Level,Assimilation,Aerosol Diagnostics (extended) V5.12.4, Greenbelt, MD, USA, Goddard Earth Sciences Data and Information Services Center (GES DISC), Accessed : July 2020*. https://doi.org/10.5067/RZIK2TV7PP38

Han, Q., Moore, J. K., Zender, C., Measures, C., & Hydes, D. (2008). Constraining oceanic dust deposition using surface ocean dissolved Al. *Global Biogeochemical Cycles*, *22*(2), n/a-n/a. https://doi.org/10.1029/2007GB002975

Hayes, C. T., Rosen, J., McGee, D., & Boyle, E. A. (2017). Thorium distributions in high- and low-dust regions and the significance for iron supply : Marine Thorium and Iron Cycles. *Global Biogeochemical Cycles*. https://doi.org/10.1002/2016GB005511

Hydes, D. J. (1979). Aluminum in seawater : Control by inorganic processes. *Science*, *205*, 1260-1262. https://doi.org/10.1126/science.205.4412.1260

Hydes, D. J., de Lange, G. J., & de Baar, H. J. W. (1988). Dissolved aluminium in the Mediterranean. *Geochimica et Cosmochimica Acta*, *52*(8), 2107-2114. https://doi.org/10.1016/0016-7037(88)90190-1

Hydes, D. J., & Liss, P. S. (1977). The behaviour of dissolved aluminium in estuarine and coastal waters. *Estuarine and Coastal Marine Science*, *5*(6), 755-769. https://doi.org/10.1016/0302-3524(77)90047-0

Hydes, D. J., Statham, P. J., & Burton, J. D. (1986). A vertical profile of dissolved trace metals (Al, Cd, Cu, Mn, Ni) over the median valley of the mid Atlantic ridge, 43°N : Implications for Hydrothermal activity. *Science of The Total Environment*, *49*, 133-145. https://doi.org/10.1016/0048-9697(86)90236-6

Jeandel, C., & Oelkers, E. H. (2015). The influence of terrigenous particulate material dissolution on ocean chemistry and global element cycles. *Chemical Geology*, *395*, 50-66. https://doi.org/10.1016/j.chemgeo.2014.12.001

Jeandel, C., Peucker-Ehrenbrink, B., Jones, M. T., Pearce, C. R., Oelkers, E. H., Godderis, Y., Lacan, F., Aumont, O., & Arsouze, T. (2011). Ocean margins : The missing term in oceanic element budgets? *Eos, Transactions American Geophysical Union*, *92*(26), 217-218. https://doi.org/10.1029/2011EO260001

Jickells, T., Church, T., Veron, A., & Arimoto, R. (1994). Atmospheric inputs of manganese and aluminium to the Sargasso Sea and their relation to surface water concentrations. *Marine Chemistry*, *46*(3), 283-292. https://doi.org/10.1016/0304-4203(94)90083-3

Jickells, T. D., An, Z. S., Andersen, K. K., Baker, A. R., Bergametti, G., Brooks, N., Cao, J. J., Boyd, P. W., Duce, R. A., Hunter, K. A., Kawahata, H., Kubilay, N., laRoche, J., Liss, P. S., Mahowald, N., Prospero, J. M., Ridgwell, A. J., Tegen, I., & Torres, R. (2005). Global Iron Connections Between Desert Dust, Ocean Biogeochemistry, and Climate. *Science*, *308*(5718), 67-71. https://doi.org/10.1126/science.1105959

Jickells, T. D., Baker, A. R., & Chance, R. (2016). Atmospheric transport of trace elements and nutrients to the oceans. *Philosophical Transactions of the Royal Society A: Mathematical, Physical and Engineering Sciences*, *374*(2081), 20150286. https://doi.org/10.1098/rsta.2015.0286

Kunde, K., Wyatt, N. J., González-Santana, D., Tagliabue, A., Mahaffey, C., & Lohan, M. C. (2019). Iron Distribution in the Subtropical North Atlantic : The Pivotal Role of Colloidal Iron. *Global Biogeochemical Cycles*, *n/a*(n/a). https://doi.org/10.1029/2019GB006326

Lacan, F., & Jeandel, C. (2005). Acquisition of the neodymium isotopic composition of the North Atlantic Deep Water. *Geochemistry, Geophysics, Geosystems*, *6*(12), n/a-n/a. https://doi.org/10.1029/2005GC000956

Lambelet, M., van de Flierdt, T., Crocket, K., Rehkämper, M., Kreissig, K., Coles, B., Rijkenberg, M. J. A., Gerringa, L. J. A., de Baar, H. J. W., & Steinfeldt, R. (2016). Neodymium isotopic composition and concentration in the western North Atlantic Ocean : Results from the GEOTRACES GA02 section. *Geochimica et Cosmochimica Acta*, *177*, 1-29. https://doi.org/10.1016/j.gca.2015.12.019

Little, S. H., Vance, D., Siddall, M., & Gasson, E. (2013). A modeling assessment of the role of reversible scavenging in controlling oceanic dissolved Cu and Zn distributions. *Global Biogeochemical Cycles*, *27*(3), 780-791. https://doi.org/10.1002/gbc.20073

Lunel, T., Rudnicki, M., Elderfield, H., & Hydes, D. (1990). Aluminium as a depth-sensitive tracer of entrainment in submarine hydrothermal plumes. *Nature*, *344*(6262), 137-139. https://doi.org/10.1038/344137a0

Lupton, J. E., Baker, E. T., Mottl, M. J., Sansone, F. J., Wheat, C. G., Resing, J. A., Massoth, G. J., Measures, C. I., & Feely, R. A. (1993). Chemical and physical diversity of hydrothermal plumes along the East Pacific Rise, 8°45′N to 11°50′N. *Geophysical Research Letters*, *20*(24), 2913-2916. https://doi.org/10.1029/93GL00906

Mackenzie, F. T., Stoffyn, M., & Wollast, R. (1978). Aluminum in Seawater : Control by Biological Activity. *Science*, *199*(4329), 680-682. https://doi.org/10.1126/science.199.4329.680

Mackin, J. E., & Aller, R. C. (1984). Processes affecting the behavior of dissolved aluminum in estuarine waters. *Marine Chemistry*, *14*(3), 213-232. https://doi.org/10.1016/0304-4203(84)90043-4

878 Maring, H. B., & Duce, R. A. (1987). The impact of atmospheric aerosols on trace metal chemistry in open ocean
879 surface seawater, 1. Aluminum. *Earth and Planetary Science Letters*, *84*(4), 381-392.
880 https://doi.org/10.1016/0012-821X(87)90003-3
881 Martinez, J. M., Guyot, J. L., Filizola, N., & Sondag, F. (2009). Increase in suspended sediment discharge of the
882 Amazon River assessed by monitoring network and satellite data. *CATENA*, *79*(3), 257-264.
883 https://doi.org/10.1016/j.catena.2009.05.011
884 Measures, C. I., & Brown, E. T. (1996). Estimating Dust Input to the Atlantic Ocean Using Surface Water Aluminium
885 Concentrations. In S. Guerzoni & R. Chester (Éds.), *The Impact of Desert Dust Across the Mediterranean* (p.
886 301-311). Springer Netherlands. https://doi.org/10.1007/978-94-017-3354-0_30
887 Measures, C. I., Brown, M. T., & Vink, S. (2005). Dust deposition to the surface waters of the western and central
888 North Pacific inferred from surface water dissolved aluminum concentrations. *Geochemistry, Geophysics,*
889 *Geosystems*, *6*(9), n/a-n/a. https://doi.org/10.1029/2005GC000922
890 Measures, C. I., Edmond, & Jickells, T. D. (1986). Aluminium in the northwest Atlantic. *Geochimica et Cosmochimica*
891 *Acta*, *50*(7), 1423-1429. https://doi.org/10.1016/0016-7037(86)90315-7
892 Measures, C. I., Hatta, M., Fitzsimmons, J., & Morton, P. (2015). Dissolved Al in the zonal N Atlantic section of the
893 US GEOTRACES 2010/2011 cruises and the importance of hydrothermal inputs. *Deep Sea Research Part II:*
894 *Topical Studies in Oceanography*, *116*, 176-186. https://doi.org/10.1016/j.dsr2.2014.07.006
895 Measures, C. I., Sato, T., Vink, S., Howell, S., & Li, Y. H. (2010). The fractional solubility of aluminium from mineral
896 aerosols collected in Hawaii and implications for atmospheric deposition of biogeochemically important trace
897 elements. *Marine Chemistry*, *120*(1), 144-153. https://doi.org/10.1016/j.marchem.2009.01.014
898 Measures, C. I., & Vink, S. (2000). On the use of dissolved aluminum in surface waters to estimate dust deposition to
899 the ocean. *Global Biogeochemical Cycles*, *14*(1), 317-327. https://doi.org/10.1029/1999GB001188
900 Menzel Barraqueta, J.-L., Schlosser, C., Planquette, H., Gourain, A., Cheize, M., Boutorh, J., Shelley, R., Pereira
901 Contreira, L., Gledhill, M., Hopwood, M. J., Lherminier, P., Sarthou, G., & Achterberg, E. P. (2018a). Aluminium
902 in the North Atlantic Ocean and the Labrador Sea (GEOTRACES GA01 section) : Roles of continental inputs and
903 biogenic particle removal. *Biogeosciences Discussions*, 1-28. https://doi.org/10.5194/bg-2018-39
904 Menzel Barraqueta, J.-L., Klar, J. K., Gledhill, M., Schlosser, C., Shelley, R., Planquette, H., Wenzel, B., Sarthou, G.,
905 & Achterberg, E. P. (2018b). Atmospheric aerosol deposition fluxes over the Atlantic Ocean : A GEOTRACES
906 case study. *Biogeosciences Discussions*, 1-25. https://doi.org/10.5194/bg-2018-209
907 Middag, R., Baar, H. de, Laan, P., & Huhn, O. (2012). *The effects of continental margins and water mass circulation*
908 *on the distribution of dissolved aluminum and manganese in Drake Passage*.
909 https://doi.org/10.1029/2011jc007434
910 Middag, R., de Baar, H. J. W., Laan, P., & Bakker, K. (2009). Dissolved aluminium and the silicon cycle in the Arctic
911 Ocean. *Marine Chemistry*, *115*(3), 176-195. https://doi.org/10.1016/j.marchem.2009.08.002
912 Middag, R., van Hulten, M. M. P., Van Aken, H. M., Rijkenberg, M. J. A., Gerringa, L. J. A., Laan, P., & de Baar, H.
913 J. W. (2015a). Dissolved aluminium in the ocean conveyor of the West Atlantic Ocean : Effects of the biological
914 cycle, scavenging, sediment resuspension and hydrography. *Marine Chemistry*, *177*, 69-86.
915 https://doi.org/10.1016/j.marchem.2015.02.015
916 Middag, R., Séférian, R., Conway, T. M., John, S. G., Bruland, K. W., & de Baar, H. J. W. (2015b). Intercomparison
917 of dissolved trace elements at the Bermuda Atlantic Time Series station. *Marine Chemistry*, *177*, 476-489.
918 https://doi.org/10.1016/j.marchem.2015.06.014
919 Moran, S. B., & Moore, R. M. (1991). The potential source of dissolved aluminum from resuspended sediments to the
920 North Atlantic Deep Water. *Geochimica et Cosmochimica Acta*, *55*(10), 2745-2751. https://doi.org/10.1016/0016-
921 7037(91)90441-7
922 Nozaki, Y., & Alibo, D. (2003). Importance of vertical geochemical processes in controlling the oceanic profiles of
923 dissolved rare earth elements in the northeastern Indian Ocean. *Earth and Planetary Science Letters*, *205*, 155-172.
924 https://doi.org/10.1016/S0012-821X(02)01027-0
925 Nozaki, Y., Horibe, Y., & Tsubota, H. (1981). The water column distributions of thorium isotopes in the western
926 North Pacific. *Earth and Planetary Science Letters*, *54*(2), 203-216. https://doi.org/10.1016/0012-821X(81)90004-
927 2
928 Orians, K. J., & Bruland, K. W. (1986). The biogeochemistry of aluminum in the Pacific Ocean. *Earth and Planetary*
929 *Science Letters*, *78*(4), 397-410. https://doi.org/10.1016/0012-821X(86)90006-3
930 Powell, C. F., Baker, A. R., Jickells, T. D., Bange, H. W., Chance, R. J., & Yodle, C. (2015). Estimation of the
931 Atmospheric Flux of Nutrients and Trace Metals to the Eastern Tropical North Atlantic Ocean. *Journal of the*
932 *Atmospheric Sciences*, *72*(10), 4029-4045. https://doi.org/10.1175/JAS-D-15-0011.1
933 Prospero, J. M. (1996). Saharan Dust Transport Over the North Atlantic Ocean and Mediterranean : An Overview. In

S. Guerzoni & R. Chester (Éds.), *The Impact of Desert Dust Across the Mediterranean* (Vol. 11, p. 133-151). Springer Netherlands. https://doi.org/10.1007/978-94-017-3354-0_13

Prospero, J. M., & Carlson, T. N. (1972). Vertical and areal distribution of Saharan dust over the western equatorial north Atlantic Ocean. *Journal of Geophysical Research*, *77*(27), 5255-5265. https://doi.org/10.1029/JC077i027p05255

Prospero, J. M., Collard, F.-X., Molinié, J., & Jeannot, A. (2014). Characterizing the annual cycle of African dust transport to the Caribbean Basin and South America and its impact on the environment and air quality. *Global Biogeochemical Cycles*, *28*(7), 757-773. https://doi.org/10.1002/2013GB004802

Rad, S., Rivé, K., Vittecoq, B., Cerdan, O., & Allègre, C. J. (2013). Chemical weathering and erosion rates in the Lesser Antilles : An overview in Guadeloupe, Martinique and Dominica. *Journal of South American Earth Sciences*, *45*, 331-344. https://doi.org/10.1016/j.jsames.2013.03.004

Radic, A., Lacan, F., & W. Murray, J. (2011). Iron isotopes in the seawater of the equatorial Pacific Ocean : New constraints for the oceanic iron cycle. *Earth and Planetary Science Letters*, *306*, 1-10. https://doi.org/10.1016/j.epsl.2011.03.015

Resing, J. A., & Measures, C. I. (1994). Fluorometric Determination of Al in Seawater by Flow Injection Analysis with In-Line Preconcentration. *Analytical Chemistry*, *66*(22), 4105-4111. https://doi.org/10.1021/ac00094a039

Resing, J. A., Sedwick, P. N., German, C. R., Jenkins, W. J., Moffett, J. W., Sohst, B. M., & Tagliabue, A. (2015). Basin-scale transport of hydrothermal dissolved metals across the South Pacific Ocean. *Nature*, *523*(7559), 200-203. https://doi.org/10.1038/nature14577

Richardson, P. L., & Walsh, D. (1986). Mapping climatological seasonal variations of surface currents in the tropical Atlantic using ship drifts. *Journal of Geophysical Research*, *91*(C9), 10537. https://doi.org/10.1029/JC091iC09p10537

Rijkenberg, M. J. A., Middag, R., Laan, P., Gerringa, L. J. A., van Aken, H. M., Schoemann, V., de Jong, J. T. M., & de Baar, H. J. W. (2014). The Distribution of Dissolved Iron in the West Atlantic Ocean. *PLOS ONE*, *9*(6), e101323. https://doi.org/10.1371/journal.pone.0101323

Roy-Barman, M., & Jeandel, C. (2016). *Marine Geochemistry : Ocean Circulation, Carbon Cycle and Climate Change* (Oxford University Press).

Rudnick, R. L., & Gao, S. (2014). Composition of the Continental Crust. In *Treatise on Geochemistry* (p. 1-51). Elsevier. https://doi.org/10.1016/B978-0-08-095975-7.00301-6

Schlitzer, R., Anderson, R. F., Dodas, E. M., Lohan, M., Geibert, W., Tagliabue, A., Bowie, A., Jeandel, C., Maldonado, M. T., Landing, W. M., Cockwell, D., Abadie, C., Abouchami, W., Achterberg, E. P., Agather, A., Aguliar-Islas, A., van Aken, H. M., Andersen, M., Archer, C., … Zurbrick, C. (2018). The GEOTRACES Intermediate Data Product 2017. *Chemical Geology*, *493*, 210-223. https://doi.org/10.1016/j.chemgeo.2018.05.040

Shelley, R. U., Landing, W. M., Ussher, S. J., Planquette, H., & Sarthou, G. (2018). Regional trends in the fractional solubility of Fe and other metals from North Atlantic aerosols (GEOTRACES cruises GA01 and GA03) following a two-stage leach. *Biogeosciences*, *15*(8), 2271-2288. https://doi.org/10.5194/bg-15-2271-2018

Stoffyn, M. (1979). Biological Control of Dissolved Aluminum in Seawater : Experimental Evidence. *Science*, *203*(4381), 651-653. https://doi.org/10.1126/science.203.4381.651

Stoffyn, M., & Mackenzie, F. T. (1982). Fate of dissolved aluminum in the oceans. *Marine Chemistry*, *11*(2), 105-127. https://doi.org/10.1016/0304-4203(82)90036-6

Tria, J., Butler, E. C. V., Haddad, P. R., & Bowie, A. R. (2007). Determination of aluminium in natural water samples. *Analytica Chimica Acta*, *588*(2), 153-165. https://doi.org/10.1016/j.aca.2007.02.048

van Hulten, M. M. P., Sterl, A., Tagliabue, A., Dutay, J.-C., Gehlen, M., de Baar, H. J. W., & Middag, R. (2013). Aluminium in an ocean general circulation model compared with the West Atlantic Geotraces cruises. *Journal of Marine Systems*, *126*, 3-23. https://doi.org/10.1016/j.jmarsys.2012.05.005

Viers, J., Dupré, B., & Gaillardet, J. (2009). Chemical composition of suspended sediments in World Rivers : New insights from a new database. *Science of The Total Environment*, *407*(2), 853-868. https://doi.org/10.1016/j.scitotenv.2008.09.053

Wagener, T., Guieu, C., & Leblond, N. (2010). Effects of dust deposition on iron cycle in the surface Mediterranean Sea. *Biogeosciences Discussions*, 2799-2830.

Weber, T., John, S., Tagliabue, A., & DeVries, T. (2018). Biological uptake and reversible scavenging of zinc in the global ocean. *Science*, *361*(6397), 72-76. https://doi.org/10.1126/science.aap8532

Wuttig, K., Wagener, T., Bressac, M., Dammshäuser, A., Streu, P., Guieu, C., & Croot, P. L. (2013). Impacts of dust deposition on dissolved trace metal concentrations (Mn, Al and Fe) during a mesocosm experiment. *Biogeosciences*, *10*(4), 2583-2600. https://doi.org/10.5194/bg-10-2583-2013

990 Ye, Y., Wagener, T., Völker, C., Guieu, C., & Wolf-Gladrow, D. A. (2011). Dust deposition : Iron source or sink? A
991 case study. *Biogeosciences*, *8*(8), 2107-2124. https://doi.org/10.5194/bg-8-2107-2011
992

3.2.3 Matériel complémentaire

[Global Biogeochemical Cycles]

Supporting Information for

[The importance of water mass transport and dissolved-particle interactions on the dissolved aluminum cycle in the subtropical North Atlantic.]

[L. Artigue[1], N. J. Wyatt[2], F. Lacan[1], C. Mahaffey[3], and M.C. Lohan[2]]

[[1] LEGOS, University of Toulouse, CNRS, CNES, IRD, UPS, 31400 Toulouse, France.

[2] Ocean and Earth Science, University of Southampton, National Oceanographic Center, Southampton, SO14 3ZH, U.K.

[3] Department of Earth, Ocean and Ecological Sciences, 4 Brownlow Street, University of Liverpool, Liverpool L69 3 GP, U.K.]

Contents of this file

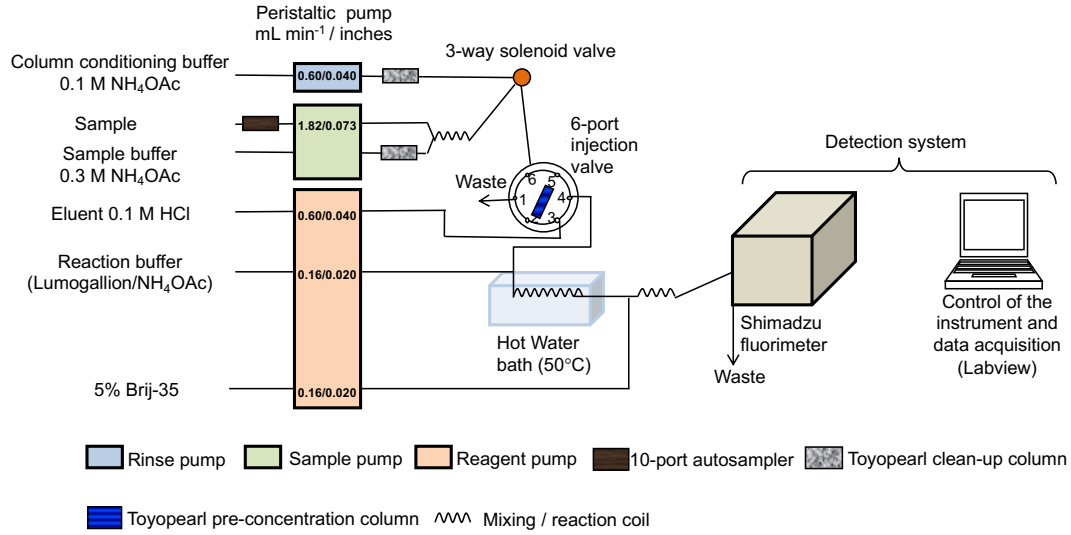

Figure S1. System of Flow Injection Analysis (FIA) with Fluorescence detection used to measure the dissolved Aluminum samples of JC150.

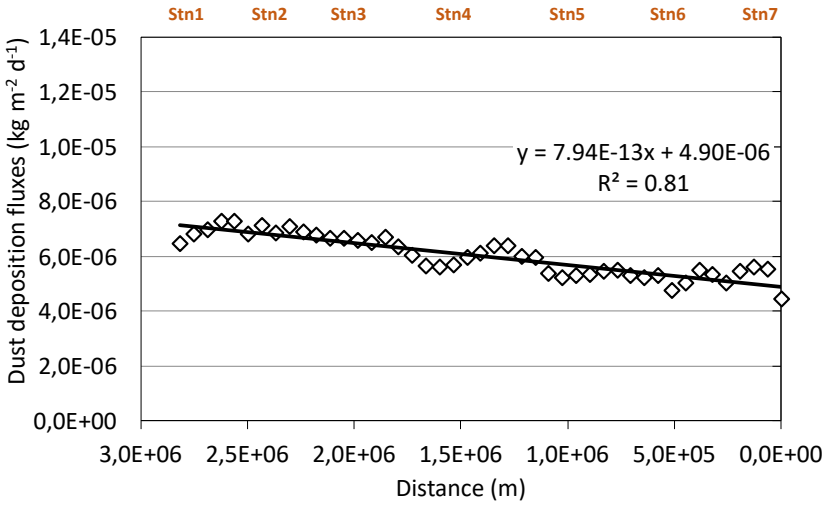

Figure S2. Mean total (wet+dry) dust deposition fluxes (white diamonds) for the latitude range 21 to 24 °N over July 2017. These fluxes were extracted from the Modern-Era Retrospective Analysis for Research and Applications version 2 (MERRA-2, Gelaro et al., 2017). The x-axis denotes the distance between station 7 (x = 0

m) and station 1 (x = 2.82 E+6 m). The linear regression line (black line), its equation and regression number are displayed.

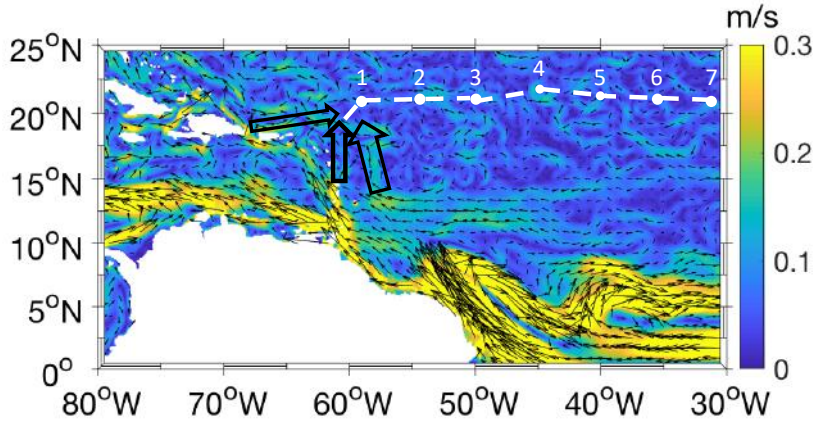

Figure S3. Current velocity field (mean over the first 100 m) during the time of the GApr08 cruise extracted from the global reanalysis GLORYS12V1 (1/12° horizontal resolution, 50 vertical levels), a CMEMS product. Black arrows highlight current pathways reaching station 1.

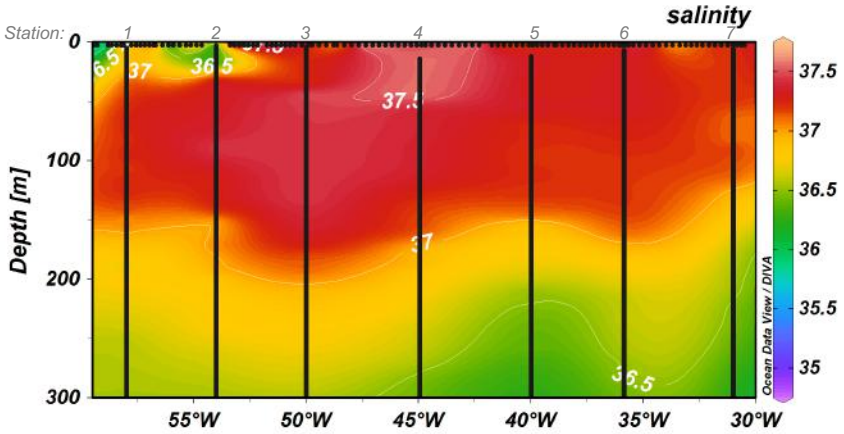

Figure S4. First 300 m of the salinity section measured along the GApr08 cruise. Data points (Fish plus bottle data) are represented by black dots.

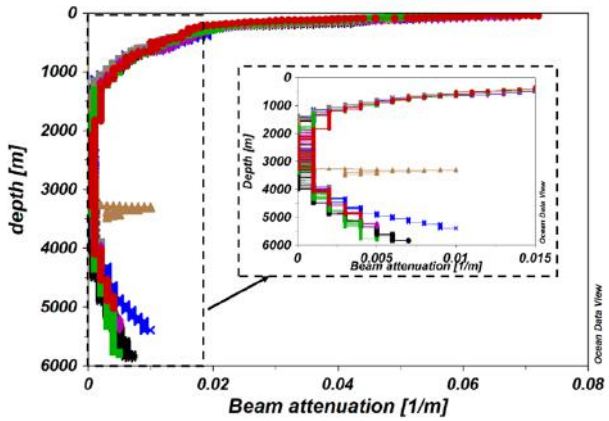

Figure S5. Full depth beam attenuation profiles of the seven JC150 stations with a zoom for values lower than 0,015 m-1.

Acronym	Name	dAl (nmol/kg)	Data sources
WNACW	West North Atlantic Central Water	26.780 ± 0.508	GA02 station 18, 22/05/2010, 33.433°N, 58.05°W, 251m
ESACW	East South Atlantic Central Water	3.376 ± 0.222	GA10 station 3, 29/12/2011, 36.348°S, 13.140°E, 497m
MW	Mediterranean Water	33.171	GA03 station 3, 19/10/2010, 35.201°N, 16°W, 986m
AAIW	Antartic Intermediate Water	2.273 ± 0.040	GA02 station 9, 14/03/2011, 32.089°S, 37.459°W, 1001m
UCDW	Upper Circumpolar Deep Water	2.566 ± 0.098	GA02 station 9, 14/03/2011, 32.089°S, 37.459°W, 1501m
LSW	Labrador Sea Water	6.732 ± 0.058	GA02 station 9, 09/05/2010, 51.821°N, 45.732°W, 996m
NEADW	North East Atlantic Deep Water	19.463 ± 0.370	GA02 station 9, 09/05/2010, 51.821°N, 45.732°W, 2512m
NWABW	North West Atlantic Bottom Water	25.395 ± 0.504	GA02 station 9, 09/05/2010, 51.821°N, 45.732°W, 4041m
AABW	Antartic Bottom Water	5.073 ± 0.118	GA02 station 13, 20/03/2011, 17.017°S, 30.599°W, 4889m

Table S1. End member water mass definitions from GEOTRACES cruises used in Artigue et al. (2020) with their respective dissolved aluminum concentrations extracted from the GEOTRACES Intermediate Data Product 2017 (Measures et al., 2015 for GA03; Middag et al., 2015 for GA02; IDP 2017 v2, Schlitzer et al., 2018).

CTD	Date	Depth	Temperature	Salinity	σ_0	γ	Beam attenuation	dAl	Uncertainty (95 %)	Conservative dAl	ΔdAl
	dd/mm/yyyy	m	°C		kg/m3	kg/m3	1/m	nmol/kg	nmol/kg	nmol/kg	nmol/kg
JC150, station 1, 22°N, 58°W, bottom depth = 5441 m											
9	02/07/2017	16	28,06	36,87	23,81	23,80	0,05	48,968	1,015	NaN	NaN
9	02/07/2017	25	27,65	36,95	23,87	23,86	0,05	40,232	0,736	NaN	NaN
9	02/07/2017	40	26,30	37,15	24,66	24,66	0,06	36,726	0,378	NaN	NaN
9	02/07/2017	80	24,85	37,24	25,04	25,04	0,05	37,279	0,774	NaN	NaN
9	02/07/2017	100	24,49	37,24	25,35	25,36	0,05	34,689	1,357	NaN	NaN
9	02/07/2017	121	24,04	37,25	25,35	25,36	0,04	13,599	0,378	NaN	NaN
9	02/07/2017	140	23,13	37,16	25,58	25,60	0,04	30,517	1,004	NaN	NaN
9	02/07/2017	151	22,54	37,05	25,50	25,51	0,04	27,090	0,391	NaN	NaN
9	02/07/2017	175	21,51	36,89	25,67	25,68	0,04	29,575	0,789	NaN	NaN
9	02/07/2017	202	20,24	36,80	26,15	26,18	0,03	27,789	0,378	NaN	NaN
9	02/07/2017	275	18,49	36,57	26,49	26,53	0,02	29,251	0,492	NaN	NaN
9	02/07/2017	351	17,50	36,45	26,65	26,69	0,02	29,068	0,647	25,58	3,49
9	02/07/2017	400	16,71	36,32	26,55	26,59	0,02	33,957	0,378	24,39	9,57
9	02/07/2017	501	14,86	36,02	26,78	26,83	0,01	29,974	2,228	21,51	8,46
9	02/07/2017	551	13,79	35,85	26,87	26,92	0,01	23,244	1,431	19,90	3,34
9	02/07/2017	600	12,61	35,68	26,94	27,00	0,01	18,409	0,378	18,36	0,05
6	30/06/2017	800	8,61	35,15	27,26	27,34	0,01	11,432	0,378	13,65	-2,21
6	30/06/2017	1001	6,35	34,98	27,55	27,67	0,00	17,490	0,378	NaN	NaN
6	30/06/2017	1500	4,42	35,03	27,82	27,96	0,00	13,786	0,459	11,64	2,15
6	30/06/2017	1751	3,93	35,00	27,81	27,94	0,00	14,466	0,378	14,09	0,37
6	30/06/2017	2001	3,56	34,99	27,80	27,94	0,00	16,490	0,378	15,90	0,59
6	30/06/2017	2500	3,01	34,95	27,87	28,04	0,00	19,040	0,463	18,49	0,55
6	30/06/2017	3000	2,67	34,92	27,85	28,03	0,00	19,982	0,378	18,98	1,01
6	30/06/2017	3500	2,40	34,90	27,92	28,16	0,00	21,770	0,584	19,69	2,08
6	30/06/2017	3999	2,29	34,89	27,92	28,16	0,00	23,748	0,378	20,13	3,61
6	30/06/2017	5001	2,03	34,85	27,89	28,15	0,01	18,252	0,491	16,65	1,60
6	30/06/2017	5351	1,98	34,84	27,89	28,15	0,01	16,423	0,378	15,52	0,90
6	30/06/2017	5402	1,99	34,84	27,89	28,15	0,01	17,515	0,378	15,47	2,05
JC150, station 2, 22°N, 54°W, bottom depth = 5868 m											
17	06/07/2017	15	27,69	36,34	23,41	23,40	0,06	35,300	1,510	NaN	NaN
17	06/07/2017	26	27,79	36,99	23,89	23,89	0,07	34,179	0,414	NaN	NaN
17	06/07/2017	41	26,66	37,33	24,47	24,47	0,07	32,299	0,378	NaN	NaN
17	06/07/2017	80	24,89	37,39	25,16	25,16	0,05	28,942	0,411	NaN	NaN
17	06/07/2017	120	23,81	37,30	25,39	25,40	0,04	33,119	0,378	NaN	NaN
17	06/07/2017	151	22,32	37,03	25,78	25,79	0,04	28,178	0,544	NaN	NaN
17	06/07/2017	181	21,08	37,00	26,03	26,05	0,03	21,840	0,411	NaN	NaN
17	06/07/2017	225	19,62	36,78	26,14	26,16	0,02	22,212	0,378	NaN	NaN
17	06/07/2017	275	18,47	36,64	26,54	26,58	0,02	23,299	0,378	NaN	NaN
17	06/07/2017	325	17,29	36,44	26,64	26,68	0,02	20,237	0,378	25,80	-5,56
17	06/07/2017	400	15,55	36,14	26,64	26,69	0,02	21,447	0,378	22,58	-1,13
17	06/07/2017	500	13,90	35,88	26,89	26,94	0,01	18,223	0,942	20,36	-2,14
17	06/07/2017	600	12,24	35,65	27,11	27,16	0,01	17,145	0,512	18,48	-1,33
19	08/07/2017	700	10,58	35,42	27,12	27,19	0,01	12,861	0,378	16,08	-3,22
19	08/07/2017	800	8,16	35,07	27,34	27,43	0,01	11,190	0,378	11,46	-0,27
19	08/07/2017	900	6,80	34,93	27,38	27,48	0,01	9,869	1,022	9,09	0,78
19	08/07/2017	1092	5,87	34,94	27,52	27,64	0,00	10,502	0,378	8,46	2,04
19	08/07/2017	1500	4,81	35,02	27,71	27,83	0,00	13,493	1,815	10,56	2,93
19	08/07/2017	2002	3,80	35,01	27,81	27,95	0,00	16,238	0,420	16,35	-0,11
19	08/07/2017	2501	3,08	34,96	27,87	28,05	0,00	19,308	1,509	18,32	0,99
19	08/07/2017	3000	2,77	34,93	27,86	28,04	0,00	20,477	0,378	18,41	2,07
19	08/07/2017	3500	2,53	34,91	27,85	28,03	0,00	20,327	0,378	18,77	1,55
19	08/07/2017	4000	2,32	34,89	27,92	28,16	0,00	19,714	0,526	18,73	0,99
19	08/07/2017	5000	2,02	34,85	27,89	28,15	0,00	17,123	0,378	16,50	0,62
19	08/07/2017	5808	2,07	34,84	27,90	28,16	0,01	17,252	0,378	15,94	1,31
19	08/07/2017	5856	2,08	34,84	27,90	28,16	0,01	15,954	0,378	15,79	0,16
JC150, station 3, 22°N, 50°W, bottom depth = 4390 m											
27	14/07/2017	16	27,18	37,25	24,42	24,42	0,06	29,502	0,524	NaN	NaN
27	14/07/2017	25	27,18	37,25	24,42	24,42	0,06	30,018	0,440	NaN	NaN
27	14/07/2017	41	25,95	37,45	24,88	24,89	0,06	27,944	0,580	NaN	NaN
27	14/07/2017	80	24,12	37,44	25,50	25,51	0,05	26,786	0,498	NaN	NaN
27	14/07/2017	121	23,64	37,44	25,50	25,51	0,04	26,153	0,378	NaN	NaN
27	14/07/2017	130	23,55	37,44	25,50	25,51	0,04	26,843	0,378	NaN	NaN
27	14/07/2017	160	23,05	37,36	25,74	25,75	0,03	24,300	0,378	NaN	NaN
27	14/07/2017	199	21,28	37,05	26,07	26,09	0,03	23,107	0,639	NaN	NaN
27	14/07/2017	250	19,26	36,76	26,38	26,41	0,02	23,894	0,568	NaN	NaN
27	14/07/2017	301	17,97	36,56	26,48	26,52	0,02	24,715	0,378	NaN	NaN
27	14/07/2017	326	17,49	36,47	26,66	26,70	0,02	22,503	0,378	26,18	-3,67
27	14/07/2017	400	16,39	36,27	26,75	26,79	0,02	23,204	0,378	23,87	-0,66
27	14/07/2017	451	15,30	36,09	26,83	26,88	0,01	22,019	0,378	21,91	0,11
27	14/07/2017	551	13,36	35,80	27,04	27,09	0,01	18,682	1,231	19,77	-1,09
28	15/07/2017	600	12,43	35,68	27,14	27,19	0,01	17,444	0,807	18,81	-1,37
28	15/07/2017	700	10,79	35,46	27,16	27,22	0,01	15,330	1,118	17,32	-1,99
28	15/07/2017	799	9,06	35,26	27,34	27,41	0,01	14,497	0,378	15,93	-1,43
28	15/07/2017	900	7,38	35,06	27,48	27,58	0,00	12,530	0,378	11,04	1,49
28	15/07/2017	1100	5,89	35,00	27,57	27,68	0,00	12,014	0,378	10,74	1,28
28	15/07/2017	1500	4,69	35,05	27,73	27,85	0,00	14,314	0,439	11,31	3,01
28	15/07/2017	1751	4,14	35,03	27,83	27,96	0,00	17,502	2,517	14,88	2,62
28	15/07/2017	2001	3,63	35,00	27,81	27,95	0,00	21,422	0,378	16,63	4,80
28	15/07/2017	2500	3,00	34,95	27,87	28,04	0,00	19,864	0,378	18,15	1,71
28	15/07/2017	2999	2,66	34,92	27,85	28,03	0,00	20,693	1,141	18,25	2,44
28	15/07/2017	3500	2,42	34,90	27,92	28,16	0,00	20,374	0,596	17,93	2,45
28	15/07/2017	3999	2,23	34,88	27,91	28,15	0,00	20,487	0,437	17,55	2,94
28	15/07/2017	4319	2,18	34,87	27,91	28,15	0,00	19,751	0,649	17,38	2,38
28	15/07/2017	4358	2,18	34,87	27,91	28,15	0,00	19,436	0,444	17,36	2,08

JC150, station 4, 23.367°N, 44.95°W, bottom depth = 3511 m											
32	18/07/2017	14	26,39	37,56	24,97	24,97	0,06	25,466	0,617	NaN	NaN
32	18/07/2017	26	26,39	37,56	24,97	24,98	0,06	25,381	0,414	NaN	NaN
32	18/07/2017	41	26,39	37,56	24,97	24,98	0,06	25,018	0,378	NaN	NaN
32	18/07/2017	101	23,43	37,37	25,74	25,76	0,05	23,956	0,616	NaN	NaN
32	18/07/2017	130	22,58	37,26	25,66	25,68	0,04	21,288	0,380	NaN	NaN
32	18/07/2017	150	21,96	37,17	25,88	25,90	0,04	22,334	0,378	NaN	NaN
32	18/07/2017	180	20,46	36,94	26,25	26,28	0,03	20,382	0,378	NaN	NaN
32	18/07/2017	225	18,94	36,71	26,35	26,38	0,02	21,927	0,447	NaN	NaN
32	18/07/2017	274	17,83	36,53	26,46	26,50	0,02	23,399	0,378	26,83	-3,44
32	18/07/2017	326	16,79	36,35	26,57	26,61	0,02	20,918	2,162	24,60	-3,68
32	18/07/2017	400	15,44	36,12	26,85	26,90	0,02	16,224	0,995	22,18	-5,96
32	18/07/2017	451	14,79	36,02	26,78	26,83	0,01	20,413	0,378	21,41	-1,00
32	18/07/2017	550	12,98	35,75	26,99	27,05	0,01	19,074	0,586	19,35	-0,28
31	18/07/2017	700	10,10	35,38	27,26	27,33	0,01	14,069	0,378	16,69	-2,62
31	18/07/2017	800	8,37	35,16	27,42	27,50	0,01	12,509	0,378	13,05	-0,54
31	18/07/2017	900	7,25	35,05	27,47	27,57	0,00	12,090	0,378	11,55	0,54
31	18/07/2017	1250	5,46	35,00	27,69	27,81	0,00	11,954	0,565	9,42	2,53
31	18/07/2017	1500	4,80	35,05	27,74	27,85	0,00	14,224	0,378	10,95	3,27
31	18/07/2017	1750	4,24	35,05	27,84	27,97	0,00	15,148	0,378	14,41	0,74
31	18/07/2017	2001	3,63	35,00	27,81	27,95	0,00	17,740	0,378	16,63	1,11
31	18/07/2017	2250	3,25	34,97	27,88	28,05	0,00	19,881	0,378	17,48	2,40
31	18/07/2017	2501	3,06	34,96	27,87	28,05	0,00	21,291	1,017	17,86	3,43
31	18/07/2017	3000	2,76	34,93	27,86	28,04	0,00	23,194	0,378	17,98	5,21
31	18/07/2017	3320	2,62	34,92	27,85	28,04	0,01	24,988	0,596	17,92	7,07
31	18/07/2017	3340	2,62	34,92	27,85	28,04	0,01	25,022	0,378	17,93	7,09
31	18/07/2017	3400	2,58	34,91	27,85	28,03	0,00	28,301	0,378	17,91	10,39
31	18/07/2017	3450	2,56	34,91	27,85	28,03	0,01	30,326	0,378	17,90	12,42
31	18/07/2017	3502	2,53	34,91	27,85	28,03	0,00	32,508	0,378	17,78	14,73
JC150, station 5, 23°N, 40°W, bottom depth = 5399 m											
38	23/07/2017	16	26,16	37,33	24,80	24,80	0,06	23,588	0,378	NaN	NaN
38	23/07/2017	26	26,01	37,32	24,79	24,79	0,06	23,139	0,378	NaN	NaN
38	23/07/2017	41	25,90	37,31	24,78	24,79	0,07	20,567	0,501	NaN	NaN
38	23/07/2017	80	23,37	37,25	25,65	25,67	0,06	17,823	0,394	NaN	NaN
38	23/07/2017	120	21,93	37,23	25,92	25,94	0,05	18,470	0,378	NaN	NaN
38	23/07/2017	140	21,38	37,14	26,14	26,17	0,04	19,628	0,665	NaN	NaN
38	23/07/2017	161	20,08	36,88	26,21	26,24	0,03	17,509	0,525	NaN	NaN
38	23/07/2017	201	18,51	36,62	26,28	26,31	0,02	16,934	1,054	NaN	NaN
38	23/07/2017	250	17,13	36,41	26,61	26,65	0,02	16,951	0,378	25,25	-8,30
38	23/07/2017	301	16,24	36,25	26,72	26,77	0,02	18,380	0,378	23,35	-4,97
38	23/07/2017	350	15,57	36,13	26,64	26,68	0,02	17,530	0,378	22,18	-4,65
38	23/07/2017	450	13,97	35,89	26,89	26,94	0,02	17,537	0,771	20,25	-2,72
38	23/07/2017	551	12,28	35,66	27,12	27,17	0,01	16,414	0,378	18,76	-2,35
37	23/07/2017	699	10,22	35,41	27,29	27,36	0,01	15,338	0,784	17,17	-1,83
37	23/07/2017	800	8,65	35,23	27,32	27,40	0,01	13,521	0,592	14,05	-0,53
37	23/07/2017	900	7,42	35,11	27,53	27,62	0,01	12,546	0,628	11,58	0,97
37	23/07/2017	1100	6,17	35,06	27,61	27,72	0,00	12,091	0,480	10,46	1,63
37	23/07/2017	1501	4,99	35,07	27,75	27,87	0,00	15,868	0,386	11,55	4,32
37	23/07/2017	1750	4,36	35,05	27,84	27,97	0,00	14,856	0,450	14,50	0,36
37	23/07/2017	2001	3,80	35,02	27,82	27,96	0,00	16,005	0,528	16,76	-0,76
37	23/07/2017	2500	3,15	34,97	27,88	28,05	0,00	17,127	0,378	18,53	-1,40
37	23/07/2017	3000	2,80	34,94	27,87	28,04	0,00	18,478	0,378	18,72	-0,24
37	23/07/2017	3500	2,54	34,91	27,85	28,04	0,00	21,630	0,826	18,48	3,15
37	23/07/2017	4000	2,43	34,90	27,92	28,16	0,00	19,332	0,378	18,10	1,23
37	23/07/2017	4501	2,37	34,89	27,92	28,16	0,00	21,841	0,402	17,79	4,05
37	23/07/2017	4700	2,37	34,88	27,92	28,16	0,00	19,537	0,489	17,70	1,84
37	23/07/2017	4999	2,38	34,88	27,92	28,17	0,00	19,787	0,378	17,57	2,22
37	23/07/2017	5341	2,41	34,88	27,92	28,17	0,01	19,883	0,378	17,42	2,46
37	23/07/2017	5376	2,41	34,88	27,92	28,17	0,01	18,888	0,378	17,45	1,44

JC150, station 6, 22.33°N, 35.87°W, bottom depth = 5820 m											
48	01/08/2017	15	25,41	37,32	25,10	25,11	0,06	23,545	0,378	NaN	NaN
48	01/08/2017	25	25,41	37,32	25,10	25,11	0,06	15,534	0,378	NaN	NaN
48	01/08/2017	40	25,41	37,32	25,10	25,11	0,06	21,883	0,378	NaN	NaN
48	01/08/2017	80	22,69	37,26	25,66	25,68	0,05	19,783	0,636	NaN	NaN
48	01/08/2017	120	21,59	37,21	25,90	25,93	0,04	19,579	0,378	NaN	NaN
48	01/08/2017	140	21,48	37,20	26,18	26,21	0,04	20,928	0,378	NaN	NaN
48	01/08/2017	180	19,88	36,87	26,20	26,23	0,03	23,512	0,378	NaN	NaN
48	01/08/2017	225	18,35	36,60	26,52	26,56	0,02	23,441	0,514	NaN	NaN
48	01/08/2017	276	17,48	36,50	26,69	26,73	0,02	18,937	0,818	27,18	-8,24
48	01/08/2017	326	16,41	36,32	26,78	26,82	0,02	18,044	0,747	25,05	-7,00
48	01/08/2017	401	14,72	36,01	26,77	26,82	0,01	20,057	0,378	21,45	-1,39
48	01/08/2017	499	13,35	35,80	27,03	27,08	0,01	17,128	0,467	19,57	-2,44
48	01/08/2017	600	11,54	35,56	27,05	27,11	0,01	16,082	0,378	17,90	-1,82
46	31/07/2017	700	10,00	35,39	27,28	27,34	0,01	15,902	1,164	17,26	-1,36
46	31/07/2017	799	8,49	35,22	27,46	27,55	0,01	13,300	0,534	13,21	0,09
46	31/07/2017	900	7,37	35,11	27,52	27,62	0,01	11,948	1,070	11,86	0,08
46	31/07/2017	1000	6,67	35,07	27,49	27,59	0,00	11,510	0,690	11,37	0,14
46	31/07/2017	1100	6,43	35,12	27,66	27,77	0,00	12,389	0,378	12,19	0,19
46	31/07/2017	1250	5,64	35,09	27,64	27,75	0,00	12,881	0,405	12,19	0,69
46	31/07/2017	1500	4,97	35,11	27,78	27,89	0,00	13,726	0,490	13,09	0,64
46	31/07/2017	1751	4,28	35,05	27,85	27,98	0,00	13,748	0,642	15,23	-1,48
46	31/07/2017	2000	3,74	35,01	27,82	27,95	0,00	15,070	0,378	16,95	-1,88
46	31/07/2017	2251	3,34	34,98	27,89	28,06	0,00	15,243	0,378	17,63	-2,39
46	31/07/2017	2501	3,13	34,96	27,88	28,05	0,00	16,548	0,668	18,39	-1,84
46	31/07/2017	3000	2,74	34,94	27,86	28,04	0,00	18,139	0,378	18,68	-0,54
46	31/07/2017	3500	2,50	34,91	27,93	28,16	0,00	19,540	0,590	18,35	1,19
46	31/07/2017	4000	2,40	34,90	27,92	28,16	0,00	20,167	0,670	18,01	2,16
46	31/07/2017	4500	2,38	34,89	27,92	28,16	0,00	20,111	0,649	17,76	2,35
46	31/07/2017	4699	2,39	34,89	27,92	28,17	0,00	20,318	0,378	17,68	2,64
46	31/07/2017	5000	2,39	34,88	27,92	28,17	0,00	20,005	0,633	17,60	2,40
46	31/07/2017	5250	2,41	34,88	27,92	28,17	0,00	19,910	0,633	17,49	2,42
46	31/07/2017	5400	2,42	34,88	27,92	28,18	0,00	19,361	0,744	17,48	1,89
46	31/07/2017	5601	2,44	34,88	27,92	28,18	0,00	19,453	0,385	17,49	1,96
46	31/07/2017	5773	2,46	34,88	27,92	28,18	0,00	19,384	0,378	17,39	1,99
46	31/07/2017	5803	2,46	34,88	27,92	28,18	0,01	19,306	0,480	17,35	1,95
JC150, station 7, 22°N, 31°W, bottom depth = 5020 m											
52	06/08/2017	15	25,41	37,22	25,03	25,03	0,06	12,976	0,819	NaN	NaN
52	06/08/2017	30	25,39	37,22	25,03	25,03	0,07	13,016	0,378	NaN	NaN
52	06/08/2017	41	25,21	37,22	25,02	25,03	0,07	13,959	0,378	NaN	NaN
52	06/08/2017	80	21,81	37,12	25,83	25,86	0,05	13,771	0,378	NaN	NaN
52	06/08/2017	90	21,65	37,18	25,88	25,90	0,04	17,027	0,407	NaN	NaN
52	06/08/2017	111	21,24	37,13	26,13	26,16	0,04	16,990	0,378	NaN	NaN
52	06/08/2017	141	19,80	36,87	26,20	26,23	0,03	17,400	0,378	NaN	NaN
52	06/08/2017	180	18,28	36,60	26,51	26,55	0,02	21,328	0,378	NaN	NaN
52	06/08/2017	225	17,42	36,47	26,66	26,70	0,02	20,536	0,378	26,24	-5,71
52	06/08/2017	275	16,48	36,32	26,78	26,82	0,02	19,933	0,378	24,86	-4,93
52	06/08/2017	325	15,37	36,11	26,84	26,89	0,02	16,923	0,578	22,15	-5,22
52	06/08/2017	400	13,92	35,85	26,86	26,92	0,01	15,862	0,447	19,09	-3,23
52	06/08/2017	451	13,19	35,77	27,00	27,06	0,01	16,502	0,658	19,00	-2,50
54	08/08/2017	550	11,67	35,57	27,05	27,11	0,01	15,095	0,785	17,68	-2,58
54	08/08/2017	700	9,27	35,27	27,35	27,42	0,01	13,394	1,398	15,32	-1,93
54	08/08/2017	900	6,81	35,00	27,44	27,54	0,01	10,837	0,664	10,13	0,70
54	08/08/2017	1100	6,35	35,09	27,64	27,75	0,00	13,519	0,514	11,97	1,55
54	08/08/2017	1500	4,98	35,08	27,76	27,87	0,00	15,953	1,061	11,75	4,21
54	08/08/2017	2001	3,81	35,02	27,83	27,96	0,00	15,302	0,522	16,98	-1,68
54	08/08/2017	2500	3,13	34,97	27,89	28,06	0,00	16,696	0,835	18,88	-2,18
54	08/08/2017	3000	2,71	34,93	27,86	28,04	0,00	18,718	0,378	18,58	0,14
54	08/08/2017	3500	2,49	34,91	27,93	28,16	0,00	20,634	0,433	18,21	2,42
54	08/08/2017	4000	2,38	34,89	27,92	28,16	0,00	22,123	0,378	17,78	4,34
54	08/08/2017	4500	2,38	34,89	27,92	28,16	0,00	22,933	0,378	17,60	5,34
54	08/08/2017	4748	2,40	34,89	27,92	28,17	0,00	20,430	0,378	17,61	2,81
54	08/08/2017	4999	2,42	34,88	27,92	28,17	0,00	20,564	0,467	17,51	3,05
54	08/08/2017	5014	2,42	34,88	27,92	28,17	0,00	20,351	0,611	17,43	2,92

Table S2. Bottle data from the GApr08 cruise. dAl uncertainties are given at the 95% confidence level. NAN : no data available. Calculated 'conservative' dAl, and 'biogeochemical' dAl are included; see text for details.

Sample number	Station	Date	Latitude	Longitude	Temperature	Salinity	dAl	Uncertainty (95 %)
		dd/mm/yyyy	°N	°W	°C		nmol/kg	nmol/kg
Fish 005	1	27/06/2017	18,56	59,61	28,38	34,77	33,980	2,875
Fish 006	1	28/06/2017	18,88	59,46	28,16	35,80	33,730	0,462
Fish 007	1	28/06/2017	19,23	59,30	28,06	35,83	34,573	0,978
Fish 008	1	28/06/2017	20,26	58,82	28,08	35,99	34,682	0,378
Fish 009	1	28/06/2017	20,60	58,66	27,85	36,21	35,198	0,711
Fish 010	1	28/06/2017	20,89	58,43	27,93	36,77	35,835	0,814
Fish 011	1	28/06/2017	21,06	58,25	28,02	37,14	42,026	0,378
Fish 012	1	29/06/2017	21,29	58,19	28,05	37,05	38,710	0,378
Fish 013	1	29/06/2017	21,57	58,12	28,09	36,95	38,494	0,378
Fish 017	1	03/07/2017	22,00	57,78	28,20	36,92	37,954	1,498
Fish 018	1	03/07/2017	22,00	57,58	28,15	36,91	43,310	0,849
Fish 019	1	03/07/2017	22,00	57,37	28,19	37,02	39,733	0,659
Fish 020	1	04/07/2017	22,00	57,17	28,13	37,00	38,751	1,362
Fish 021	1	04/07/2017	22,00	56,97	28,05	37,04	36,547	0,544
Fish 022	1	04/07/2017	22,00	56,78	28,07	37,03	40,512	0,700
Fish 023	1,5	04/07/2017	22,00	56,69	27,98	37,07	39,470	3,162
Fish 024	1,5	04/07/2017	22,00	56,39	27,83	36,64	40,008	0,381
Fish 025	1,5	04/07/2017	22,00	56,13	27,81	36,28	40,297	0,378
Fish 026	1,5	04/07/2017	22,00	55,91	27,89	36,30	38,466	2,648
Fish 027	1,5	04/07/2017	22,00	55,63	27,94	36,55	38,913	0,378
Fish 028	1,5	04/07/2017	22,00	55,35	27,97	36,79	38,946	0,616
Fish 029	1,5	04/07/2017	22,00	55,13	28,01	36,91	43,103	0,645
Fish 030	1,5	04/07/2017	22,00	54,88	27,94	36,83	38,422	0,814
Fish 031	1,5	04/07/2017	22,00	54,64	27,89	36,85	35,336	0,485
Fish 036	2	11/07/2017	22,00	53,39	27,34	37,42	29,384	0,594
Fish 037	2	11/07/2017	22,00	53,18	27,44	37,41	29,747	0,378
Fish 038	2	11/07/2017	22,00	52,98	27,47	37,41	28,943	1,591
Fish 039	2	11/07/2017	22,00	52,78	27,52	37,41	28,760	0,784
Fish 040	2	11/07/2017	22,00	52,57	27,46	37,41	29,715	1,019
Fish 041	2	11/07/2017	22,00	52,37	27,31	37,41	30,622	0,574
Fish 042	2	11/07/2017	22,00	52,16	27,34	37,52	28,313	0,378
Fish 044	2	11/07/2017	22,00	51,74	27,19	37,46	26,898	0,378
Fish 045	2	11/07/2017	22,00	51,54	27,16	37,56	26,781	0,378
Fish 046	2	12/07/2017	22,00	51,33	27,08	37,51	26,069	0,431
Fish 047	2	12/07/2017	22,01	51,13	27,10	37,51	26,343	0,378
Fish 048	2	12/07/2017	22,01	50,92	27,14	37,56	30,284	0,378
Fish 049	2	12/07/2017	22,00	50,72	27,11	37,61	29,186	1,615
Fish 050	2	12/07/2017	22,00	50,51	27,17	37,31	27,398	0,796
Fish 051	3	12/07/2017	22,00	50,19	27,19	37,24	27,843	0,745
Fish 053	3	15/07/2017	22,03	49,89	27,35	37,35	30,112	0,378
Fish 054	3	15/07/2017	22,07	49,73	27,45	37,38	28,413	0,544
Fish 055	3	15/07/2017	22,15	49,44	27,36	37,32	28,432	0,414
Fish 056	3	16/07/2017	22,24	49,12	27,33	37,07	29,693	0,378
Fish 057	3	16/07/2017	22,33	48,80	27,34	37,04	28,429	0,674
Fish 058	3	16/07/2017	22,37	48,63	27,31	37,07	28,048	0,378
Fish 059	3	16/07/2017	22,46	48,31	27,19	37,22	27,414	0,667
Fish 060	3	16/07/2017	22,55	47,98	27,04	37,33	26,908	0,679
Fish 061	3	16/07/2017	22,64	47,66	26,69	37,64	21,523	0,406
Fish 062	3	16/07/2017	22,72	47,35	26,61	37,57	22,052	0,620
Fish 063	3	16/07/2017	22,80	47,05	26,55	37,61	22,378	0,461
Fish 064	3	16/07/2017	22,88	46,77	26,60	37,60	22,072	0,378
Fish 065	3	16/07/2017	22,95	46,48	26,64	37,58	21,704	0,378
Fish 066	3	16/07/2017	23,03	46,19	26,56	37,62	22,908	0,573
Fish 067	3	16/07/2017	23,11	45,91	26,85	37,38	24,905	0,378
Fish 068	3	16/07/2017	23,18	45,63	26,78	37,45	23,700	0,794
Fish 069	3	17/07/2017	23,26	45,34	26,53	37,54	22,859	0,882
Fish 070	4	17/07/2017	23,33	45,09	26,55	37,56	25,624	0,660
Fish 071	4	20/07/2017	23,36	44,87	26,79	37,48	23,702	0,378
Fish 072	4	20/07/2017	23,35	44,70	26,84	37,47	24,082	0,378
Fish 073	4	20/07/2017	23,33	44,43	26,72	37,53	25,933	0,378
Fish 074	4	20/07/2017	23,31	44,13	26,67	37,55	25,747	0,378
Fish 075	4	21/07/2017	23,28	43,82	26,61	37,50	22,738	0,399

Fish 076	4	21/07/2017	23,26	43,51	26,52	37,51	23,970	0,378
Fish 077	4	21/07/2017	23,24	43,21	26,35	37,57	22,314	0,448
Fish 078	4	21/07/2017	23,22	42,91	26,23	37,57	21,380	0,584
Fish 079	4	21/07/2017	23,19	42,62	26,13	37,56	20,813	0,378
Fish 080	4	21/07/2017	23,17	42,32	25,92	37,56	23,717	0,634
Fish 082	4	21/07/2017	23,13	41,74	26,07	37,29	20,993	0,469
Fish 083	4	21/07/2017	23,11	41,47	26,21	37,26	22,020	0,456
Fish 084	4	21/07/2017	23,09	41,20	26,18	37,19	22,562	0,492
Fish 085	4	21/07/2017	23,07	40,93	26,16	37,24	21,822	0,550
Fish 086	4	21/07/2017	23,05	40,65	26,14	37,21	22,205	0,582
Fish 087	4	22/07/2017	23,03	40,36	26,16	37,22	22,595	0,378
Fish 088	5	22/07/2017	23,01	40,11	26,02	37,21	22,496	0,378
Fish 089	5	25/07/2017	22,99	39,93	26,18	37,29	22,762	0,403
Fish 090	5	25/07/2017	22,95	39,72	26,15	37,28	21,418	0,428
Fish 091	5	25/07/2017	22,92	39,50	26,06	37,26	21,186	0,546
Fish 092	5	25/07/2017	22,88	39,25	26,05	37,27	16,572	0,378
Fish 093	5	26/07/2017	22,83	38,97	25,99	37,24	21,435	0,378
Fish 094	5	26/07/2017	22,82	38,87	25,96	37,28	21,494	0,378
Fish 095	5	26/07/2017	22,77	38,61	25,93	37,28	21,790	0,378
Fish 096	5	26/07/2017	22,73	38,34	25,99	37,22	21,570	1,706
Fish 097	5	26/07/2017	22,69	38,09	25,96	37,24	22,207	0,390
Fish 098	5	26/07/2017	22,65	37,83	25,92	37,24	22,558	0,585
Fish 099	5	26/07/2017	22,61	37,57	25,81	37,30	20,922	0,378
Fish 100	5	26/07/2017	22,57	37,32	25,85	37,29	21,473	0,515
Fish 101	5	26/07/2017	22,52	37,07	26,00	37,24	23,278	0,378
Fish 102	5	26/07/2017	22,48	36,81	26,03	37,22	22,060	0,378
Fish 103	5	26/07/2017	22,44	36,55	25,88	37,23	21,777	0,378
Fish 104	5	26/07/2017	22,40	36,31	25,68	37,22	19,995	0,378
Fish 105	5	27/07/2017	22,36	36,07	25,65	37,21	21,252	0,378
Fish 108	6	02/08/2017	22,33	35,84	25,65	37,34	18,021	0,378
Fish 109	6	02/08/2017	22,32	35,67	25,55	37,42	17,105	0,378
Fish 110	6	02/08/2017	22,30	35,45	25,65	37,37	16,941	0,412
Fish 111	6	02/08/2017	22,28	35,18	25,52	37,40	16,594	0,438
Fish 112	6	02/08/2017	22,26	34,88	25,49	37,41	17,547	0,378
Fish 113	6	03/08/2017	22,24	34,59	25,53	37,28	17,878	0,378
Fish 114	6	03/08/2017	22,22	34,30	25,72	37,15	19,294	0,378
Fish 115	6	03/08/2017	22,21	34,01	25,72	37,12	19,281	0,378
Fish 116	6	03/08/2017	22,18	33,71	25,68	37,07	20,319	0,425
Fish 117	6	03/08/2017	22,16	33,40	25,56	37,09	17,629	0,378
Fish 118	6	03/08/2017	22,15	33,13	25,49	36,99	13,629	0,378
Fish 119	6	03/08/2017	22,13	32,88	25,45	37,21	14,693	0,378
Fish 120	6	03/08/2017	22,11	32,63	25,58	37,13	16,523	0,378
Fish 121	6	03/08/2017	22,09	32,37	25,71	37,12	16,815	0,378
Fish 122	6	03/08/2017	22,07	32,09	25,70	37,13	18,712	0,744
Fish 123	6	03/08/2017	22,06	31,82	25,50	37,34	16,577	0,378
Fish 124	6	03/08/2017	22,04	31,54	25,51	37,19	14,853	0,378
Fish 125	6	04/08/2017	22,02	31,26	25,52	37,21	14,415	0,378
Fish 126	7	04/08/2017	22,01	31,08	25,32	37,22	12,971	0,530
Fish 127	7	08/08/2017	22,01	30,98	25,78	37,21	15,724	0,378
Fish 128	7	08/08/2017	22,07	30,84	25,67	37,19	14,016	0,404
Fish 129	7	08/08/2017	22,14	30,67	25,69	37,26	15,688	0,378
Fish 130	7	08/08/2017	22,21	30,51	25,74	37,29	15,632	0,378

Table S3. Towed fish data from the GApr08 cruise. Samples were taken at 2-3 m off the starboard side of the ship. dAl uncertainties are given at the 95% confidence level.

3.3 Conclusion

Dans le contexte de la campagne GApr08, nos mesures de dAl renseignent sur les apports lithogéniques des autres éléments traces fer et zinc mesurés au cours de cette campagne par des membres de l'Université de Southampton, National Oceanographic Center (NOC).
Dans un contexte plus global, cette étude souligne l'importance de prendre en compte les processus de transport de masse d'eau pour interpréter les distributions de dAl dans la colonne d'eau à l'échelle locale et à celle du bassin. Premièrement, dans les régions où les gradients horizontaux et les flux sont importants (en particulier dans les couches de surface), le processus d'advection est significatif et ne doit pas être négligé. Deuxièmement, en supprimant la partie du signal de dAl due au transport par les masses d'eau, nous avons acquis de nouvelles connaissances sur le cycle biogéochimique de dAl de l'Atlantique Nord subtropical :
- De manière paradoxale, sous les forts dépôts atmosphériques saharien, nous suggérons, qu'à l'échelle du bassin, le bilan net dans les 1000 premiers mètres est une soustraction d'aluminium dissous (probablement par adsorption sur les particules)
- A l'inverse en profondeur, nous mettons en évidence une source interne d'aluminium dissous, que nous attribuons à une libération depuis les particules, via le processus de scavenging réversible.
L'ensemble de ces connaissances est résumé dans la Figure 16.

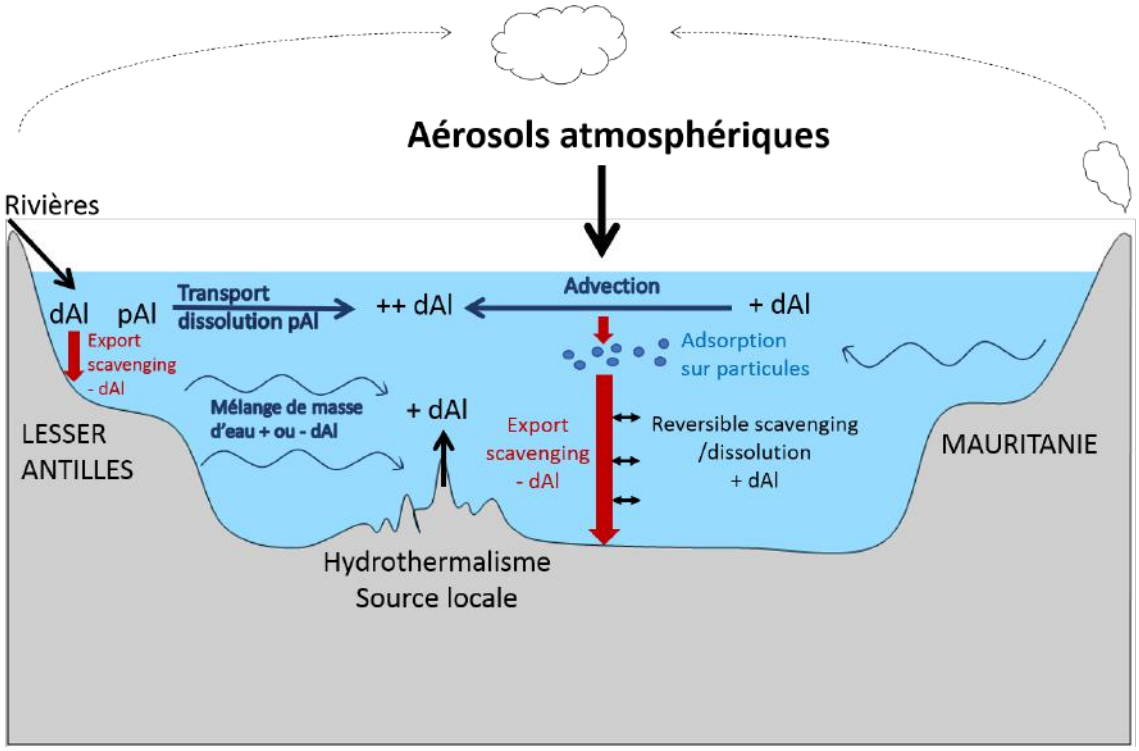

Figure 16 : Schéma illustrant les sources externes et les processus internes du cycle de l'aluminium dissous dans l'Atlantique Nord subtropical le long de la campagne GApr08.

4 Isotopes du fer : Traceurs des cycles biogéochimiques dans une zone naturellement fertilisée de l'océan Austral

4.1 Biogéochimie du fer dans l'océan

Le fer (Fe) est le quatrième élément le plus abondant de la croûte terrestre (3.9 % en masse, Rudnick & Gao, 2014). Tout comme l'aluminium, cet élément est seulement présent à l'état de traces dans l'eau de mer, de l'ordre du nanomolaire (10^{-9} mol/L). Le cycle du fer est beaucoup plus complexe que celui de l'aluminium du fait qu'il existe de nombreuses sources externes de fer à l'océan mais aussi de nombreux processus dans lesquels le fer est impliqué.

4.1.1 Spéciation physico-chimique

Le fer existe sous différentes formes physiques, chimiques et biologiques (différentes spéciations). La Figure 17 schématise ces différentes spéciations.
En termes de spéciation physique, la fraction particulaire est généralement considérée comme celle qui se dépose sur un filtre de porosité 0.2 à 0.4 µm. La fraction colloïdale est la fraction comprise entre 0.4/0.2 µm et 0.02 µm. La fraction soluble est la fraction qui passe à travers un filtre de porosité 0.02 µm. Les deux fractions, colloïdale et soluble, constituent la fraction dissoute i.e. qui passe à travers un filtre de porosité 0.4 ou 0.2 µm.
On peut également distinguer la spéciation redox (ou inorganique) de la spéciation organique. La spéciation redox sépare le fer suivant ses deux états d'oxydation dans l'eau de mer : le Fe(II) et le Fe(III). Le Fe(II) est la forme la plus soluble de Fe mais la moins stable thermodynamiquement en présence d'oxygène. A l'exception de quelque zones océaniques, l'océan étant un milieu oxydant, le Fe(II) y est rapidement oxydé par le dioxygène ou le peroxyde d'hydrogène avec une vitesse de réaction de l'ordre de la minute (Millero et al., 1987). Les deux espèces inorganiques de Fe(II) les plus abondantes dans l'eau de mer à pH=8 sont (par ordre décroissant) Fe^{2+} et $FeCO_3$ (de Baar & De Jong, 2001). Le Fe(III) est caractérisé par une très faible solubilité. En l'absence d'autres facteurs, le Fe(III) précipiterait rapidement pour former des oxydes et hydroxydes de fer comme $Fe(OH)_3$ (de Baar & De Jong, 2001) et ses concentrations dans l'eau de mer seraient extrêmement faibles. Mais la présence de ligands organiques auxquels le fer est complexé prévient cette précipitation et maintient le fer sous forme dissoute, plus précisément colloïdale (près de 100 % du Fe(III) dissous est complexé avec des ligands organiques, Rue & Bruland, 1995). Ces ligands organiques semblent toujours en excès par rapport au fer dissous (Gerringa et al., 2008). La complexation organique du Fer est par conséquent un acteur majeur de nombreux aspects du cycle biogéochimique du fer dans l'océan (ex. dissolution , précipitation, scavenging, uptake biologique Gledhill & Buck, 2012). Elle permet notamment d'augmenter significativement la solubilité du Fe(III) dans l'eau de mer en le stabilise dans la phase dissoute (Johnson et al.,

1997). Malgré le fait que la complexation organique semble jouer un rôle majeur sur la distribution du Fer dans l'océan, la nature, l'origine et les propriétés chimiques des ligands organiques restent encore peu connues (Bruland & Lohan, 2006).

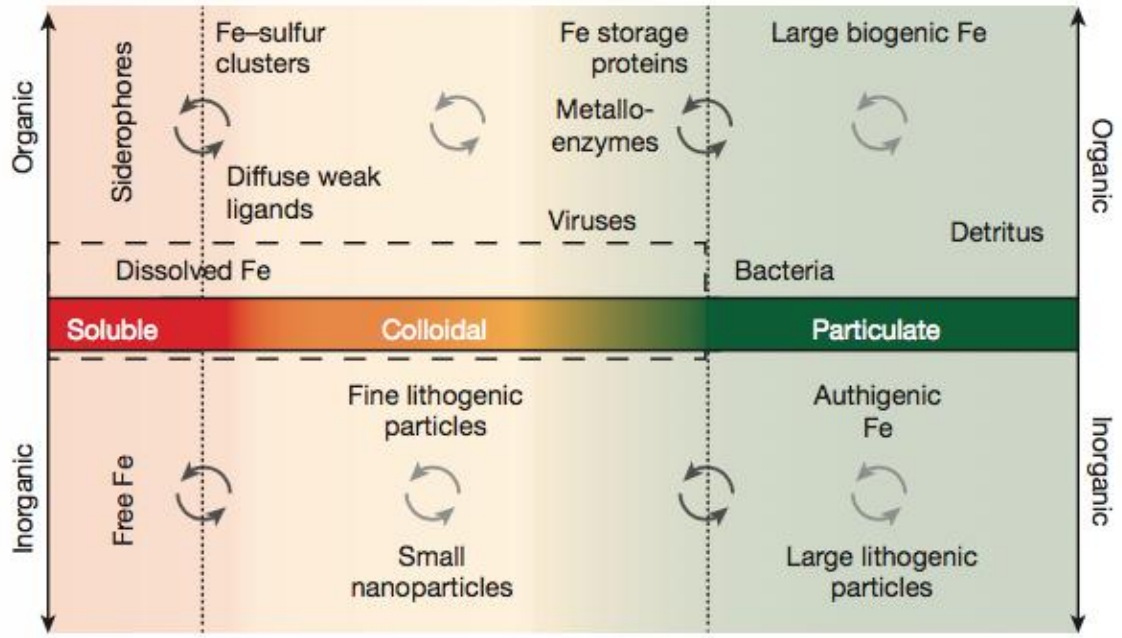

Figure 17 : Spéciation physique, inorganique et organique du Fer (Tagliabue et al., 2017).

4.1.2 Sources externes de Fe à l'océan

La dominance de certaines sources de Fe à l'océan par rapport à d'autres dépend de la région étudiée (Tagliabue et al., 2017).

4.1.2.1 Source atmosphérique

En estimant que les poussières contiennent 3.9 % de fer (Rudnick & Gao, 2014), et que les apports totaux de poussière atmosphériques à l'océan sont de 450 10^{12} g/an (Jickells et al., 2005), les poussières atmosphériques apporteraient 17.6 10^{12} g/an de fer à l'océan. En supposant une solubilité moyenne de 1.15 % de fer contenu dans les aérosols (Bonnet & Guieu, 2004), ce flux correspondrait à 20 10^{10} g/an de fer dissous apporté à l'océan. Du fait de ces fort flux, l'apport de poussières atmosphériques, provenant majoritairement des grands déserts des régions arides et semi-aride, a longtemps été considéré comme la source dominante d'apport de fer à l'océan (Jickells et al., 2005; Tagliabue et al., 2017). Cependant, un certain nombre d'observations et de modélisations suggèrent que les rejets de fer lors des processus de combustion (incluant les combustions anthropiques, la combustion de biocarburants ou de et de matière organique fossile et la combustion de biomasse mondiale) pourraient également constituer une source importante de fer à l'océan de surface (Guieu et al., 2005; Ito et al., 2019; Ito & Shi, 2016; Luo et al., 2008; Sedwick et al., 2007; Sholkovitz et al., 2009). Comme présenté dans l'introduction, les estimations des flux atmosphériques de fer dissous à l'océan sont principalement limitées par des incertitudes sur la solubilité du fer mesuré entre 0.01 % à 80 % (Mahowald et al., 2005 et ses références).

Depuis une quinzaine d'années, de nombreux travaux suggèrent que d'autres sources, notamment l'hydrothermalisme profond et peu profond, sont importantes, voire plus importantes que les dépôts atmosphériques dans certaines régions (ex. Guieu et al., 2018; Resing et al., 2015; Tagliabue et al., 2014).

4.1.2.2 Source fluviale

Avec un flux global à l'océan de fer particulaire et de fer dissous estimé à 625-962 10^{12} g/an et 1.5 10^{12} g/an respectivement, les rivières sont des sources majeures de fer à l'océan (Jickells et al., 2005; Poulton & Raiswell, 2002). Cependant, comme présenté dans l'introduction, il est estimé que près de 90 % du fer dissous serait éliminé dans les estuaires par des processus de floculation et/ou d'adsorption dû à des changements de force ioniques suivi de sédimentation (Boyle et al., 1977). Quant au fer particulaire, bien qu'une grande majorité se dépose sur les marges continentales, une petite partie s'échappe de l'estuaire et est directement transportée vers l'océan ouvert (Slemons et al., 2010) et serait transporté vers les sédiments profonds du talus continental. La remobilisation des particules fluviales qui se sont déposées sur les marges continentales est discutée dans la section suivante.

4.1.2.3 Source sédimentaire

Au cours des deux dernières décennies, de nombreuses études ont révélé l'importance des apports sédimentaires des marges continentales comme source de métaux et de fer à l'océan. L'apport de Fe dissous via les sédiments des marges continentales a été mis en évidence dans de nombreuses régions océaniques : le long et au loin des marges continentales (Abadie et al., 2017; Chase et al., 2005; Elrod et al., 2004; Lam et al., 2006; Radic et al., 2011; Slemons et al., 2010), ou dans le sillage de certaines îles comme les îles Kerguelen (Blain et al., 2008b) ou encore les îles Crozet (Pollard et al., 2009). Cet apport de fer dissous très loin des marges continentales dans les couches de subsurfaces et profondes est dû à des mécanismes d'advection rapide et/ou à la présence de tourbillon (Bowie et al., 2009). Par la suite ce fer peut, grâce au transport vertical (« upwelling »), atteindre les eaux de surfaces et être consommé par le phytoplancton. Moore et Braucher (2008) estiment que le flux total de fer dissous provenant des sédiments est de 179 10^{10} g/an. Ce flux serait donc du même ordre de magnitude (voir supérieur) à celui provenant des poussières atmosphériques. Ces dernières années, l'apport de l'outil isotopique a permis de faire des avancées notables sur la compréhension des processus responsables de ce relargage de fer dissous à l'interface sédiment/eau de mer. Actuellement, les processus sédimentaires identifiés comme pouvant relarguer du Fe à l'océan sont (i) la réduction dissimilatoire du fer (DIR), (ii) la dissolution non réductrice du fer (NRD). La DIR a longtemps été le processus de libération de fer à partir des sédiments le plus étudié et considéré comme étant le plus important. La DIR a lieu au sein de sédiments anoxiques par réduction microbienne du Fe(III) en Fe(II). Le Fe(II) produit dans les sédiments est soluble et sera donc rejeté dans les eaux interstitielles. Une partie de ce Fe(II) diffuse vers le bas et se retrouve piégé par la formation de solides soufrés (FeS, FeS_2). Une autre partie de Fe(II) est diffusée vers le haut et, au contact des eaux poreuses oxygénées, va rapidement s'oxyder en Fe(III) puis former de minéraux amorphes insolubles de Fe-(oxy)hydroxyde. Lorsque la couche de sédiments oxiques est mince, une partie du Fe(II) arrive à s'échapper des sédiments. Ce Fe(II) s'oxyde alors rapidement dans l'eau de

mer oxygénée et précipite en grande partie, mais une autre partie peut être complexée par des ligands organiques et ainsi se stabiliser dans la colonne d'eau (Radic, 2011b; Slomp et al., 1997). La NRD est un processus de libération de Fe dissous par dissolution partielle du sédiment qui n'a été que récemment proposée (Radic, 2011a, 2011b). Ce processus pourrait avoir lieu dans la colonne d'eau et à l'interface sédiment/océan par des mécanismes de désorption et/ou dissolution favorisés par les ligands. Contrairement à la DIR, ce processus serait indépendant de conditions redox au sein de la colonne d'eau (Labatut et al., 2014; Radic et al., 2011a) et des sédiments (Homoky et al., 2013). Ainsi, au vu de l'étendue des marges océaniques, cette source pourrait constituer une des sources majeures de Fe à l'océan voire même la source majeure de Fe à l'océan. Bien que de récentes études d'isotopie du fer s'intéressent à ce processus (Abadie et al., 2017; Conway & John, 2014; Klar et al., 2018; Labatut et al., 2014), cette source reste encore mal contrainte (flux de Fe apporté par NRD à déterminer…).

4.1.2.4 Source hydrothermale

Comme vu dans l'introduction générale, l'hydrothermalisme est une source majeure d'éléments traces dont de fer à l'océan. Cependant cette source de fer dissous a longtemps été considérée comme négligeable du fait de l'oxydation (Fe-oxyhydroxyde) suivi de la précipitation rapide du fer dissous à proximité directe de la cheminé (German et al., 1991). Ainsi le fer dissous provenant des sources hydrothermales était considéré comme n'ayant pas d'impact sur la production primaire. De nombreuses études récentes ont remis en question ce point de vue et montrent que le fer dissous est stabilisé à la sortie de la source hydrothermale par complexation organique ce qui permet son transport sur de longues distances (Fitzsimmons et al., 2014; Sander & Koschinsky, 2011; Yücel et al., 2011). Resing et al (2015) a observé un transport de fer dissous à plus de 4000 km de la source hydrothermale et a estimé un flux hydrothermal de fer dissous à l'océan intérieur de 168 à 223 10^9 g/an. L'intégration de l'hydrothermalisme comme source de fer dans les modèles biogéochimiques a notamment permis de révéler (i) qu'il était crucial de prendre en compte cette source pour expliquer les distributions de fer dissous observées dans l'océan Austral (Tagliabue et al., 2010), (ii) que des moyens de stabilisation physico-chimiques étaient nécessaires pour expliquer le transport observé de fer dissous (Resing et al., 2015), (iii) et que le fer issu des sources hydrothermales soutient une grande partie de la production exportée de l'océan Austral (Resing et al., 2015).

4.1.2.5 Autres sources

A l'échelle locale, d'autres sources comme la fonte des glaces aux hautes latitudes (Raiswell et al., 2008) ou les décharges d'eaux souterraines en zone côtière (Moore, 2010) peuvent avoir un impact significatif sur les distributions de Fe.

4.1.3 Cycle interne du fer dans l'océan

Nous avons vu dans l'introduction que le fer est un micronutriment largement impliqué dans la production primaire en tant que cofacteur enzymatique, dans les différentes étapes du cycle de l'azote, et en tant que transporteur d'électrons au cours des processus de photosynthèse et de respiration (Figure 1, Morel & Price, 2003). Le fer est donc très fortement impacté par l'activité biologique qui constitue (i) un puit de fer dissous dans la couche de surface (euphotique) de l'océan par assimilation phytoplanctonique puis (ii) une source de fer dissous à des profondeurs intermédiaires au cours des processus de reminéralisation.
De nombreux travaux ont décrit que le fer était « scavengé » par différents types de particules tels que les oxydes de ferromanganèses, les argiles minérales, les groupements fonctionnels organiques, des minéraux d'origine atmosphérique ou encore des virus. Des travaux récent Abadie et al (2017) proposent, sur la base de mesures isotopiques, que le fer est soumis non pas simplement à des processus de scavenging mais de reversible scavenging.
Le fer étant impacté par l'activité biologique et le scavenging, il présente dans l'océan un profil dit de type « Hybride » (Figure 18, Bruland & Lohan, 2006).

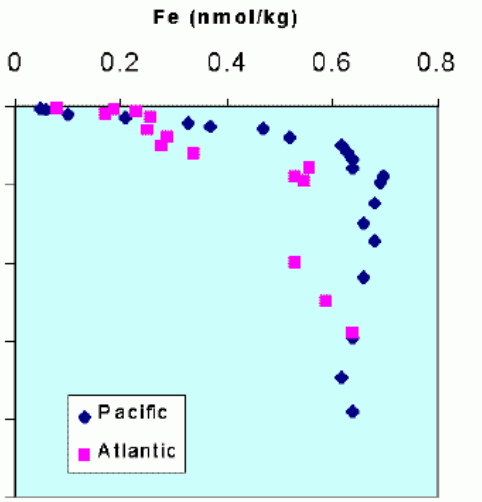

Figure 18 : Profil vertical de type « hybride » des concentrations de fer dissous dans l'Atlantique et le Pacifique ("Periodic Table of Elements in the Ocean," 2015).

La Figure 19 présente l'état actuel des connaissances sur les principaux processus impliqués dans le cycle du fer dans l'océan Atlantique.

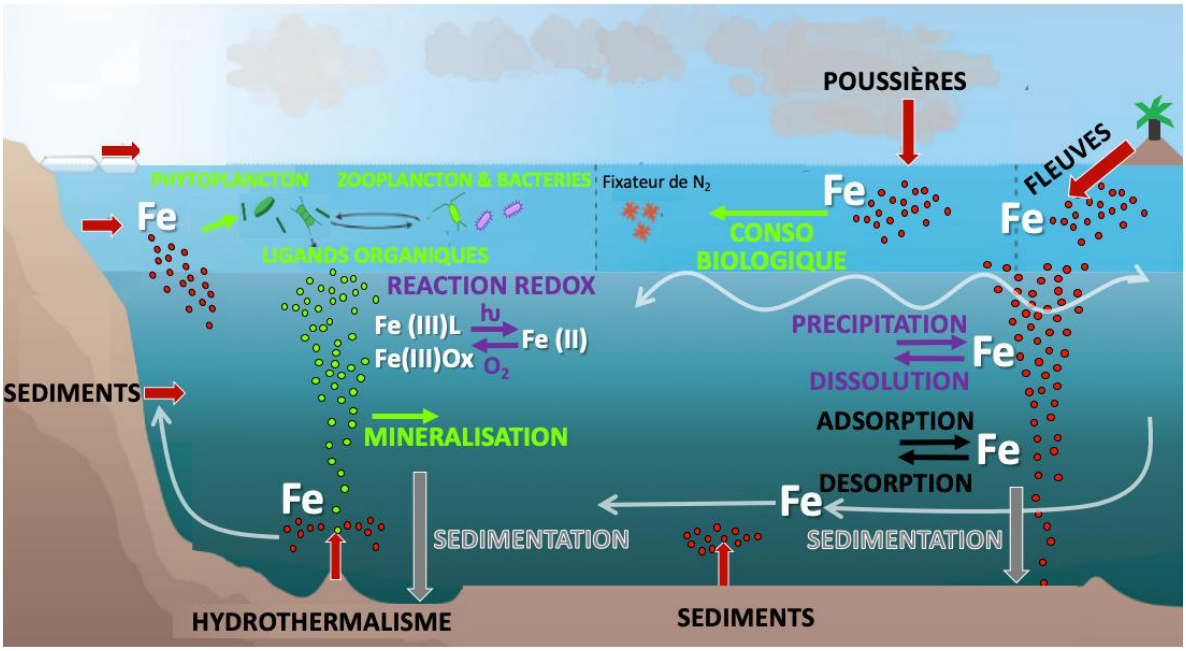

Figure 19 : Représentation de l'état actuel des connaissances sur les principaux processus impliqués dans le cycle du fer dans l'océan Atlantique (adaptée de Tagliabue et al., 2017).

Cependant, les rôles des différents processus biologiques, chimiques et physiques sur le cycle du fer doivent encore être clarifiés (Tagliabue et al., 2017). Dans ce but, l'utilisation de l'outil isotopique permet de fournir de nouvelles informations sur les processus impliqués dans le cycle du fer (Abadie et al., 2017; Conway et al., 2018; Conway & John, 2014; Klar et al., 2017b; Radic et al., 2011a).

4.2 Les isotopes du fer dans l'océan

Le fer possède six isotopes allant de la masse 54 à la masse 60. Quatre d'entre eux sont stables : le ^{54}Fe, ^{56}Fe, ^{57}Fe, et le ^{58}Fe avec une abondance respective de 5.80 %, 91.71 %, 2.20 % et 0.28 % (Figure 20).

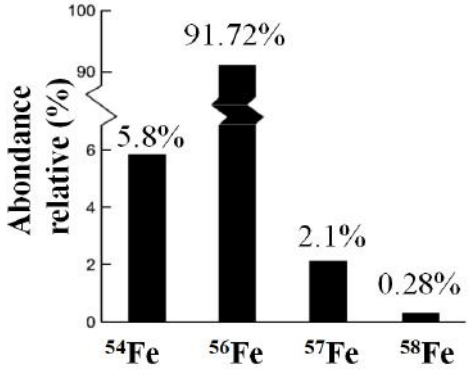

Figure 20 : Abondances relatives des isotopes stables du fer sur terre

Dans cette thèse, la composition isotopique de fer sera toujours exprimée en $\delta^{56}Fe$ qui exprime la déviation du rapport $^{56}Fe/^{54}Fe$ de l'échantillon par rapport à celui d'une référence, ici le standard isotopique du fer certifié IRMM-14 (équation 1, Taylor et al., 1993). Le $\delta^{56}Fe$ s'exprime en ‰.

$$\delta^{56}Fe\ (‰) = \left[\frac{(^{56}Fe/^{54}Fe)_{sample}}{(^{56}Fe/^{54}Fe)_{IRMM\text{-}14}} - 1 \right] \times 10^3 \qquad (1)$$

Les différentes sources de fer possèdent différentes compositions isotopiques ($\delta^{56}Fe$). Elles ne sont pas toujours distinctes. Ainsi, la mesure de $\delta^{56}Fe$ dans l'océan permet de tracer les sources de fer dans une certaine mesure. La Figure 21 synthétise les signatures isotopiques ($\delta^{56}Fe$) des sources de fer à l'océan.

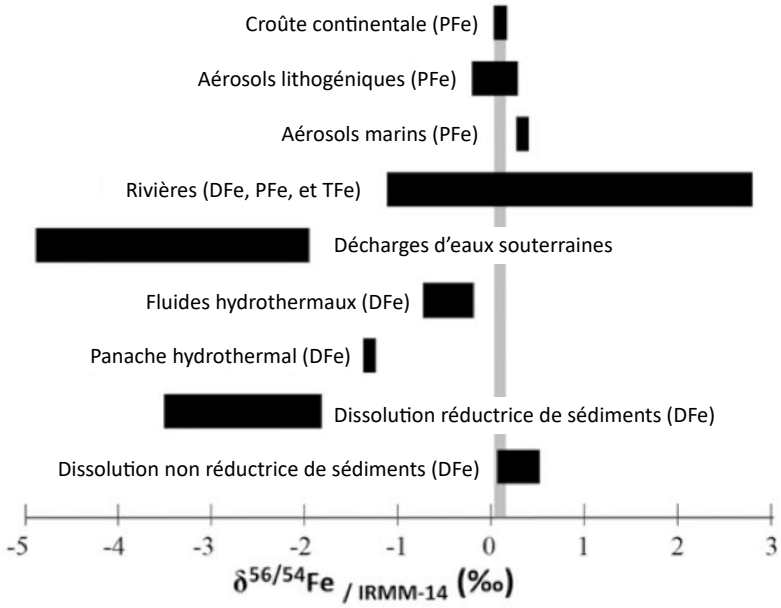

Figure 21 : Composition isotopique (δ^{56}Fe) des sources de fer à l'océan (modifiée de Abadie et al., 2017). Les références utilisées dans la figure sont les suivantes : croûte continentale (Poitrasson, 2006), aérosols lithogéniques (Beard et al., 2003), aérosols marins (Labatut et al., 2014), rivières (Escoube et al., 2015), décharges d'eaux souterraines (Rouxel et al., 2008b), fluides hydrothermaux (Rouxel et al., 2008a), panache hydrothermal (Conway & John, 2014), dissolution réductrice de sédiments (John et al., 2012; Severmann et al., 2010), dissolution non réductrice de sédiments (Homoky et al., 2013; Labatut et al., 2014; Radic et al., 2011a).

Les compositions isotopiques (δ^{56}Fe) des sources internes et externes de fer peuvent être modifiées par des processus de fractionnement isotopique. Le fractionnement isotopique est le transfert préférentiel de certains isotopes d'un réservoir vers un autre (ou entre deux phases ou espèces chimiques), via un processus physique, chimique ou biologique. Ceci crée des différences de composition isotopiques entre les réservoirs.

On définit le facteur de fractionnement isotopique α_{A-B} entre les réservoirs A et B pour le rapport ^{56}Fe/^{54}Fe par l'équation suivante :

$$\alpha_{A-B}^{56/54} = \frac{(Fe^{56}/Fe^{54})_A}{(Fe^{56}/Fe^{54})_B} = \frac{1+\frac{\delta^{56/54}Fe_A}{1000}}{1+\frac{\delta^{56/54}Fe_B}{1000}} \quad (2)$$

$\delta/1000$ étant très inférieur à 1, on simplifie l'équation (2) et on définit $\Delta^{56}Fe_{A\text{-}B}$, la différence isotopique, ou fractionnement isotopique, entre les réservoirs A et B :

$$\Delta^{56}Fe_{A-B} = \delta^{56/54}Fe_A - \delta^{\frac{56}{54}}Fe_B \approx 10^3 \ln(\alpha_{A-B}^{\frac{56}{54}}) \quad (3)$$

L'ensemble des fractionnements isotopiques mis en évidence pour le fer seraient dépendants de la masse (Dauphas et al., 2017). α_{A-B} peut refléter soit un fractionnement thermodynamique ou à l'équilibre soit un fractionnement cinétique.

La Figure 22 présente les fractionnements isotopiques ($\Delta^{56}Fe_{A-B}$) de processus important pour le cycle océanique du fer.

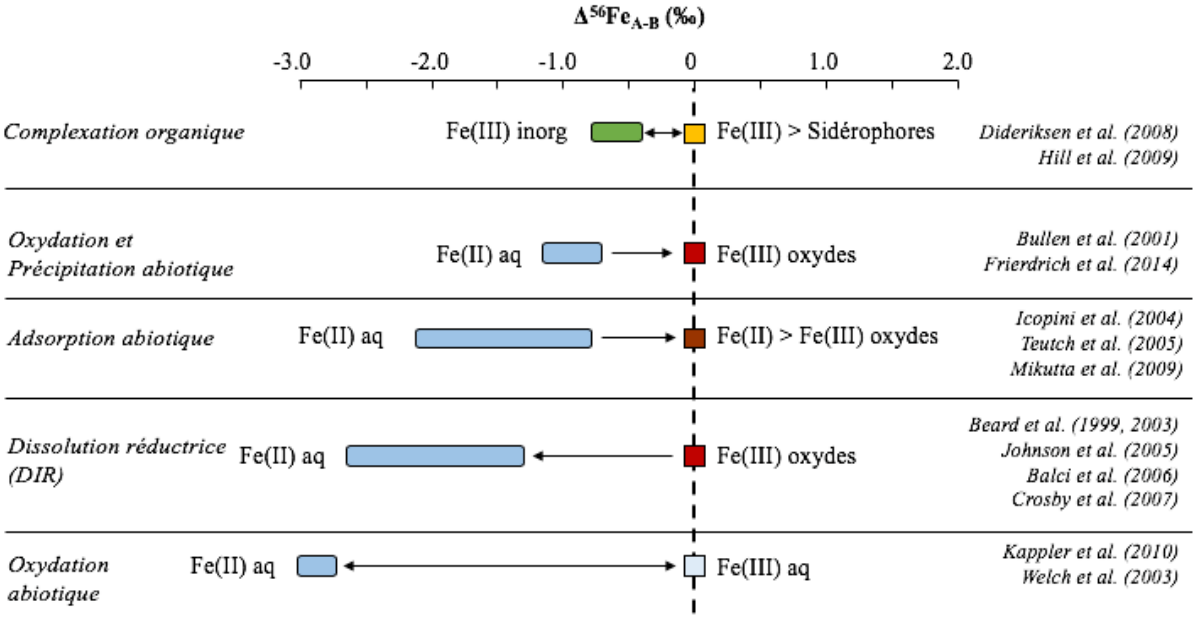

Figure 22 : Synthèse des fractionnements isotopiques ($\Delta^{56}Fe_{A-B}$) générés par des processus biologiques ou abiotiques.

Les réactions redox dominent les fractionnements isotopiques du fer dans l'environnement. L'oxydation abiotique du fer induit un fractionnement très important qui enrichit la fraction Fe(II) en isotopes légers et la fraction Fe(III) en isotopes lourds, avec un $\Delta^{56}Fe_{(FeIII-FeII)}$ à l'équilibre de 3‰ (Welch et al., 2003). La DIR, induit également un fractionnement de grande amplitude qui enrichit la fraction Fe(II) en isotopes légers avec un $\Delta^{56}Fe_{(FeIII-FeII)}$ compris entre -2.6 à -1.3‰ (Beard et al., 1999; Beard et al., 2003; Crosby et al., 2007; Johnson et al., 2005).

L'oxydation de Fe(II) aqueux en Fe(III) suivi de la précipitation des particules d'oxyde de Fe(III) est un processus important à certaines interfaces (sédimentaires, hydrothermales). Elle favorise les isotopes lourds dans le précipité, enrichissant ainsi la phase dissoute en isotopes légers (Bullen et al., 2001).

Concernant la complexation organique, les sidérophores complexeraient préférentiellement le Fe(III) inorganique léger, avec un Δ56Fe à l'équilibre de ~ 0.6‰ (Dideriksen et al., 2008).

Concernant la consommation phytoplanctonique et la reminéralisation (non présentées dans la Figure 22), les fractionnements isotopiques associés à ces processus ne font pas consensus. Radic et al (2011) et Ellwood (2015) suggèrent que le phytoplancton consommerait préférentiellement des isotopes de fer légers contrairement à Conway et al (2014) qui suggère

l'inverse i.e. le phytoplancton consommerait préférentiellement des isotopes de fer lourds. Klar (2018) suggèrent que la reminéralisation de la matière organique libère des isotopes de fer lourds, alors que Abadie (2017) suggèrent que la reminéralisation libère des isotopes de fer légers.

4.3 Méthode de mesure des concentrations et des isotopes du fer

Les mesures de DFe et δ^{56}DFe présentées dans ce chapitre ont été réalisées, pour la majorité, dans le cadre de cette thèse (Annexe 7.2) au sein de l'observatoire Midi-Pyrénées en suivant le protocole schématisé en Figure 23.

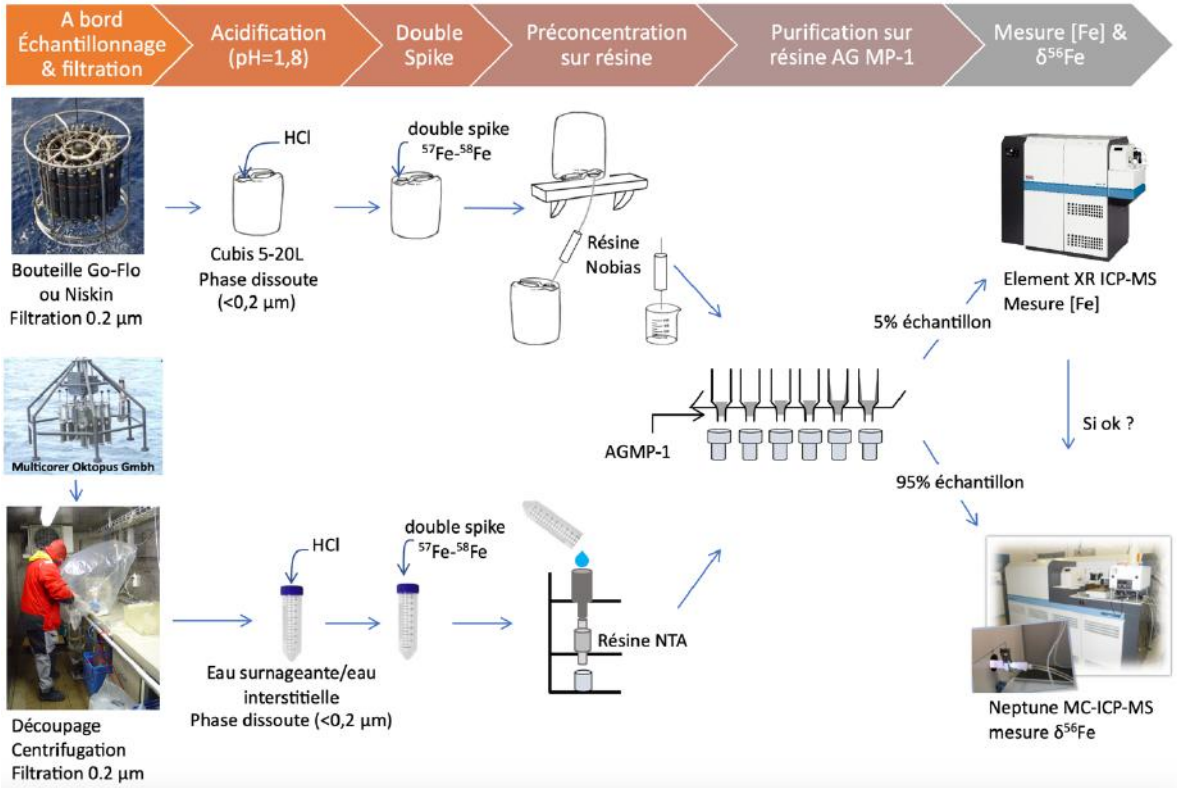

Figure 23 : Étapes nécessaires à la mesure des concentrations et isotopes de fer dissous de l'échantillonnage en mer à la mesure par spectromètre de masse.

Ce protocole regroupe les différentes étapes nécessaires à la mesure. Tout d'abord les différents types d'échantillons (eaux interstitielles sédimentaires, eaux surnageantes aux carottes sédimentaires et colonne d'eau) sont prélevés et filtrés à bord, s'en suit une étape d'acidification dans les 24h. Au laboratoire, le double spike (^{57}Fe-^{58}Fe) est ajouté aux échantillons, s'en suit une étape de préconcentration sur résine chelatante (Nobias ou NTA), puis de purification sur résine anionique (AGMP-1). Enfin, les concentrations multi-élémentaires des échantillons sont mesurées avec un spectromètre de masse à source plasma à secteur magnétique et à haute résolution (Element XR-ICP-MS) et les rapports isotopiques mesurés avec un spectromètre de masse à source plasma et à multi-collection (Neptune MC-ICP-MS).

Ces mesures ont nécessité des étapes de développement analytique réalisées au cours de cette thèse. Brièvement, nous avons identifié des problèmes de contamination en Fer des résines de l'entreprise Savillex®. Malgré des lavages extrêmement puissants sur une longue durée (de 5 à 26 jours), avec des acides en concentration très forte (eau régale brute 9/10 + acide fluorhydrique 1/10, soude 4 M) et à des températures élevées (160 °C), les contaminations en Fer ont persisté jusqu'à ce que l'entreprise Savillex® modifie la composition de ses résines.
Avec les résines anioniques AGMP-1, utilisées lors des étapes de purifications des échantillons, nous avons dû augmenter d'un facteur 100 les concentrations en peroxyde d'hydrogène des solutions d'élution du fer utilisées pour éliminer correctement le molybdène de ces résines anioniques. Les tests d'élutions sont présentés en Annexe 7.4.
Nous avons également réalisé de nombreux tests sur les éléments pouvant provoquer de possible interférences (le calcium) et effets de matrice (notamment le potassium, manganèse, molybdène) sur les mesures de la composition isotopique du fer par MC-ICPMS. Ces tests ont conduit à une publication soumise et présentée en Annexe 7.5.

4.4 Les isotopes du fer dans le contexte des campagnes KEOPS

L'océan Austral est la plus grande région HNLC de l'océan mondial (Figure 24a). Cependant, de larges « blooms » de phytoplancton (floraisons du phytoplancton) sont observés dans certaines zones, notamment dans le secteur indien de l'océan Austral au niveau du plateau des îles Kerguelen (cf. la carte de chlorophylle *a* de la zone, Figure 24b). Dans le cadre de cette thèse, nous avons effectué des mesures de concentration en fer dissous (DFe) et d'isotopie (δ^{56}DFe) dans des échantillons prélevés aux alentours des îles Kerguelen dans le cadre des campagnes KEOPS 1 (2005) et KEOPS 2 (2011, Figure 24a).

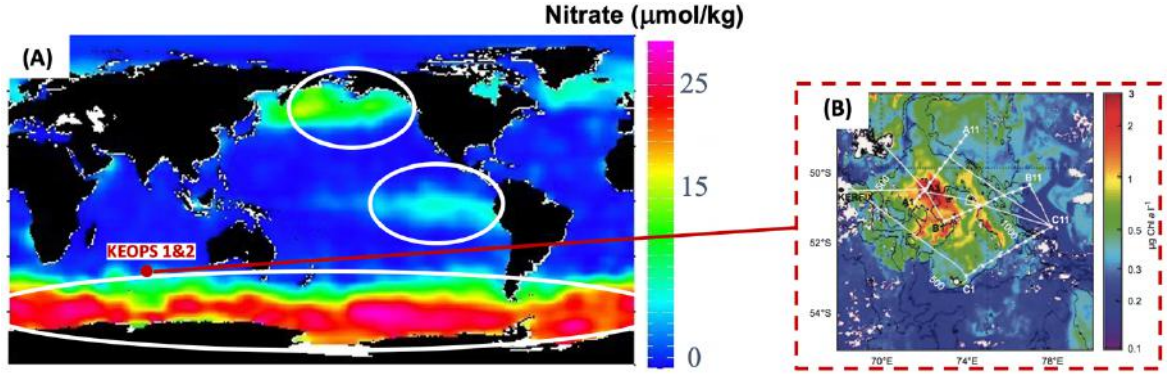

Figure 24 : (A) Concentrations de nitrate à la surface des océans (µmol/kg, données provenant du Levitus World Ocean Atlas 1994) mettant en évidence les régions HNLC entourées en blanc. Les campagnes KEOPS 1&2 sont indiquées. (B) Concentrations de chlorophylle *a*, à la surface des îles Kerguelen (Blain et al., 2007).

Les projets KEOPS (Kerguelen Plateau and Ocean compared Study) 1 et 2 visent à étudier la fertilisation naturelle en fer au niveau des îles Kerguelen (Blain et al., 2008a). Plus précisément, les objectifs du projet sont de :

- Démontrer l'**existence de la fertilisation naturelle en fer** au-dessus du plateau.
- Identifier les **mécanismes de fertilisation.**
- Décrire **le fonctionnement des écosystèmes.**
- Étudier les **impacts de la fertilisation naturelle sur les cycles biogéochimiques** (Blain et al., 2008a).

KEOPS 1 a eu lieu durant l'été Austral (18 juin- 13 févier 2005), au moment du déclin de la floraison phytoplanctonique, au niveau du plateau des Kerguelen (Figure 25).

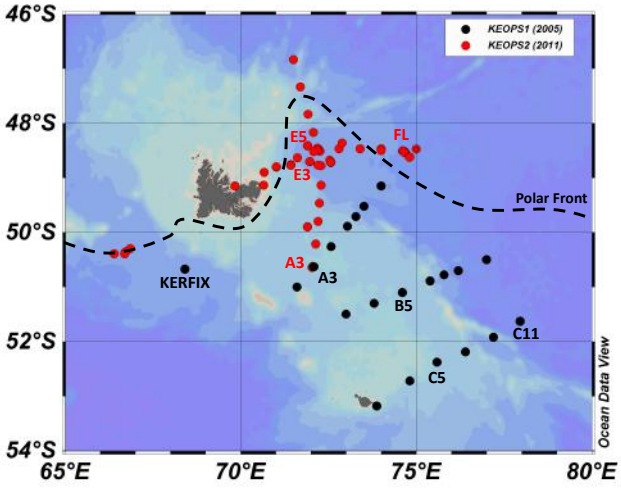

Figure 25 : Stations échantillonnées au niveau de l'archipel des Kerguelen durant les campagnes KEOPS1 (points noirs, 2005) et KEOPS 2 (points rouges, 2011).

KEOPS 1 a permis de confirmer qu'il y a bien une fertilisation naturelle en fer des eaux de surface au niveau du plateau des Kerguelen. Deux principales sources de fer ont été identifiées. La première, une source de fer provenant des sédiments du plateau, notamment car les distributions verticales de DFe augmentent au-dessus du plateau des Kerguelen (Figure 26, Blain et al., 2008b). La seconde, une source provenant de l'advection latérale d'eau préalablement en contact avec le plateau continental de l'île de Heard au sud. Cette source a été identifiée grâce à l'utilisation de traceurs géochimiques (terres rares, isotopes de radium) et des calculs de budgets de fer dissous et de fer particulaire apparent (Chever et al., 2010; van Beek et al., 2008; Zhang et al., 2008).

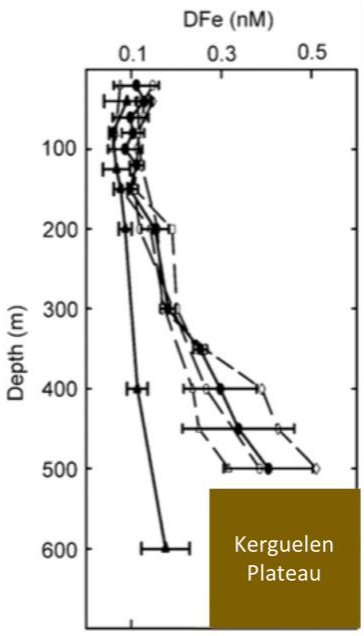

Figure 26 : Profils verticaux de fer dissous aux stations A3 et en dehors du plateau (adaptée de Blain et al., 2008b).

KEOPS 2 a eu lieu six années plus tard au printemps austral (7 octobre -11 novembre 2011) dans les premiers stades de la floraison, en amont et en aval du plateau (Figure 25). Cette campagne a permis d'améliorer la couverture spatiale et temporelle de la région des Kerguelen (Bowie et al., 2015). Au cours de cette campagne, une fertilisation massive en fer a été observée à l'échelle de centaines de milliers de kilomètres carrés produisant une mosaïque de blooms phytoplanctoniques (Bowie et al., 2015). KEOPS 2 a permis de mettre en évidence des environnements régionaux distincts régis par une circulation régionale et des voies de transport complexes qui seraient responsables de différences dans les modes et l'amplitude d'apport du fer (Bowie et al., 2015). Au niveau du plateau, ce serait l'apport vertical de fer provenant des sédiments du plateau qui dominerait, comme déjà identifié durant KEOPS 1 (Bowie et al., 2015). A l'est du plateau, ce serait l'advection latérale d'eau riche en fer, originaire du plateau et/ou de la marge de l'île principale des Kerguelen, qui fertiliserait la zone en fer (Bowie et al., 2015; d'Ovidio et al., 2015; Sanial et al., 2015).

C'est dans ce contexte que les mesures de DFe et δ^{56}DFe d'échantillons prélevées au cours des campagnes KEOPS 1&2 et présentées dans cette thèse vont pouvoir nous aider à identifier les processus dominants l'apport de fer dans les différentes régions des îles Kerguelen.

4.5 Article en préparation: *Iron isotopes as tracers of biogeochemical cycles in the naturally fertilized area of the Kerguelen Plateau*

4.4.1 Résumé

Les eaux interstitielles et surnageantes des stations du plateau de Kerguelen (KEOPS 1) révèlent un fort enrichissement en DFe au-dessus du sédiment associé à un signal lourd (positif) de δ^{56}DFe que nous attribuons à un mécanisme de dissolution non réductrice (NRD) du matériel lithogénique déposé sur le plateau. La signature positive de cet enrichissement n'est plus visible dans la colonne d'eau dès que l'on s'éloigne de plus de 100 m des sédiments. L'apport sédimentaire de DFe ne semble donc pas être responsable de l'enrichissement en DFe des eaux de surface et donc à l'origine du « bloom » phytoplanctonique. Cela est confirmé par les résultats obtenus dans les stations de la zone de recirculation (KEOPS 2) qui présentent des enrichissements en DFe ayant une signature isotopique légère (négative) à 40, 400 et 800 m. Ces observations suggèrent un apport latéral de DFe à partir de la marge de l'île Kerguelen par des processus de réduction du matériel lithogénique dans les sédiments (« dissimilatory iron reduction », DIR). Par conséquent, nous suggérons que le « bloom » phytoplanctonique au voisinage des îles Kerguelen est davantage lié à un apport latéral de Fe provenant de la marge des îles par un processus de DIR du matériel lithogénique sédimentaire plutôt qu'à un apport vertical de Fe provenant des sédiments du plateau (situé à 500m de fond) par un processus de NRD du matériel lithogénique. Un des autres objectifs de cet article est d'observer les variations isotopiques de certaines masses d'eau de l'océan Austral en comparant les signaux de δ^{56}DFe mesurés dans les masses d'eau durant la campagne Bonus GoodHope (BGH, le long du méridien 0°) à celui mesuré dans la région de Kerguelen, située environ 4500 km en aval dans le Courant Circumpolaire Antarctique. Pour la majorité des masses d'eau, il apparait que leurs signatures isotopiques sont bien conservées (i.e. très peu modifiées). Finalement, nous proposons une tentative de quantification du fractionnement isotopique par la consommation phytoplanctonique.

4.4.2 Article

Iron isotopes as tracers of biogeochemical cycles in the naturally fertilized area of the Kerguelen Plateau.

L. Artigue[1], F. Lacan[1], J. Klar[2], C. Pradoux[1], G. Sarthou[3], E. Viollier[4], S. Blain[5].

[1] LEGOS, University of Toulouse, CNRS, CNES, IRD, UPS, 31400 Toulouse, France.

[2] Université de Perpignan Via Domitia, Centre de Formation et de Recherche sur les Environnements Méditerranéens, UMR 5110, F-66860 Perpignan cedex, France.

[3] Laboratoire des Sciences de l'Environnement Marin (LEMAR), UMR 6539, IUEM, Technopôle Brest Iroise, 29280 Plouzané, France.

[4] Laboratoire de Géochimie des Eaux (Groupe de I'URA 17152), Université Denis Diderot (Paris 7) et I.P.G. Paris Case 7O52, France.

[5] Aix-Marseille Université, CNRS, LOB-UMR 6535, Laboratoire d'Océanographie et de Biogéochimie, OSU/Centre d'Océanologie de Marseille, France

Abstract

Iron (Fe) isotopes have proven their high potential to provide new information about the Fe oceanic cycle. This paper present dissolved iron (DFe) concentration and isotopic (δ^{56}DFe) data obtained the water column in the vicinity of the Kerguelen Island in the framework of the KEOPS 1 and 2 GEOTRACES process studies. In addition, it reports sediment pore waters and sediment overlying waters from the central Kerguelen Plateau (~500m depth). The sediment data reveal a heavy δ^{56}DFe enrichment of bottom waters above the Plateau attributed to non-reductive sediment dissolution (NRD). The positive δ^{56}DFe signature of this enrichment is no more detectable 50 m above the sediments reflecting the little impact of this sedimentary source, through vertical transport, onto the surface waters. Downstream of the Kerguelen Island, station E presents sporadic, but significant, enrichments at 40, 400, and 800 m, characterized by a light isotope signature. This light δ^{56}DFe signature suggest lateral supply of Fe from the Kerguelen Island margin by dissimilatory iron reduction (DIR). Therefore, we attribute the Fe natural enrichment in the vicinity of the Kerguelen Island to lateral supply of Fe from the Kerguelen Island margin through DIR processes rather than vertical Fe supply from the plateau sediment through NRD processes. A comparison between Bonus Goodhope station (along the 0° meridian) and KEOPS stations allowed us to observe that while Atlantic Antarctic Intermediate Water display significant δ^{56}DFe variations, Winter Water, Upper Circumpolar Deep Water and Lower Circumpolar Deep Water δ^{56}DFe signals remain roughly constant.

1 Introduction

Oceanic primary production plays a major role on global biogeochemical cycles, notably, carbon cycle, and hence on climate (Volk & Hoffert, 1985). Iron (Fe) is an essential micronutrients being involved, as an enzyme cofactor, in the different stages of the nitrogen cycle, and as an electron transporter during the processes of photosynthesis and respiration (Morel & Price, 2003). Modelling studies suggest that the availability of iron limits primary productivity in 30-50 % of the world ocean (Moore & Braucher, 2008). A better knowledge of the distributions and internal cycling of such important micronutrient is thus crucial in the context of global change. In the last decade, enormous progress has been made in our ability to observe ocean iron distributions notably through the GEOTRACES program. However, the

roles of different biological, chemical and physical processes on the Fe cycle still require clarification (Tagliabue et al., 2017). Fe isotopes have proven their high potential to provide new information on the Fe cycle processes (Conway & John, 2014; John et al., 2012, 2018; Jessica K. Klar et al., 2017; F. Lacan et al., 2008; Radic et al., 2011). KEOPS (Kerguelen Plateau and Ocean compared Study) 1 and 2 cruises aimed at studying a natural iron fertilization area in the Southern Ocean i.e. in the largest high-nutrient low chlorophyll (HNLC) region of the global ocean. Both of these projects took place in the vicinity of the Kergulen islands (Indian sector of the Southern Ocean, Fig.1). This paper presents and discusses dissolved Fe (dFe) concentration and isotope ($\delta^{56}Fe$) data from measured in various types of samples (sediment interstitial water, overlying water and water column water) from both KEOPS 1 and 2 cruises, with the aim to provide more understanding on the Fe cycle in the Kerguelen area. Specifically, this paper gives new insights on the dominant processes responsible for the Fe supply in a fertilized area of the Southern Ocean (sediment supply, lateral transport), and on the iron isotopic signal variations within the Southern Ocean water masses as they travel over about 4500 km, from the 0° meridian (Bonus Goodhope section, Abadie et al., 2017) and the Kerguelen area.

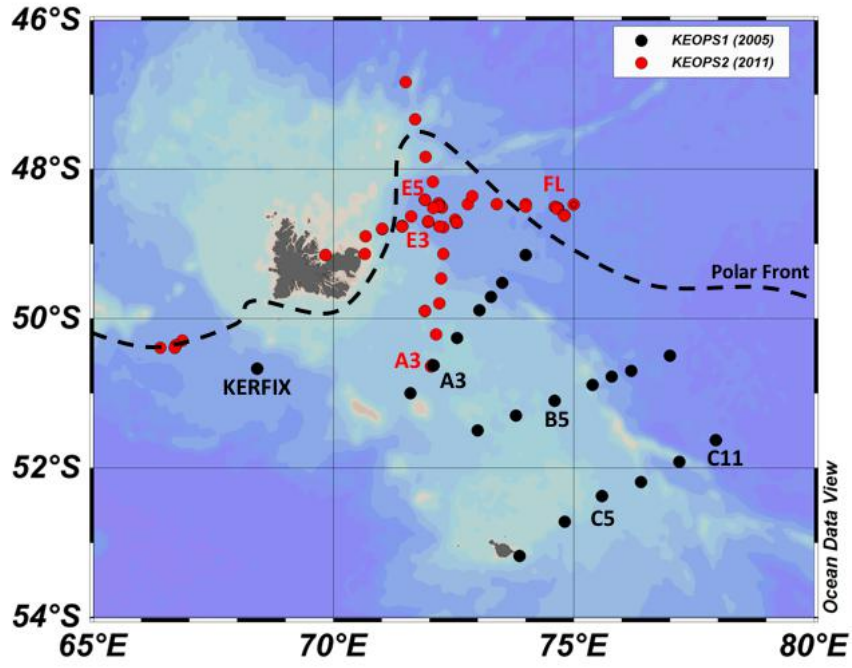

Figure 1. Stations sampled during the KEOPS 1 (black dots, 2005) and KEOPS 2 (red dots, 2011) cruises in the vicinity of the Kerguelen archipelago. Station numbers correspond to the station sampled for Fe isotopes and discussed in the present paper. The polar front line is relative to the KEOPS 2 cruise.

2 Materials and Methods

The KEOPS-1 campaign took place between 19 January and 13 February 2005 (in the early stages of the bloom) on board the RV Marion Dufresne. Three transects (A, B, C) were conducted and 19 stations sampled south of the polar front, on and off the Kerguelen Plateau (Fig. 1). The KEOPS-2 campaign took place between 7 October and 30 November 2011 (during the start of the decline of the bloom) on board the RV Marion Dufresne. 32 stations were

sampled on the Kerguelen plateau, in a recirculation area and in the HNLC area north and south of the polar front (Fig. 1).

2.1 Sampling and processing

This section presents the sampling and processing strategy introduced to sample (i) seawater and cores during KEOPS 1, and (ii) seawater during KEOPS 2.

During KEOPS 1, seawater samples were collected using ten trace-metal clean Go-Flo bottles deployed on a 3000 m kevlar line. Upon recovery, the Go-Flo bottles were transferred into a clean container, pressured with N_2 (high purity grade) to allow sub sampling. 4 L samples were filtered on-line through 0.2 µm cartridges (Sartobran) for Fe isotope analysis, and acidified using 7N HCL. Sediment core were collected with an Oktopus Gmbh (Germany) multiple corer (head version MUC 8/100) equipped with 8 transparent polycarbonate cylinders. Upon recovery, overlying water was first sampled. The cores were then sliced (5 mm resolution down to 12 cm depth), under nitrogen atmosphere in a gloves bag (to avoid redox reactions), in a cool chamber in conditions close to deep waters (darkness, in situ temperature) at 2 ± 1 °C. The pore waters were separated from the solid phases by centrifugation (10-25 min 9000 xg) , filtered through 0.2 µm membranesand acidified.

During KEOPS 2, trace metals seawater samples were collected at the first station (A3-1), using acid-cleaned Go-Flo bottles mounted on a 6 mm Kevlar hydrowire. For the other stations, seawater was collected using a Trace Metal Clean Rosette (TMR, General Oceanics Inc. Model 1018 Intelligent Rosette), attached to a 6 mm Kevlar line. Immediately after collection, Go-Flo or Niskin bottles were transferred into a clean container for sampling, and processed under a laminar flow unit. Dissolved trace metals were filtered on-line through 0.2 µm filter cartridges (SARTOBRAN® 300, Sartorius or Pall Supor membrane, Acropak 200). All samples were acidified within 24 h of collection with ultrapure hydrochloric acid (HCl, Merck, 250 µL, final pH 1.7).

2.2 Dissolved Fe and Fe isotope analysis

Samples were analysed for DFe and DFe IC at the shore-based laboratory (LEGOS, Toulouse, France) based on the protocol of Lacan et al, (2010). Briefly this procedure consists of adding a ^{57}Fe–^{58}Fe double spike to the filtered seawater with a spike-to-sample ratio ranging from 1 to 3. Iron from the spike samples was subsequently preconcentrated using a Nobias resin and purified using an AG MP-1 anionic resin. Five percent of the solution was taken for multielemental analysis with an Element XR inductively coupled plasma-mass spectrometer (ICPMS) (Observatoire Midi Pyrénées, Toulouse, France). The accuracy of DFe concentrations was determined with the geostandard SLRS-5. Then, the nighty five percent of the solution remaining were analysed for iron isotope with a Neptune Multiple Collector - ICPMS (Observatoire Midi Pyrénées, Toulouse, France). The external precision of the Neptune was measured from repeated analysis of hematite standard. From these measurement, the iron isotopic composition ($\delta^{56}Fe$) was deduce relative to the IRMM-14 reference material as follows:

$$\delta^{56}Fe\ (‰) = \left[\frac{(^{56}Fe/^{54}Fe)_{sample}}{(^{56}Fe/^{54}Fe)_{IRMM\text{-}14}} - 1 \right] \times 10^3 \quad (1)$$

3 Results and discussion

DFe concentration and δ^{56}Fe water column profiles from KEOPS 1 (KERFIX, A3, C5 and C11 stations) and KEOPS 2 (A3, E3, E5, and FL stations) cruises are presented in Figure 2 and compared to DFe concentration and δ^{56}Fe data obtained by Abadie (2017) along the Bonus Good Hope (BGH) section upstream in the Antarctic Circumpolar Current (stations S2, S3, and S4)

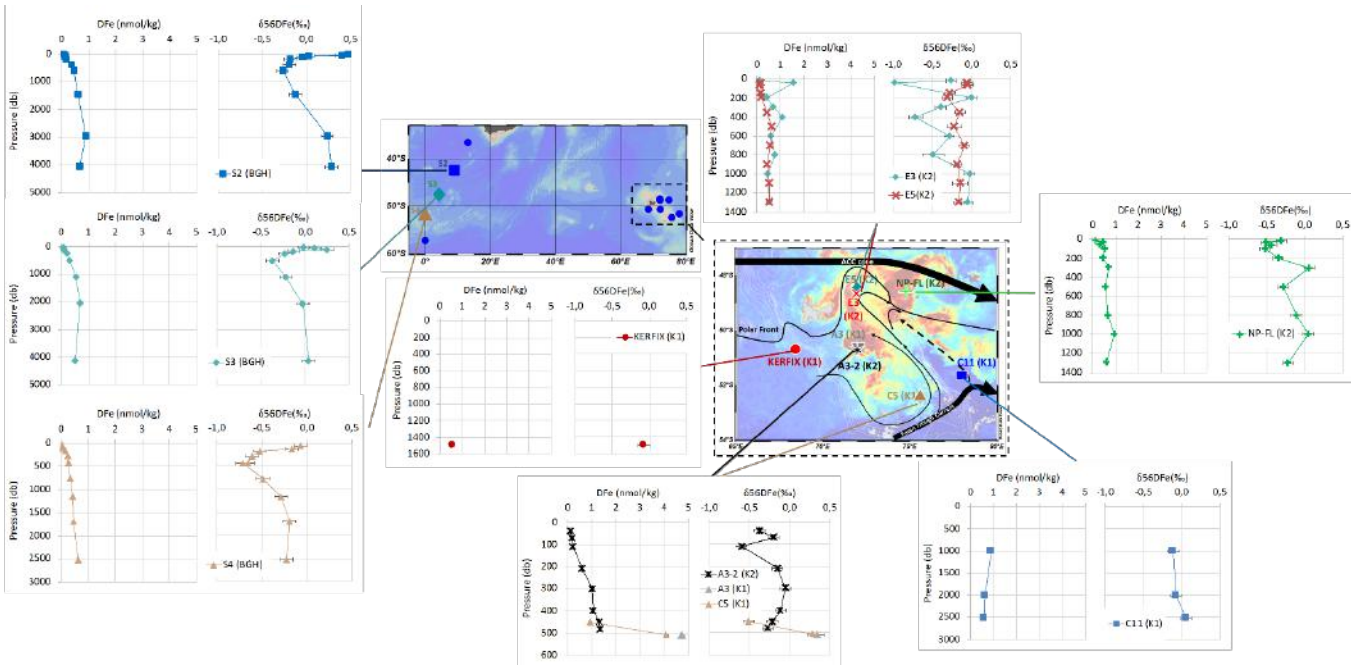

Figure 2. water column profiles from KEOPS 1 (KERFIX, A3, C5 and C11 stations) and KEOPS 2 (A3, E3, E5, and FL stations) cruises. These data are compared to DFe concentration and δ^{56}Fe data obtained by Abadie (2017) at Bonus GoodHope (BGH) section (stations S2, S3, and S4). Both KEOPS and BGH stations are located on the map. Topography is indicated on the large scale map, while the zoom on the Kuerguen area displays the satellite-derived surface chlorophyll-a distribution over the last week of the KEOPS 2 (Cavagna et al., 2015). The arrows schematize the mean circulation as described by Park et al (2008; 2014) for the KEOPS 1 and 2 cruises.

DFe concentration and δ^{56}Fe pore water profiles from the KEOPS 1 cruise (A3, B5, C5 and C11stations) are presented in Figure 3.

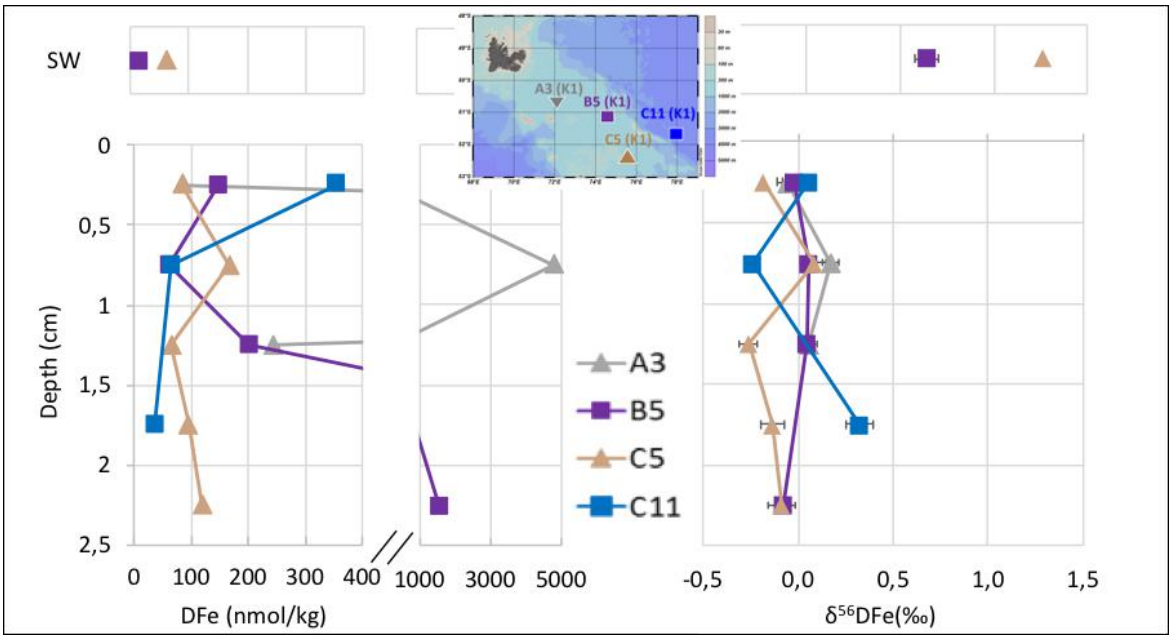

Figure 3. DFe concentration (A) and δ^{56}Fe (B) profiles in sediment interstitial waters (bottom panels), and overlying waters (top panels, SW) during KEOPS 1 cruise.

The discussion is organized in four sections. First, the sediment/seawater interface as a source of Fe is discussed for stations located south of the Island,above the central part of the Kerguelen Plateau. Second, the temporal variability of the DFe concentration and isotopic signal are discussed at station E located in a bathymetrically trapped recirculation system. Third, the water mass Fe concentration and isotope variation are discussed by comparison of the observed values at KEOPS stations to the values measured during the BGH section located along the 0° meridian (~4500 km upstream in the ACC). Finally, DFe isotope fractionations associated to phytoplankton uptake are studied.

4.1 Sources at the sediments

Sediments has been suggested as an important source delivering dFe to deep waters in the vicinity of the Kerguelen Island during both KEOPS 1 and 2 cruises (Blain et al., 2008; Bowie et al., 2015; Quéroué et al., 2015). However, a lot of question remains relative to the impact of such enrichment in the whole water column as well as the exact processes involved at the seawater/sediment interface.

The central Kerguelen Plateau (south of the Island) waters have been characterized by deep samples, taken close to the sediments during KEOPS 1 at station A3 and C5 (Fig. 2), and by a full water column profile at the same station A3 (A3-2) during KEOPS2 (Fig. 2). At A3 (KEOPS 1) deep water sampled only 21 m above the seafloor presents a very high DFe concentration (4.76 nmol/kg) associated to a positive δ^{56}DFe signal (+0.35 ‰). The deepest water measured at station C5, i.e. 54 m above the seafloor, is very similar with very high DFe concentration (4.11 nmol/kg) associated with a similarly positive δ^{56}DFe signal (+0.29 ‰). Therefore, a sediment source of dFe associated to positive δ^{56}DFe values seems to impact the bottom samples of the plateau stations. However, its signature quickly vanishes as the distance

from the sediment increases. Indeed, at C5, the sample measured 112 m above the seafloor present a DFe concentration of 0.93 nmol/kg (lower by a factor four compared to the deepest sample situated just 58 m below) and a negative isotope signal (-0.51 ‰). At A3-2 (KEOPS 2), DFe concentrations progressively increase from the surface to the bottom, to reach values around 1 nmol/kg between 300 m and 480 m i.e. between 230 to 50 m above the seafloor. These high DFe concentrations were interpreted as reflecting the vertical transport of sediment enrichment (Quéroué 2015). However, the high DFe concentrations measured at A3-2 are associated to light δ^{56}DFe values (between -0.05 at 300 m to -0.27 ‰ at 480 m). These light isotopic values measured at both C5 and A3-2 station between 50 to 112 m above the seafloor do not reflect the positive δ^{56}DFe sediment enrichment. They are similar to what was previously observed for this water mass, the UCDW. The UCDW was identified by its oxygen minimum below 450 at A3-2. Its δ^{56}DFe signal measured at -0.24 ‰ is in excellent agreement with the UCDW δ^{56}DFe signal measured at -0.22 ‰ at station 3 during the BGH cruise (Abadie 2017). Therefore, while the high DFe concentration measured in the water column at A3-2 seems to reflect a vertical Fe enrichment from the sediment to the waters above (bottom to 300 m; i.e. about 200m above the sediments), the isotopes do not allow to trace this sediment enrichment signature more than 50 m above the sediments.

To better understand the processes involved in this dFe release at the seawater/sediment interface, DFe concentration and isotopes were measured from sediment pore water samples taken ar KEOPS 1 B5, C5, A3 and C11 stations (Fig. 3). The pore water DFe concentration were very high, mainly in the range 37-350 nmol/kg except for two extremely high DFe concentrations measured at station A3 and B5 (4771 nmol/kg at 0.75 cm depth and 1564 nmol/kg at 2.25 cm depth respectively). Once released in the overlying waters, the DFe concentrations decrease (14.41 nmol/kg at B5 and 77.10 nmol/kg at C5) but stay extremely high compared to usual DFe water column concentrations (mean of 0.6 nmol/kg over our KEOPS2 stations). The dilution of these high overlying water DFe concentrations may very well explain the water column values around 5 nmol/kg found at A3 and C5 stations, 20 to 50 m above the sediments. In the pore waters, the δ^{56}DFe profiles remain roughly constant around 0 ‰ at all stations. Once released in the overlying water, the δ^{56}DFe values get positive at both B5 and C5 station (+0.64 and +1.26 ‰ respectively). These positive values are also in very good agreement with the δ^{56}DFe values measured, 20 to 50 m above sediment at A3 and C5 station (+0.3 to +0.4 ‰). This is a robust confirmation that the sediment pore waters are the source of the seawater enrichments found 20 and 50m above the interface. The more positive isotopic signal found in the overlying waters (+0.64 to +1.26 ‰) compared to the interstitial waters (around 0‰) likely result from the significant DFe removal occurring as DFe is transferred from the pore waters to the overlying seawater, across the interface. Kinetic fractionations during precipitation have been shown (experimentally) to favor light isotopes in the precipitate and therefore to enrich the remaining DFe in heavy isotopes (Beard & Johnson, 2004). This has been observed previously in the Celtic Sea, with overlying waters 1 to 2‰ heavier than interstitial waters just below the interface (J. K. Klar et al., 2017).
While the water column above the seafloor is well oxygenated (197 to 235 µM), the oxygen penetration depth measured in the core samples reveals that the cores are anoxic below a few mm. Under anoxic conditions, dissimilatory iron reduction (DIR) could occurs leading to the microbial reduction of Fe(III) to Fe(II) (Burdige, 2006; Canfield, 1989). However, the Fe(II) concentrations measured in the pore waters are close to 0 nmol/kg (data not shown). This indicates that, even if the sediment is anoxic, the Fe released in pore waters over the Kerguelen plateau is not in its reduced state (Fe(II)) but in its oxidized state i.e. Fe(III). This is confirmed by the measured δ^{56}DFe values in the pore water around 0‰ away from the light Fe(II) isotopic signature in the range -3 to -1 ‰ (John et al., 2012; Severmann et al., 2006). Therefore, DIR

seems to not be the mechanism releasing dFe to the overlying waters over the Kerguelen Plateau.

Another possible mechanism that could occur is the Non-reductive dissolution (NRD) of sediments. The term NRD first introduced by Radic et al (2011), refer to the release of dissolved iron from particles without reduction processes. It has been suggested to occur at the sediment/seawater interface (Conway & John, 2014; John et al., 2018; J. K. Klar et al., 2018; Radic et al., 2011), in the water column (Abadie et al., 2017; Labatut et al., 2014) and within the sediments (Homoky et al., 2013). While occurring in the water column, it has been suggested that dissolution and adsorption of dFe onto particles (exchange between both phases) occur simultaneously leading to a net release of dFe from particles (Labatut et al., 2014). The isotopic fractionation associated to NDR has been estimated to impact the DFe with a slightly heavier isotopic composition than the particulate Fe, in the order of a few tenths of a ‰ (Δ56FeDFe–PFe = + 0.3‰, Labatut et al., 2014). Water column δ^{56}DFe values from -0.3 to +0.4 ‰ have been attributed to reflect NRD of lithogenic material (e.g. Abadie et al., 2017; Conway & John, 2014; John et al., 2018; J. K. Klar et al., 2018; Labatut et al., 2014; Radic et al., 2011). We therefore suggest that our observed values of δ^{56}DFe from -0, 26 to +0.33 ‰ in pore waters also also reflect NRD of lithogenic material.

4.2 Temporal variability

Station E was located in a bathymetrically trapped recirculation system, within the chlorophyll plume extending downstream of the Kerguelen Plateau. It was reoccupied 3 times during KEOPS 2 (E1, E3 and E5), over 20 days. While its hydrological properties remained mainly stable, its biogeochemical features were highly variable (Bowie et al., 2015; Lasbleiz et al., 2014; Quéroué et al., 2015). It was analyzed twice for iron isotopes at stations E3 and E5. The DFe concentration and isotope profiles of these two occupations are very different (refer to Fig. 2).

The E5 concentration profile displays a classical shape, with low values, around 0.13 nmol/kg, from the surface to 150 m, then increases progressively to reach a maximum around 0.5 nmol/kg at 500 m and remain roughly constant around this value down to 1300m. This profile is in very good agreement with another DFe concentration profile measured one day before at the same station by Flow Injection Analysis (FIA, Quéroué et al., 2015). Its DFe isotopic composition is mostly homogeneous with values around δ^{56}DFe = -0.15 ‰. This value is comparable to that mostly found at the other KEOPS 1&2 stations, for instance along most of the water column at station A3 (Plateau), or below 200m at station FL (easternmost station).

On the opposite, the E3 DFe concentration profile displays an unusual shape, with strong peaks at 40, 400 and 800 m. Except these peaks, it displays concentrations in good agreement with our E5 profile and with another DFe concentration profile measured the same day from this station (FIA, Quéroué et al., 2015). The peaks are highest in the surface and decrease with depth (1.56, 1.09, 0.76 nmol/kg at 40, 400 and 800m respectively). Such high values have been reported before at approximately the same location, with DFe concentrations reaching 1.5nmol/kg at 100 and 280m (Bucciarelli et al., 2001; their station K10). The DFe isotope profile mirrors the concentration profile with strong isotopically light peaks in these samples. Apart from these samples, the rest of the profile displays a rather homogeneous isotopic composition, similar to that of E5, around δ^{56}DFe = -0.15‰.

This suggest that the E3 profile could result from an initial state, represented by E5, to which isotopically light DFe would have been added (where the peaks were found). Combining the data from the two profiles allows to calculate the isotopic signature of the added DFe at any particular depth, according to the following equation.

$$[DFe]_{E5} \times \delta^{56}DFe_{E5} + ([DFe]_{E3} - [DFe]_{E5}) \times \delta^{56}DFe_{ad.} = [DFe]_{E3} \times \delta^{56}DFe_{E3} \quad (2)$$

where δ^{56}DFead. is the δ^{56}DFe value of the added DFe

that leads to $\delta^{56}DFe_{ad.} = \frac{[DFe]_{E3} \times \delta^{56}DFe_{E3} - [DFe]_{E5} \times \delta^{56}DFe_{E5}}{([DFe]_{E3} - [DFe]_{E5})}$ (3)

This leads to $\delta^{56}DFe_{ad.}$ = -1.08 ± 0.08, -1.15 ± 0.17 and -1.10 ± 0.41‰ at 40, 400 and 800 m respectively. For the E3 40 m sample, the 38 m E5 data was used, for the E3 400 and 800 m samples the E5 350/500m and 700/900m data were interpolated relative to depth. Uncertainties were calculated by propagating the concentration and δ^{56}DFe uncertainties (they increase as the magnitude of the addition decreases). This remarkable agreement for the 3 additions suggests the same kind of source for the 3 peaks.

This kind of zigzag profile could suggest a contamination. On the one hand, the difference between the present E3 concentration profile with the other DFe profile obtained at the same station (by FIA), the same day, supports this hypothesis. On the other hand, several points argue in favor of the validity of these data. Amongst the 37 KEOPS-2 samples analyzed for Fe isotopes, only those three display such peaks, all at the same station. Sampling for the present samples was carried out by the same group and with the same protocol (notably filtration) as for the FIA profile. The peak intensity decreases with depth, which, if one assumes that these additions originated from the Kerguelen Island and margin and were transported to E3, is consistent with a more efficient transport at the surface compared to depth (i.e. current velocity decreasing with depth). These concentration values (up to 1.6 nmol/kg) remain in a reasonable range given the fact that (i) this area has been suggested to be enriched by inputs originating from the Kerguelen Island and margin during the ANTARES 3 and KEOPS-2 cruises (Bowie et al., 2015; Bucciarelli et al., 2001; van der Merwe et al., 2015; Quéroué et al., 2015; Sanial et al., 2015), and (ii) particulate iron concentrations as high as 2.4 nmol/kg were measured during KEOPS 2 (Bowie et al., 2015) and DFe concentrations as high as 1.5nmol/kg have been previously reported at the same location (Bucciarelli et al., 2001). Finally, as mentioned above, the high temporal variability of the biogeochemical properties of this area was underlined in several other KEOPS 2 studies, notably about iron concentrations (Bowie et al., 2015; Lasbleiz et al., 2014; Quéroué et al., 2015). For these reasons, and because we could not find any other reason to invalidate these data, we will assume in the following that they do reflect natural DFe enrichments.

Isotopically light DFe enrichments have been previously observed in oxygen depleted waters, notably off the Californian, Mauritanian, Senegalese and Peruvian margins, with δ^{56}DFe values ranging from -0.3 to -3.5‰ (Chever et al., 2015; Conway & John, 2014; John et al., 2012, 2018; J. K. Klar et al., 2018), but also in oxygenated waters, notably in the Celtic Sea, with values around -1‰ (NW European Shelf; J. K. Klar et al., 2017). These enrichments are attributed to sedimentary Fe reduction processes (DIR ; Johnson et al., 2008), releasing reduced DFe to the water column (Severmann et al., 2006, 2010). Despite rapid re-oxidation of Fe, the very negative signature of the source persists in the water column. However, as discussed above, sediment pore waters and overlying waters sampled on the Kerguelen Plateau, at depths of approximately 500 m, displayed δ^{56}DFe values of ~0 and in the range 0.6 to 1.3 ‰, respectively (Fig. 3). Therefore, a sediment enrichment cannot explain our light isotopes enrichment at

station E3. However, several works suggest that the DFe enrichments found at station E mainly originate from the Kerguelen Island coasts and margins rather than from the Plateau sediments. Radium isotope data suggest that Kerguelen coastal sedimentary inputs are transported across the Polar front to reach this location in timescales of a few days (Sanial et al., 2015). PFe/PAl ratios also suggest inputs originating from the Kerguelen Island and transported across the Polar Front to station E recirculation area (van der Merwe et al., 2015). The study of Fe budgets during KEOPS-2 lead to the conclusion that lateral transport was the dominant Fe fertilization mode in this area (Bowie et al., 2015). Finally two studies of DFe distributions also lead to the conclusion that the DFe found in station E area originates from the Kerguelen Island and margin sediments (Bucciarelli et al., 2001; Quéroué et al., 2015 ; for ANTARES 3 and KEOPS-2, respectively). Here the light iron isotopic signatures suggest that Fe reduction is involved in the process releasing DFe at the Kerguelen margin. High levels of primary production close to the Kerguelen shore could lead to significant levels of organic matter deposition rates on the Kerguelen margin, themselves leading to reductive conditions in the sediments (due to bacterial respiration). These processes have been evidenced in several areas (as noted above), including in the oxygenated waters of the Celtic Sea (J. K. Klar et al., 2017). Our DFe isotope data therefore confirm that the station E recirculation area is enriched in DFe originating from the Kerguelen Island sediments by lateral supply rather than by vertical supply from the Plateau sediments, and suggest that dissimilatory iron reduction in the Kerguelen sediments supply this DFe to the water column.

4.3 Evolution of the water masses δ^{56}DFe signal during their transit within the ACC

In this section, we investigate possible variations of the δ^{56}DFe signatures of the Lower Circumpolar Deep Water (LCDW), the Upper Circumpolar Deep Water (UCDW), the Atlantic Antarctic Intermediate Water (A-AAIW), and the Winter Water (WW) during their transit within the ACC from the Bonus-GoodHope section (BGH along the 0° meridian, Abadie et al., 2017) to the KEOPS stations (~ 75 °E) located roughly 4500km downstream. Because our aim here is to study potential variations due to processes occurring within the water masses (such as dissolve-particle interactions, organic matter remineralization, or reversible scavenging) or possible external DFe sources (such as dust deposition), as the water masses transit in the open ocean, we exclude from the discussion the KEOPS stations previously identified as impacted by local DFe sources (C5, A3-2, and E3). We use potential temperature and salinity to identify samples from the two locations taken in the same water masses (i.e. with similar θ-S values).

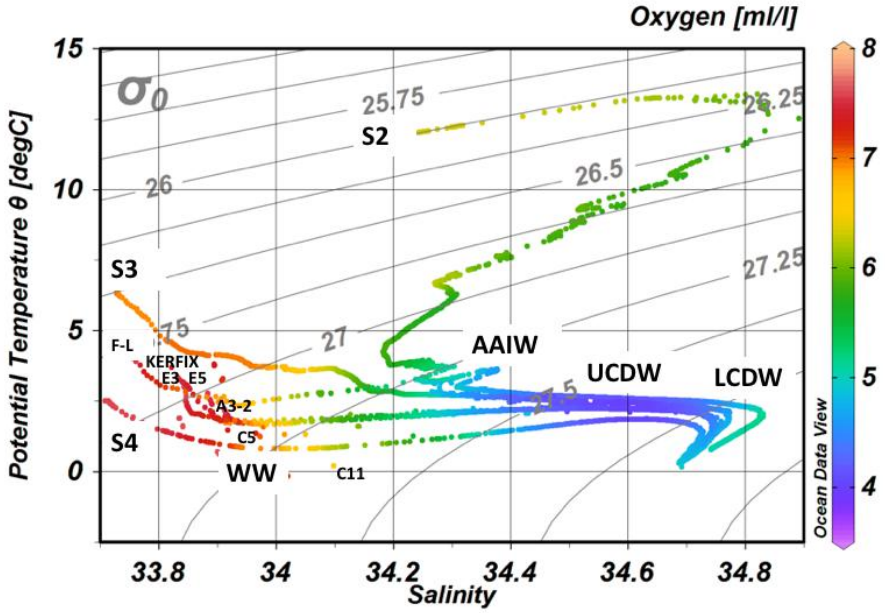

Figure 4. Potential temperature vs salinity diagram of KEOPS 1 (KERFIX, C5 and C11 stations), KEOPS 2 (A3, E3, E5, and FL stations) and BGH stations (S2, S3, S4). Isopycnal (in kg/m^3) and dissolved oxygen concentration (colors) are reported. Water masses: Winter Water (WW), Antarctic Intermediate Water (AAIW), Upper Circumpolar Deep Water (UCDW), and Lower Circumpolar Deep Water (LCDW) are indicated.

LCDW is identifiable in the θ-S diagram (Fig. 4) with its salinity maximum at low temperature. At stations S4 (BGH), this water mass was sampled at three depths between 772 and 1693 m. We use its average properties: θ = 1.27 ± 0.94 °C, S = 34.71 ± 0.02, DFe = 0.41 ± 0.11 nmol/kg, and δ^{56}DFe = -0.32 ± 0.30 ‰. This water mass was sampled six times on the KEOPS cruises at KERFIX, C11, E3/E5, and F-L stations between 1008 and 1500 m, with on average θ =1.90 ± 0.63 °C, S = 34.73 ± 0.03, DFe = 0.62 ± 0.29 nmol/kg, and δ^{56}DFe = -0.11 ± 0.13 ‰. Given the data uncertainties, LCDW Fe isotopic signature and concentrations can be considered to remain constant, along the 4500 km between BGH and KEOPS stations.

UCDW is characterized by its oxygen minimum (Fig. 4). At stations S3 (BGH), it was sampled at 1100 m with θ = 2.45 °C, S = 34.59, DFe = 0.55 nmol/kg, and δ^{56}DFe = -0.22 ‰. During KEOPS 1&2 it was sampled nine times at C5, A3-2, E3/E5, and F-L stations between 450 and 900 m with on average θ = 2.20 ± 0.09 °C, S = 34.45 ± 0.23. To discuss the DFe and δ^{56}DFe potential variations along the transit of this water mass, we only consider E5 and F-L stations, because the others (C5 and A3-2) have been identified as impacted by local DFe sources at the depths of the UCDW. E5, and F-L stations present an average DFe concentration of 0.55 ± 0.20 nmol/kg (n=4), and δ^{56}DFe signal of -0.17 ± 0.17 ‰ (n=4). Therefore, UCDW keeps a very constant δ^{56}DFe signal (-0.22 to -0.17‰) and DFe concentration (0.55 to 0.55-0.62 nmol.kg) along the 4500 km transit between BGH and KEOPS stations.

The Atlantic Antarctic Intermediate Water (A-AAIW) is characterized by its temperature up to 3 °C, its density at about 27.3 kg/m^3 and is located above the oxygen minimum of the UCDW (Fig. 4). As A-AAIW is formed by subduction across the Subantarctic front, it is only found north of it (SAF, Talley et al., 2011). It was sampled at station S2 (BGH) and at F-L station (KEOPS2), both located north of the polar front. The A-AAIW sampled at 625 m at station S2 (θ = 4 °C, S = 34.19, and σ_θ = 27.14 kg/m^3) is a little bit too shallow to be directly compared

to the station F-L 300 m sample (θ = 2.98 °C, S = 34.21, and σ_θ =27.26 kg/m^3). To allow an accurate comparison of these two stations, we performed a vertical interpolation at station S2, relative to density, between the samples measured at 625 m (σ_θ = 27.14 kg/m^3) and at 1485 m (σ_θ = 27.59 kg/m^3). We obtain an interpolated sample, at 849 m with σ_θ = 27.26 kg/m^3, DFe = 0.49 ± 0.02 nmol/kg, and δ^{56}DFe = -0.22 ± 0.05 ‰. We compare this sample with the one measured at the same density at F-L with DFe = 0.70 ± 0.03 nmol/kg, and a δ^{56}DFe signal of +0.06 ± 0.07 ‰. Therefore, along the 4500 km transit between BGH and KEOPS stations, A-AAIW δ^{56}DFe signal gets heavier (-0.22 to +0.06 ‰) and its DFe concentration increases (from 0.49 to 0.70 nmol/kg). A mass balance calculation allows to calculate that the isotopic composition of the added DFe is 0.74 ± 0.29 ‰ (the uncertainty is calculated by propagation of the concentration and isotopic composition uncertainties of the BGH and KEOPS data). This heavy signature suggests that reduction processes are not involved in this DFe addition.

Winter Water (WW) is characterized in our θ-S diagram (Fig. 4) by its low temperature at low salinity, just below the surface mixed layer. During BGH, WW was identified at 255 m at station 3 (θ = 3.66 °C, S = 34.10, σ_θ =27.10 kg/m^3) and at 175 m at station S4 (θ = 0.85 °C, S = 34.08, and σ_θ =27.31 kg/m^3). Then this water mass was sampled at five times during KEOPS 1 & 2 at A3-2, and E3/E5 station between 150 and 300 m with in average θ = 1.85 ± 0.23 °C, S = 33.99 ± 0.20, and σ_θ = 27.18 ± 0.15 kg/m^3. Because of the occurrence local inputs evidenced at A3-2 and E3, only E5 is considered in the following. The E5 WW is characterized by theta and S. This is in the range of the WW sampled at S3 and S4. Therefore, we realized an interpolation relative to density between the S3 and S4 WW samples. We obtain an interpolated sample at 226 m with σ_θ = 27.18 kg/m^3, DFe = 0.19 nmol/kg, and δ^{56}DFe signal = -0.31 ‰. For the reasons explained above, to discuss the DFe and δ^{56}DFe variation along the transit of this water mass, we only look at E5 station. E5 present an average DFe = 0.17 ± 0.03 nmol/kg (n=2), and δ^{56}DFe = -0.30 ± 0.07 ‰ (n=2). Therefore, WW keeps a very constant δ^{56}DFe signal (-0.31 to -0.30‰) and DFe concentration (0.19 to 0.17 nmol.kg) along the 4500 km transit between BGH and KEOPS stations.

In summary, the deep LCDW and UCDW and the shallow WW keep a rather constant δ^{56}DFe signature and DFe concentration during their transit between BGH and KEOPS On the opposite, A-AAIW δ^{56}DFe signature gets heavier during its transit, through the addition of material characterized by δ^{56}DFe = 0.74 ± 0.29 ‰, reflecting the absence of reduction associated to this source.

The δ^{56}DFe observed within water masses during KEOPS 1 and 2 cruises is summarize in Figure 5.

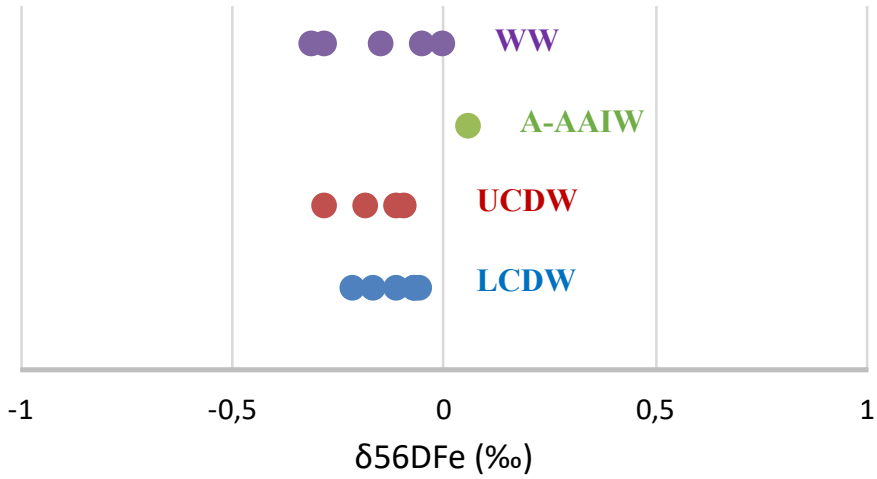

Figure 5. Range of δ^{56}DFe(‰) values for the water masses observed along KEOPS 1 and 2 cruises.

4.4 Biological uptake

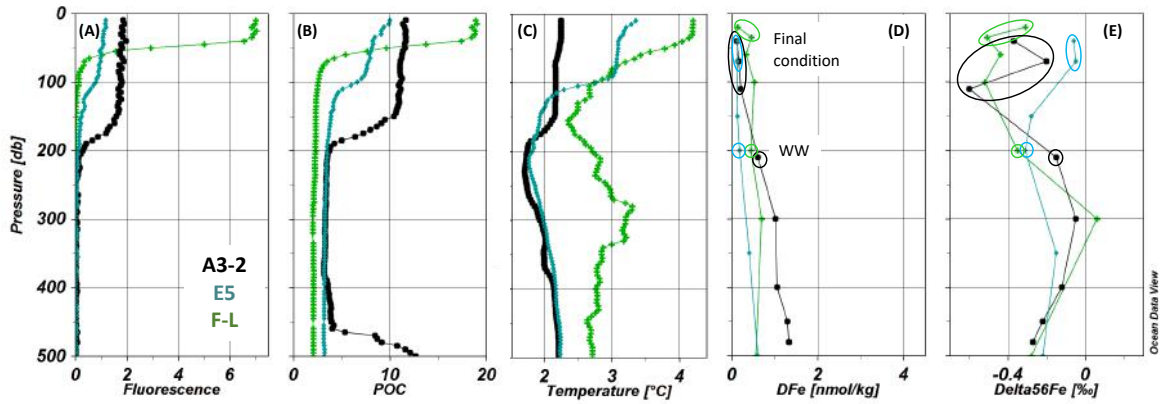

Figure 6. Profiles on the first 500 m of (A) Fluorescence, (B) POC, (C) Total Chlorophyll a, (D) dissolved iron (DFe), and (E) δ^{56}DFe values for KEOPS 2 stations A3-2, E5, and F-L. Ellipse indicated DFe and δ^{56}DFe samples chosen for biologic fractionation calculation at initial (Winter Water (WW)) and final conditions.

Fe isotopic fractionation associated with biological uptake is a debated topic. Radic et al (2011) and Ellwood (2015) suggested a preferential uptake of isotopically light δ^{56}DFe by phytoplankton in the seawater of the equatorial Pacific Ocean, and in subtropical waters within the mesoscale eddy field east of New Zealand, respectively. On the contrary, Conway et al (2014) observed isotopically light δ^{56}DFe associated with deep fluorescence maxima reflecting a possible preferential uptake of isotopically heavy Fe by phytoplankton in the North Atlantic, while Klar et al. (2018) also suggested a preferential uptake of heavy Fe isotopes from signals observed in remineralized Fe.

KEOPS 2 stations A3-2, E3, E5, and F-L were all sampled within the phytoplanktonic bloom (cf. the satellite-derived surface chlorophyll-a map of the Kerguelen area in Fig. 2). E3 has been shown to be impacted by significant external inputs, at 40 m depth, therefore these data cannot

be used to study phytoplankton uptake isotopic fractionation. The three other stations are used in the following. As indicated by the fluorescence and POC profiles (Fig. 6), at A3-2, three DFe samples at 39, 70, and 110 db were sampled in the chlorophyll maximum (upper 140 db) and display in average a DFe concentration of 0.17 ± 0.08 nmol/kg and a δ^{56}DFe of -0.39 ± 0.40 ‰. At E5, two DFe samples at 38, and 68 db were sampled in the chlorophyll maximum (upper 90 db) and display in average a DFe concentration of 0.14 ± 0.02 nmol/kg and a δ^{56}DFe of -0.06 ± 0.02 ‰. At F-L, two DFe samples at 18, and 34 db were sampled in the chlorophyll maximum (upper 35 db) and display in average a DFe concentration of 0.30 ± 0.46 nmol/kg and a δ^{56}DFe of -0.41 ± 0.28 ‰.

These samples associated with the fluorescence maxima may be considered as reflecting the impact of the biological uptake on the δ^{56}Fe of the surrounding seawater. They all present isotopically light δ^{56}DFe values possibly reflecting an isotopically heavy Fe uptake by phytoplankton. If some assumptions can be made on the initial concentration and isotope composition of the waters (before the onset of the bloom), then as in Radic et al (2011), assuming that the phytoplankton uptake follows a Rayleigh fractionation, the isotopic fractionation associated with the biological DFe removal can be estimated using the following equation :

$$\Delta^{56}Fe_{phyto\ DFe-SW\ DFE} \approx (\delta^{56}Fe^{f}_{SW\ DFe} - \delta^{56}Fe^{f=1}_{SW\ DFe})/\ln(f) \quad (4)$$

where f is the fraction of DFe remaining in the water relative to the initial DFe concentration, $\delta^{56}Fe^{f}_{SW\ DFe}$ the δ^{56}DFe of the seawater at a given f, and $\delta^{56}Fe^{f=1}_{SW\ DFe}$ the initial δ^{56}DFe of the seawater (f = 1).

The initial conditions can be estimated by the samples taken just below the mixed layer, in the so-called Winter Water, which is considered as the remnant of the winter mixed layer. At A3-2, the initial composition values were chosen at 210 db with a DFe concentration of 0.61 ± 0.03 nmol/kg and a δ^{56}DFe of -0.15 ± 0.07 ‰. At E5, they were chosen at 200 db with a DFe concentration of 0.19 ± 0.03 nmol/kg and a δ^{56}DFe of -0.31 ± 0.07 ‰. And at F-L, they were chosen at 100 db with a DFe concentration of 0.53 ± 0.03 nmol/kg and a δ^{56}DFe of -0.52 ± 0.07 ‰.

Comparison of the initial and final conditions suggests that there is a DFe biological uptake of 0.44, 0.05, and 0.23 nmol/kg at A3-2, E5, and F-L stations respectively. Following equation 4, we can calculate an isotopic fractionation of $\Delta^{56}Fe_{phyto\text{-}SW\ DFe}$ of 0.19 ± 0.23 ‰, -0.81 ± 0.38‰, and -0.19 ± 0.32‰ at A3-2, E5, and F-L stations respectively. These results present high uncertainties due to the high variability of DFe and δ^{56}DFe values in surface waters and do not allow to conclude about the isotopic fractionation associated to phytoplankton uptake in the Kerguelen area. The above-mentioned hypotheses may not be verified. In particular the initial conditions remain hypothetical. To better constrain these processes, incubation experiments were realized on board during KEOPS 2 at station E1. Unfortunately, filtration issues prevented to correctly separate the dissolved from the particulate (assumed to represent phytoplankton)

phases, so that the samples got lost. This kind of experiments seem however necessary to characterize phytoplankton uptake DFe isotopic fractionation.

5 Conclusions

This paper provides new insights into sedimentary DFe supply to the water column in the Kerguelen area (Southern Ocean), the evolution of the DFe isotopic signatures of the water mass between the zero meridian and the Kerguelen area, i.e. over ~4500km, and DFe isotope fractionation by phytoplankton uptake. Firstly, pore waters and sediment overlying seawater from the ~500 m deep central Kerguelen plateau reveal a high DFe enrichment of bottom waters associated to a heavy δ^{56}DFe signal that we attribute to non-reductive dissolution (NRD) of lithogenic material. Significant DFe removal at the interface is suggested to make the remaining DFe significantly heavier (around +1‰) than the pore waters themselves (around 0‰). However, this significantly positive δ^{56}DFe signature quickly vanishes as the distance from the sediment increases. It is not detectable more than 50 m above the sediments. This argues against a significant impact of this sediment source onto the surface waters.

Downstream of the Kerguelen Plateau within the chlorophyll plume, two profiles were obtained at the same station (station E) in a recirculation area, 14 days apart. They display very variable DFe concentrations and δ^{56}DFe signals. While E5 displays unperturbed and typical DFe profiles, E3 displays significant DFe enrichments associated to a light δ^{56}DFe signal at 40, 400, and 800 m. This light δ^{56}DFe enrichment at various depths suggest lateral supply of Fe from the Kerguelen Island margin by dissimilatory iron reduction (DIR) of lithogenic material. This result confirms that, as suggest by previous studies, station E is enriched in DFe originating from the Kerguelen Island margin by lateral supply rather than by vertical supply from the Plateau sediments.

A comparison between BGH station (along the 0° meridian) and KEOPS stations (around 70°E) allowed to examine the δ^{56}DFe signal variations within WW, A-AAIW, UCDW, and LCDW. While A-AAIW flowing around 600 and 1500 m display significant δ^{56}DFe variations, we observed that WW, UCDW and LCDW (flowing between 150-300 m, 450-900 m and 1000-1500 m respectively) δ^{56}DFe signals remain roughly constant.

We tried to determine the iron fractionation due to diatom uptake from the observed isotope composition of the surface waters with hypotheses about the initial conditions. This exercise was not conclusive. We suggest that incubation experiments should be carried out to better constrain isotopic fractionation due to phytoplankton uptake. This seems an essential step given the importance of the biological cycles on the iron oceanic cycle.

References

Abadie, C., Lacan, F., Radic, A., Pradoux, C., & Poitrasson, F. (2017). Iron isotopes reveal distinct dissolved iron sources and pathways in the intermediate versus deep Southern Ocean. *Proceedings of the National Academy of Sciences*, *114*(5), 858–863. https://doi.org/10.1073/pnas.1603107114

Beard, B. L., & Johnson, C. M. (2004). Fe Isotope Variations in the Modern and Ancient Earth and Other Planetary Bodies. *Reviews in Mineralogy and Geochemistry*, *55*(1), 319–357. https://doi.org/10.2138/gsrmg.55.1.319

Blain, S., Sarthou, G., & Laan, P. (2008). Distribution of dissolved iron during the natural iron-fertilization experiment KEOPS (Kerguelen Plateau, Southern Ocean). *Deep Sea Research Part II: Topical Studies in Oceanography*, *55*(5–7), 594–605.

Bowie, A. R., van der Merwe, P., Quéroué, F., Trull, T., Fourquez, M., Planchon, F., et al. (2015). Iron budgets for three distinct biogeochemical sites around the Kerguelen Archipelago (Southern Ocean) during the natural fertilisation study, KEOPS-2. *Biogeosciences*, *12*(14), 4421–4445. https://doi.org/10.5194/bg-12-4421-2015

Bucciarelli, E., Blain, S., & Treguer, P. (2001). Iron and manganese in the wake of the Kerguelen Islands (Southern Ocean). *Marine Chemistry*, *73*, 21–36.

Burdige, D. J. (2006). *Geochemistry of Marine Sediments*. Princeton University Press.

Canfield, D. E. (1989). Reactive iron in marine sediments. *Geochimica et Cosmochimica Acta*, *53*(3), 619–632. https://doi.org/10.1016/0016-7037(89)90005-7

Cavagna, A. J., Fripiat, F., Elskens, M., Mangion, P., Chirurgien, L., Closset, I., et al. (2015). Production regime and associated N cycling in the vicinity of Kerguelen Island, Southern Ocean. *Biogeosciences*, *12*(21), 6515–6528. https://doi.org/10.5194/bg-12-6515-2015

Chever, F., Rouxel, O. J., Croot, P. L., Ponzevera, E., Wuttig, K., & Auro, M. (2015). Total dissolvable and dissolved iron isotopes in the water column of the Peru upwelling regime. *Geochimica et Cosmochimica Acta*, *162*, 66–82. https://doi.org/10.1016/j.gca.2015.04.031

Conway, T. M., & John, S. G. (2014). Quantification of dissolved iron sources to the North Atlantic Ocean. *Nature*, *511*(7508), 212–215. https://doi.org/10.1038/nature13482

Ellwood, M. J., Hutchins, D. A., Lohan, M. C., Milne, A., Nasemann, P., Nodder, S. D., et al. (2015). Iron stable isotopes track pelagic iron cycling during a subtropical phytoplankton bloom. *Proceedings of the National Academy of Sciences*, *112*(1), E15–E20. https://doi.org/10.1073/pnas.1421576112

Homoky, W. B., John, S. G., Conway, T. M., & Mills, R. A. (2013). Distinct iron isotopic signatures and supply from marine sediment dissolution. *Nature Communications*, *4*. https://doi.org/10.1038/ncomms3143

John, S. G., Mendez, J., Moffett, J., & Adkins, J. (2012). The flux of iron and iron isotopes from San Pedro Basin sediments. *Geochimica et Cosmochimica Acta*, *93*, 14–29. https://doi.org/10.1016/j.gca.2012.06.003

John, S. G., Helgoe, J., Townsend, E., Weber, T., DeVries, T., Tagliabue, A., et al. (2018). Biogeochemical cycling of Fe and Fe stable isotopes in the Eastern Tropical South Pacific. *Marine Chemistry*, *201*, 66–76. https://doi.org/10.1016/j.marchem.2017.06.003

Johnson, C. M., Beard, B. L., & Roden, E. E. (2008). The iron isotope fingerprints of redox and biogeochemical cycling in the modern and ancient Earth. *Annual Review of Earth and Planetary Sciences*, *36*, 457–493.

Klar, J. K., Homoky, W. B., Statham, P. J., Birchill, A. J., Harris, E. L., Woodward, E. M. S., et al. (2017). Stability of dissolved and soluble Fe(II) in shelf sediment pore waters and

release to an oxic water column. *Biogeochemistry*, 1–19. https://doi.org/10.1007/s10533-017-0309-x

Klar, J. K., Schlosser, C., Milton, J. A., Woodward, E. M. S., Lacan, F., Parkinson, I. J., et al. (2018). Sources of dissolved iron to oxygen minimum zone waters on the Senegalese continental margin in the tropical North Atlantic Ocean: Insights from iron isotopes. *Geochimica et Cosmochimica Acta*, *236*, 60–78. https://doi.org/10.1016/j.gca.2018.02.031

Klar, Jessica K., James, R. H., Gibbs, D., Lough, A., Parkinson, I., Milton, J. A., et al. (2017). Isotopic signature of dissolved iron delivered to the Southern Ocean from hydrothermal vents in the East Scotia Sea. *Geology*, *45*(4), 351–354. https://doi.org/10.1130/G38432.1

Labatut, M., Lacan, F., Pradoux, C., Chmeleff, J., Radic, A., Murray, J. W., et al. (2014). Iron sources and dissolved-particulate interactions in the seawater of the Western Equatorial Pacific, iron isotope perspectives. *Global Biogeochemical Cycles*, *28*(10), 1044–1065. https://doi.org/10.1002/2014GB004928

Lacan, F., Radic, A., Jeandel, C., Poitrasson, F., Sarthou, G., Pradoux, C., & Freydier, R. (2008). Measurement of the isotopic composition of dissolved iron in the open ocean. *Geophysical Research Letters*, *35*(24). https://doi.org/10.1029/2008GL035841

Lacan, Francois, Radic, A., Labatut, M., Jeandel, C., Poitrasson, F., Sarthou, G., et al. (2010). High-Precision Determination of the Isotopic Composition of Dissolved Iron in Iron Depleted Seawater by Double Spike Multicollector-ICPMS. *Analytical Chemistry*, *82*(17), 7103–7111. https://doi.org/10.1021/ac1002504

Lasbleiz, M., Leblanc, K., Blain, S., Ras, J., Cornet-Barthaux, V., Hélias Nunige, S., & Quéguiner, B. (2014). Pigments, elemental composition (C, N, P, and Si), and stoichiometry of particulate matter in the naturally iron fertilized region of Kerguelen in the Southern Ocean. *Biogeosciences*, *11*(20), 5931–5955. https://doi.org/10.5194/bg-11-5931-2014

van der Merwe, P., Bowie, A. R., Quéroué, F., Armand, L., Blain, S., Chever, F., et al. (2015). Sourcing the iron in the naturally fertilised bloom around the Kerguelen Plateau: particulate trace metal dynamics. *Biogeosciences*, *12*(3), 739–755. https://doi.org/10.5194/bg-12-739-2015

Moore, J. K., & Braucher, O. (2008). Sedimentary and mineral dust sources of dissolved iron to the world ocean. *Biogeosciences*, *5*(3), 631–656.

Morel, F. M. M., & Price, N. M. (2003). The Biogeochemical Cycles of Trace Metals in the Oceans. *Science*, *300*(5621), 944–947. https://doi.org/10.1126/science.1083545

Park, Y.-H., Roquet, F., Durand, I., & Fuda, J.-L. (2008). Large-scale circulation over and around the Northern Kerguelen Plateau. *Deep Sea Research Part II: Topical Studies in Oceanography*, *55*(5–7), 566–581.

Park, Young-Hyang, Durand, I., Kestenare, E., Rougier, G., Zhou, M., d'Ovidio, F., et al. (2014). Polar Front around the Kerguelen Islands: An up-to-date determination and associated circulation of surface/subsurface waters. *Journal of Geophysical Research: Oceans*, *119*(10), 6575–6592. https://doi.org/10.1002/2014JC010061

Quéroué, F., Sarthou, G., Planquette, H. F., Bucciarelli, E., Chever, F., van der Merwe, P., et al. (2015). High variability in dissolved iron concentrations in the vicinity of the Kerguelen Islands (Southern Ocean). *Biogeosciences*, *12*(12), 3869–3883. https://doi.org/10.5194/bg-12-3869-2015

Radic, A., Lacan, F., & Murray, J. W. (2011). Isotopic composition of dissolved iron in the equatorial Pacific Ocean: new constraints for the oceanic iron cycle. *Earth And Planetary Science Letters*, *306*, 1–10. https://doi.org/10.1016/j.epsl.2011.03.015

Sanial, V., van Beek, P., Lansard, B., Souhaut, M., Kestenare, E., d'Ovidio, F., et al. (2015). Use of Ra isotopes to deduce rapid transfer of sediment-derived inputs off Kerguelen. *Biogeosciences*, *12*(5), 1415–1430. https://doi.org/10.5194/bg-12-1415-2015

Severmann, S., Johnson, C. M., Beard, B. L., & McManus, J. (2006). The effect of early

diagenesis on the Fe isotope compositions of porewaters and authigenic minerals in continental margin sediments. *Geochimica et Cosmochimica Acta*, *70*, 2006-2022. doi:10.1016/j.gca.2006.01.007.

Severmann, S., McManus, J., Berelson, W. M., & Hammond, D. E. (2010). The continental shelf benthic iron flux and its isotope composition. *Geochimica et Cosmochimica Acta*. https://doi.org/10.1016/j.gca.2010.04.022

Tagliabue, A., Bowie, A. R., Boyd, P. W., Buck, K. N., Johnson, K. S., & Saito, M. A. (2017). The integral role of iron in ocean biogeochemistry. *Nature*, *543*(7643), 51–59. https://doi.org/10.1038/nature21058

Talley, L. D., Pickard, G. L., Emery, W. J., & Swift, J. H. (2011). *Descriptive Physical Oceanography: an introduction* (6th ed). Academic Press Elsevier.

Volk, T., & Hoffert, M. I. (1985). Ocean carbon pumps: analysis of relative strengths and efficiencies in ocean-driven atmospheric CO2 changes. *The Carbon Cycle and Atmospheric CO 2 : Natural Variations Archean to Present. Chapman Conference Papers, 1984*, 99–110

4.5.3 Matériel complémentaire

Goflo Cast	GoFlo bottle	Pressure (db)	[DFe] (nmol kg-1)	[DFe] uncertainty	δ^{56}DFe (‰)	δ^{56}DFe uncertainty (‰)	θ (°C)	S	[O_2] (µmol/kg)	σ_θ (kg/m3)	γ (kg/m3)	Water Mass
KEOPS2, station A3-2, start 5:42pm 50° 37.4450'S-072° 03.2970'E, end 6:09pm 50° 37.4467'S-072° 03.2991'E, Cast Goflo 1-2-3-4-5-7-8-9-11-12, 16/11/2011, bottom depth = 530 m												
259	11&12	39	0,13	0,03	-0,37	0,07	2,19	33,91	334,5	27,08	27,24	
259	9	70	0,17	0,03	-0,20	0,07	2,17	33,91	333,0	27,09	27,24	
259	7&8	110	0,21	0,03	-0,60	0,07	2,15	33,91	332,0	27,09	27,25	
259	5	210	0,61	0,03	-0,15	0,07	1,70	33,98	294,9	27,18	27,33	WW
259	4	300	1,02	0,03	-0,05	0,07	2,00	34,16	242,0	27,30	27,46	WW
259	3	400	1,06	0,03	-0,12	0,07	2,12	34,30	210,9	27,40	27,59	
259	2	450	1,30	0,03	-0,22	0,07	2,17	34,36	197,7	27,45	27,64	UCDW
259	1	480	1,34	0,03	-0,27	0,07	2,18	34,35	204,3	27,44	27,68	UCDW
KEOPS2, station NP-FL, start 2:30pm 48° 37.1300'S-074° 48.2600'E, end 3:48pm 48° 37.1700'S-074° 48.3231'E, Cast Goflo 1-2-3-4-5-6-7-8-9-10-11-12, 07/11/2011, bottom depth = 2700 m												
190	11&12	18	0,14	0,03	-0,31	0,07	4,10	33,75	338,9	26,78	26,88	
190	9&10	34	0,46	0,03	-0,51	0,07	3,95	33,76	329,4	26,80	26,88	
190	8	60	0,34	0,03	-0,44	0,07	3,40	33,78	314,8	26,88	26,99	
190	7	100	0,53	0,03	-0,52	0,07	2,85	33,86	304,1	26,99	27,14	
190	6	200	0,45	0,03	-0,35	0,07	2,69	34,02	271,9	27,13	27,30	
190	5	300	0,70	0,03	0,06	0,07	2,98	34,21	224,8	27,26	27,45	A-AAIW
190	4	500	0,57	0,03	-0,28	0,07	2,65	34,37	189,5	27,42	27,63	UCDW
190	3	800	0,66	0,03	-0,11	0,07	2,42	34,56	174,6	27,58	27,80	UCDW
190	2	1000	0,93	0,03	0,05	0,07	2,40	34,65	177,5	27,66	27,89	
190	1	1300	0,60	0,03	-0,22	0,07	2,19	34,72	185,5	27,73	27,97	LCDW
KEOPS2, station E3, start 1:13 pm 48° 41.9899'S-071° 58.0161'E, end 2:14pm 48° 41.9870'S-071° 58.0150'E, Cast Goflo 1-2-3-4-5-6-7-9-10-11-12, 03/11/2011, bottom depth = 1750 m												
149	11&12	19	0,11	0,03	-0,26	0,07	3,01	33,84	7,59	26,96	27,10	
149	9&10	40	1,56	0,03	-0,98	0,07	2,74	33,85	7,62	26,99	27,13	
149	7	200	0,42	0,03	0,00	0,07	1,82	33,97	6,55	27,17	27,33	WW
149	6	300	0,68	0,03	-0,40	0,07	2,05	34,22	5,14	27,35	27,54	
149	5	400	1,09	0,03	-0,72	0,08	2,12	34,34	4,68	27,43	27,64	
149	4	600	0,60	0,03	-0,28	0,07	2,28	34,53	4,03	27,58	27,79	UCDW
149	3	800	0,76	0,03	-0,49	0,14	2,22	34,61	4,06	27,65	27,87	UCDW
149	2	1000	0,47	0,03	-0,02	0,07	2,17	34,66	4,11	27,69	27,92	
149	1	1300	0,51	0,03	-0,05	0,07	2,06	34,72	4,27	27,75	27,99	LCDW
KEOPS2, station E5, start 09:58 am 48° 24.7030'S-071° 53.9730'E, end 11:17 am 48° 24.7040'S-071° 53.9710'E, Cast Goflo 1-2-3-4-5-6-7-8-9-10-11-12, 19/11/2011, bottom depth = 1920 m												
290	11&12	38	0,15	0,03	-0,06	0,07	3,09	33,85	7,45	26,96	27,09	
290	9&10	68	0,13	0,03	-0,05	0,07	3,06	33,85	7,42	26,96	27,09	
290	8	150	0,14	0,03	-0,28	0,07	1,93	33,89	7,36	27,09	27,25	WW
290	7	200	0,19	0,03	-0,31	0,07	1,81	33,95	6,89	27,14	27,31	WW
290	6	350	0,41	0,03	-0,15	0,07	2,07	34,30	4,80	27,41	27,61	
290	5	500	0,61	0,03	-0,22	0,10	2,21	34,45	4,31	27,51	27,73	
290	4	700	0,54	0,03	-0,09	0,07	2,24	34,56	4,07	27,60	27,83	UCDW
290	3	900	0,42	0,03	-0,18	0,07	2,24	34,64	4,04	27,67	27,89	UCDW
290	2	1100	0,53	0,03	-0,14	0,10	2,17	34,69	4,16	27,72	27,95	
290	1	1300	0,53	0,03	-0,16	0,07	2,04	34,73	4,28	27,75	27,99	LCDW

Table S1. Bottle data from the KEOPS2 cruise. DFe and δ^{56}DFe uncertainties are given at the 95% confidence level.

Goflo Cast	GoFlo bottle	Pressure (db)	[DFe] (nmol kg-1)	[DFe] uncertainty	δ^{56}DFe (‰)	δ^{56}DFe uncertainty (‰)	θ (°C)	S	[O_2] (µmol/kg)	σ_θ (kg/m3)	γ (kg/m3)	Water Mass
KEOPS1, station C11, 51.63°S-77.96°E, 26/01/2005, bottom depth = 3350 m												
GONI #12	10	1008	0,9	0,01	-0,11	0,07	2,00	34,73	4,27	27,76	28,00	LCDW
GONI #14	8	2020	0,64	0,01	-0,07	0,07	1,31	34,75	4,60	27,83	28,12	LCDW
GONI #14	10	2531	0,61	0,01	0,06	0,07	0,96	34,73	4,66	27,837	28,159	
KEOPS1, station C5, 52.38°S-75.59°E, 52.38°S-75.59°E, 07/02/2005, bottom depth = 562 m												
GONI #28	8	450	0,93	0,01	-0,51	0,07	2,17	34,41	4,69	27,49	27,69	UCDW
GONI #28	9	508	4,11	0,01	0,29	0,07	2,08	34,43	4,83	27,51	27,72	
KEOPS1, station A3, 50.63°S-72.08°E, 11/02/2005, CTD bottom depth = 530 m												
GONI #33		509	4,76	0,01	0,35	0,07	2,15	34,38	4,60	27,47	27,67	
KEOPS1, station KERFIX, 50.67°S-68.41°E, 10/02/2005, CTD bottom depth = 1614 m												
GONI #32	10	1500	0,55	0,01	-0,07	0,07	1,79	34,76	4,60	27,80	28,06	LCDW

Table S2. Bottle data from the KEOPS1 cruise. DFe and δ^{56}DFe uncertainties are given at the 95% confidence level.

Nom Ech	Depth (cm)	[DFe] (nmol kg-1)	[DFe] uncertainty	δ^{56}DFe (‰)	δ^{56}DFe uncertainty (‰)
KEOPS1, station A3, MUCO-01, 50.63°S-72.08°E, 23/01/2005,overlying water oxygen = 222 µM, oxygen penetration depth = 6 mm, bottom depth = 530 m					
A3-1	0,25	85,95	0,55	-0,06	0,05
A3-2	0,75	4770,60	20,82	0,17	0,04
A3-3	1,25	242,61	1,55	0,06	0,04
KEOPS1, station B5, MUCO-03, 51.10°S-74.60°E, 01/02/2005, overlying water oxygen = 197 µM, oxygen penetration depth = 9 mm, bottom depth = 545 m					
B5-ES	-0,5	14,41	0,09	0,64	0,06
B5-1	0,25	147,57	0,15	-0,02	0,04
B5-2	0,75	61,01	0,39	0,05	0,03
B5-3	1,25	199,42	0,24	0,05	0,04
B5-5	2,25	1563,54	52,77	-0,08	0,07
KEOPS1, station C5, MUCO-05, 52.38°S-75.59°E, 07/02/2005,overlying water oxygen = 216 µM, oxygen penetration depth = 7 mm, bottom depth = 562 m					
C5-ES	-0,5	77,10	0,09	1,26	0,00
C5-1	0,25	83,79	0,54	-0,18	0,06
C5-2	0,75	167,22	1,07	0,09	0,05
C5-3	1,25	64,56	0,42	-0,26	0,06
C5-4	1,75	95,68	0,62	-0,13	0,07
C5-5	2,25	119,64	0,77	-0,08	0,06
KEOPS1, station C11, MUCO-02, 51.63°S-77.96°E, 28/01/2005, overlying water oxygen = 235 µM, oxygen penetration depth >40 mm, bottom depth = 3350 m					
C11-1	0,25	354,28	0,03	0,06	0,00
C11-2	0,75	64,74	0,41	-0,24	0,04
C11-4	1,75	36,86	0,24	0,33	0,07

Table S3. Pore water data from the KEOPS1 cruise. DFe and δ^{56}DFe uncertainties are given at the 95% confidence level.

4.6 Conclusion

Dans le contexte des campagnes KEOPS 1 et 2, nos mesures de concentrations et d'isotopes du fer dissous apportent de nouvelles informations sur les processus à l'origine de la fertilisation naturelle en fer dissous de la zone du plateau des Kerguelen. Elles nous renseignent aussi sur la stabilité des signatures isotopiques des masses d'eau sur plus de 4500 km. Cette étude montre qu'il est difficile de déterminer le fractionnement isotopique du fer dû à la consommation phytoplanctonique à partir d'échantillons prélevés ponctuellement dans la colonne d'eau. Nous concluons qu'il semble incontournable de réaliser des expériences d'incubation pour déterminer ces fractionnements. De telles expériences avaient été réalisées à bord, leurs concentrations et composition isotopique de Fe ont été mesurées au cours de cette thèse (résultats non présentés dans ce manuscrit) mais des problèmes de filtration à bord n'ont pas permis d'exploiter les échantillons. Nous suggérons donc le renouvèlement de ce type d'expérience dans le futur.

5 Conclusions et perspectives

5.1 Conclusions

L'objectif général de cette thèse était de progresser sur la compréhension des cycles biogéochimiques océaniques (sources, cycles internes, puits) à l'aide des traceurs que constituent la concentration en aluminium dissous et la composition isotopique du fer dissous dans l'eau de mer, combinées à des outils hydrodynamiques.

L'aluminium étant considéré comme un traceur lithogénique, nous nous sommes intéressés à l'étude de sa distribution (concentration) dans l'Atlantique Nord subtropical, une zone fortement influencée par les dépôts de poussières atmosphériques principalement d'origine saharienne. Le fer étant un micronutriment essentiel à la production primaire, nous nous sommes intéressés à sa distribution et à sa signature isotopique au niveau d'une zone naturellement fertilisée de l'océan Austral, les îles Kerguelen. Ces études, ont été réalisées dans le cadre de trois « process study » GEOTRACES : GApr08 pour l'Al et KEOPS 1&2 pour le Fe. Ce cadre GEOTRACES nous a permis un accès simple aux autres données collectées au cours de ces campagnes, ce qui s'est révélé d'une grande utilité notamment pour la réalisation d'une analyse de masses d'eau dans l'Atlantique Nord subtropical.

Plus précisément, nous avons réalisé au cours de cette thèse (i) une analyse de masse d'eau combinant pour la première fois une analyse multiparamétrique de masse d'eau (extented Optimum Multiparameter Analysis, eOMPA) à une étude de rétro-trajectoires modélisées (Lagrangian Particule Tracking Experiment, LPTE), (ii) des mesures de concentrations de dAl dans l'Atlantique Nord subtropical que nous avons interprétées, dans la couche de surface, à l'aide d'un modèle 1D - d'advection-dépôt de poussières et, dans les couches intermédiaires et profondes, en utilisant les résultats de l'analyse de masse d'eau pour déconvoluer les composantes transportées par les masses d'eau de celles résultant de processus biogéochimiques, et (iii) des mesures de concentrations et d'isotopes de dFe dans la région des îles Kerguelen.

Dans l'introduction générale, section 1.4, nous avions mis en lumière certains points qui restent à résoudre pour mieux comprendre les cycles biogéochimiques des métaux traces. Les travaux présentés dans cette thèse nous ont permis d'avancer sur ces points et de dégager les résultats suivants :

- **Au niveau des sources externes**

  - **Sources atmosphériques** : Dans le cadre du programme GEOTRACES, les dépôts atmosphériques sont souvent estimés à partir d'un modèle dit "MADCOW" dont le principe est de combiner des mesures de concentrations d'aluminium en surface avec une estimation du temps de résidence de cet élément dans la couche mélangée de surface afin d'en dériver un flux de dépôt atmosphérique d'aluminium (Measures & Brown, 1996; Measures & Vink, 2000). De là, en utilisant des rapports de concentrations entre l'aluminium et d'autres éléments (ex. le fer) dans ces dépôts atmosphériques, les flux de dépôts atmosphériques de ces éléments peuvent être estimés. Outre le fait que ces estimations sont linéairement liées à la valeur du temps de résidence utilisé (ce qui peut entrainer des incertitudes importantes), cette méthode néglige les transports horizontaux. Les données d'aluminium de la campagne GApr08 le long de 22 °N dans l'Atlantique, sous le panache de poussières sahariennes montrent que, même dans cette zone où les dépôts sont particulièrement intenses, le transport horizontal par les courants de surface est un facteur majeur du cycle de l'aluminium dans la couche de mélange. Négliger ce transport, comme cela est fait dans de nombreux travaux utilisant le modèle MADCOW (Measures et al., 2005; Measures & Brown, 1996; Measures & Vink, 2000; Menzel Barraqueta et al., 2018), semble par conséquent injustifié et source potentielle d'erreurs.

  - **Sources fluviales** : La dissolution de particules lithogéniques déchargées par les rivières sur les marges continentales a été proposée comme une source significative voire dominante de certains éléments à l'océan. Cela a été le cas pour certains traceurs notamment les terres rares dont le néodyme, et pour des micronutriments, notamment le fer (Beghoura et al., 2019; Lacan & Jeandel, 2001; Mackey et al., 2002). Ce type de processus a notamment été mis en évidence dans des régions à fortes topographies et fortes précipitations qui engendrent de fortes érosions (ex. la Papouasie Nouvelle Guinée; Lacan & Jeandel, 2001; Milliman et al., 1999). Les excès d'aluminium que nous avons documentés dans l'ouest de la section GApr08 (vers 58°W 22°N) suggèrent que ce type de processus participe aussi de manière significative au cycle océanique de l'aluminium. Nous soulignons que, contrairement à ce qui est trop souvent considéré, l'aluminium dissous n'est pas simplement un traceur des dépôts atmosphériques (“a dust tracer” Han et al., 2008; Middag et al., 2015; Tria et al., 2007), il doit avant tout être considéré comme un traceur d'apports lithogéniques.

  - **Sources sédimentaires** : Les mécanismes à l'œuvre à l'interface sédiment/océan restent très mal connus. Ils peuvent dépendre des éléments et des conditions environnementales. Les isotopes du fer suggèrent en effet deux types de processus distincts à cette interface : la réduction dissimilatoire du fer (DIR) qui a lieu dans des conditions anoxiques et la dissolution non réductrice (NRD) qui serait indépendante des conditions redox. Nous avons pu observer ces deux processus de DIR et de NRD de matériel lithogénique sédimentaire au niveau de la marge des îles Kerguelen et des sédiments du plateau (situé à 500 m de fond) respectivement. Nous suggérons que la

floraison phytoplanctonique au voisinage des îles Kerguelen est davantage liée à l'apport latéral de fer provenant de la marge des îles par un processus de DIR du matériel lithogénique sédimentaire plutôt qu'à un apport vertical de fer provenant des sédiments du plateau par un processus de NRD du matériel lithogénique. Contrairement au fer, l'aluminium ne semble pas impacté par les cycles redox. Nous suggérons donc que le processus de relargage d'aluminium à partir des sources sédimentaires se rapproche du processus de NDR défini initialement pour le fer.

- **Sources hydrothermales** : Depuis quelque années, l'idée que les sources hydrothermales ne constituent pas une source majeure de métaux traces à l'océan a été remise en question pour certains éléments. L'hydrothermalisme est aujourd'hui considéré comme une source majeure de dFe à l'océan et cette source est intégrée dans les modèles biogéochimiques de fer (Resing et al., 2015; Tagliabue et al., 2010). L'importance de l'hydrothermalisme comme source de dAl fait encore débat. Certaines études estiment que cette source est négligeable (Middag, 2010; van Hulten et al., 2013) d'autres qu'elle est significative (Measures et al., 2015; Resing et al., 2015). Un résultat particulièrement marquant est celui de Resing et al (2015) qui observe dans le Pacifique Est un transport de dAl à plus de 3000 km de la source hydrothermale. Cependant, à l'heure actuelle les sources hydrothermales de dAl sont encore négligées dans les modèles biogéochimiques d'aluminium (van Hulten et al., 2013). Nos mesures de dAl dans l'Atlantique Nord subtropical montrent un apport local significatif de dAl à des profondeurs de plus de 3340 m au niveau de la source hydrothermale Snakepit. Cependant nous n'observons pas de transport de ce signal à plus de 500 km de distance de la source. Cela nous amène à nous interroger sur les processus responsables du transport de dAl et des autres éléments dans l'océan profond.

- **Au niveau des cycles internes** :

  - **Interaction dissous-particules** : Dans l'Atlantique Nord subtropical, entre 200 et 800m, alors qu'on se situe dans une zone de fort dépôts atmosphériques (sous le panache saharien), nous avons observé de manière inattendue, voire même paradoxale, que les fortes concentrations de dAl résultent du transport océanique et non pas d'une dissolution des particules. En effet, le bilan net des interactions dissous-particules révèle au contraire une soustraction de dAl à ces profondeurs, probablement par adsorption sur les particules.

    En dessous de 1000 m, l'effet des interactions dissous-particules semble s'inverser et devenir une source nette de dAl. Nous proposons donc que le scavenging réversible ou la dissolution d'aluminium particulaire constitue une source de dAl en profondeur. Le processus de scavenging réversible a été montré dans des études précédentes comme étant une source en profondeur de thorium, protactinium, terres rares, cuivre, fer, et zinc dissous (Abadie et al., 2017; Bacon & Anderson, 1982; Little et al., 2013; Nozaki & Alibo, 2003; Roy-Barman et al., 1996; Tagliabue et al., 2018). Van Hulten (2013) propose, à notre connaissance, la seule étude de modélisation qui inclut ce type de processus pour l'aluminium. Ce type de comportement, lié aux interactions

dissous/particules, qui résulte en une soustraction d'espèces dissoutes dans la partie supérieure de la colonne d'eau et en une source d'espèces dissoutes dans la partie profonde de la colonne d'eau, a notamment été proposé précédemment pour les terres rares dans l'Atlantique tropical (Tachikawa et al. 1999).

- **Hydrodynamique** : La prise en compte de l'hydrodynamique a été essentielle, pour interpréter la distribution de dAl dans l'Atlantic Nord subtropical. Sans cette prise en compte, il aurait été très difficile de comprendre le gradient de dAl mesuré en surface et il n'aurait pas été possible de voir l'effet des interactions dissous-particules sur la distribution de dAl notamment avec la soustraction de dAl dans les 800 premiers mètres et l'enrichissement de dAl en dessous de 1000 m. Malheureusement, un tel travail n'a pas pu être réalisé dans le cadre des projets KEOPS. Néanmoins, la prise en compte de manière qualitative de la circulation et du transport du fer par les masses d'eau, suggère l'importance du transport horizontal dans les distributions de dFe observées à KEOPS (ce qui a également été mis en évidence dans d'autres études, ex. Bowie et al., 2015; Quéroué et al., 2015). Ainsi ces deux études concourent à la même conclusion : la prise en compte quantitative du transport par les masses d'eau est essentielle pour la compréhension des cycles biogéochimiques. Et ceci, non seulement dans des zones dynamiques ou côtières, telle la zone des campagnes KEOPS, mais aussi au large tel que dans l'Atlantique tropical.

- **Au niveau des trajectoires des masses d'eau** :

Notre analyse de masses d'eau dans l'Atlantique Nord subtropical nous a notamment permis d'obtenir trois résultats inattendus. (i) Bien que la contribution de la *Mediterranean Water* soit majoritaire à 700 m de profondeur, il semble que cette masse d'eau soit présente jusqu'à une profondeur de 3500 m (même si en faible quantité, de l'ordre de 5%). (ii) Nous suggérons que la *Labrador Sea Water* coule vers le sud depuis l'Atlantique Nord Est jusqu'à l'est de l'Atlantique subtropical. (iii) La *North West Atlantic Bottom Water* est présente dans des proportions significatives à l'est de la dorsale médio-atlantique, ce qui suggère que cette masse d'eau traverse la dorsale, probablement par la zone de fracture de Kane. Ces résultats jusqu'à présent non identifiés illustrent que certaines incertitudes demeurent sur la circulation des masses d'eau profondes. Même s'il est vrai que la circulation profonde a un impact moins direct sur la production primaire et le climat que la circulation de surface, il est essentiel de bien la décrire et de bien la comprendre. En effet, il existe des sources profondes d'éléments à l'océan (hydrothermalisme, remobilisation sédimentaire) dont l'impact potentiel sur les grands cycles océaniques et la production primaire reste à comprendre et à quantifier. Pour cela, une bonne modélisation de la circulation profonde et des processus de mélange verticaux est nécessaire.

5.2 Perspectives

Au cours de cette thèse, je me suis posée de nombreuses questions qui conduisent aux perspectives suivantes :

- **Au niveau des sources externes**

  - **Sources atmosphériques** : Lors de la réalisation de notre modèle 1D- d'advection-dépôt de poussières atmosphériques dans les eaux de surface de l'Atlantique Nord subtropical, plusieurs hypothèses ont été faites. L'une d'elle concerne la solubilité de l'aluminium provenant des poussières atmosphériques. Cette solubilité est estimée avec une gamme de variation très large de 0.2%-87% dans l'Atlantique (Baker et al., 2013). Ces larges gammes de solubilité sont aussi observées pour d'autres éléments comme le fer (0.1%-98% dans l'Atlantique, Sholkovitz et al., 2012), ou encore le manganèse (4.5%-96% dans l'Atlantique, Baker et al., 2013). Ces gammes de variation engendrent de grandes incertitudes dans l'estimation des flux de métaux dissous issus des dépôts atmosphériques. Ces solubilités variant en fonction du type de dépôts atmosphériques, de la région source de poussières atmosphériques, de la saison d'échantillonnage, ou encore de la méthode de mesure, il serait idéal de réaliser des mesures de solubilité de métaux lors de chaque campagne océanographique en se basant sur une méthode identique pour réellement estimer l'apport atmosphérique des métaux traces à l'océan.
    Au cours de cette thèse, nous avons réalisé l'importance de la prise en compte des processus d'advection en plus du dépôt de poussières atmosphériques pour expliquer la distribution de dAl dans l'Atlantique le long de 22 °N. Ce processus est systématiquement négligé dans le modèle « MADCOW ». De plus, le temps de résidence est également une hypothèse forte de ce modèle. Nous suggérons donc d'utiliser d'autre techniques que la mesure de dAl pour estimer les flux de dépôts atmosphériques à l'océan. Parmi ces techniques, on peut citer la mesure du radionucléide beryllium-7 dans les aérosols, ou des isotopes du thorium dans les eaux de surface (Anderson et al., 2016). L'avantage de ces techniques est qu'elles exploitent la radioactivité naturelle qui inclut une dimension temporelle et ainsi permettent de mesurer directement des flux (contrairement au modèle MADCOW dont la dimension temporelle provient du temps de résidence de dAl qui n'est généralement pas mesuré, mais prescrit). Ces deux techniques ont notamment déjà été utilisées pour quantifier les flux de poussières atmosphériques lors des campagnes US-GEOTRACES Atlantique 2010 et 2011.
  - **Sources sédimentaires** : Les mesures d'isotopes du fer ont révélé un apport vertical de dFe provenant de sources sédimentaires non réductrices (NRD) au niveau du plateau des Kerguelen mais également un apport latéral de dFe provenant de sources sédimentaires réductrices (DIR) des île Kerguelen. Quels sont les facteurs qui conduisent à ces deux processus différents de remobilisation sédimentaire au sein d'une même zone d'étude ? Plus généralement, les sources sédimentaires de métaux traces à l'océan posent de nombreuses questions. Quels sont les métaux libérés par les

sédiments ? Quels sont les flux ? Quels sont les processus impliqués ? Quels sont les processus qui permettent de stabiliser les éléments libérés sous formes dissoutes ? Pour répondre à ces questions nous suggérons la mise en place d'expériences à l'interface sédiment/océan. Pour étudier quels métaux sont libérés par les sédiments et pour caractériser les flux associés, des séries temporelles de mesures de métaux traces pourraient être réalisées en milieu naturel ou en laboratoire dans des réacteurs propres. En laboratoire, il serait possible de faire varier différents paramètres physico-chimiques (T, O2, pH, énergie cinétique) et l'effet de la biologie pourrait également être testé. En plus des informations fournies par les mesures de concentrations de métaux traces provenant de séries temporelles, les mesures isotopiques apporteraient des informations complémentaires sur les processus qui sous-tendent ces flux. De nouvelles connaissances sur les paramètres contrôlant les sources de micronutriments à l'interface sédiment/océan contribueront à améliorer les modèles biogéochimiques océaniques.

- **Au niveau des cycles internes**

  - **Interactions dissous-particules** : Il est apparu que les interactions dissous-particules jouent un rôle majeur dans le cycle du dAl et du dFe dans l'océan (érosion, scavenging réversible, remobilisation sédimentaire etc.). Cependant pour les deux éléments étudiés au cours de cette thèse nous avons été limités par le manque de données d'aluminium et de fer particulaire. Il nous aurait été particulièrement utile d'avoir des mesures d'aluminium particulaire dans le panache de l'Amazone et à proximité des petites Antilles pour valider notre hypothèse sur les sources de dAl à l'ouest de l'Atlantique Nord subtropical. L'échantillonnage des particules pour des mesures d'isotopes du fer aurait également été un véritable plus pour mieux comprendre les processus dissous-particules, observés aux interfaces ou dans la colonne d'eau, sur les campagnes KEOPS. Les mesures de métaux dans les phases dissoutes restent aujourd'hui beaucoup plus nombreuses que les mesures dans les phases particulaires. Les données d'aluminium particulaire vs dissoutes mesurées au cours des campagnes GEOTRACES l'illustrent parfaitement (Figure 27). Cependant ces dernières années, beaucoup plus de données de particules ont été produites. Il serait vraiment très intéressant d'échantillonner systématiquement les phases dissoutes et particulaires des éléments. Idéalement, il serait encore plus intéressant de réussir à échantillonner de façon plus systématique les différentes formes physique et chimiques (différentes spéciations) des éléments dans chacune de ces phases.

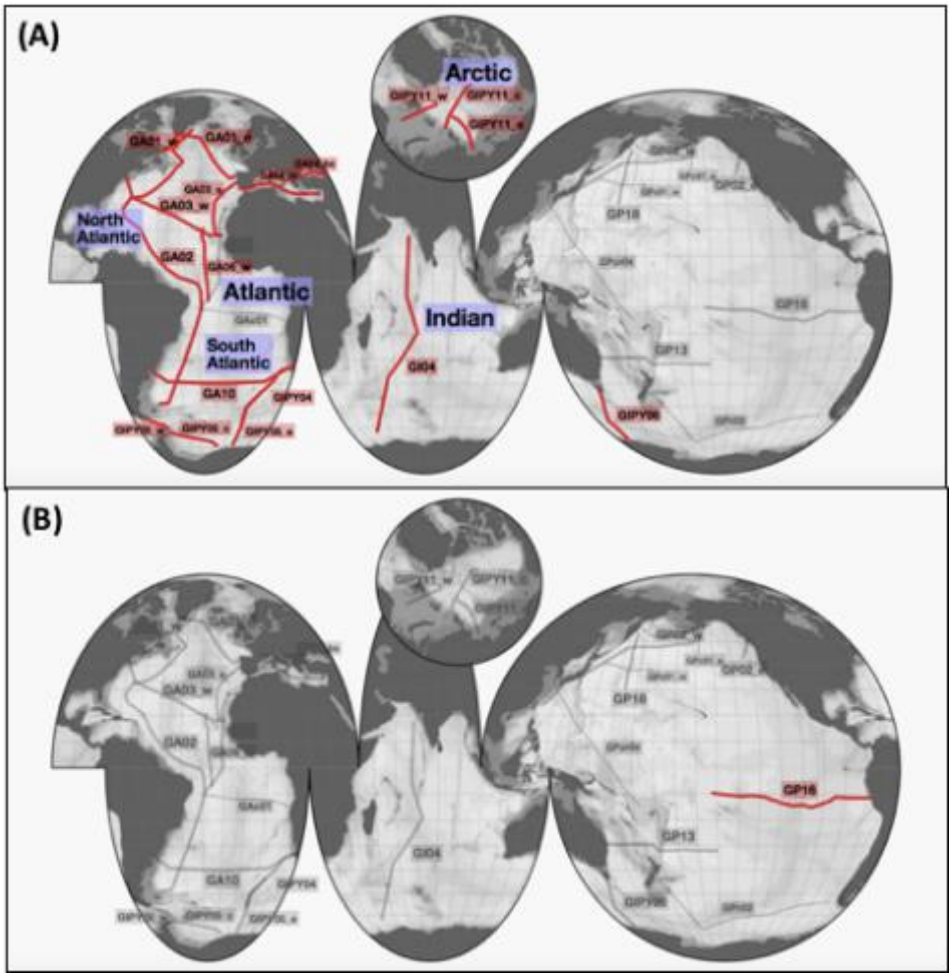

Figure 27 : Sont indiquées en rouge, les campagnes GEOTRACES durant lesquelles ont été réalisées des mesures (A) d'aluminium dissous et (B) d'aluminium particulaire, telles que dans l'intermediate data product 2017 (eGEOTRACES Electronic Atlas, Schlitzer et al., 2018).

- **Impact de la biologie** : Au cours de cette thèse nous ne sommes pas parvenus à estimer de manière concluante le fractionnement isotopique du fer lié à l'assimilation phytoplanctonique à partir des mesures in situ. Des problèmes de filtration lors d'expériences d'incubation à bord de KEOPS 2 ne nous ont pas non plus permis de conclure sur ce point. Il est cependant absolument nécessaire au vu de l'importance des cycles biologiques sur le cycle du fer d'être capable de quantifier ce fractionnement isotopique. Nous suggérons la mise en place d'autres expériences d'incubation du type de celles mise en place pour KEOPS 2 à l'avenir.

6 Références

Abadie, C., Lacan, F., Radic, A., Pradoux, C., & Poitrasson, F. (2017). Iron isotopes reveal distinct dissolved iron sources and pathways in the intermediate versus deep Southern Ocean. *Proceedings of the National Academy of Sciences*, *114*(5), 858–863. https://doi.org/10.1073/pnas.1603107114

Anderson, R. F., Cheng, H., Edwards, R. L., Fleisher, M. Q., Hayes, C. T., Huang, K.-F., Kadko, D., Lam, P. J., Landing, W. M., Lao, Y., Lu, Y., Measures, C. I., Moran, S. B., Morton, P. L., Ohnemus, D. C., Robinson, L. F., & Shelley, R. U. (2016). How well can we quantify dust deposition to the ocean? *Philosophical Transactions of the Royal Society A: Mathematical, Physical and Engineering Sciences*, *374*(2081), 20150285. https://doi.org/10.1098/rsta.2015.0285

Arsouze, T., Dutay, J.-C., Lacan, F., & Jeandel, C. (2009). Reconstructing the Nd oceanic cycle using a coupled dynamical – biogeochemical model. *Biogeosciences*, *6*(12), 2829–2846. https://doi.org/10.5194/bg-6-2829-2009

Aumont, O., Maier-Reimer, E., Blain, S., & Monfray, P. (2003). An ecosystem model of the global ocean including Fe, Si, P colimitations. *Global Biogeochemical Cycles*, *17*(2). ://000183554600001

Bacon, M. P., & Anderson, R. F. (1982). Distribution of thorium isotopes between dissolved and particulate forms in the deep sea. *Journal of Geophysical Research: Oceans*, *87*(C3), 2045–2056. https://doi.org/10.1029/JC087iC03p02045

Baker, A. R., Adams, C., Bell, T. G., Jickells, T. D., & Ganzeveld, L. (2013). Estimation of atmospheric nutrient inputs to the Atlantic Ocean from 50°N to 50°S based on large-scale field sampling: Iron and other dust-associated elements. *Global Biogeochemical Cycles*, *27*(3), 755–767. https://doi.org/10.1002/gbc.20062

Baker, A. R., & Jickells, T. D. (2006). Mineral particle size as a control on aerosol iron solubility. *Geophysical Research Letters*, *33*(17). https://doi.org/10.1029/2006GL026557

Beard, B. L., Johnson, C. M., Cox, L., Sun, H., Nealson, K. H., & Aguilar, C. (1999). Iron isotope biosignatures. *Science*, *285*(5435), 1889–1892.

Beard, B. L., Johnson, C. M., Von Damm, K. L., & Poulson, R. L. (2003). Iron isotope constraints on Fe cycling and mass balance in oxygenated Earth oceans. *Geology*, *31*, 629–632.

Beghoura, H., Gorgues, T., Aumont, O., Planquette, H. F., Tagliabue, A., & Auger, P.-A. (2019). Impact of Inorganic Particles of Sedimentary Origin on Global Dissolved Iron and Phytoplankton Distribution. *Journal of Geophysical Research: Oceans*, *124*(12), 8626–8646. https://doi.org/10.1029/2019JC015119

Berman-Frank, I., Cullen, J. T., Shaked, Y., Sherrell, R. M., & Falkowski, P. G. (2001). Iron availability, cellular iron quotas, and nitrogen fixation in Trichodesmium. *Limnology and*

Oceanography, *46*(6), 1249–1260. https://doi.org/10.4319/lo.2001.46.6.1249

Blain, S., Quéguiner, B., Armand, L., Belviso, S., Bombled, B., Bopp, L., Bowie, A., Brunet, C., Brussaard, C., Carlotti, F., Christaki, U., Corbière, A., Durand, I., Ebersbach, F., Fuda, J.-L., Garcia, N., Gerringa, L., Griffiths, B., Guigue, C., … Wagener, T. (2007). Effect of natural iron fertilization on carbon sequestration in the Southern Ocean. *Nature*, *446*(7139), 1070–1074. https://doi.org/10.1038/nature05700

Blain, S., Quéguiner, B., & Trull, T. (2008a). The natural iron fertilization experiment KEOPS (KErguelen Ocean and Plateau compared Study): An overview. *Deep Sea Research Part II: Topical Studies in Oceanography*, *55*(5–7), 559–565. https://doi.org/10.1016/j.dsr2.2008.01.002

Blain, S., Sarthou, G., & Laan, P. (2008b). Distribution of dissolved iron during the natural iron-fertilization experiment KEOPS (Kerguelen Plateau, Southern Ocean). *Deep Sea Research Part II: Topical Studies in Oceanography*, *55*(5–7), 594–605. https://doi.org/10.1016/j.dsr2.2007.12.028

Bonnet, S., & Guieu, C. (2004). Dissolution of atmospheric iron in seawater. *Geophysical Research Letters*, *31*(3). https://doi.org/10.1029/2003GL018423

Bowie, A. R., Lannuzel, D., Remenyi, T. A., Wagener, T., Lam, P. J., Boyd, P. W., Guieu, C., Townsend, A. T., & Trull, T. W. (2009). Biogeochemical iron budgets of the Southern Ocean south of Australia: Decoupling of iron and nutrient cycles in the subantarctic zone by the summertime supply. *Global Biogeochemical Cycles*, *23*(4). https://doi.org/10.1029/2009GB003500

Bowie, A. R., van der Merwe, P., Quéroué, F., Trull, T., Fourquez, M., Planchon, F., Sarthou, G., Chever, F., Townsend, A. T., Obernosterer, I., Sallée, J.-B., & Blain, S. (2015). Iron budgets for three distinct biogeochemical sites around the Kerguelen Archipelago (Southern Ocean) during the natural fertilisation study, KEOPS-2. *Biogeosciences*, *12*(14), 4421–4445. https://doi.org/10.5194/bg-12-4421-2015

Boyd, P. W. (2019). *Multi-faceted particle pumps drive carbon sequestration in the ocean*. 9.

Boyd, P. W., Jickells, T., Law, C. S., Blain, S., Boyle, E. A., Buesseler, K. O., Coale, K. H., Cullen, J. J., de Baar, H. J. W., Follows, M., Harvey, M., Lancelot, C., Levasseur, M., Owens, N. P. J., Pollard, R., Rivkin, R. B., Sarmiento, J., Schoemann, V., Smetacek, V., … Watson, A. J. (2007). Mesoscale Iron Enrichment Experiments 1993-2005: Synthesis and Future Directions. *Science*, *315*(5812), 612–617. https://doi.org/10.1126/science.1131669

Boyle, E. A., Edmond, J. M., & Sholkovitz, E. R. (1977). The mechanism of iron removal in estuaries. *Geochim. Cosmo- Chim. Acta 41, 1313.*

Broecker, W. S., Takahashi, T., & Takahashi, T. (1985). Sources and flow patterns of deep-ocean waters as deduced from potential temperature, salinity, and initial phosphate concentration. *Journal of Geophysical Research*, *90*(C4), 6925. https://doi.org/10.1029/JC090iC04p06925

Brown, M. T., & Bruland, K. W. (2008). An improved flow-injection analysis method for the determination of dissolved aluminum in seawater. *Limnology and Oceanography: Methods*, *6*(1), 87–95. https://doi.org/10.4319/lom.2008.6.87

Browning, T. J., Achterberg, E. P., Rapp, I., Engel, A., Bertrand, E. M., Tagliabue, A., & Moore, C. M. (2017). Nutrient co-limitation at the boundary of an oceanic gyre. *Nature*, *551*(7679), 242–246. https://doi.org/10.1038/nature24063

Bruland, K. W., & Lohan, M. C. (2006). *6.02 Controls of Trace Metals in Seawater*. 25.

Buesseler, K., Ball, L., Andrews, J., Benitez-Nelson, C., Belastock, R., Chai, F., & Chao, Y. (1998). Upper ocean export of particulate organic carbon in the Arabian Sea derived from thorium-234. *Deep Sea Research Part II: Topical Studies in Oceanography*, *45*(10), 2461–2487. https://doi.org/10.1016/S0967-0645(98)80022-2

Bullen, T. D., White, A. F., Childs, C. W., Vivit, D. V., & Schulz, M. S. (2001). Demonstration of significant abiotic iron isotope fractionation in nature. *Geology*, *29*(8), 699–702. https://doi.org/10.1130/0091-7613(2001)029<0699:DOSAII>2.0.CO;2

Canfield, D. E., Thamdrup, B., & Hansen, J. W. (1993). The anaerobic degradation of organic matter in Danish coastal sediments: Iron reduction, manganese reduction, and sulfate reduction. *Geochimica et Cosmochimica Acta*, *57*(16), 3867–3883. https://doi.org/10.1016/0016-7037(93)90340-3

Chase, Z., Johnson, K. S., Elrod, V. A., Plant, J. N., Fitzwater, S. E., Pickell, L., & Sakamoto, C. M. (2005). Manganese and iron distributions off central California influenced by upwelling and shelf width. *Marine Chemistry*, *95*(3), 235–254. https://doi.org/10.1016/j.marchem.2004.09.006

Chever, F., Sarthou, G., Bucciarelli, E., Blain, S., & Bowie, A. R. (2010). *An iron budget during the natural iron fertilisation experiment KEOPS (Kerguelen Islands, Southern Ocean)*. 14.

Conway, T. M., Hamilton, D. S., Shelley, R. U., Aguilar-Islas, A. M., Landing, W. M., Mahowald, N. M., & John, S. G. (2019). Tracing and constraining anthropogenic aerosol iron fluxes to the North Atlantic Ocean using iron isotopes. *Nature Communications*, *10*(1), 2628. https://doi.org/10.1038/s41467-019-10457-w

Conway, T. M., & John, S. G. (2014). Quantification of dissolved iron sources to the North Atlantic Ocean. *Nature*, *511*(7508), 212–215. https://doi.org/10.1038/nature13482

Conway, T. M., Palter, J. B., & Souza, G. F. de. (2018). Gulf Stream rings as a source of iron to the North Atlantic subtropical gyre. *Nature Geoscience*, *11*(8), 594–598. https://doi.org/10.1038/s41561-018-0162-0

Crosby, H. A., Roden, E. E., Johnson, C. M., & Beard, B. L. (2007). The mechanisms of iron isotope fractionation produced during dissimilatory Fe(III) reduction by Shewanella putrefaciens and Geobacter sulfurreducens. *Geobiology*, *5*(2), 169–189.

Cullen, J., Lane, T., & Sherrell, R. (1999). Modulation of cadmium uptake in phytoplankton by seawater CO2 concentration. *Nature*, *442*, 1025–1028. https://doi.org/10.1038/46007

d'Ovidio, F., Della Penna, A., Trull, T. W., Nencioli, F., Pujol, M.-I., Rio, M.-H., Park, Y.-H., Cotté, C., Zhou, M., & Blain, S. (2015). The biogeochemical structuring role of horizontal stirring: Lagrangian perspectives on iron delivery downstream of the Kerguelen Plateau. *Biogeosciences*, *12*(19), 5567–5581. https://doi.org/10.5194/bg-12-5567-2015

Dauphas, N., John, S. G., & Rouxel, O. (2017). Iron Isotope Systematics. *Reviews in Mineralogy and Geochemistry*, *82*(1), 415–510. https://doi.org/10.2138/rmg.2017.82.11

de Baar, H. J. W., & De Jong, J. (2001). Distributions, sources and sinks of iron in seawater. In *IUPAC Ser. Anal. Phys. Chem. Environ. Syst.* (Vol. 7, pp. 123–253).

Dideriksen, K., Baker, J. A., & Stipp, S. L. S. (2008). Equilibrium Fe isotope fractionation between inorganic aqueous Fe(III) and the siderophore complex, Fe(III)-desferrioxamine B. *Earth and Planetary Science Letters*, *269*, 280–290.

Duce, R. A., Liss, P. S., Merrill, J. T., Atlas, E. L., Buat-Menard, P., Hicks, B. B., Miller, J. M., Prospero, J. M., Arimoto, R., Church, T. M., Ellis, W., Galloway, J. N., Hansen, L., Jickells, T. D., Knap, A. H., Reinhardt, K. H., Schneider, B., Soudine, A., Tokos, J. J., … Zhou, M. (1991). The atmospheric input of trace species to the world ocean. *Global Biogeochemical Cycles*, *5*(3), 193–259. https://doi.org/10.1029/91GB01778

Ellwood, M. J., Hutchins, D. A., Lohan, M. C., Milne, A., Nasemann, P., Nodder, S. D., Sander, S. G., Strzepek, R., Wilhelm, S. W., & Boyd, P. W. (2015). Iron stable isotopes track pelagic iron cycling during a subtropical phytoplankton bloom. *Proceedings of the National Academy of Sciences*, *112*(1), E15–E20. https://doi.org/10.1073/pnas.1421576112

Elrod, V., Berelson, W., Coale, K., & Johnson, K. (2004). The Flux of Iron from Continenetal Shelf Sediments: A Missing Source of Global Budgets. *Geophysical Research Letters*, *31*. https://doi.org/10.1029/2004GL020216

Escoube, R., Rouxel, O. J., Pokrovsky, O. S., Schroth, A., Max Holmes, R., & Donard, O. F. X. (2015). Iron isotope systematics in Arctic rivers. *Comptes Rendus Geoscience*, *347*(7–8), 377–385. https://doi.org/10.1016/j.crte.2015.04.005

Fitzsimmons, J. N., Boyle, E. A., & Jenkins, W. J. (2014). Distal transport of dissolved hydrothermal iron in the deep South Pacific Ocean. *Proceedings of the National Academy of Sciences*, *111*(47), 16654–16661. https://doi.org/10.1073/pnas.1418778111

Gaillardet, J., Dupré, B., Louvat, P., & Allègre, C. J. (1999). Global silicate weathering and CO2 consumption rates deduced from the chemistry of large rivers. *Chemical Geology*, *159*(1), 3–30. https://doi.org/10.1016/S0009-2541(99)00031-5

Gaillardet, J., Viers, J., & Dupré, B. (2003). Trace Elements in River Waters. *Treatise on Geochemistry*, *5*, 605. https://doi.org/10.1016/B0-08-043751-6/05165-3

García-Ibáñez, M. I., Pardo, P. C., Carracedo, L. I., Mercier, H., Lherminier, P., Ríos, A. F.,

& Pérez, F. F. (2015). Structure, transports and transformations of the water masses in the Atlantic Subpolar Gyre. *Progress in Oceanography*, *135*, 18–36. https://doi.org/10.1016/j.pocean.2015.03.009

García-Ibáñez, M. I., Pérez, F. F., Lherminier, P., Zunino, P., Mercier, H., & Tréguer, P. (2018). Water mass distributions and transports for the 2014 GEOVIDE cruise in the North Atlantic. *Biogeosciences*, *15*(7), 2075–2090. https://doi.org/10.5194/bg-15-2075-2018

Geibert, W., Hanfland, C., & Dauelsberg, H.-J. (2002). Actinium-227 as a deep-sea tracer: Sources, distribution and applications. *Earth and Planetary Science Letters*, *198*, 147–165. https://doi.org/10.1016/S0012-821X(02)00512-5

German, C. R., Campbell, A. C., & Edmond, J. M. (1991). Hydrothermal scavenging at the Mid-Atlantic Ridge: Modification of trace element dissolved fluxes. *Earth and Planetary Science Letters*, *107*(1), 101–114. https://doi.org/10.1016/0012-821X(91)90047-L

Gerringa, L. J. A., Blain, S., Laan, P., Sarthou, G., Veldhuis, M., Brussaard, C., Viollier, E., & Timmermans, K. R. (2008). Fe-binding dissolved organic ligands near the Kerguelen Archipelago in the Southern Ocean (Indian sector). *Deep Sea Research Part II: Topical Studies in Oceanography*, *55*(5–7), 606–621. https://doi.org/10.1016/j.dsr2.2007.12.007

Gledhill, M., & Buck, K. N. (2012). The organic complexation of iron in the marine environment: A review. *Frontiers in Microbiology*, *3*, 69. https://doi.org/10.3389/fmicb.2012.00069

Goldberg, E. D. (1954). Marine Geochemistry 1. Chemical Scavengers of the Sea. *Journal of Geology*, *62*, 249–265. https://doi.org/10.1086/626161

Guieu, C., Bonnet, S., Petrenko, A., Menkes, C., Chavagnac, V., Desboeufs, K., Maes, C., & Moutin, T. (2018). Iron from a submarine source impacts the productive layer of the Western Tropical South Pacific (WTSP). *Scientific Reports*, *8*(1), 9075. https://doi.org/10.1038/s41598-018-27407-z

Guieu, C., Bonnet, S., Wagener, T., & Loÿe-Pilot, M.-D. (2005). Biomass burning as a source of dissolved iron to the open ocean? *Geophysical Research Letters*, *32*(19). https://doi.org/10.1029/2005GL022962

Han, Q., Moore, J. K., Zender, C., Measures, C., & Hydes, D. (2008). Constraining oceanic dust deposition using surface ocean dissolved Al. *Global Biogeochemical Cycles*, *22*(2), n/a-n/a. https://doi.org/10.1029/2007GB002975

Hassler, C. S., van den Berg, C. M. G., & Boyd, P. W. (2017). Toward a Regional Classification to Provide a More Inclusive Examination of the Ocean Biogeochemistry of Iron-Binding Ligands. *Frontiers in Marine Science*, *4*. https://doi.org/10.3389/fmars.2017.00019

Hayes, C. T., Anderson, R. F., Jaccard, S. L., François, R., Fleisher, M. Q., Soon, M., & Gersonde, R. (2013). A new perspective on boundary scavenging in the North Pacific Ocean. *Earth and Planetary Science Letters*, *369–370*, 86–97.

https://doi.org/10.1016/j.epsl.2013.03.008

Homoky, W. B., John, S. G., Conway, T. M., & Mills, R. A. (2013). Distinct iron isotopic signatures and supply from marine sediment dissolution. *Nature Communications*, *4*(1), 2143. https://doi.org/10.1038/ncomms3143

Hydes, D. J. (1979). Aluminum in seawater: Control by inorganic processes. *Science*, *205*, 1260–1262. https://doi.org/10.1126/science.205.4412.1260

Hydes, D. J., de Lange, G. J., & de Baar, H. J. W. (1988). Dissolved aluminium in the Mediterranean. *Geochimica et Cosmochimica Acta*, *52*(8), 2107–2114. https://doi.org/10.1016/0016-7037(88)90190-1

Hydes, D. J., & Liss, P. S. (1977). The behaviour of dissolved aluminium in estuarine and coastal waters. *Estuarine and Coastal Marine Science*, *5*(6), 755–769. https://doi.org/10.1016/0302-3524(77)90047-0

Ito, A., Myriokefalitakis, S., Kanakidou, M., Mahowald, N. M., Scanza, R. A., Hamilton, D. S., Baker, A. R., Jickells, T., Sarin, M., Bikkina, S., Gao, Y., Shelley, R. U., Buck, C. S., Landing, W. M., Bowie, A. R., Perron, M. M. G., Guieu, C., Meskhidze, N., Johnson, M. S., … Duce, R. A. (2019). Pyrogenic iron: The missing link to high iron solubility in aerosols. *Science Advances*, *5*(5). https://doi.org/10.1126/sciadv.aau7671

Ito, A., & Shi, Z. (2016). Delivery of anthropogenic bioavailable iron from mineral dust and combustion aerosols to the ocean. *Atmospheric Chemistry and Physics*, *16*(1), 85–99. https://doi.org/10.5194/acp-16-85-2016

Jeandel, C. (1993). Concentration and isotopic composition of Nd in the South Atlantic Ocean. *Earth and Planetary Science Letters*, *117*(3), 581–591. https://doi.org/10.1016/0012-821X(93)90104-H

Jeandel, C., & Oelkers, E. H. (2015). The influence of terrigenous particulate material dissolution on ocean chemistry and global element cycles. *Chemical Geology*, *395*, 50–66. https://doi.org/10.1016/j.chemgeo.2014.12.001

Jeandel, C., Peucker-Ehrenbrink, B., Jones, M. T., Pearce, C. R., Oelkers, E. H., Godderis, Y., Lacan, F., Aumont, O., & Arsouze, T. (2011). Ocean margins: The missing term in oceanic element budgets? *Eos, Transactions American Geophysical Union*, *92*(26), 217–218. https://doi.org/10.1029/2011EO260001

Jenkins, W. J. (2003). Tracers of Ocean Mixing. In *The Oceans and Marine Geochemistry* (Elsevier Ltd, Vol. 6, pp. 223–246).

Jenkins, W. J., Smethie, W. M., Boyle, E. A., & Cutter, G. A. (2015). Water mass analysis for the U.S. GEOTRACES (GA03) North Atlantic sections. *Deep Sea Research Part II: Topical Studies in Oceanography*, *116*, 6–20. https://doi.org/10.1016/j.dsr2.2014.11.018

Jickells, T., Church, T., Veron, A., & Arimoto, R. (1994). Atmospheric inputs of manganese and aluminium to the Sargasso Sea and their relation to surface water concentrations. *Marine Chemistry*, *46*(3), 283–292. https://doi.org/10.1016/0304-4203(94)90083-3

Jickells, T. D., An, Z. S., Andersen, K. K., Baker, A. R., Bergametti, G., Brooks, N., Cao, J. J., Boyd, P. W., Duce, R. A., Hunter, K. A., Kawahata, H., Kubilay, N., laRoche, J., Liss, P. S., Mahowald, N., Prospero, J. M., Ridgwell, A. J., Tegen, I., & Torres, R. (2005). Global Iron Connections Between Desert Dust, Ocean Biogeochemistry, and Climate. *Science*, *308*(5718), 67–71. https://doi.org/10.1126/science.1105959

Jickells, T. D., Baker, A. R., & Chance, R. (2016). Atmospheric transport of trace elements and nutrients to the oceans. *Philosophical Transactions of the Royal Society A: Mathematical, Physical and Engineering Sciences*, *374*(2081), 20150286. https://doi.org/10.1098/rsta.2015.0286

John, S. G., Mendez, J., Moffett, J., & Adkins, J. (2012). The flux of iron and iron isotopes from San Pedro Basin sediments. *Geochimica et Cosmochimica Acta*, *93*, 14–29. https://doi.org/10.1016/j.gca.2012.06.003

Johnson, C. M., Roden, E. E., Welch, S. A., & Beard, B. L. (2005). Experimental constraints on Fe isotope fractionation during magnetite and Fe carbonate formation coupled to dissimilatory hydrous ferric oxide reduction. *Geochimica et Cosmochimica Acta*, *69*(4), 963–993. https://doi.org/10.1016/j.gca.2004.06.043

Johnson, K. S., Gordon, R. M., & Coale, K. H. (1997). What controls dissolved iron concentrations in the world ocean? *Marine Chemistry*, *57*(3), 137–161. https://doi.org/10.1016/S0304-4203(97)00043-1

Journet, E., Desboeufs, K. V., Caquineau, S., & Colin, J.-L. (2008). Mineralogy as a critical factor of dust iron solubility. *Geophysical Research Letters*, *35*(7). https://doi.org/10.1029/2007GL031589

Klar, J. K., Homoky, W. B., Statham, P. J., Birchill, A. J., Harris, E. L., Woodward, E. M. S., Silburn, B., Cooper, M. J., James, R. H., Connelly, D. P., Chever, F., Lichtschlag, A., & Graves, C. (2017a). Stability of dissolved and soluble Fe(II) in shelf sediment pore waters and release to an oxic water column. *Biogeochemistry*, *135*(1), 49–67. https://doi.org/10.1007/s10533-017-0309-x

Klar, J. K., James, R. H., Gibbs, D., Lough, A., Parkinson, I., Milton, J. A., Hawkes, J. A., & Connelly, D. P. (2017b). Isotopic signature of dissolved iron delivered to the Southern Ocean from hydrothermal vents in the East Scotia Sea. *Geology*, *45*(4), 351–354. https://doi.org/10.1130/G38432.1

Klar, J. K., Schlosser, C., Milton, J. A., Woodward, E. M. S., Lacan, F., Parkinson, I. J., Achterberg, E. P., & James, R. H. (2018). Sources of dissolved iron to oxygen minimum zone waters on the Senegalese continental margin in the tropical North Atlantic Ocean: Insights from iron isotopes. *Geochimica et Cosmochimica Acta*, *236*, 60–78. https://doi.org/10.1016/j.gca.2018.02.031

Labatut, M., Lacan, F., Pradoux, C., Chmeleff, J., Radic, A., Murray, J. W., Poitrasson, F., Johansen, A. M., & Thil, F. (2014). Iron sources and dissolved-particulate interactions in the seawater of the Western Equatorial Pacific, iron isotope perspectives. *Global Biogeochemical Cycles*, *28*(10), 1044–1065. https://doi.org/10.1002/2014GB004928

Lacan, F., & Jeandel, C. (2001). Tracing Papua New Guinea imprint on the central Equatorial Pacific Ocean using neodymium isotopic compositions and Rare Earth Element patterns. *Earth and Planetary Science Letters*, *186*(3), 497–512. https://doi.org/10.1016/S0012-821X(01)00263-1

Lacan, F., & Jeandel, C. (2005). Neodymium isotopes as a new tool for quantifying exchange fluxes at the continent-ocean interface. *Earth and Planetary Science Letters*, *232*, 245–257. https://doi.org/10.1016/j.epsl.2005.01.004

Lam, P. J., Bishop, J. K. B., Henning, C. C., Marcus, M. A., Waychunas, G. A., & Fung, I. Y. (2006). Wintertime phytoplankton bloom in the subarctic Pacific supported by continental margin iron. *Global Biogeochemical Cycles*, *20*(1). https://doi.org/10.1029/2005GB002557

Lam, P. J., & Marchal, O. (2015). Insights into Particle Cycling from Thorium and Particle Data. *Annual Review of Marine Science*, *7*(1), 159–184. https://doi.org/10.1146/annurev-marine-010814-015623

Lane, T. W., & Morel, F. M. M. (2000). A biological function for cadmium in marine diatoms. *Proceedings of the National Academy of Sciences*, *97*(9), 4627–4631. https://doi.org/10.1073/pnas.090091397

Lazier, J., Hendry, R., Clarke, A., Yashayaev, I., & Rhines, P. (2002). Convection and restratification in the Labrador Sea, 1990–2000. *Deep Sea Research Part I: Oceanographic Research Papers*, *49*(10), 1819–1835. https://doi.org/10.1016/S0967-0637(02)00064-X

Libes, S. (2009). *Introduction to Marine Biogeochemistry—2nd Edition*. https://www.elsevier.com/books/introduction-to-marine-biogeochemistry/libes/978-0-12-088530-5

Little, S. H., Vance, D., Siddall, M., & Gasson, E. (2013). A modeling assessment of the role of reversible scavenging in controlling oceanic dissolved Cu and Zn distributions. *Global Biogeochemical Cycles*, *27*(3), 780–791. https://doi.org/10.1002/gbc.20073

Lunel, T., Rudnicki, M., Elderfield, H., & Hydes, D. (1990). Aluminium as a depth-sensitive tracer of entrainment in submarine hydrothermal plumes. *Nature*, *344*(6262), 137–139. https://doi.org/10.1038/344137a0

Luo, C., Mahowald, N., Bond, T., Chuang, P., Artaxo, P., Siefert, R., Chen, Y., & Schauer, J. (2008). Combustion iron distribution and deposition. *Global Biogeochemical Cycles*, *22*. https://doi.org/10.1029/2007GB002964

Mackey, D. J., O'Sullivan, J. E., & Watson, R. J. (2002). Iron in the western Pacific: A riverine or hydrothermal source for iron in the Equatorial Undercurrent? *Deep-Sea Research Part I-Oceanographic Research Papers*, *49*(5), 877–893.

Mackin, J. E., & Aller, R. C. (1984). Processes affecting the behavior of dissolved aluminum in estuarine waters. *Marine Chemistry*, *14*(3), 213–232. https://doi.org/10.1016/0304-

4203(84)90043-4

Mahowald, N. M., Baker, A. R., Bergametti, G., Brooks, N., Duce, R. A., Jickells, T. D., Kubilay, N., Prospero, J. M., & Tegen, I. (2005). Atmospheric global dust cycle and iron inputs to the ocean. *Global Biogeochemical Cycles*, *19*(4). https://doi.org/10.1029/2004GB002402

Maring, H. B., & Duce, R. A. (1987). The impact of atmospheric aerosols on trace metal chemistry in open ocean surface seawater, 1. Aluminum. *Earth and Planetary Science Letters*, *84*(4), 381–392. https://doi.org/10.1016/0012-821X(87)90003-3

Martin, J. H., & Fitzwater, S. E. (1988a). Iron deficiency limits phytoplancton growth in the north-east Pacific subarctic. *Nature*, *331*, 341–343.

Martin, J. H., & Gordon, R. M. (1988b). Northeast Pacific iron distribution in relation to phytoplancton productivity. *Deep-Sea Research*, *35*, 177–196.

Measures, C. I., & Brown, E. T. (1996, November 12). *Estimating dust input to the atlantic ocean using surface water aluminium concentrations*. http://onlinelibrary.wiley.com/journal/10.1002/%28ISSN%292324-9250

Measures, C. I., Brown, M. T., & Vink, S. (2005). Dust deposition to the surface waters of the western and central North Pacific inferred from surface water dissolved aluminum concentrations. *Geochemistry, Geophysics, Geosystems*, *6*(9). https://doi.org/10.1029/2005GC000922

Measures, C. I., Hatta, M., Fitzsimmons, J., & Morton, P. (2015). Dissolved Al in the zonal N Atlantic section of the US GEOTRACES 2010/2011 cruises and the importance of hydrothermal inputs. *Deep Sea Research Part II: Topical Studies in Oceanography*, *116*, 176–186. https://doi.org/10.1016/j.dsr2.2014.07.006

Measures, C. I., Sato, T., Vink, S., Howell, S., & Li, Y. H. (2010). The fractional solubility of aluminium from mineral aerosols collected in Hawaii and implications for atmospheric deposition of biogeochemically important trace elements. *Marine Chemistry*, *120*(1), 144–153. https://doi.org/10.1016/j.marchem.2009.01.014

Measures, C. I., & Vink, S. (2000). On the use of dissolved aluminum in surface waters to estimate dust deposition to the ocean. *Global Biogeochemical Cycles*, *14*(1), 317–327. https://doi.org/10.1029/1999GB001188

Menzel Barraqueta, J.-L., Klar, J. K., Gledhill, M., Schlosser, C., Shelley, R., Planquette, H., Wenzel, B., Sarthou, G., & Achterberg, E. P. (2018). Atmospheric aerosol deposition fluxes over the Atlantic Ocean: A GEOTRACES case study. *Biogeosciences Discussions*, 1–25. https://doi.org/10.5194/bg-2018-209

Middag, R. (2010). *Dissolved aluminium and manganese in the polar oceans*. s.n.] ; University Library Groningen] [Host. http://irs.ub.rug.nl/ppn/328865095

Middag, R., Baar, H. de, Laan, P., & Huhn, O. (2012). *The effects of continental margins and water mass circulation on the distribution of dissolved aluminum and manganese in Drake*

Passage. https://doi.org/10.1029/2011jc007434

Middag, R., de Baar, H. J. W., Laan, P., & Bakker, K. (2009). Dissolved aluminium and the silicon cycle in the Arctic Ocean. *Marine Chemistry*, *115*(3), 176–195. https://doi.org/10.1016/j.marchem.2009.08.002

Middag, R., van Hulten, M. M. P., Van Aken, H. M., Rijkenberg, M. J. A., Gerringa, L. J. A., Laan, P., & de Baar, H. J. W. (2015). Dissolved aluminium in the ocean conveyor of the West Atlantic Ocean: Effects of the biological cycle, scavenging, sediment resuspension and hydrography. *Marine Chemistry*, *177*, 69–86. https://doi.org/10.1016/j.marchem.2015.02.015

Millero, F. J., Sotolongo, S., & Izaguirre, M. (1987). The oxidation kinetics of Fe(II) in seawater. *Geochimica et Cosmochimica Acta*, *51*(4), 793–801. https://doi.org/10.1016/0016-7037(87)90093-7

Milliman, J. D., Farnsworth, K. L., & Albertin, C. S. (1999). Flux and fate of fluvial sediments leaving large islands in the East Indies. *Journal of Sea Reasearch*, *41*, 97–107.

Moore, C. M., Mills, M. M., Arrigo, K. R., Berman-Frank, I., Bopp, L., Boyd, P. W., Galbraith, E. D., Geider, R. J., Guieu, C., Jaccard, S. L., Jickells, T. D., La Roche, J., Lenton, T. M., Mahowald, N. M., Marañón, E., Marinov, I., Moore, J. K., Nakatsuka, T., Oschlies, A., … Ulloa, O. (2013). Processes and patterns of oceanic nutrient limitation. *Nature Geoscience*, *6*(9), 701–710. https://doi.org/10.1038/ngeo1765

Moore, J. K., & Braucher, O. (2008). Sedimentary and mineral dust sources of dissolved iron to the world ocean. *Biogeosciences*, *5*(3), 631–656. https://doi.org/10.5194/bg-5-631-2008

Moore, J. K., Doney, S. C., & Lindsay, K. (2004). Upper ocean ecosystem dynamics and iron cycling in a global three-dimensional model. *Global Biogeochemical Cycles*, *18*(4). https://doi.org/10.1029/2004GB002220

Moore, W. (2010). The Effect of Submarine Groundwater Discharge on the Ocean. *Annual Review of Marine Science*, *2*, 59–88. https://doi.org/10.1146/annurev-marine-120308-081019

Moore, W. S. (1996). Large groundwater inputs to coastal waters revealed by 226Ra enrichments. *Nature*, *380*, 612–614.

Moran, S. B., & Moore, R. M. (1991). The potential source of dissolved aluminum from resuspended sediments to the North Atlantic Deep Water. *Geochimica et Cosmochimica Acta*, *55*(10), 2745–2751. https://doi.org/10.1016/0016-7037(91)90441-7

Morel, F. M. M., & Price, N. M. (2003). The biogeochemical cycles of trace metals in the oceans. *Science (New York, N.Y.)*, *300*(5621), 944–947. https://doi.org/10.1126/science.1083545

Nozaki, Y., & Alibo, D. (2003). Importance of vertical geochemical processes in controlling the oceanic profiles of dissolved rare earth elements in the northeastern Indian Ocean.

Earth and Planetary Science Letters, *205*, 155–172. https://doi.org/10.1016/S0012-821X(02)01027-0

Nozaki, Y., Horibe, Y., & Tsubota, H. (1981). The water column distributions of thorium isotopes in the western North Pacific. *Earth and Planetary Science Letters*, *54*(2), 203–216. https://doi.org/10.1016/0012-821X(81)90004-2

Oelkers, E. H., Gislason, S. R., Eiriksdottir, E. S., Jones, M., Pearce, C. R., & Jeandel, C. (2011). The role of riverine particulate material on the global cycles of the elements. *Applied Geochemistry*, *26*, S365–S369. https://doi.org/10.1016/j.apgeochem.2011.03.062

Orians, K. J., & Bruland, K. W. (1986a). The biogeochemistry of aluminium in the Pacific Ocean. *Earth and Planetary Science Letters*, *78*, 397–410.

Orians, K. J., & Bruland, K. W. (1986b). The biogeochemistry of aluminum in the Pacific Ocean. *Earth and Planetary Science Letters*, *78*(4), 397–410. https://doi.org/10.1016/0012-821X(86)90006-3

Peers, G., & Price, N. M. (2006). Copper-containing plastocyanin used for electron transport by an oceanic diatom. *Nature*, *441*(7091), 341–344. https://doi.org/10.1038/nature04630

Peers, G., Quesnel, S.-A., & Price, N. M. (2005). *Copper requirements for iron acquisition and growth of coastal and oceanic diatoms*. 10.

Periodic Table of Elements in the Ocean. (2015, November 19). *MBARI*. https://www.mbari.org/science/upper-ocean-systems/chemical-sensor-group/periodic-table-of-elements-in-the-ocean/

Peters, B. D., Jenkins, W. J., Swift, J. H., German, C. R., Moffett, J. W., Cutter, G. A., Brzezinski, M. A., & Casciotti, K. L. (2018). Water mass analysis of the 2013 US GEOTRACES eastern Pacific zonal transect (GP16). *Marine Chemistry*, *201*, 6–19. https://doi.org/10.1016/j.marchem.2017.09.007

Pickard, G. L., & Emery, W. J. (2016). *Descriptive Physical Oceanography: An Introduction*. Elsevier.

Planquette, H., Statham, P. J., Fones, G. R., Charette, M. A., Moore, C. M., Salter, I., Nedelec, F. H., Taylor, S. L., French, M., Baker, A. R., Mahowald, N., & Jickells, T. D. (2007). Dissolved iron in the vicinity of the Crozet Islands, Southern Ocean. *Deep Sea Research Part II: Topical Studies in Oceanography*, *54*(18–20), 1999–2019. https://doi.org/doi:10.1016/j.dsr2.2007.06.019

Poitrasson, F. (2006). On the iron isotope homogeneity level of the continental crust. *Chemical Geology*, *235*(1), 195–200. https://doi.org/10.1016/j.chemgeo.2006.06.010

Pollard, R., Salter, I., Sanders, R., Lucas, M., Moore, C., Mills, R., Statham, P., Allen, J., Baker, A., Bakker, D., Charette, M., Fielding, S., Fones, G., French, M., Hickman, A., Holland, R., Hughes, J., Jickells, T., Lampitt, R., … Zubkov, M. (2009). Southern Ocean deep-water carbon export enhanced by natural iron fertilization. *NATURE*, *457*(7229), 577-U81. https://doi.org/10.1038/nature07716

Poulton, S. W., & Raiswell, R. (2002). *THE LOW-TEMPERATURE GEOCHEMICAL CYCLE OF IRON: FROM CONTINENTAL FLUXES TO MARINE SEDIMENT DEPOSITION*. https://doi.org/10.2475/ajs.302.9.774

Quéroué, F., Sarthou, G., Planquette, H. F., Bucciarelli, E., Chever, F., van der Merwe, P., Lannuzel, D., Townsend, A. T., Cheize, M., Blain, S., d'Ovidio, F., & Bowie, A. R. (2015). High variability in dissolved iron concentrations in the vicinity of the Kerguelen Islands (Southern Ocean). *Biogeosciences*, *12*(12), 3869–3883. https://doi.org/10.5194/bg-12-3869-2015

Radic, A., Lacan, F., & W. Murray, J. (2011a). Iron isotopes in the seawater of the equatorial Pacific Ocean: New constraints for the oceanic iron cycle. *Earth and Planetary Science Letters*, *306*, 1–10. https://doi.org/10.1016/j.epsl.2011.03.015

Radic, A. (2011b). *Thèse: Les isotopes du fer dans l'eau de mer: Un nouveau traceur de la biogéochimie océanique*.

Raiswell, R., Benning, L. G., Tranter, M., & Tulaczyk, S. (2008). Bioavailable iron in the Southern Ocean: The significance of the iceberg conveyor belt. *Geochemical Transactions*, *9*(1), 7. https://doi.org/10.1186/1467-4866-9-7

Resing, J. A., & Measures, C. I. (1994). Fluorometric Determination of Al in Seawater by Flow Injection Analysis with In-Line Preconcentration. *Analytical Chemistry*, *66*(22), 4105–4111. https://doi.org/10.1021/ac00094a039

Resing, J. A., Sedwick, P. N., German, C. R., Jenkins, W. J., Moffett, J. W., Sohst, B. M., & Tagliabue, A. (2015). Basin-scale transport of hydrothermal dissolved metals across the South Pacific Ocean. *Nature*, *523*(7559), 200–203. https://doi.org/10.1038/nature14577

Roether, W. (1994). Studying Thermohaline Circulation in the Ocean by Means of Transient Tracer Data. In P. Malanotte-Rizzoli & A. R. Robinson (Eds.), *Ocean Processes in Climate Dynamics: Global and Mediterranean Examples* (pp. 157–171). Springer Netherlands. https://doi.org/10.1007/978-94-011-0870-6_7

Rouxel, O., Shanks III, W. C., Bach, W., & Edwards, K. J. (2008a). Integrated Fe- and S-isotope study of seafloor hydrothermal vents at East Pacific Rise 9–10°N. *Chemical Geology*, *252*(3–4), 214–227. https://doi.org/10.1016/j.chemgeo.2008.03.009

Rouxel, O., Sholkovitz, E., Charette, M., & Edwards, K. J. (2008b). Iron isotope fractionation in subterranean estuaries. *Geochimica et Cosmochimica Acta*, *72*(14), 3413–3430. https://doi.org/10.1016/j.gca.2008.05.001

Roy-Barman, M., Chen, J. H., & Wasserburg, G. J. (1996). 230Th232Th systematics in the central Pacific Ocean: The sources and the fates of thorium. *Earth and Planetary Science Letters*, *139*(3), 351–363. https://doi.org/10.1016/0012-821X(96)00017-9

Roy-Barman, M., & Jeandel, C. (2016). *Marine Geochemistry: Ocean Circulation, Carbon Cycle and Climate Change* (Oxford University Press).

Rudnick, R. L., & Gao, S. (2014). Composition of the Continental Crust. In *Treatise on Geochemistry* (pp. 1–51). Elsevier. https://doi.org/10.1016/B978-0-08-095975-7.00301-6

Rue, E. L., & Bruland, K. W. (1995). Complexation of iron(III) by natural organic ligands in the Central North Pacific as determined by a new competitive ligand equilibration/adsorptive cathodic stripping voltammetric method. *Marine Chemistry*, 22.

Ryther, J. H., & Kramer, D. D. (1961). Relative Iron Requirement of Some Coastal and Offshore Plankton Algae. *Ecology*, *42*(2), 444–446. https://doi.org/10.2307/1932105

Sander, S., & Koschinsky, A. (2011). Sander SG, Koschinsky A.. Metal flux from hydrothermal vents increased by organic complexation. Nat Geosci 4: 145-150. *Nature Geoscience*, *4*. https://doi.org/10.1038/ngeo1088

Sanial, V., van Beek, P., Lansard, B., Souhaut, M., Kestenare, E., d'Ovidio, F., Zhou, M., & Blain, S. (2015). Use of Ra isotopes to deduce rapid transfer of sediment-derived inputs off Kerguelen. *Biogeosciences*, *12*(5), 1415–1430. https://doi.org/10.5194/bg-12-1415-2015

Schlitzer, R., Anderson, R. F., Dodas, E. M., Lohan, M., Geibert, W., Tagliabue, A., Bowie, A., Jeandel, C., Maldonado, M. T., Landing, W. M., Cockwell, D., Abadie, C., Abouchami, W., Achterberg, E. P., Agather, A., Aguliar-Islas, A., van Aken, H. M., Andersen, M., Archer, C., … Zurbrick, C. (2018). The GEOTRACES Intermediate Data Product 2017. *Chemical Geology*, *493*, 210–223. https://doi.org/10.1016/j.chemgeo.2018.05.040

Sedwick, P. N., Sholkovitz, E. R., & Church, T. M. (2007). Impact of anthropogenic combustion emissions on the fractional solubility of aerosol iron: Evidence from the Sargasso Sea. *Geochemistry, Geophysics, Geosystems*, *8*(10). https://doi.org/10.1029/2007GC001586

Severmann, S., McManus, J., Berelson, W. M., & Hammond, D. E. (2010). The continental shelf benthic iron flux and its isotope composition. *Geochimica et Cosmochimica Acta*, *74*(14), 3984–4004. https://doi.org/10.1016/j.gca.2010.04.022

Sholkovitz, E. R., & Copland, D. (1981). The coagulation, solubility and adsorption properties of Fe, Mn, Cu, Ni, Cd, Co and humic acids in a river water. *Geochimica et Cosmochimica Acta*, *45*(2), 181–189. https://doi.org/10.1016/0016-7037(81)90161-7

Sholkovitz, E. R., Sedwick, P. N., & Church, T. M. (2009). Influence of anthropogenic combustion emissions on the deposition of soluble aerosol iron to the ocean: Empirical estimates for island sites in the North Atlantic. *Geochimica et Cosmochimica Acta*, *73*(14), 3981–4003. https://doi.org/10.1016/j.gca.2009.04.029

Sholkovitz, E. R., Sedwick, P. N., Church, T. M., Baker, A. R., & Powell, C. F. (2012). Fractional solubility of aerosol iron: Synthesis of a global-scale data set. *Geochimica et Cosmochimica Acta*, *89*, 173–189. https://doi.org/10.1016/j.gca.2012.04.022

Slemons, L. O., Murray, J. W., Resing, J., Paul, B., & Dutrieux, P. (2010). Western Pacific coastal sources of iron, manganese, and aluminum to the Equatorial Undercurrent. *Global*

Biogeochemical Cycles, *24*(3). https://doi.org/10.1029/2009GB003693

Slomp, C. P., Malschaert, J. F. P., Lohse, L., & Van Raaphorst, W. (1997). Iron and manganese cycling in different sedimentary environments on the North Sea continental margin. *Continental Shelf Research*, *17*, 1083–1117. https://doi.org/10.1016/S0278-4343(97)00005-8

Stoffyn, M., & Mackenzie, F. T. (1982). Fate of dissolved aluminum in the oceans. *Marine Chemistry*, *11*(2), 105–127. https://doi.org/10.1016/0304-4203(82)90036-6

Strzepek, R. F., & Harrison, P. J. (2004). Photosynthetic architecture differs in coastal and oceanic diatoms. *Nature*, *431*(7009), 689–692. https://doi.org/10.1038/nature02954

Sunda, W. G., & Huntsman, S. A. (1995). Iron uptake and growth limitation in oceanic and coastal phytoplankton. *Marine Chemistry*, *50*(1), 189–206. https://doi.org/10.1016/0304-4203(95)00035-P

Tagliabue, A., Aumont, O., & Bopp, L. (2014). The impact of different external sources of iron on the global carbon cycle. *Geophysical Research Letters*, *41*(3), 920–926. https://doi.org/10.1002/2013GL059059

Tagliabue, A., Bopp, L., Dutay, J.-C., Bowie, A. R., Chever, F., Jean-Baptiste, P., Bucciarelli, E., Lannuzel, D., Remenyi, T., Sarthou, G., Aumont, O., Gehlen, M., & Jeandel, C. (2010). Hydrothermal contribution to the oceanic dissolved iron inventory. *Nature Geoscience*, *3*(4), 252–256. https://doi.org/10.1038/ngeo818

Tagliabue, A., Bowie, A. R., Boyd, P. W., Buck, K. N., Johnson, K. S., & Saito, M. A. (2017). The integral role of iron in ocean biogeochemistry. *Nature*, *543*(7643), 51–59. https://doi.org/10.1038/nature21058

Tagliabue, A., Hawco, N. J., Bundy, R. M., Landing, W. M., Milne, A., Morton, P. L., & Saito, M. A. (2018). The Role of External Inputs and Internal Cycling in Shaping the Global Ocean Cobalt Distribution: Insights From the First Cobalt Biogeochemical Model. *Global Biogeochemical Cycles*, *32*(4), 594–616. https://doi.org/10.1002/2017GB005830

Talley, L. D., Pickard, G. L., Emery, W. J., & Swift, J. H. (Eds.). (2011). *Descriptive physical oceanography: An introduction* (6. ed). Elsevier.

Taylor, P. D. P., Maeck, R., Hendrickx, F., & De Bièvre, P. (1993). The gravimetric preparation of synthetic mixtures of iron isotopes. *International Journal of Mass Spectrometry and Ion Processes*, *128*(1–2), 91–97. https://doi.org/10.1016/0168-1176(93)87018-N

Tomczak, M. (1981). A multi-parameter extension of temperature/salinity diagram techniques for the analysis of non-isopycnal mixing. *Progress in Oceanography*, *10*(3), 147–171. https://doi.org/10.1016/0079-6611(81)90010-0

Tomczak, M. (1999). Some historical, theoretical and applied aspects of quantitative water mass analysis. *Journal of Marine Research*, *57*(2), 275–303. https://doi.org/10.1357/002224099321618227

Tortell, P. D., Rau, G. H., & Morel, F. M. M. (2000). Inorganic carbon acquisition in coastal Pacific phytoplankton communities. *Limnology and Oceanography*, *45*(7), 1485–1500. https://doi.org/10.4319/lo.2000.45.7.1485

Tria, J., Butler, E. C. V., Haddad, P. R., & Bowie, A. R. (2007). Determination of aluminium in natural water samples. *Analytica Chimica Acta*, *588*(2), 153–165. https://doi.org/10.1016/j.aca.2007.02.048

Turekian, K. K. (1977). The fate of metals in the oceans. *Geochimica et Cosmochimica Acta*, *41*(8), 1139–1144. https://doi.org/10.1016/0016-7037(77)90109-0

van Beek, P., Bourquin, M., Reyss, J.-L., Souhaut, M., Charette, M. A., & Jeandel, C. (2008). Radium isotopes to investigate the water mass pathways on the Kerguelen Plateau (Southern Ocean). *Deep Sea Research Part II: Topical Studies in Oceanography*, *55*(5–7), 622–637. https://doi.org/10.1016/j.dsr2.2007.12.025

van Hulten, M. M. P., Sterl, A., Tagliabue, A., Dutay, J.-C., Gehlen, M., de Baar, H. J. W., & Middag, R. (2013). Aluminium in an ocean general circulation model compared with the West Atlantic Geotraces cruises. *Journal of Marine Systems*, *126*, 3–23. https://doi.org/10.1016/j.jmarsys.2012.05.005

Viers, J., Dupré, B., & Gaillardet, J. (2009). Chemical composition of suspended sediments in World Rivers: New insights from a new database. *Science of The Total Environment*, *407*(2), 853–868. https://doi.org/10.1016/j.scitotenv.2008.09.053

Vink, S., & Measures, C. I. (2001). The role of dust deposition in determining surface water distributions of Al and Fe in the South West Atlantic. *Deep Sea Research Part II: Topical Studies in Oceanography*, *48*(13), 2787–2809. https://doi.org/10.1016/S0967-0645(01)00018-2

Welch, S. A., Beard, B. L., Johnson, C. M., & Braterman, P. S. (2003). Kinetic and equilibrium Fe isotope fractionation between aqueous Fe(II) and Fe(III). *Geochimica et Cosmochimica Acta*, *67*(22), 4231–4250. https://doi.org/10.1016/S0016-7037(03)00266-7

Yücel, M., Gartman, A., Chan, C. S., & Luther, G. W. (2011). Hydrothermal vents as a kinetically stable source of iron-sulphide-bearing nanoparticles to the ocean. *Nature Geoscience*, *4*(6), 367–371. https://doi.org/10.1038/ngeo1148

Zhang, Y., Lacan, F., & Jeandel, C. (2008). Dissolved rare earth elements tracing lithogenic inputs over the Kerguelen Plateau (Southern Ocean). *Deep Sea Research Part II: Topical Studies in Oceanography*, *55*(5–7), 638–652. https://doi.org/10.1016/j.dsr2.2007.12.029

7 Annexes

7.1 La campagne GEOTRACES GA13-FRidge

La campagne GEOTRACES GA13, FRidge, a débuté le 20 décembre 2017 de Southampton (UK) et s'est terminée le 1er février 2018 à Point-à-Pitre (Guadeloupe, France). L'objectif de cette campagne était l'étude de la distribution des métaux traces le long de la dorsale médio-atlantique et aux niveaux des sites hydrothermaux comme Rainbow et TAG.
Mon rôle sur la campagne était l'échantillonnage aux côtés des membres de l'équipe « Trace metal clean » de l'ensemble des métaux traces prélevés à l'aide de la rosette Titanium.
Au cours de cette campagne j'ai également réalisé le blog : https://liseatsea.wordpress.com/ dont le but était de présenter les prélèvements et expériences réalisées à bord de la campagne GA13, les méthodes utilisées ainsi que l'ensemble des scientifiques et leur objectifs scientifiques.
La section suivante présente deux des articles que j'ai écrit à bord qui présente des techniques de prélèvement (The Trace Metal Team) et de mesures (Around and in the bubble) dites « ultra-propres ».

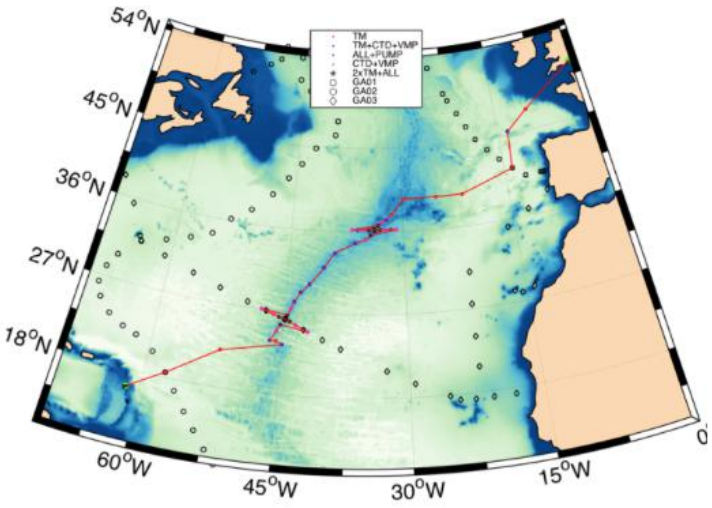

Figure : Transect de la campagne GA13-FRidge-JC156 (JC156 cruise report).

Bye FRidge JC156... this is just the beginning.

The trace metal team

Between two rosettes

Pioneering Physics Team

Meet the stainless steel rosette team (part 2)

Meet the stainless steel rosette team (part 1)

Measuring Sulfidic compounds at sea

Around and in the bubble

The Radium Team

The Trace Metal Team

Prof. Maeve Lohan from the University of Southampton is on the Fridge cruise JC156 as the team leader of the Titanium rosette. The Titanium rosette is used to cleanly sample trace metals. Indeed, many trace metals are present at extremely low concentrations in seawater or the samples can be highly susceptible to contamination during each step of the sampling process (from the ship and the sampling equipment to the human water collection). To avoid this, we need to use clean sample equipment (rosette, cable and winch) and a clean subsampling area (clean van) where we can collect the water quickly after the sampling. The resulting data sets will therefore be at a sufficient resolution to resolve and interpret the data. On Fridge JC156 the titanium rosette used is composed of twenty-four 10 litre bottles that are teflon coated inside. The clean van is divided into two sections separated by an internal door with an air conditioning unit and a laminar hood.

1- The deployment

Before the first deployment, all the Niskins bottles have been cleaned by milli-Q water and have been deployed at least once to condition them with seawater. The Niskins bottles are removed from the clean van where they are stored between deployments. The bottle taps are protected with gloves. The bottles are then placed on the rosette frame, and the trigger lanyard is put under tension by opening the bottle's top cap and tying it with the bottom caps. When it is time to deploy, the gloves are removed from the taps and the rosette lowered into the water. Immediately after, data from the CTD, Eh and LSS sensors (attached to the rosettes) are followed by Alessandro Tagliabue, Maeve Lohan, technicians and engineers to decide at which depth the bottles have to be closed. They will be closed on the way back to the surface. Once the rosette is back on deck, the taps are protected with plastic gloves. Bottles are then removed individually from the rosette frame and carried into the clean van, where they are secured to a purpose-built rack. All the trace metal team is required for the deployment steps to be sure to always carry the bottles as cleanly and quickly as possible.

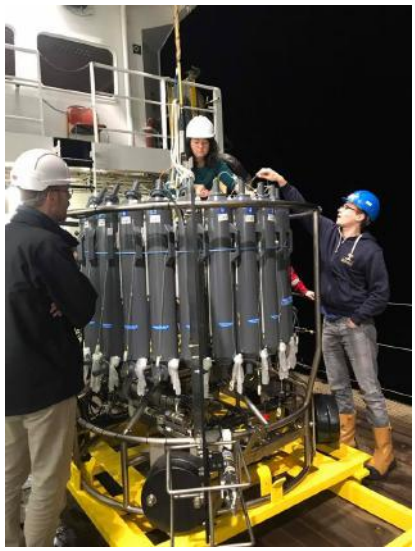

Figure 1: Titanium rosette getting prepared for deployment (on the left) and coming back on deck (on the right). © Lise Artigue

2- The sampling

Once the bottles are in the van, the air vents at the top of the bottles are rinsed and gloves are removed from the tap that are then rinsed. It is time for the trace metal team to begin the subsampling of the bottles. The sampling process (bottles, volume of water ...) depends on the chemical species that will be analyzed. Generally, the sampling begins with the time-dependent and unfiltered species: Fe (II), total organic carbon (TOC), kFe, pH, chlorophyll, nutrients, unfiltered sulfide (H2S), total dissolved trace metal (TDTm) and total dissolved manganese (TDMn). Once this is done, we move to filtered sampling. To do so, the bottles are clamped and pressurized with compressed air. For the niskins where particulate trace metal (PTm) will be collected, a prior checking is necessary. Subsamples are filtered through 0.4-µm removal filters for the PTm and through 0.4-µm sartobran filters for the others. The filtered species sampled are collected for large volume isotope measurements of iron, lead, cadmium and chromium isotopes (1 to 4 liters). Then smaller volumes of sea water (15 to 300ml) are filtered for: dissolved Fe (dFe), soluble Fe (sFe), dissolved trace metals (dTm), dissolved manganese and aluminium, Fe and Cu speciation, filtered sulfite, Fe(II) aged, dissolved organic carbon (DOC), Nitrate Isotope, Arsenic and at the very end Salinity. After the collection, the samples will be following different chemical and storage steps. The soluble Fe samples have to be re-filtered just after collection through 0.2-µm filters in a laminar hood. Most of the samples are then acidified and stored for further analysis.

Figure 2: Maeve Lohan, David González Santana, Dakota Gibbs, Wenhao Wang, Travis Mellet, Arthur Gourain and Lise Artigue sampling in the clean van.

The difficulties of these measurements, is to avoid contamination that can occur at all steps and to manage the amount of water needed to measure as much species as possible.

The trace metal team is composed of:

- Maeve Lohan (Team Leader, Prof at Southampton University, NOCS, UK)
- Lise Artigue (PhD student at Toulouse University, LEGOS, France)
- Arthur Gourain (PhD student at Liverpool University, UK)
- Dakota Gibbs (PhD student at Southampton University, UK)

- Wenhao Wang (PhD student at Southampton University, NOCS, UK)
- Travis Mellet (PhD student at Florida State University, USA)
- David González Santana (PhD Student at Brest University, France)
- Alastair Lough (Post doc at Southampton University, NOCS, UK)

All the trace metal team wants to say a special thanks to Prof. Maeve Lohan that taught us the trace metal sampling with constant support and always a smile.

Around and In the bubble

The micronutrient iron is widely recognized for its key role in ocean productivity and biogeochemistry. Very abundant in continents, is very low concentration at sea force us to sample and to analyse Iron being as clean as possible. To do that the sample techniques used at sea is the Trace Metal Rosette. This sample technique will be detailed in another post.
Once the iron samples have been collected, they go directly in a clean bubble.
In this bubble, two laminar hoods are present with filters that clean the incoming air. The accumulation of that clean air in the sealed plastic room forms then the « clean bubble ».

Figure 1 : The iron men David González Santana (on the left) and Dr. Alastair Lough (on the right) in the clean bubble entrance © Lise Artigue

In this bubble two oxidation states of iron are measured. PhD student from Brest University, David González Santana is in charge of the Fe (II) concentration measurement and Dr. Alastair Lough from Southampton University is measuring the total dissolved Fe (TdFe) concentration. These two forms are measured because they give complementary information and allow us to know if there is an Fe input in the water. Measuring the Fe(II) is important as it is more easily used by microorganisms. Moreover, it helps us to know the Iron oxidation kinetics as Fe (II) is quickly oxidised to Fe (III). But this Fe (II) short half-life is also what make this component hard to analyse and explained why the analyse have to be done on board very quickly after the sampling. Measuring the TdFe is useful because Fe (III) will then form oxyhydroxides that stick together, forming larger particles that sink in the ocean. If the TdFe is detected at higher concentrations away from the ridge, then that would indicate that Iron has been transported further into the deep ocean. If it's not, then the iron is forming particles that sink to the sediments on the seafloor.

To measure the Fe (II) and Fe (III) concentration, the technique used in both cases is the FIA (Flow Injection Analysis) with chemiluminescence. This technique, based on the injection of a liquid sample into a moving continuous carrier stream follow this steps (Ref. Dr. Alastair Lough).

- Fe separated from sea water using resin column.
- Fe removed from column and reacts with other reagents (luminol) producing chemiluminescence.

- The light given off by reaction is proportional to the amount of Fe and detected.

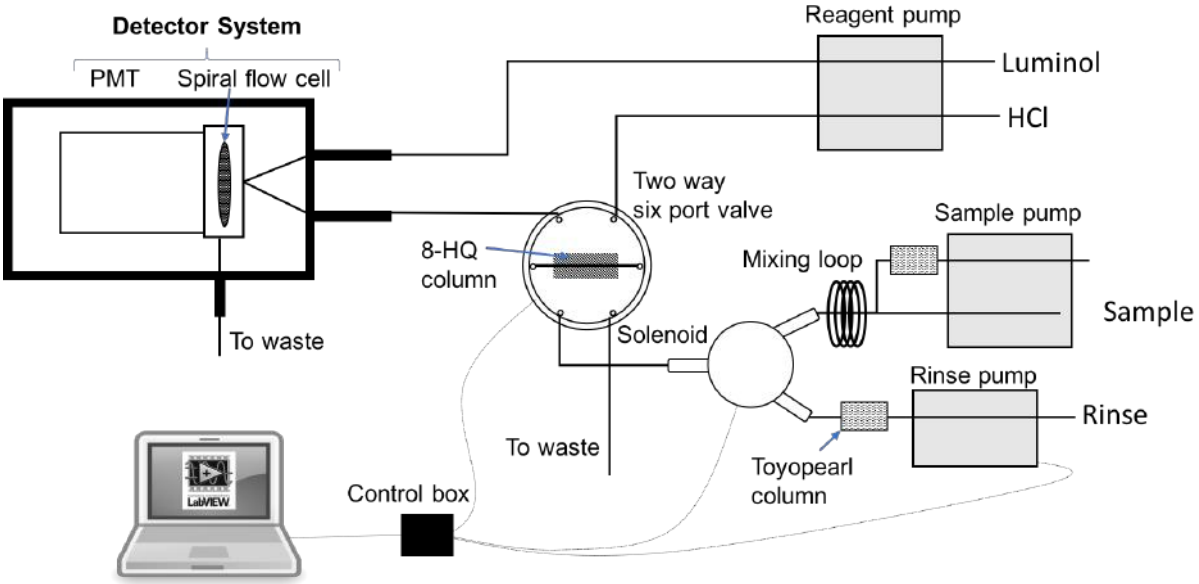

Figure 2 : FIA by chemioluminescence scheme ©David González Santana

The only difference existing between the Fe (II) and Fe (III) analysis is that the Fe(III) analysis uses a reagent (Hydroxyde peroxyde) that oxidises all the Fe(II) to Fe(III) to detect all the TdFe. The reaction of luminol with Fe (II) is also much faster than with TdFe. To control the amount of reagent used the tubing diameter can be used and also the pumps speed in the case of David González Santana FIA. The drawback with this method is that a calibration curve have to be done every day with the standard addition method (aged sea water obtained from the last cast doped with different Fe amount).

Figure 3 : PhD student David González Santana (on the left) and Dr. Alastair Lough (on the right) behind their FIA © Lise Artigue

During this cruise David González Santana and Dr. Alastair Lough expect to see thanks to their Fe (II) and TdFe data :

- A possible Fe input from Azores plateau or from the ridge at depth
- A high increase in Fe concentration next to the vent about 40 nM.
- An Fe oxidation rate faster than in other ocean (Atlantic Ocean more oxidise than the Pacifique for example).

It is then interesting to compare the Fe concentrations data with the Manganese (Mn) and Aluminium (Al) concentration data obtained by Dr. Joe Resing from University of Washington and the Pacific Marine Environment laboratory just outside the bubble. With the Mn and Al, there is no need to be as clean as for the Fe. The Mn and Al samples are the only

metal coming from both on-board rosettes (the Titanium and the Stainless-Steel rosette) allowing us to do a data comparison between these two rosettes.
Mn is a good hydrothermal plume tracer as it is quite conservative (more than Iron that react quickly). Aluminium is a lithogenic input tracer to look at dust/aerosol deposition in surface water and sediment resuspension in deep water.
To measure these two components Joe Resing also used FIA techniques but instead of chemioluminescence, fluorescence (from reaction between Al and lumogalium) is used to detect Aluminium and a colorimetric method is used to detect Mn. Al is very concentrated in Atlantic.
During this cruise Joe Resing exept to see thanks to Mn and Al data:

- Surface Dust deposition
- High Mn concentration in deep water close to the hydrothermal sites.
- If there is a hydrothermal source of Al.

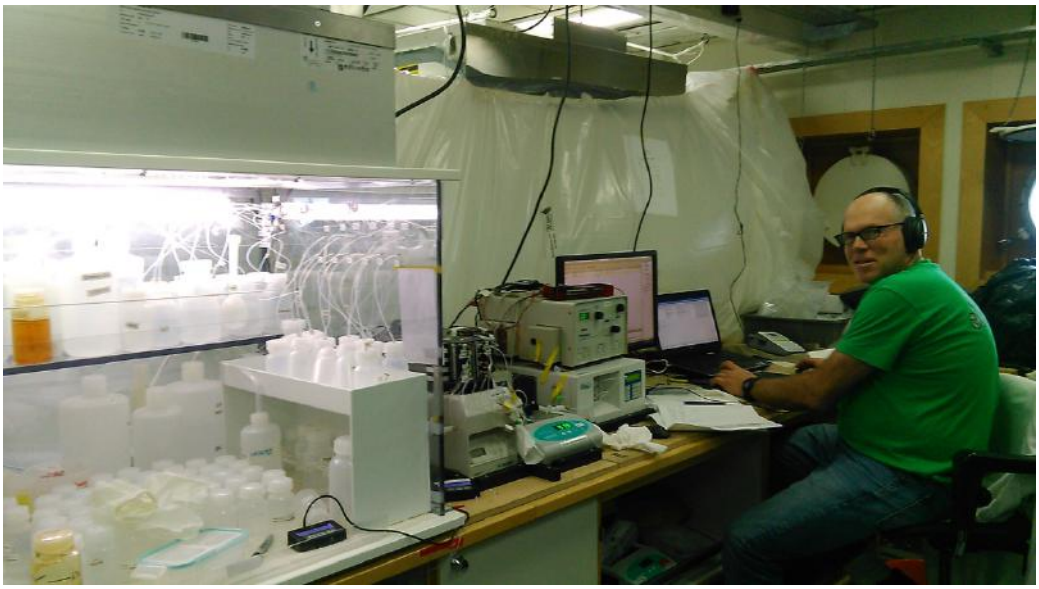

Figure 4 : Dr. Joe Resing behind his FIA © Lise Artigue

7.2 Contribution personnelle à ces travaux de thèse

Participation campagne : L'ensemble des travaux que je présente en papier 1 et 2 (chapitre 2 et 3 de cette thèse) ont pu être réalisés suite à un partenariat que j'ai établi en 2018 avec Maeve Lohan au cours de la campagne GA13-Fridge durant laquelle je travaillais sous sa supervision dans l'équipe de prélèvement de métaux traces.
Durant cette thèse j'ai embarqué sur une seule campagne, la campagne GA13-Fidge. Durant cette campagne j'ai participé à l'échantillonnage de la rosette propre et j'ai écrit un blog de vulgarisation scientifique (Annexe 7.1). L'objectif était d'apprendre l'échantillonnage propre.
Je n'ai pas embarqué sur la campagne GApr08 2017 (présenté en chapitre 2 et 3), ni sur les campagnes KEOPS 1&2 qui ont eu lieu respectivement en 2005 et 2011 (chapitre 4).

Dans les paragraphes suivant quand je parle de ma contribution c'est avec les initiales **LA**.

Papier 1 – Chapitre 2 : Artigue, Lise, Lacan, F., van Gennip, S., Lohan, M. C., Wyatt, N. J., Woodward, E. M. S., Mahaffey, C., Hopkins, J., & Drillet, Y. (2020). Water mass analysis along 22 °N in the subtropical North Atlantic for the JC150 cruise (GEOTRACES, GApr08). *Deep Sea Research Part I: Oceanographic Research Papers*, *158*, 103230. https://doi.org/10.1016/j.dsr.2020.103230

LA a réalisé l'eOMPA (choix des end-members, des paramètres etc.) sous Matlab (en modifiant le code Matlab de l'eOMPA fourni par omp.geomar pour l'ajuster à nos besoins) avec l'aide de F. Lacan.
LA a réalisé l'analyse de Monte Carlo sous Matlab.
LA et F. Lacan ont eu l'idée d'établir une collaboration avec Mercator Ocean pour obtenir les trajectoires lagrangiennes.
S. van Gennip a produit les LPTE. **LA** a par la suite analysé et interprété l'ensemble des résultats LPTE (plus de 4000 figures générées).
LA a rédigé l'ensemble du manuscrit sous la direction de FL et avec l'aide de S. van Gennip pour la partie méthode Lagrangienne.
C. Mahaffey est la chef scientifique de la campagne GApr08. C. Mahaffey, M.C. Lohan, N.J. Wyatt, E. M. S. Mahaffey ont participé à l'échantillonnage de toutes les données hydrographiques présentées dans ce papier et ils ont tous avec J. Hopkins produit les données. Tous ont relu le manuscrit.

Papier 2 – Chapitre 3 : Artigue, L, Wyatt, N. J., Lacan, F., Mahaffey, C., & Lohan, M. C. (soumis 2020) *The importance of water mass transport and dissolved-particle interactions on the dissolved aluminum cycle in the subtropical North Atlantic.*

LA a obtenu une bourse de l'école des docteurs de Toulouse pour réaliser ce travail à l'université de Southampton.
LA et N.J. Wyatt ont mis en place le système FIA pour l'analyse de l'aluminium au National Oceanographic Center (NOC, Southampton). C'est la première fois que ce système pour l'analyse de l'aluminium a été mis en place au sein de l'équipe de M. C. Lohan.
LA a mesuré l'ensemble des 315 échantillons présentés dans ce papier (fish + colonne d'eau) au NOC durant les 6 semaines de visite.
LA a réalisé le modèle 1D advection-dust deposition et appliqué l'eOMPA aux données d'aluminium. **LA** a rédigé l'ensemble du manuscrit. Tout cela sous la direction de F. Lacan.

C. Mahaffey était la chef scientifique de la campagne GApr08. M.C. Lohan et N.J. Wyatt ont relu le manuscrit plusieurs fois.

Papier 3– Chapitre 4 : Artigue, L, Lacan, F., Klar, J., Pradoux, C., Sarthou, G., Viollier, E., Blain, S. (en preparation 2020) *Iron isotopes as tracers of biogeochemical cycles in the naturally fertilized area of the Kerguelen Plateau.*

Cette partie a représenté mes 15 premiers mois de thèse.
LA a tout d'abord réalisé 6 mois de tests de blancs et de rendements sur l'ensemble du protocole de mesure de fer isotopique. Après 6 mois **LA** a pu mettre en évidence une contamination en fer de la nouvelle résine de l'entreprise Savillex©. Tous les béchers Savillex réalisés avec cette résine ont été retirés du marché international pour les mesures de fer. Une compensation financière (en matériel) a été reversée à l'équipe TIM, LEGOS, Toulouse par Savillex©. Nous avions pensé faire une publication « technique » car de nombreux protocoles de lavage ont été testés. Mais cela n'a pas été réalisé.

LA a pré-concentré, purifié et mesuré à l'élément XR et au MC ICPMS les concentration et la composition isotopique de fer des échantillons provenant des expériences d'incubation de la campagne KEOPS 2 (3 mois d'analyse). Malheureusement les résultats n'ont pas été concluants et en discutant avec G. Sarthou il a été mis en évidence que des problèmes de filtration avaient eu lieu en amont à bord de la campagne KEOPS 2 rendant ces échantillons non valables pour analyse. Ces expériences d'incubations bien que mentionnées dans le papier 3 ne sont pas présentées dans cette thèse.
Au total les 9 premiers mois de cette thèse ont été considérés comme « perdus » d'où une prolongation de 5 mois financée par le laboratoire LEGOS (3 mois) et l'équipe TIM (2 mois).

LA a analysé l'ensemble des échantillons de concentration et composition isotopique de KEOPS 2 présentés dans le papier 3 (de la préconcentration, purification à la mesure par MC-ICPMS). Cela représente 37 échantillons. En parallèle **LA** a modifié le protocole de purification de la résine AGMP-1 (annexe 7.4) et a mesuré au MC-ICPMS des solutions d'hématite dopées avec du Cr, Ni, Na, Mg, Ca etc. d'où la contribution au papier Annexe 7.5 soumis dont **LA** a participé à plusieurs relectures.
K. Pradoux a analysé les échantillons d'eau interstitielles présentées dans le papier 3 et les échantillons KEOPS 1 colonne d'eau.
LA a interprété et rédigé le manuscrit « en préparation » avec l'aide de F. Lacan.
Aucun des co-auteurs de ce papier (excepté F. Lacan) n'a relu le papier pour l'instant.

Bourses obtenues pendant ce doctorat :

2019: CNRS/LEGOS bourse pour 3 mois supplémentaires de doctorat.

2019: Bourse de la Gordon research conference afin de participer en tant qu'orateur invitée au « 2019 Chemical Oceanography Gordon Research Seminar (GRS) ».

2018: Bourse de l'école des docteurs de l'Université de Toulouse pour une mobilité de 6 semaines au sein du groupe dirigé par Maeve Lohan à l'Université de Southampton, National Oceanographic Center (NOC).

2018: Bourse du LEGOS pour participer à l' Ocean Science Meeting 2018 et à la campagne en mer Fridge (décembre 2018-février 2019).

2017: Bourse de la Société Française des IsotopeS (SFIS) pour participer à la GEOTRACES Summer School 2017.

2016: Bourse ministériel (MESR) pour 3 ans de doctorats.

Posters et Talk :

Artigue L., Wyatt N, Lacan F, van Gennip S, Lohan M. C., (2019) Dissolved aluminium distribution in the subtropical North Atlantic coupled with an OMPA and modeled backward trajectories: implications for North Atlantic biogeochemical cycling, **Talk at the Chemical Oceanography Gordon Research Seminar (GRS).**

Gonzalez-Santana D, Artigue L, Lough A.J.M, Tagliabue A, Planquette H, Sarthou G, Lohan M. C. (2018) dFe(II) variability across hydrothermal vents in the Mid Atlantic Ridge, **Poster at Goldschmidt conference.**

Artigue L, Lacan F, Klar J.K, Pradoux C & Sarthou G (2018) Iron Isotopic insights into the iron cycle around the Kerguelen Islands, **Poster at Ocean Science Meeting conference.**

Artigue L, Lacan F, Pradoux C & Sarthou G (2017) Iron Isotopic Fractionation by Phytoplancton Uptake off Kerguelen Islands, **Poster at Goldschmidt conference et à la GEOTRACES summer school.**

7.3 Mise en place d'un protocole analytique de mesure de l'aluminium dissous par flow injection analysis (FIA)

This protocol was inspired from Resing et Measures (1994) modified by Brown et Bruland (2008).

1- Instrumental setting

This section presents the FIA system setting for aluminum analysis set up at the University of Southampton in May 2018 by Lise Artigue and Neil Wyatt.

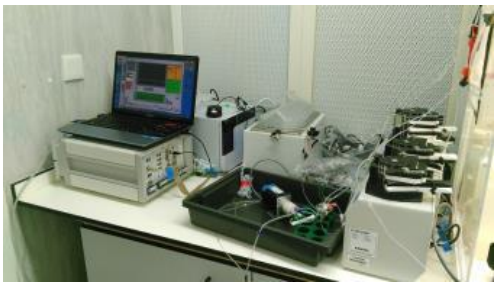

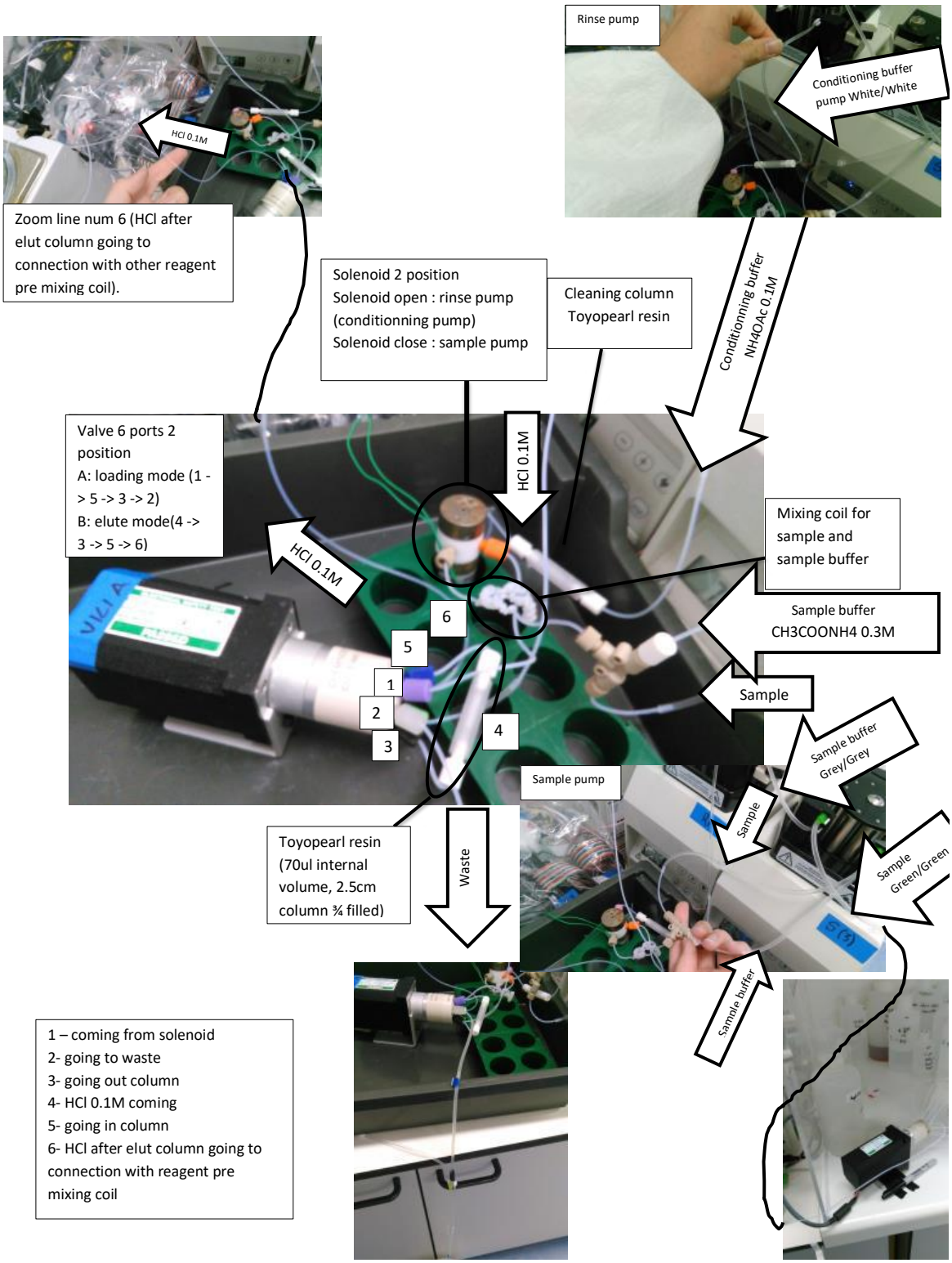
Rinse pump
Conditioning buffer pump White/White
HCl 0.1M
Zoom line num 6 (HCl after elut column going to connection with other reagent pre mixing coil).
Solenoid 2 position
Solenoid open : rinse pump (conditionning pump)
Solenoid close : sample pump
Cleaning column Toyopearl resin
Conditionning buffer NH4OAc 0.1M
Valve 6 ports 2 position
A: loading mode (1 -> 5 -> 3 -> 2)
B: elute mode(4 -> 3 -> 5 -> 6)
HCl 0.1M
HCl 0.1M
Mixing coil for sample and sample buffer
Sample buffer CH3COONH4 0.3M
Sample
Sample buffer Grey/Grey
Sample pump
Sample
Sample Green/Green
Toyopearl resin (70ul internal volume, 2.5cm column ¾ filled)
Waste
Sample buffer
1 – coming from solenoid
2- going to waste
3- going out column
4- HCl 0.1M coming
5- going in column
6- HCl after elut column going to connection with reagent pre mixing coil

Remote control

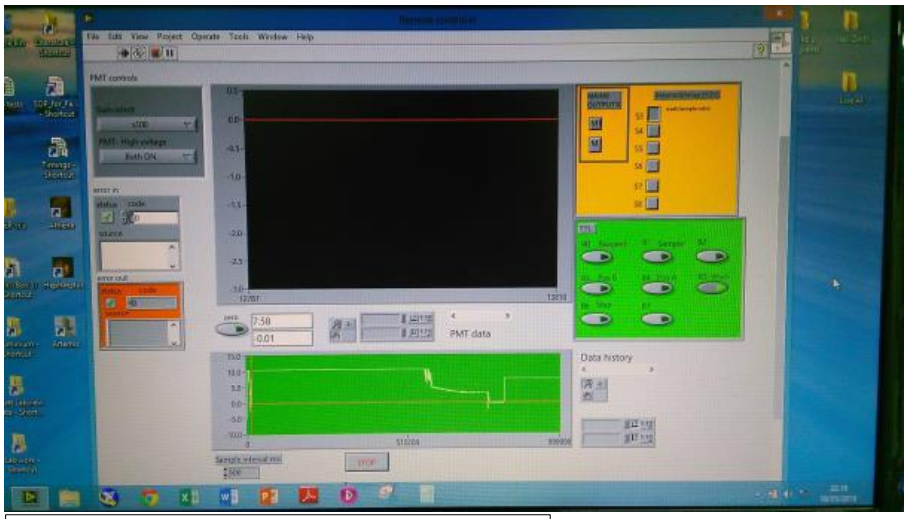

Al 15s _preconc_60s load_ 150s elute

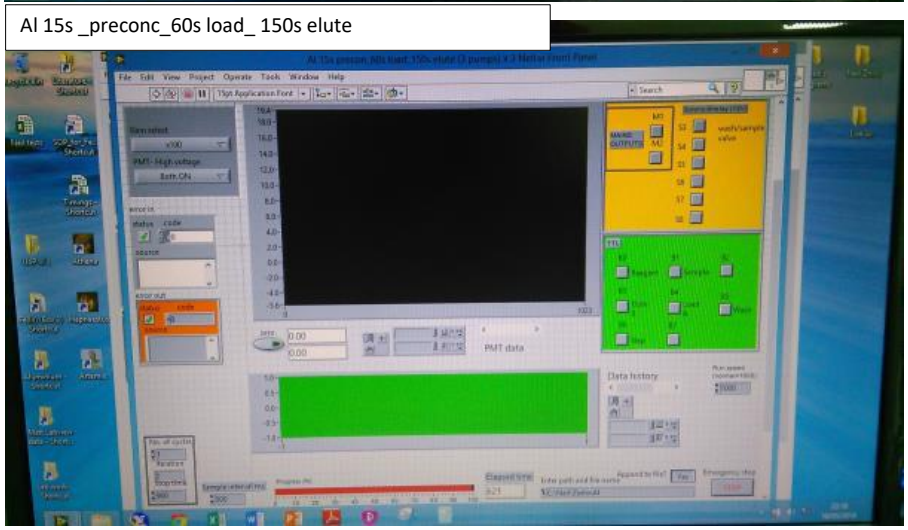

Analysis

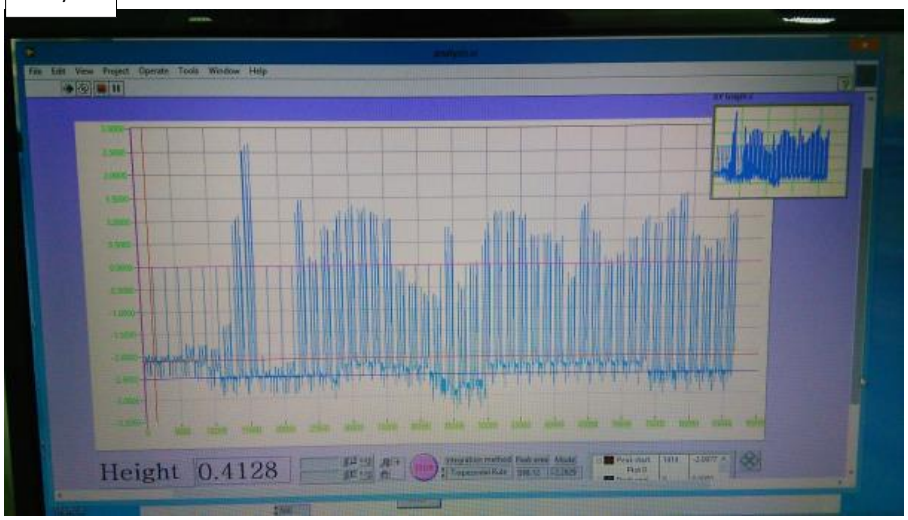

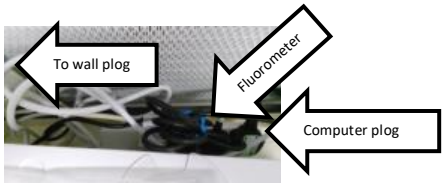
To wall plog
Fluorometer
Computer plog


RF-20A

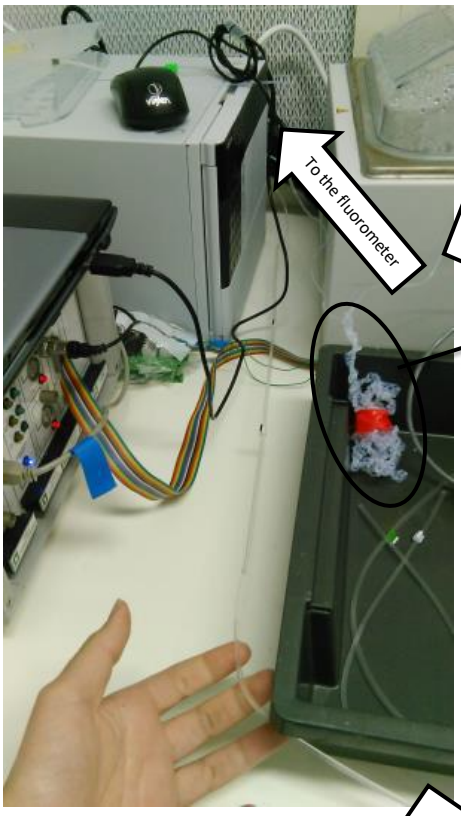
To the fluorometer
Brij-35 + Lumogallion/CH3COONH4 & HCl after mixing coil
Mixing coil (4m) for Hcl post elution and reagents (brij + lumogallion + reaction buffer)
Waste

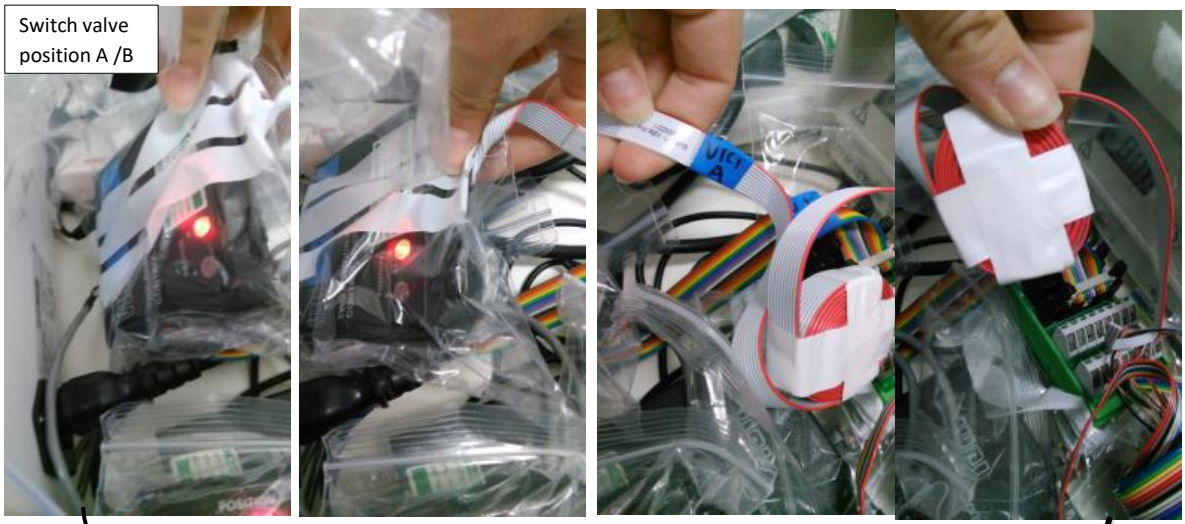
Switch valve
position A /B

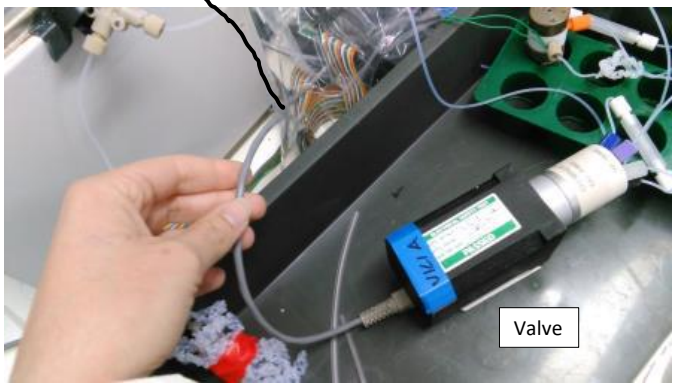
Valve

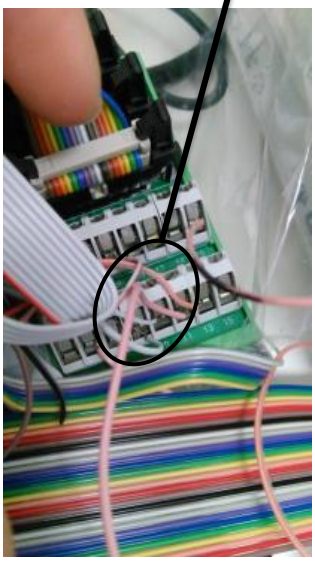

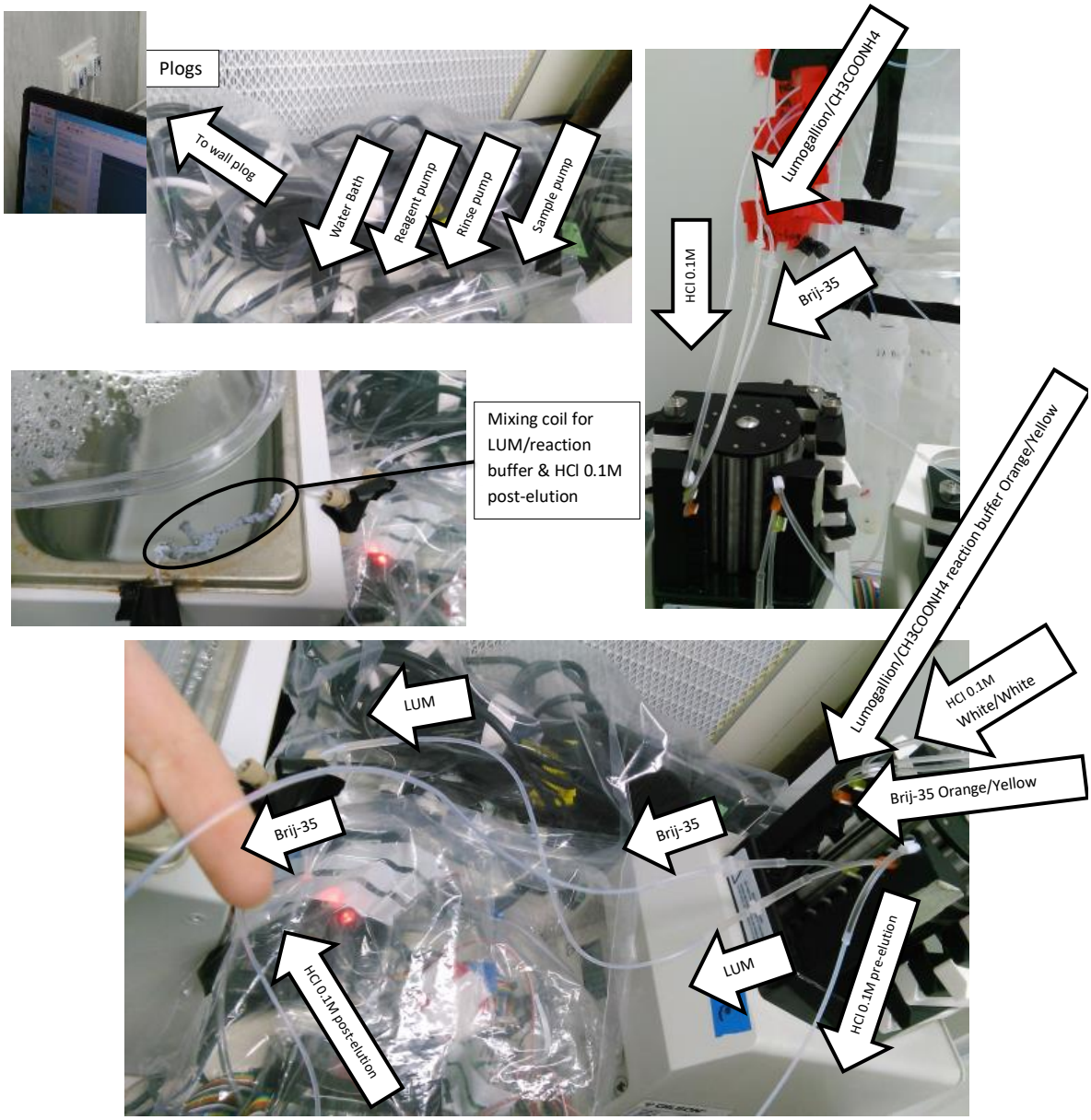
Plogs
To wall plog
Water Bath
Reagent pump
Rinse pump
Sample pump
Lumogallion/CH3COONH4
HCl 0.1M
Brij-35
Mixing coil for LUM/reaction buffer & HCl 0.1M post-elution
Lumogallion/CH3COONH4 reaction buffer Orange/Yellow
HCl 0.1M White/White
Brij-35 Orange/Yellow
LUM
Brij-35
Brij-35
LUM
HCl 0.1M pre-elution
HCl 0.1M post-elution

Solenoid
(Open/close: Rinse pump/Sample pump).

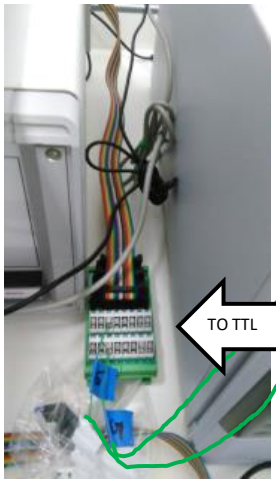

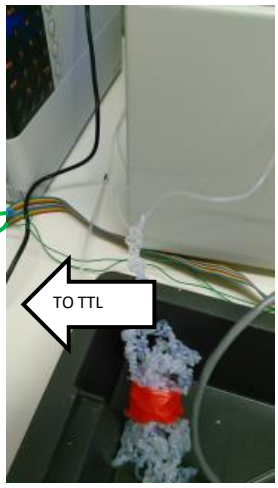

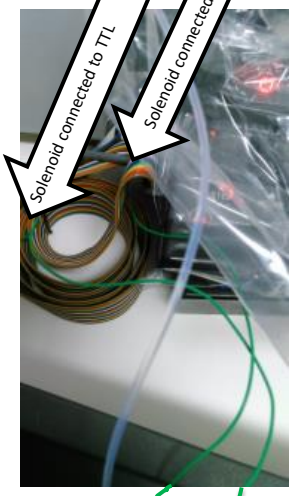

Solenoid TTL

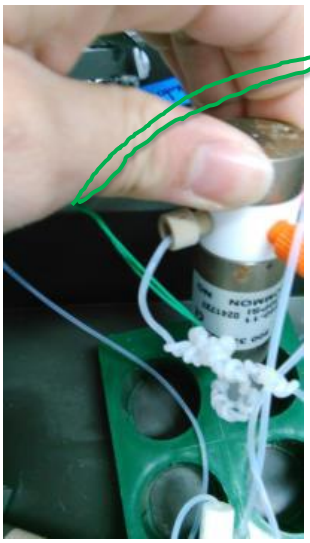

Connexion solenoid TTL to the control bow (behind)

Autosampler

Step box (up)
Control manual if deplog left side or control by computer if left plog in.

To TTL

To TTL

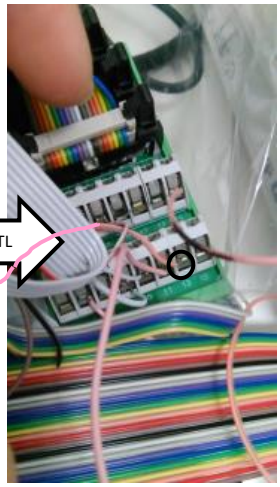

Autosampler (down)

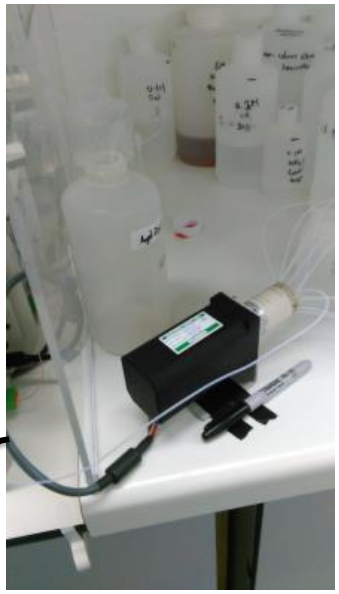

To solenoid

Pumps

Sample pump

Rinse pump

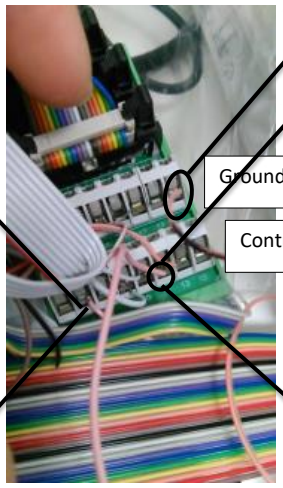

Ground

Control box conection

Rinse pump aussi relié à la terre

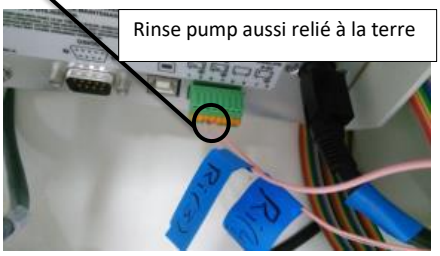

Reagent pump
Manual control, not connected to TTL

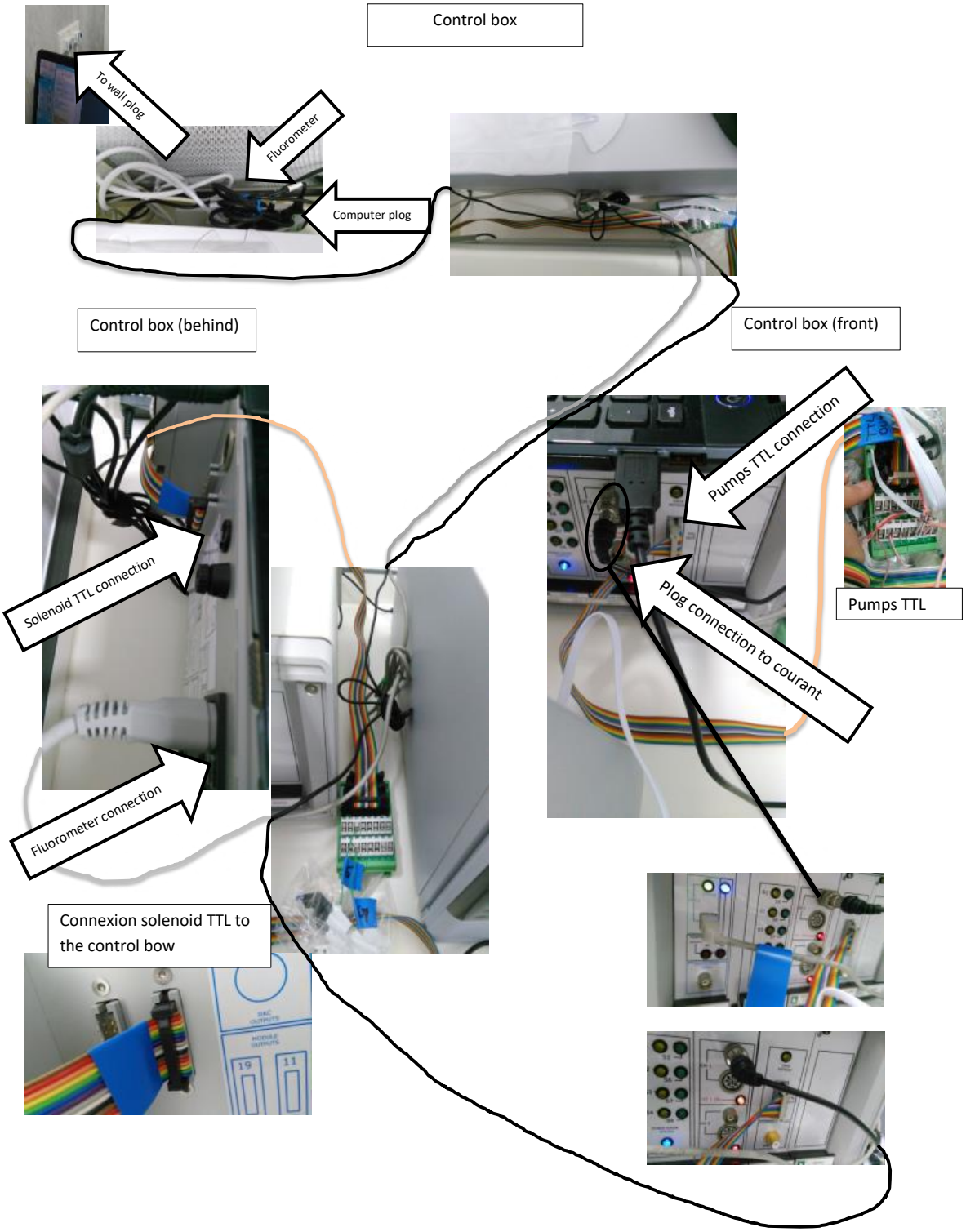
Control box
To wall plog
Fluorometer
Computer plog
Control box (behind)
Control box (front)
Pumps TTL connection
Pumps TTL
Solenoid TTL connection
Plog connection to courant
Fluorometer connection
Connexion solenoid TTL to the control bow

2- Reagents

Standards: An aluminium AAS standard CAS [7446-70-0] MW=133.34g/mol Sigma Aldrich is used to do our calibration curve. This standard solution has a concentration of 1000ppm Al in HCl. So it represents 37064 µmol Al/L (1g/26.98g/mol = 0.03706 molAl/L). To obtain a stock solution of Al at **3.33 µm** a serial dilution is done.

We dilute 2mL of the stock Al AAS standard dilute with 28mL of MQ water and 60µL of HCl 12M (Acid Romil-SpA Super Purity Acid Al<1ppb) to obtain a **30 ml 2 470,96 µM Al** solution.

We dilute 40.5 µL of the **2 470,96 µM Al** prepared before in 30mL of MQ water with 60µL of HCl 12M to obtain a **30 ml 3 335,8 nM Al** solution.

Primary standards are then made from this **3.33 µm** Al solution into acidified column-cleaned seawater (so low in Al). The resulting primary standards ranged from 0 nM Al to ~30 nM Al. This range was chosen because standard curves have been found to be linear up to concentrations of 175 nM Al (Brown and Bruland 2008).

Standard (nM)	Corrected Standard (nM)	Volume (mL)	Stock (µM)	$V_{3.33\ \mu m}$ Al solution stock taken to do the standards (µL)
0	0.00	100	3.33	0
0.5	0.50	100	3.33	15
1	1.00	100	3.33	30
5	5.00	100	3.33	150
10	9.98	100	3.33	300
20	19.90	100	3.33	600
30	29.75	100	3.33	900

Sample buffer: A 250ml 2 M CH3COONH4 (ammonium acetate) solution was first prepared by diluting 100ml of an ammonia solution (CAS [1336-21-6] MW=17.03 d=0.92 Romil-SpA Super Purity Reagent Code H058 Al<1ppb) with 30ml of acetic acid and 120 ml of mQ water. The obtain solution have a pH around 10. Then a 1000ml **0.3 M CH3COONH4** is prepared diluting 150 ml of the previous solution in MQ water. This solution was then adjusted to pH~6.7 with acetic acid (around 22ml).

Column Conditionning buffer: A 250ml 0.1 M CH3COONH4 (ammonium acetate) solution was prepared by diluting 0.71ml of an ammonia solution (CAS [1336-21-6] MW=17.03 d=0.92 Romil-SpA Super Purity Reagent Code H058 Al<1ppb) with 1.43ml of acetic acid and 248 ml of MQ water. The obtain solution have a pH around 4.3. This solution was then adjusted to pH~5.5 with ~1.3ml of the trace metal grade ammonia solution.

Reaction buffer: A 1000ml 4 M CH3COONH4 (ammonium acetate) solution was prepared by diluting 114.3ml (~114) of an ammonia solution (CAS [1336-21-6] MW=17.03 d=0.92 Romil-SpA Super Purity Reagent Code H058 Al<1ppb) with 228.6ml (~229) of acetic acid and 657 ml of MQ water. The obtain solution have a pH around 4.4. This solution was then adjusted to pH=6.3±0.1 with ~230ml of the trace metal grade ammonia solution. **A**

lumogallion/CH3COONH4 reaction buffer solution was then prepared by adding 10mL of the 4.8 nM lumogallion stock solution to 1L of **4M CH3COONH4buffer.**

5% Brij-35 solution: for 1000 ml dilute 50 ml of Brij 35 solution (Merck KGa A for biochemistry (30% w/w in water), 100ml bottle). The Brij 35 commercial solution need to be heated at ~ 35°C to be used.

Eluent 0.1 M HCl: A 0.1M HCl column-eluent is prepared by diluting 8.3 ml of 12M Hydrochloric Acid Romil-SpA Super Purity Acid Al<1ppb in Q-Pod MQ for a 1000ml solution.

Lumogallion stock solution: A 4.8mM lumogallion stock solution was prepared by adding 50 mg lumogallion to 30ml MQ water. This solution is supposed to be at least stable for 2 months (Resing and Measures 1994).

Sample: filtered seawater samples are acidified to pH ~ 1.8 with HCl. The sample will be buffered in line with the **0.3 M CH3COONH4** sample buffer.

Resin: The preconcentration resin we use is a **Toyopearl AF Chelate resin column**. A 2,5 cm, 70uL column is ¾ filled with the Toyopearl resin.

Column-cleaned seawater (CCSW): Made in 2L batches, CCSW was prepared by pumping seawater across a **Chelex 100 resin**. The resin and the tubing were previously cleaned with ~200mL of HCl 0.5M and after flushing out the rest of HCl (by reversing the pump and pumping air) the resin is filled with the 0.1 M CH3COONH4 Column Conditionning buffer. The seawater is acidified at ph ~6 to be in the range of aluminium preconcentration. After flushing out the column conditioning buffer as describe previously, the seawater is pumped and the first 100mL thrown up (~1h is necessary to pass ~100mL of seawater in the resin linked to a green/green tubing).
The obtained CCSW at pH~6 is then acidified at pH between 1.7 to 1.8 with a ratio of ~100 µL of 12M Hydrochloric Acid (Romil-SpA Super Purity Acid Al<1ppb) for ~60 mL CCSW. The Al content of this CCSW is then measured and if it is not low enough cleaned again across the resin. The seawater (initially at 8-6nM in Al) is passed twice in our Chelex 100 resin to reach 1nM Al.

Acid wash: Several **0.5 M HCl** solutions are prepared to clean tubing and tips.

Before the first use, tubing is cleaned outside with methanol to remove organic trace.

Spectrofluorometer settings.
To be able to see full Al peaks (In our case until 150nM Al peaks) the chosen setting of the fluorometer is 2 in Sensitivity and 3 in Gain so a signal magnification x512 and on labview the Gain chosen is 100 so a final magnification x51200.

3- Method

-Start/Stop system: The pump tubing is putted on. The laptop is opened and the button start pressed on the file Remote control. The 2 walls plogs linked to the water bath, the reagent pump, the rinse pump, the sample pump and the fluorometer are turned on. The fluorometer is turned on. On the Remote control interface, the solenoid position is checked and the good communication between the laptop with the valve and all the pumps. The reagent pumps (only pump manually controlled) is opened in a clock sense. The pumps lines are cleaned in HCl 0.5M for 10min and then in mQ water for 5 minutes (the rinse pump and sample pump can't be cleaned as the same time. To clean the rinse pump the solenoid needs to be open while to clean the sample pump it needs to be closed). Every position of the autosampler is cleaned for 10s each with HCl 0.5M then mQ water.
To Stop the system this steps are did in the reverse order. The pumps line stay in mQ water for night and weekends.
-Introduce reagents: The lines corresponding with the good flow rates are putted in the reagents (cf. Table1). The good flow of the reagent is check. Before the measurement can start we need to have a baseline as low as possible (On the fluorometer, Emission wl<8nm). For that remove all the air bubbles from the system is essential. To remove the bubbles from the reagent pump the button "rabit" can be pressed ~2-3s several times, then the lines need to be manually hit until all the bubbles are out. The lines of the rinse and sample pump need to be hit the same. Once the baseline is ~20nm it will go down by itself waiting ~30-40min to have a stabilized system at around 8nm.
- **pH checking:** Every measurements days fresh mQ water is acidified at pH between 1.7 to 1.8 with a ratio of ~120 µL of 12M Hydrochloric Acid (Romil-SpA Super Purity Acid Al<1ppb) for ~60 mL mQ water. This acidified mQ water is used as a sample to check the reaction pH, the sample pH and the system blanks.

> **The sample pH** can be measured from the waste line coming out of the 6 ports valve. It should be at a pH between 5 and 7.4 to have optimum aluminium preconcentration onto the Toyopearl resin column (Brown and Bruland 2008). In our case we try to be at a pH ~ 5.75.
> **The reaction pH** can be measured from the waste line coming out of the detector. It should be at a pH of 5.1-5.6 (Resing and Measures 1994). In our case are at a pH ~ 5.55.

-**Sample measurement:** The sequence is ready to start. Remote control is stop and the "Al 15spreconc_60sload_150s elute(3pumps)x3" analysis program start continuously after giving a name to the data file associated. The analysis setting is: Preconc=15s; Load=60s; Elute=150s (for more details cf. Table2). This setting allows an Al triplicate peaks with a signal coming back down to the baseline between consecutive peaks. This setting stayed for the entire sample set. The sequence always starts with acidified mQ water measured 2/3 times, this represent the blank of the measures. If these blanks are low enough (~0.5/0.6 nM in our case), the primary standard are passed to obtain a calibration line. If the calibration line have a high slope (around 0.19), a good correlation coefficient (R^2=0.999) and a low linear zero (around 1nM) the references materials are measured to check the reproducibility

and repeatability of the measurement (cf. Table 3.). If these references materials values are valid, the samples can be measured.
Every 10 samples a standard from the middle of the calibration line is runned (5 or 10nM). If the difference in the peak height is more than 5% we correct the measurement including the mass drift.
The system can be stopped while analysing pressing on Stop in the "Al 15spreconc_60sload_150s elute(3pumps)x3" file and start the Remote control to stop the rinse pump if it is still working.
The obtain peaks can be measured directly on an Analysis program running the data file obtained previously.

Table 1. Tubbing settings:

Chemicals	Pump	Tubing ($_{ml/min/inches}$)
Sample buffer (0.3 M CH3COONH4)	Sample pump	Grey/Grey (?/0.05)
Sample	Sample pump	Green/Green (1.82/0.073)
Column conditioning buffer (0.1 M CH3COONH4)	Rinse/Conditioning pump	White/White (0.60/0.040)
Reaction buffer (Lumogallion/CH3COONH4)	Reagent pump	Orange/Yellow (0.16/0.020)
Eluent 0.1M HCl	Reagent pump	White/White (0.60/0.040)
5% Brij-35 solution	Reagent pump	Orange/Yellow (0.16/0.020)

Table 2. Al 15spreconc_60sload_150s elute(3pumps) x3

Step	Sample pump	Rinse/Conditioning pump	IVA (valve position A= loading)	IVB (valve position B= elute)	Solenoid (same as rinse pump, have to be open during rinsing and close otherwise)	Autosampler	End
0	15-75s (60s loading time)	0-15s (pre-conditioning column)	0-2s (load)	75-77 (elute for 150s)	0-15s	525 (switch next sample 100s before 585 the end to pre-load time)	End 900= 465s position in load)+60s(loading)+150s(elution)+225 (to be able to see the Al triplicate picks).
1	240-300s (60s loading next measure)	225-240s (pre-conditioning column for 2nd measure)	225-227 (150s elute time+75)	300-302s (elute 2nd duplicate)	225-240s		
2	465-525s	450-465s (pre-conditioning column for 3rd measure)	450(150+300)-452s	525-527s (elute 3rd sample)	450-465s		

Table 3. Reference material

Reference material	Value expected
Safe S (496)	Value expected ~1.67 nM. Used to check the reproducibility and repeatability of the measurement.
DY021 SW (Internal standard 25m Candy Floss station 471)	No value expected. Used to see how long it takes after acidification to obtain a stable Al measure.
GSC204	No value expected. Value of our measurements ~0,628nM. Used to check repeatability of the measurement.
GSP37	No value expected. Value of our measurements ~1.356nM. Used to check repeatability of the measurement.
Fish sample 130	One of our samples measured several time to check repeatability of the measurement.

7.4 Tests d'élution du Molybdène sur AGMP-1

Problématique : Le Molybdène (Mo) n'est pas bien éliminé en HCL 6M donc nous avons fait des tests pour définir quelles conditions permettent de limiter son élution en même temps que le fer.
Nous avons préparé une solution étalon n°7 dil 10 dans HNO3 0.32 M dopé à 100 ppb en Mo et 100 ppb en Fe et dopé en In-Re. 2.5 ml de cette solution on été chargés sur les colonnes soit **250 ng de Mo et Fe**.
3 tests ont été réalisés où **seule l'étape d'élution Fe a été modifiée**:

- Test 1 : test normal (sans changement), élution avec HCl 1M + H_2O_2 0.32M, 5 fractions récupérées a = 0.3 ml, b = 0.15 ml, c = 0.15 ml, d = 0.15 ml, e = 0.15 ml
- Test 2 : test avec HCl 2M, élution avec **HCl 2M** + H_2O_2 0.32M, 5 fractions récupérées a = 0.6 ml, b = 0.3 ml, c = 0.3 ml, d = 0.3ml, e = 0.3 ml
- Test 3 : test avec 100 fois plus de H2O2, élution avec HCl 1M + **H_2O_2 32M**, 1 fraction récupérée de 0.9 ml.

Les tests 1 et 2 ont été réalisés sur 2 colonnes chacun donc le résultat présente une moyenne des rendements des 2 colonnes pour chaque test, un blanc pour le test 2 a aussi été réalisé. Le test 3 a été réalisé sur une seule colonne.
Résultats :
Pour le test 1 (normal), 0.6% de Mo et 95.9 % de Fe ont été élué (dans l'étape élution Fe).
Pour le test 2 (avec HCl 2M +0.32mM H_20_2), 2.1% de Mo et 91.1 % de Fe ont été élué (dans l'étape élution Fe).
Pour le test 3 (avec HCl 1M +32mM H_20_2), 0.08% de Mo et 93.74 % de Fe ont été élué (dans l'étape élution Fe).
Conclusion : Après mes tests nous sommes passés à une solution de HCl 1M + H_2O_2 0.32M à une solution d'**HCl 1M +32mM H_2O_2 (test3) pour l'élution du Fe.**

7.5 Interférences et effets de matrice sur les mesures de la composition isotopique du fer par MC-ICPMS

7.5.1 Résumé en français

Les spectromètres de masse à plasma à couplage inductif (MC-ICPMS) sont aujourd'hui largement utilisés pour mesurer les isotopes du fer. Ces mesures peuvent être perturbées par des interférences (notamment de Cr et Ni) et des effets de matrice (notamment des éléments majeurs). Ces perturbations peuvent être corrigées, mais, si les perturbations dépassent certains seuils, les corrections entraînent des inexactitudes importantes. Alors que ces seuils ont été déterminés précédemment pour les corrections de « standard bracketing » et de biais de masse interne, cela n'avait jamais été signalé dans le cas du double dopage (doble spiking). Ce faisant, nous avons constaté que les corrections d'interférence isobare ^{54}Cr et ^{58}Ni sont extrêmement efficaces, car il est possible de corriger avec précision jusqu'à ~12 % g(Cr)/g(Fe naturel) et 4 % g(Ni)/g(Fe naturel). Nous avons constaté que les mesures d'une solution de 200 10^{-9} g/g de Fe naturel restaient précises même lorsqu'elle était dopée avec les substances suivantes [Na] = 27 ppm, [Mg] = 2 ppm, [K] = 0,5 ppm ou [Mo] = 15 ppm (ppm = 10^{-6} g/g). Enfin, nous avons constaté que le calcium pouvait provoquer des interférences importantes (par exemple, $^{40}Ca^{16}O$), même à de faibles concentrations (0,5 ppm Ca pour une solution naturelle de Fe de 200 10^{-9} g/g), si le plateau est relativement faible (200 ppm). En revanche,10 ppm Ca ne perturbent pas les mesures avec un plateau plus large (295 ppm). Lorsque nous travaillons avec des échantillons à teneur potentiellement élevée en calcium (tels que des minéraux ou des tests de calcite, des os et des dents, ou des échantillons marins), nous préconisons de prendre soigneusement en compte le Ca lors du réglage de l'instrument et de la vérification de la précision des mesures avec des étalons isotopiques (c'est-à-dire en dopant l'étalon isotopique avec des niveaux de Ca comparables à ceux des échantillons).

7.5.2 Article soumis: *Interferences and matrix effects on iron isotopic composition measurements by double-spike multi-collection inductively coupled plasma mass spectrometry (MC-ICPMS); the importance of calcium interferences*

L'article suivant a été soumis dans la revue Journal of Analytical Atomic Spectrometry.

Journal Name

ARTICLE

Interferences and matrix effects on iron isotopic composition measurements by ^{57}Fe-^{58}Fe double-spike multi-collection inductively coupled plasma mass spectrometry (MC-ICPMS); the importance of calcium interferences.

Received 00th January 20xx,
Accepted 00th January 20xx

DOI: 10.1039/x0xx00000x

www.rsc.org/

F. Lacan[a], C. Pradoux[a], L. Artigue[a], J.K. Klar[a], J. Chmeleff[b]

Inductively Coupled Plasma Mass Spectrometers (MC-ICPMS) are nowadays widely used for Fe isotope measurements. The latter may be perturbed by interferences (notably from Cr and Ni) and matrix effects (notably from major elements). These perturbations may be corrected for, but, if perturbations exceed certain thresholds, the corrections lead to significant inaccuracies. While these thresholds have been determined previously for standard bracketing and internal doping mass bias corrections[1], this had never been reported in the case of double spiking. Doing so, we found that ^{54}Cr and ^{58}Ni isobaric interference corrections are extremely efficient, as up to ~12% g(Cr)/g(natural Fe) and 4% g(Ni)/g(natural Fe) can be accurately corrected for. We found that measurements of a 200 10^{-9} g/g natural Fe solution remained accurate even when doped with the following: [Na]=27ppm, [Mg]=2ppm, [K]=0.5ppm or [Mo]=15ppm (ppm=10^{-6}g/g). Finally we found that calcium could cause significant interferences (e.g., $^{40}Ca^{16}O$), even at low concentrations (0.5ppm Ca for a 200 10^{-9} g/g natural Fe solution), if the plateau (Fe shoulder where the measurements are done) is relatively small (200ppm), while 10ppm Ca do not perturb the measurements with a wider plateau (295ppm). While working with samples with potentially high calcium contents (such as calcite minerals or tests, bones and teeth, or marine samples), we preconize to carefully take into account Ca while tuning the instrument and checking the measurement accuracy with isotopic standards (i.e. doping the isotopic standard with Ca levels comparable to those of the samples).

Introduction

Iron isotopic compositions are nowadays widely used in Earth and planetary sciences, environmental research, and also in biological and medical research[2–5]. They are most commonly expressed as $\delta^{56}Fe$ defined as follows:

$$\delta^{56}\mathrm{Fe}\ (‰) = \left[\frac{(^{56}\mathrm{Fe}/^{54}\mathrm{Fe})_{\mathrm{sample}}}{(^{56}\mathrm{Fe}/^{54}\mathrm{Fe})_{\mathrm{IRMM\text{-}14}}} - 1 \right] \times 10^{3}$$

Almost all of these measurements are now carried out with multi-collection inductively coupled plasma mass spectrometers (MC-ICPMS). While these instruments allow very reliable and accurate measurements when operated in certain conditions, the measurements may suffer from a variety of perturbations, which include spectral interferences and matrix effects.

A spectral interference is the process by which an ion other than the analyte is detected as if it was the analyte, because its mass to charge ratio is indistinguishable from that of the analyte. There are three main types of spectral interferences in ICPMS: isobaric interferences, produced by mono-atomic ions (e.g., $^{54}Cr^{+}$ and $^{58}Ni^{+}$ may interfere with $^{54}Fe^{+}$ and $^{58}Fe^{+}$, respectively), poly-atomic interference, produced by molecular ions (e.g., $^{14}N^{40}Ar^{+}$ or $^{27}Al_2^{+}$ may interfere with $^{54}Fe^{+}$) and doubly charged ion interferences (e.g., $^{112}Cd^{++}$ on $^{56}Fe^{+}$). A matrix effect is the process by which the instrument behaviour varies in response to a variation in the sample composition. It is caused by dissolved ions in the solution (other than that of interest). It can be divided in two types: a signal drift with time due to salt deposition on the cones and/or a modification of the mass bias (instrumental mass fractionation) due to a modification of the ionization environment in the plasma (i.e. of the isotope distribution in the plasma; the so called space charge effect)[6,7]. For instance, the mass bias may suddenly vary between a very well purified isotopic standard solution containing almost exclusively the analyte and an insufficiently purified sample solution containing significant levels of other compounds. Mass bias correction is a major aspect of the Fe isotopic ratio measurements, because it is typically of the order of 1% per atomic mass unit, which is about 100 times larger than the order of magnitude of the typical targeted accuracy of 0.1‰. Three main methods are commonly used for Fe mass bias corrections,

[a] LEGOS, University of Toulouse, CNRS, CNES, IRD, UPS, Toulouse, France.
[b] GET, University of Toulouse, CNRS, CNES, IRD, UPS, Toulouse, France.

† Footnotes relating to the title and/or authors should appear here.
Electronic Supplementary Information (ESI) available: [details of any supplementary information available should be included here]. See DOI: 10.1039/x0xx00000x

standard bracketing, internal doping with another element of similar mass, usually Ni or Cu, and double spiking.

Some of the above-mentioned perturbations, interferences and matrix effects, may be quantified and corrected for, but corrections are never perfect. In addition some perturbations cannot be quantified nor corrected. Therefore these perturbations degrade the measurement trueness and precision. The thresholds above which these degradations become significant need to be determined. They depend on many aspects of the analysis, including the type of instrument and its setting, the type of introduction system, and the mass bias correction method. Several works have documented these perturbations and thresholds in different conditions, including different instruments (e.g. Micromass IsoProbe[8], Thermoelemental Axiom[9], Nu Plasma[10–13] and Thermo-Scientific Neptune[14,15]), different introduction systems (liquid, with[9–12] or without[14,15] desolvatation, and laser ablation[13]) and different mass bias correction methods (notably standard bracketing[12,14,15] and double spiking[9–11]).

The present work presents a study of the impact of interferences (Cr, Ni and Ca) and matrix effects (Na, Mg, Ca, K, Mo) on iron isotope measurements using a Thermo-Scientific Neptune MC-ICPMS (most commonly used nowadays for Fe isotope analyses) and a mass bias correction with a ^{57}Fe-^{58}Fe double-spike (most commonly used double spike for about a decade[3,16]). These results allow to improve the reliability of such measurements.

Experimental

All analyses were made using the Neptune MC-ICPMS (Thermo-Scientific) of the Observatoire Midi Pyrenees (Toulouse, France), equipped with a Ni X skimmer cone and operated with a high resolution slit (25µm). The samples, dissolved in 0.32 mol L^{-1} HNO_3, were introduced via a 75µL/min PFA MicroFlow nebulizer (Elemental Scientific) and an Apex-IR dessolvator (Elemental Scientific). Operation parameters are detailed in Table 1. Collector configuration is given in Table 2.

With such instruments (most commonly used nowadays for Fe isotope studies), Fe isotope measurements may suffer from poly-atomic ion interferences due to argon oxy-hydroxides (e.g. $^{40}Ar^{16}O$ and $^{40}Ar^{16}O^{1}H$) and argon-nitrogen species (e.g. $^{40}Ar^{14}N$). These elements, Ar, O, H, and N, were present in all of our measurements, either supplied by the argon gas or by the HNO_3. The mass resolving power (a quantification of the resolution[17]) of this type of instrument does not allow to fully separate the Fe peaks from the interference peaks. However, because the Fe isotopes are slightly lighter than these interferences, their peaks only partially overlap (Fig. 1). The light part of the Fe peaks are virtually free of interference, i.e. the light peak tails of the interferences do not significantly contribute to the Fe signals (given that the Fe to interference intensity ratios are not too small). This has been extensively described previously [17] and is commonly referred to as measuring on the Fe "shoulder" of the peaks.

Table 1. MC-ICPMS and dessolvator operation parameters

Neptune MC-ICPMS (Thermo-Scientific)	
RF power	1230 W
Acceleration voltage	10 kV
Mass analyser pressure	$1.9.10^{-8}$mbar
Extraction lens	-2000 V
Apex-IR dessolvator (Elemental Scientific)	
Heater temperature	105°C
Chiller temperature	2°C
Nitrogen gas flow	0
Nebulizer	ESI MicroFlow PFA 75
Sample uptake rate	65-85 µL min^{-1}
Transmission efficiency	0.03%
Mass discrimination	2.4% per atomic mass unit

Table 2. Faraday cup configuration and isotopic abundances for Fe, Cr and Ni

Nominal Mass		53	54	56	57	58	60	61
Isotope abundance (%)	Cr	9.5	2.37					
	Fe		5.8	91.7	2.2	0.28		
	Ni					68.3	26.1	1.13
Collector configuration		L4	L2	L1	H1	H2	H3	H4

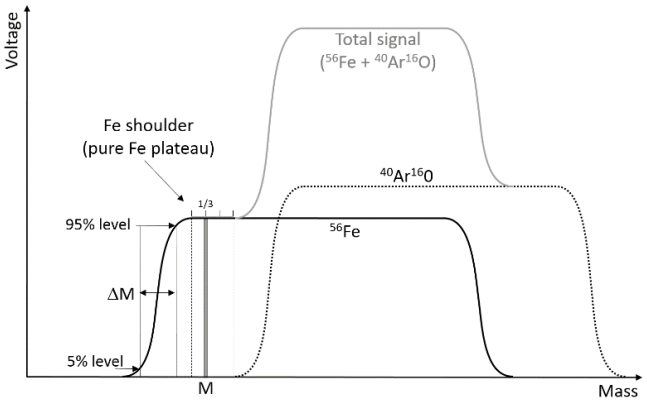

Figure 1. Schematic of the peak shapes for ^{56}Fe and the $^{40}Ar^{16}O$ interference. The instrument is set to perform the measurements at mass M, chosen at 1/3 of the pure Fe plateau (free of interference), i.e. the Fe shoulder, which is defined as the flat part of the Fe peak left of the $^{40}Ar^{16}O$ signal. The resolving power, R_{power}(5%, 95%), is calculated as ΔM/M. Adapted from Weyer and J. B. Schwieters [6]

We used a ^{57}Fe-^{58}Fe double spike, composed of 0.11%, 3.21%, 59.2% and 37.5% of ^{54}Fe, ^{56}Fe, ^{57}Fe and ^{58}Fe, respectively. The sample to spike Fe mass ratio was 2/3 (i.e. the sample-double spike mixture is composed of 40% w/w of sample and 60% of double spike), in order to maximize beam intensities on the four Fe collectors and minimize error propagation[16,18,19].

Samples were run following the typical sequence: IRMM14 - HEM - IRMM14 - SAMPLE-1 - IRMM14 - SAMPLE-2 - IRMM14 - HEM - IRMM14 - SAMPLE-3 … and so on. Where "HEM" is an in-house hematite standard of known Fe isotopic composition and negligible contents of other elements [19–21], which allowed monitoring measurement accuracy.

In between each of the above, the background was measured via the measurement of a 0.32 mol L^{-1} HNO_3 solution in which all samples were dissolved.

Data extraction was performed as follows. The mean background signals (over a sequence, typically 12 hours) were subtracted from the raw data of each sample or standard. Cr and Ni isobaric interferences (on ^{54}Fe and ^{58}Fe) were corrected for by estimating ^{54}Cr and ^{58}Ni, from the ^{53}Cr and ^{60}Ni signals, the natural Cr and Ni abundances and the instrumental isotopic fractionation. The latter was computed for Fe from the background and isobaric interference corrected signals, using the Siebert et al. iterative calculation[22]. Instrumental mass fractionations for Cr and Ni were therefore assumed to be the same as for Fe. The above procedure is circular because it requires the instrumental mass fractionation to estimate the Cr and Ni interferences, but it also requires the Cr and Ni interferences to estimate the instrumental mass fractionation. This problem was circumvented through another iterative calculation. Finally, for each sample the $\delta^{56}Fe$ value was calculated relative to the mean of its two bracketing IRMM14.

In order to determine the impact of interferences and matrix effects, samples were prepared as follows. A 200 ppb (10^{-9} g(Fe)/g(HNO_3)) hematite solution, mixed with the double spike (300 ppb) was doped with variable amounts of mono-elemental standard solutions of Cr, Ni, Cr + Ni, Na, Mg, K, Ca, Mo, and Na + Mg + K + Ca + Mo. These elements were chosen either because they produce spectral interferences (Cr, Ni and Ca), or because they might be found at significant levels in the final purified solutions (either because of their high initial abundances in natural samples or because of imperfect chemical separation). These mixtures were measured to assess whether or not the correct isotopic composition of the hematite could be determined. The doubly charged effect is often negligible as doubly charged ions are rare in the conditions of the plasma[23], therefore Cd was not investigated.

Results and discussion

The effect of ^{54}Cr and ^{58}Ni isobaric interferences on the hematite measurements are displayed in Figure 2 and 3. Figure 2 shows that even when the hematite was doped with 11.9% g(Cr)/g(hematite Fe) (i.e. the solution analysed was 200ppb hematite Fe + 24ppb Cr + 300ppb double spike; 200ppbx11.9%=24ppb), which lead to a $^{54}Cr/^{54}Fe$ slightly larger than 5% (mol/mol), the correct isotopic composition of the hematite was found. The presence of a small quantity of Ni (leading to 1% $^{58}Ni/^{58}Fe$ (mol/mol) in the analysed solution) did not significantly change the results. This demonstrates that, up to this level, the ^{54}Cr interference can be successfully corrected for. This value is similar to the threshold documented earlier with the same type of instrument (Neptune) but with a standard bracketing mass bias correction[15]. Note that these results are obtained thanks to the interference correction; without correction, significant errors (of the order of 1‰) occur as soon as the Cr content reaches 0.1% g(Cr)/g(hematite Fe) and this error increases dramatically with increasing Cr content (it reaches 39‰ for 11.9% g(Cr)/g(hematite Fe)).

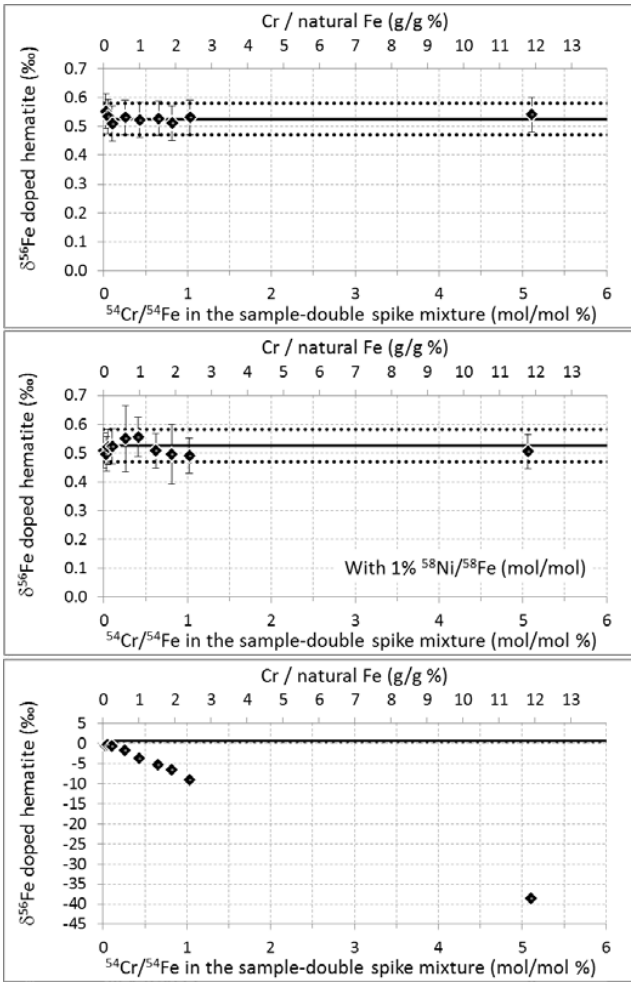

Figure 2. Top: $\delta^{56}Fe$ of hematite (200ppb natural Fe) doped with variable amounts of Cr. Middle: same as top but with an addition of Ni leading to 1% $^{58}Ni/^{58}Fe$ (mol/mol) in all samples. Bottom: same as top but with no Cr interference correction (note the different vertical scale). The level of Cr doping is expressed in two ways: i) the level of Cr (all isotopes) compared to that of natural Fe (i.e. not taking into account the double spike, top x axis), and ii) the level of ^{54}Cr compared to ^{54}Fe in the analysed solution, i.e. in the sample-double spike mixture (bottom x axis). Diamonds are the averages of duplicate measurements. Error bars are 2 standard deviations of the duplicate measurements or the long term internal precision (2SD) of our instrument (0.06‰), whichever the greatest (they are smaller than the symbol size on the bottom panel). The horizontal black lines show the $\delta^{56}Fe$ of pure (un-doped) hematite measured during the same analytical session; mean value (solid line) ± 2 standard deviations (dotted lines).

Figure 3 shows that when the hematite was doped with up to 3.9% g(Ni)/g(hematite Fe) (i.e. 200ppb hematite + 8ppb Ni + 300ppb double spike), the correct hematite isotopic composition was found. Above that threshold it was not the case anymore. The presence of a small quantity of Cr (leading to 0.1% $^{54}Cr/^{54}Fe$ (mol/mol) in the analysed solution) did not significantly change the results. As for Cr, these results are obtained thanks to the interference corrections; without correction, very significant errors (of the order of 8‰) occur as soon as the Ni content reaches 0.3% g(Ni)/g(hematite Fe) and

this error increases dramatically with increasing Ni content (it reaches 88‰ for 3.9% g(Ni)/g(hematite Fe)).

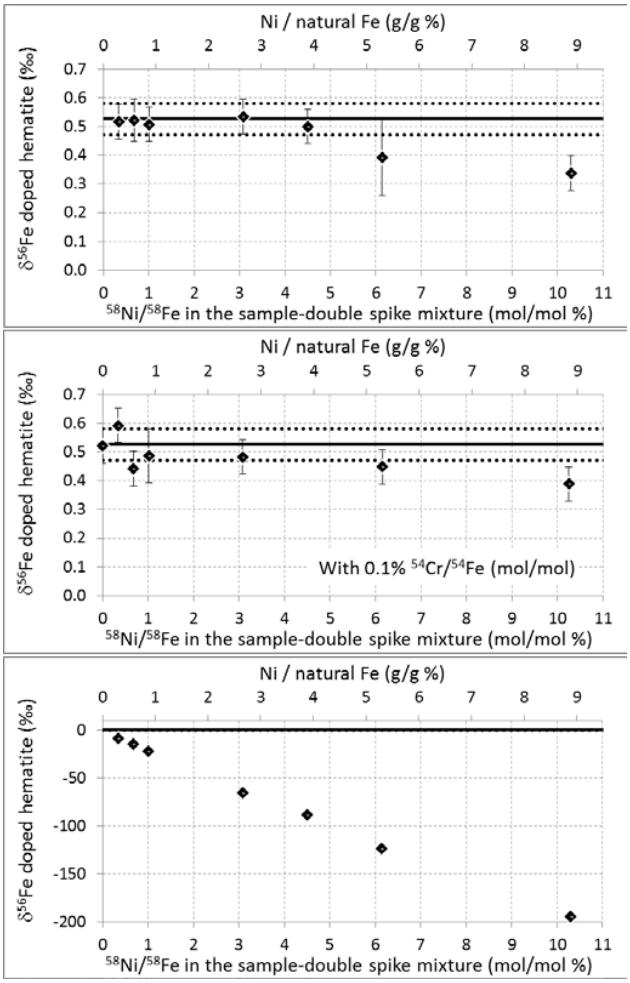

Figure 3. Top: Same as Figure 2, but for variable amounts of Ni. Middle: same as top but with an addition of Cr leading to 0.1% $^{54}Ni/^{54}Fe$ (mol/mol) in all samples. Bottom: same as top but with no Ni interference correction (note the different vertical scale).

Figure 4 shows the effect of Na, Mg, K, and Mo doping (on the 200ppb natural Fe solution, mixed with 300ppb double spike). It shows that, for these doping concentrations (up to 27ppm Na, 2ppm Mg, 0.5ppm K and 15ppm Mo), the correct isotopic composition of the hematite was found. This demonstrates that, up to these levels and despite the lower ionization energies (and thus higher degrees of ionization) of these elements compared to Fe (Table 3), these matrix effects are negligible, or at least accurately corrected for with the double spike. These levels were chosen because they represent the maximum values we encounter with purified seawater samples we usually work on. They correspond to Na/Fe=135 and Mg/Fe=10 (where Fe is natural Fe). These ratios are significantly larger than those documented previously (Na/Fe=5 and Mg/Fe=2, with a ^{54}Fe-^{58}Fe double spike and a different instrument, Thermoelemental AXIOM MC-ICPMS)[9], which allows extending the range within which Na and Mg matrix effects can be neglected.

The effects of calcium doping, shown in Figure 5, are more significant and more complicated. Calcium may perturb the

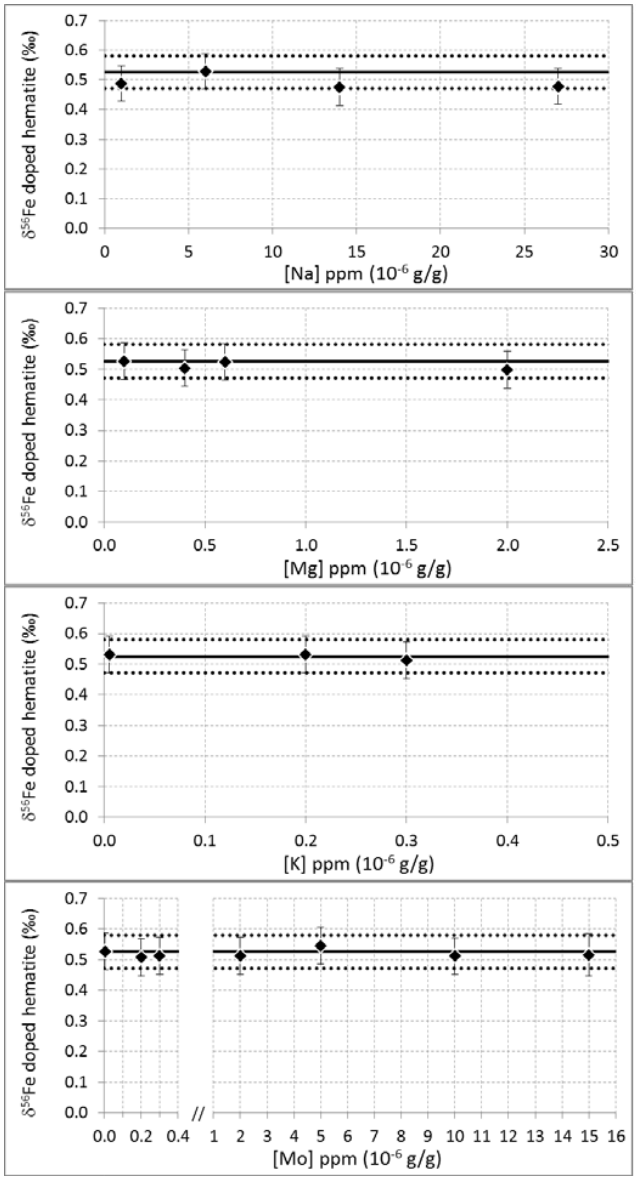

Figure 4. $\delta^{56}Fe$ of hematite (200ppb natural Fe) doped with variable amounts of Na, Mg, K and Mo. Diamonds are the averages of duplicate measurements. Error bars are 2 standard deviations of the duplicate measurements or the long term internal precision (2SD) of our instrument (0.06‰), whichever the greatest. The horizontal black lines show the $\delta^{56}Fe$ of pure (un-doped) hematite measured during the same analytical session; mean value (solid line) ± 2 standard deviations (dotted lines).

$\delta^{56}Fe$ measurements in two ways. Because it is a major element in many natural samples (e.g. rocks, waters, shells), significant levels could be expected in some purified samples, which could lead to matrix effects. In addition, similarly to Ar, Ca may also cause poly-atomic interferences on Fe isotopes, as shown previously[9] . The molecular ions $^{40}Ca^{14}N$, $^{40}Ca^{16}O$, $^{40}Ca^{16}O^{1}H$ and $^{42}Ca^{16}O$ may interfere on ^{54}Fe, ^{56}Fe, ^{57}Fe and ^{58}Fe, respectively. The weak Ca ionization energy compared to Fe (and thus high

degree of ionization, cf. Table 3) potentially reinforces both perturbations.

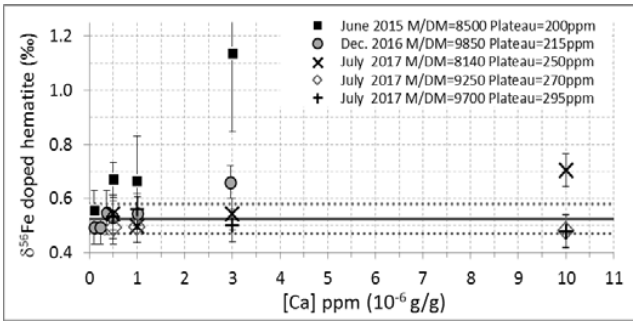

Figure 5. δ^{56}Fe of hematite (200ppb natural Fe) doped with variable amounts of Ca, for 5 measurement sessions. Data points are the averages of replicate measurements (n=2 to 5). Error bars are 2 standard deviations of the replicate measurements for the 2015-16 data and the long term internal precision (2SD) of our instrument (0.06‰) for the 2017 data (no replicate). The horizontal black lines show the δ^{56}Fe of pure (un-doped) hematite measured during the same analytical session; mean value (solid line) ± 2 standard deviations (dotted lines).

Table 3. Ionization energies and degrees of ionization for element of interest [23]. Degree of ionization calculated from Saha equation with T plasma: 7500°K and $n_e = 10^{15}$ cm^{-3} (where n_e is the electron density)[23,24].

Element	Ionisation Energy (eV)	Degree of ionization (%)
Na	5.14	100
Mg	7.64	98
K	4.34	100
Ca	6.11	99
Ar	15.76	0.04
Fe	7.90	96
Ni	7.64	91
Mo	7.10	98

Measurements performed in June 2015, together with the other tests presented above, show that with only 0.5ppm Ca, the measurement of the hematite δ^{56}Fe was significantly biased; it was found to be 0.67‰ instead of 0.52‰±0.06(2SD) (black squares in Fig. 5). This evidences a much higher δ^{56}Fe measurement sensitivity to the Ca contents compared to other elements tested for matrix effects (e.g. no perturbation up to 27ppm Na or 15ppm Mo). This observation suggest that the observed perturbations are more likely due to interferences rather than to matrix effects. This confirms previous works[9] and is further confirmed by additional information given below.

As explained at the beginning of the Experimental section, measurements are performed on the peak shoulders, in order to stay away from the ArO, ArOH and ArN interferences (cf. Fig. 1). This is usually done by looking at the peak shapes produced by pure Fe solutions and by tuning the instrument in order to maximize the width of the Fe shoulder, i.e. the Fe plateau, and the slope of the peak flanks, i.e. the mass resolving power. Then, the absence of significant interference contributions to the Fe signal is checked by comparing the peak shapes produced by pure Fe solutions (where both Fe and the interferences contribute to the peak shapes) and HNO_3 solutions (where only interferences are present)[17]. ^{40}Ca is very slightly heavier than ^{40}Ar (M^{40}Ca= 39.96259 u, M^{40}Ar= 39.96238 u). Therefore, if the Fe plateau is free of the Ar molecular ion interference and if Ca molecular ions are not significantly more abundant than argon ones, then Ca should not cause any significant interference on the Fe measurements. However, the Ca concentrations may vary from one sample to another, and the calcium and argon molecular ion formation rates may be different. Therefore, resolving the argon molecular ion interferences is not a warranty that calcium molecular ion interferences will be resolved (even if ^{40}Ca is slightly heavier than ^{40}Ar). The effects of potential Ca molecular ion interferences needs therefore to be quantified.

Figure 5 displays the results obtained for the hematite doped with variable Ca amounts, during 5 different measurement sessions, for which the mass resolving power (aka resolution, R_{power} 5%, 95%[17]) and plateau width were different. It shows that during the sessions with the largest mass resolving power and plateau width, the perturbations were the smallest. For instance, with a mass resolving power of 9700 and a plateau of 295ppm, no perturbation was detected even with 10ppm Ca (for 200ppb natural Fe). This corresponds to Ca/Fe=50 (where Fe is Natural Fe). Again, this is significantly larger than the threshold documented previously (Ca/Fe=0.1, with a ^{54}Fe-^{58}Fe double spike and a different instrument, Thermoelemental AXIOM MC-ICPMS)[9].

The relations between mass resolving power, plateau width and perturbations are further displayed in Fig. 6. The latter shows, for the maximum Ca concentration of the 5 different measurement sessions (3ppm for the 2015 and 2016 tests and 10ppm for the 2017 tests), the magnitude of the perturbation (i.e. absolute value of the difference between the measured and the expected values) normalized to the Ca concentration, as a function of the mass resolving powers and the plateau widths. For instance, in June 2015, the maximum Ca concentration tested was 3ppm, the magnitude of the perturbation for this maximum Ca concentration was 0.6‰; this leads to 0.2‰ perturbation per ppm Ca, for a resolution and plateau width of 8500 and 200ppm respectively. While no relation is seen as a function of mass resolving power, the figure clearly shows that the perturbation decreases with increasing plateau width. The relationship between plateau width and magnitude of the perturbation unambiguously shows that the perturbations are caused by interferences and not by matrix effects.

Unlike Cr and Ni, Ca polyatomic ion interferences cannot be corrected for. While ^{54}Cr and ^{58}Ni interferences can be deduced from the measurement of ^{53}Cr and ^{60}Ni (cf. Experimental section), the intensity of Ca polyatomic ion interference depends on i) the Ca concentration, ii) the rate of production of the various Ca polyatomic ions, and iii) the precise mass (M in Fig. 1) at which the measurements are performed. While the first point could be measured (in dynamic mode), the 2 last points depend on many uncontrolled and potentially variable parameters, such as the efficiency of the desolvating system, the plasma temperature or the magnetic field intensity (that

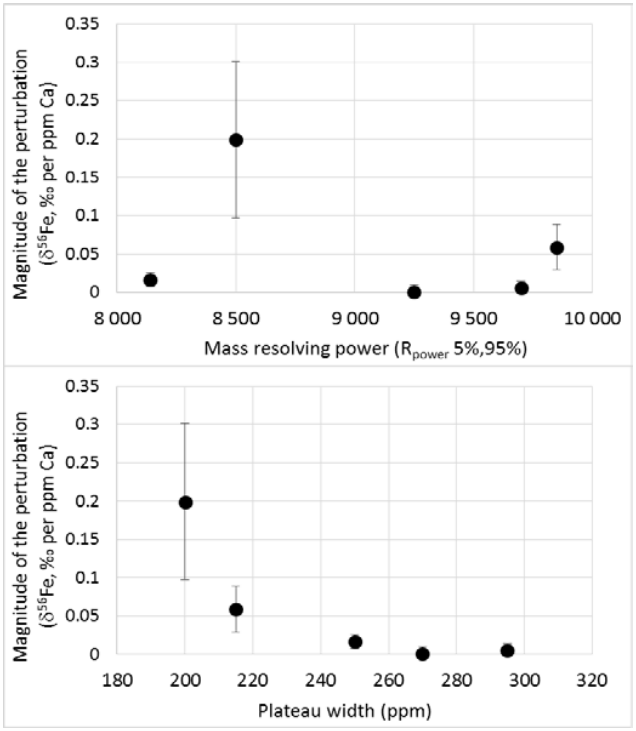

Figure 6. For the 5 different settings presented in Fig. 4 (variable resolutions and plateau widths), and for the maximum Ca concentration tested in each of these settings (3ppm for the 2015 and 2016 tests and 10ppm for the 2017 tests), the magnitude of the perturbation (i.e. the absolute value of the difference between the measured and the expected values) normalized to the Ca concentration, is shown as a function of the mass resolving power (top) and plateau width (bottom). Error bars show the uncertainties propagated from those shown (and described) in Fig. 4.

varies very slightly). Because Ca polyatomic ion interferences cannot be corrected for, they have to be reduced to an insignificant level.

In this aim, we preconize the following procedure. The calcium and iron concentrations should be determined in all purified samples prior to the MC-ICPMS measurements. Then, while tuning the MC-ICPMS (cups alignments, peak shape optimization), in addition to pure Fe and HNO_3 solutions, a pure Ca solution, with a Ca concentration at least equal to that of the highest Ca concentration found in samples, should be introduced and its peak shape measured, in order to verify that the Ca polyatomic ion interference level at mass M is comparable to (and not larger than) that of the HNO_3. Finally, an isotopic standard doped with this Ca level should be measured, to make sure that this Ca level does not significantly perturb the measurements. This is especially important for samples with high initial calcium contents, such as calcite minerals or tests, bones and teeth, but also marine samples, including seawater[25–30].

Conclusions

We have tested the effect of the following perturbations on the accuracy of the Fe isotopic composition measurement with a Neptune MC-ICPMS, using a ^{58}Fe-^{57}Fe double spike mass bias correction:

- Cr and Ni interferences;
- Na, Mg, K, Ca, Mo matrix effects;
- Ca polyatomic ion interferences.

We found that, for 200 ppb natural Fe solutions (mixed with 300 ppb double spike), the measurements (after Cr and Ni interference and mass bias corrections) were unperturbed up to these levels:

- [Cr]= 24ppb, i.e. 11.9% (g/g) of the natural [Fe]
- [Ni]= 8ppb, i.e. 3.9% (g/g) of the natural [Fe]
- [Na]= 27ppm; [Mg] =2ppm; [K] =0.5ppm; [Mo]=15ppm
- For Ca, the perturbation was shown to be related to the width of the Fe plateau, and therefore to be due to Ca polyatomic ion interferences ($^{40}Ca^{14}N$, $^{40}Ca^{16}O$, $^{40}Ca^{16}O^{1}H$ and $^{42}Ca^{16}O$), rather than to matrix effects. In our case (with our instruments), it was found that significant perturbations could occur with only 0.5ppm Ca for a plateau width of 200ppm, while no perturbation could be detected with 10ppm Ca for a plateau width of 295ppm. While such thresholds are published here for the first time for Cr, Ni, K and Mo,

As stressed earlier, we recall that, while working with samples with potentially high calcium contents (including purified seawater), Ca should carefully be taken into account (in addition to Cr and Ni) while 1) tuning the instrument and 2) checking the measurement accuracy with isotopic standards (i.e. doping the isotopic standard with Ca levels comparable to those of the samples).

Conflicts of interest

There are no conflicts to declare.

Acknowledgements

A. Marquet is thanked for her help within the Midi Pyrenees Observatory ICPMS facility. The French National Center for Research (CNRS) provided funding for FL, CP and JC, and Toulouse University for LA and JK. This study was fully funded by French public funds.

Notes and references

1 R. Schoenberg and F. von Blanckenburg, *Int. J. Mass Spectrom.*, 2005, **242**, 257–272.
2 B. L. Beard and C. M. Johnson, *Rev. Mineral. Geochem.*, 2004, **55**, 319–357.
3 N. Dauphas, S. G. John and O. Rouxel, *Rev. Mineral. Geochem.*, 2017, **82**, 415–510.
4 F. Albarède, P. Télouk and V. Balter, *Rev. Mineral. Geochem.*, 2017, **82**, 851–885.
5 C. Abadie, F. Lacan, A. Radic, C. Pradoux and F. Poitrasson, *Proc. Natl. Acad. Sci.*, 2017, **114**, 858–863.
6 J. Barling and D. Weis, *J. Anal. At. Spectrom.*, 2012, **27**, 653–662.
7 G. R. Gillson, D. J. Douglas, J. E. Fulford, K. W. Halligan and S. D. Tanner, *Anal. Chem.*, 1988, **60**, 1472–1474.
8 F. Albarède and B. Beard, *Rev. Mineral. Geochem.*, 2004, **55**, 113–152.
9 K. Dideriksen, J. A. Baker and S. L. S. Stipp, *Geochim. Cosmochim. Acta*, 2006, **70**, 118–132.

10 M.-A. Millet, J. A. Baker and C. E. Payne, *Chem. Geol.*, 2012, **304**–**305**, 18–25.
11 V. A. Finlayson, J. G. Konter and L. Ma, *Geochem. Geophys. Geosystems*, 2015, **16**, 4209–4222.
12 J. Sun, X. Zhu, S. Tang and Y. Chen, *Chin. J. Geochem.*, 2013, **32**, 1–6.
13 X.-Y. Zheng, B. L. Beard and C. M. Johnson, *J. Anal. At. Spectrom.*, 2018, **33**, 68–83.
14 Y. He, S. Ke, F.-Z. Teng, T. Wang, H. Wu, Y. Lu and S. Li, *Geostand. Geoanalytical Res.*, 2015, **39**, 341–356.
15 N. Dauphas, A. Pourmand and F.-Z. Teng, *Chem. Geol.*, 2009, **267**, 175–184.
16 J. F. Rudge, B. C. Reynolds and B. Bourdon, *Chem. Geol.*, 2009, **265**, 420–431.
17 S. Weyer and J. B. Schwieters, *Int. J. Mass Spectrom.*, 2003, **226**, 355–368.
18 J. G. John, *J. Anal. At. Spectrom.*, 2012, **27**, 2123–2131.
19 F. Lacan, A. Radic, M. Labatut, C. Jeandel, F. Poitrasson, G. Sarthou, C. Pradoux, J. Chmeleff and R. Freydier, *Anal. Chem.*, 2010, **82**, 7103–7111.
20 F. Poitrasson and R. Freydier, *Chem. Geol.*, 2005, **222**, 132–147.
21 F. Lacan, A. Radic, C. Jeandel, F. Poitrasson, G. Sarthou, C. Pradoux and R. Freydier, *Geophys. Res. Lett.*, , DOI:10.1029/2008GL035841.
22 C. Siebert, T. F. Nägler and J. D. Kraners, *Geochem. Geophys. Geosystems*, 2001, **2**, 2000GC000124.
23 R. S. Houk, *Anal. Chem.*, 1986, **58**, 97A–105A.
24 P. W. J. M. Boumans, in *Theory of Spectrochemical Excitation*, Springer, Boston, MA, 1966, pp. 156–232.
25 A. Heimann, C. M. Johnson, B. L. Beard, J. W. Valley, E. E. Roden, M. J. Spicuzza and N. J. Beukes, *Earth Planet. Sci. Lett.*, 2010, **294**, 8–18.
26 S. Emmanuel, J. A. Schuessler, J. Vinther, A. Matthews and F. von Blanckenburg, *Biogeosciences*, 2014, **11**, 5493–5502.
27 K. Jaouen, V. Balter, E. Herrscher, A. Lamboux, P. Telouk and F. Albarède, *Am. J. Phys. Anthropol.*, 2012, **148**, 334–340.
28 B. N. Revels, D. C. Ohnemus, P. J. Lam, T. M. Conway and S. G. John, *Deep Sea Res. Part II Top. Stud. Oceanogr.*, 2015, **116**, 321–331.
29 M. Labatut, F. Lacan, C. Pradoux, J. Chmeleff, A. Radic, J. W. Murray, F. Poitrasson, A. M. Johansen and F. Thil, *Glob. Biogeochem. Cycles*, 2014, 2014GB004928.
30 J. K. Klar, R. H. James, D. Gibbs, A. Lough, I. Parkinson, J. A. Milton, J. A. Hawkes and D. P. Connelly, *Geology*, 2017, **45**, 351–354.